University of Nevada, Reno

CFD Simulation of Chemical Looping Combustion System

A dissertation submitted in partial fulfillment of the
requirements for the degree of Doctor of Philosophy in
Chemical Engineering

by

Md Helal Uddin

Dr. Charles J. Coronella/ Dissertation Advisor

December, 2016

THE GRADUATE SCHOOL

We recommend that the dissertation
prepared under our supervision by

MD HELAL UDDIN

Entitled

CFD Simulation Of Chemical Looping Combustion System

be accepted in partial fulfillment of the
requirements for the degree of

DOCTOR OF PHILOSOPHY

Dr. Charles J. Coronella , Advisor

Dr. Victor R. Vasquez, Committee Member

Dr. Sage R. Hiibel, Committee Member

Dr. Mustafa Hadj-Nacer, Committee Member

Dr. Aleksey Telyakovskiy , Graduate School Representative

David W. Zeh, Ph. D., Dean, Graduate School

December, 2016

Abstract

Emerging technologies for greenhouse-gas mitigation have assumed growing importance due to the imminent threat of climate change. The American Clean Energy Security Act and the American Power Act project that about 30% of fossil-fuel-based electricity generation to come from power plants with carbon capture and sequestration (CCS) by 2040, rising to approximately 59% by 2050. Chemical looping combustion (CLC) is one of the most promising cost-effective technologies that can be retrofitted onto existing power plants for CCS. The main drawback attributed to CLC is a very low confidence level as a consequence of the lack of maturity of the technology. Use of computational fluid dynamics (CFD) has the potential to boost the development and implementation of commercial-scale CLC units. This dissertation focuses on designing a novel semi-batch CLC unit using fluidized-bed reactors and modeling the hydrodynamics of fluidized bed reactors with use of CFD. The National Energy Technology Laboratory's (NETL, USA) open-source code MFIX is used in this study as flow solver for CFD models.

In this dissertation, a conceptual design is developed that leads to fabrication of a 100-kW$_{th}$ semi-batch CLC prototype unit by ZERE Energy and Biofuels, Inc. San Jose, California. The hydrodynamics of the prototype unit are extensively studied using mathematical modeling and CFD. A multi-stage numerical model has been developed to investigate the behavior of a fuel reactor used in CLC unit. To predict the behavior of mass transfer in the CLC reactor, a combination of perturbation theory and semi-empirical correlation is suggested.

Much of the work presented in this dissertation is focused on improving the ability to use CFD for process development. The grid size used in numerical simulations should be sufficiently small so that the meso-scale structures prevailing in the gas-fluidized beds can be captured explicitly. This restricts CFD in studying industrial-scale fluidized bed reactors. Thus, a generalized grid size that is sufficient to obtain a grid-independent solution of two-fluid CFD model is suggested in this study. In order to fully understand the complex interaction between fluid phases of CFD models, a 3-D face-masking algorithm is developed and applied to assist post-processing CFD results for identification and tracking of gas bubbles in a fluidized bed. Finally, the hydrodynamics of multiphase flow reactor at high-temperature is investigated through the particle-particle restitution coefficient in numerical simulations. In conclusion, findings of this dissertation will be useful for scale-up, design, or process optimization for reliable commercial CLC plants reducing economic risk, and potentially allowing for rapid scale-up.

Acknowledgements

I solemnly remember and pray to Allah for everything HE has blessed on me.
I would like to begin by sincerely thanking my advisor, Prof. Charles J. Coronella for his constant support, guidance and mentorship over the course of this dissertation. His training, advice and insight into things have been invaluable. Whenever I was bereft of ideas, my discussions with him and his insights always helped me get back on the right track. He has always encouraged me to explore a wide variety of opportunities. I have truly learnt a lot from him over the past 5 years and for this, I am very grateful.

I would like to thank my dissertation committee members, Dr. Victor R. Vasquez, Dr. Sage R. Hiibel, Dr. Aleksey Telyakovskiy and Dr. Mustafa Hadj-Nacer for being on the committee and for their cooperation and suggestions. Specially, I am grateful to Dr. Victor R. Vasquez, a wonderful mentor and source of inspiration.

I am indebted to my parents for everything they did for me; their generous support, motivation and trust in me since childhood, which helped me aim higher from time to time. Thanks to my sisters and brothers and their respective families for being a constant source of inspiration. It would not have been possible to come in the U.S, if Ms. Shaheen and her family were not there for me. Thanks to my wife and her family for being helpful and inspirational.

I am grateful to Dr. Toufiq Reza, my fellow junior country friend who was there for in need of anything from household to lab in the U.S. He has taught me so much and has been invaluable in enabling me to conduct research. His emotional support and kindness has meant so much to me during my graduate school experience. Special thanks to Dr.

Joan G. Lynam, the most helpful person in University of Nevada Reno (UNR), for her enormous invaluable suggestions, personal encouragements, emotional and moral supports.

Thanks to all my wonderful friends in Bangladesh and at UNR. Thanks also to all my relatives whose confidence in me further encouraged my performance and betterment. I sincerely thanks to all my teachers since childhood, who have been instrumental in installing knowledge and morals in me and in shaping me.

Finally, I want to thank the California Energy Commission and ZERE Energy and Biofuels, Inc. San Jose, California for their financial support. I gratefully acknowledge meaningful discussions with Marisa Zuzga, the chief of technical team of ZERE.

Table of contents

LIST OF TABLES

LIST OF FIGURES

CHAPTER 1

Introduction

1.1 Global climate change and CO_2 mitigation

Climate change is obvious now globally. The Intergovernmental Panel on Climate Change (IPCC) and the NASA Goddard Institute for Space Studies [1] reported that the average surface temperature of the earth has increased during the twentieth century by about 0.6° ± 0.2°C. "Human influence on the climate is clear" and human activities—primarily the burning of fossil fuels for energy production—have increased the greenhouse gas (GHG) content of the earth's atmosphere significantly over the same period [2]. This finding is supported by the detection of land and sea temperature rise, the changes in global water cycle, the reductions in snow and ice, sea-level rise, and the changes in climate extremes [3]. The climate researchers agree that carbon dioxide (CO_2) is one of the most important greenhouse gases because it traps heat near the planet's surface. It represents about 75% of the global anthropogenic GHG and it has a high residence time in the atmosphere [3].

NOAA's Mauna Loa Observatory [4] lab records a gradual increase of global GHG from a pre-industrial value of about 280 ppm to 400 ppm in 2016, as shown in Figure 1- 1. The climate researchers and the nations that participated in 1997 Kyoto Protocol [5] have suggested limiting the global CO_2 concentration to 450 ppm in order to avoid the most catastrophic changes on Earth. To achieve this goal, it is provisioned for a mean reduction in the GHG emissions of the developed countries of 5.2% over the period 2008-2012 compared to 1990 levels.

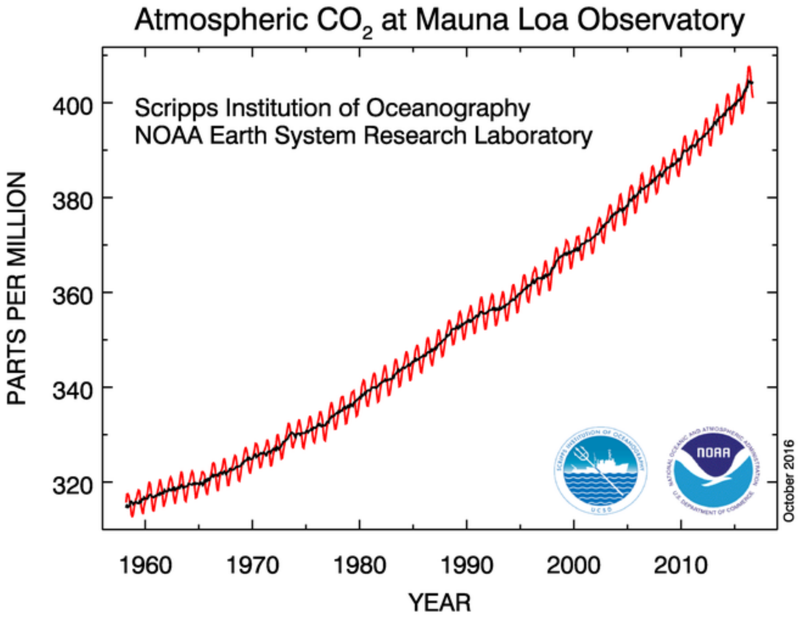

Figure 1- 1. Atmospheric carbon dioxide at Mauna Loa Observatory, Hawai‘i, 1958-2016. NOAA-ESRL, 2016 [4]. In the above figure, the red line represents the yearly mean values, centered on the middle of each month. The black line represents the same, after correction for the average seasonal cycle.

According to IPCC assessment report on CO_2 emission from 1970 to 2010 [2], fossil fuel combustion and industrial processes contributed about 78% increase of the total GHG emissions. However, dependency on fossil fuel is likely inescapable as the U.S. Energy Information Administration’s (EIA) has predicted that 78% of energy from fossil sources -gas, oil and coal will still satisfy the demand during the first part of the 21st century [6]. Even though consumption of renewable fuels – wind, solar, geothermal, hydro, biomass – is expected to rise faster than consumption of fossil fuels, these energy sources will not yet be ready to be substituted massively in the near future.

Therefore, the reduction of GHG emissions from combustion and industrial processes is urgently needed to maintain a sustainable economic development as well as to avoid catastrophic climate change impact. The IPCC special report on GHG reduction [7] recognized several technological alternatives and advocated for the development of chemical or physical technologies for carbon capture and storage (CCS). The U.S. Interagency Task Force on CCS [8] reported that CCS technology can play a major role in reducing GHG emissions globally. Independent analysis made by the IPCC [7] and IEA [9] suggested that CCS technology could substantially reduce CO_2 emission by 15–55% through a cumulative mitigation effort worldwide by 2100. However, widespread cost-effective deployment of CCS will occur only if the technology is commercially available at economically competitive prices.

1.2 Carbon capture and storage (CCS)

The CCS technology involves three-step process that includes (1) the capture of CO_2 produced at large energy and industrial plants, (2) compressing it for transportation, and (3) injecting it into receptive geologic formations on land or at sea where it is stored permanently. CCS would thus allow fossil fuels to be used with low emissions of greenhouse gases. An excellent overview of the CCS processes is laid out in IPCC Special Report on Carbon Dioxide Capture and Storage [7]. Figure 1- 2 illustrates the three main components of the CCS process: capture, transport and storage.

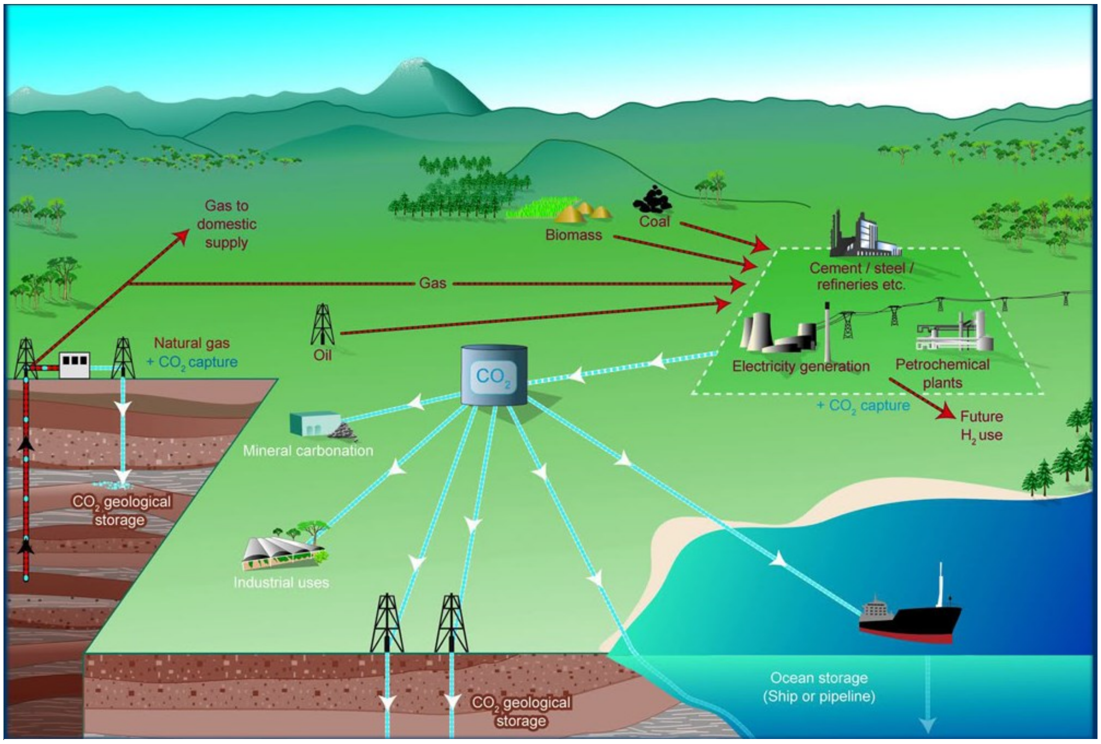

Figure 1- 2. Carbon capture and storage (CCS) systems showing carbon sources for which CCS might work and showing transport and storage options. This figure is adopted from IPCC, 2005 [7].

Technologies exist for all three components of CCS, but they have not yet been deployed at the scale necessary to help achieve GHG reduction targets. For CCS to achieve the estimated economic and environmental potential, several hundreds to thousands of CO_2 capture systems would need to be installed over the coming century, each capturing 1–5 $MtCO_2$ per year [10]. It is the most promising technology that is compatible with the most current energy infrastructures that exists around the world.

The U.S. Interagency Task Force on CCS [8] estimated the cost of current technology for CCS in energy and industrial plants ranges between \$60 and \$114 per ton of CO_2 avoided depending on the plant type. Approximately 70–90% of that cost is associated with capture and compression [11]. Thus, the successful development of advanced CO_2 capture technologies is critical for maintaining the cost-effectiveness of fossil fuel-based power and production industries and to achieve the future goal of global GHG emissions reduction.

1.2.1 Current status of carbon capture technologies

The identified technologies for carbon capture can be divided into three main categories: (i) post-combustion capture; (ii) pre-combustion capture; and (iii) oxy-fuel combustion capture. Toftegaard et al. [12] compiled an excellent review on the current status of these technologies. Figure 1- 3 shows the main operations concerned with the post-, pre-, and oxy-fuel combustion technologies.

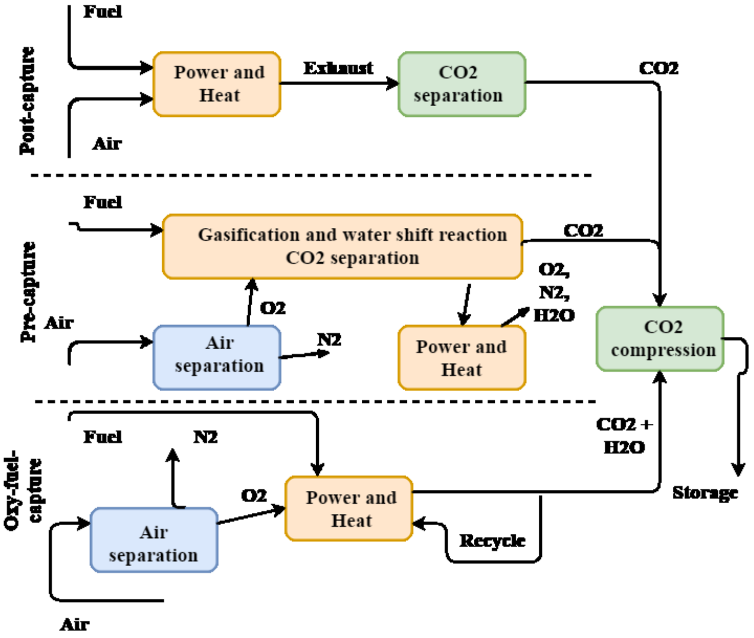

Figure 1- 3. Possible, overall plant configurations for the three main categories of carbon capture technologies [12].

1.2.2 Post-combustion capture

Post-combustion refers capturing of CO_2 from combustion flue gases prior to discharge to the atmosphere. It is primarily applicable to conventional pulverized coal (PC)-fired power plants [13]. Post-combustion capture is achieved through chemical or physical absorption process.

Glycol dimethylethers (Selexol) and propylene carbonate are the most common physical absorption solvents used for post-combustion capture. In chemical absorption systems, initially, a liquid scrubber absorbs CO_2 from the flue gas and later a desorber separates the absorption liquid and CO_2. Commercially available aqueous alkaline solvent such as monoethanolamine (MEA), chilled ammonia, activated methyl diethanolamine (aMDEA) or hot potassium carbonate solutions can be used. The chemical absorption process is undoubtedly the most applied technique for CO_2 capture in post-combustion processes [14].

1.2.3 Pre-combustion capture

In pre-combustion capture, CO_2 is removed from fossil fuels before combustion. Typically, this is conducted in integrated gasification combined cycle (IGCC) power plants where fuel such as coal is partially oxidized in steam and oxygen/air under high temperature and pressure to form synthesis gas. Applying the water-gas shift reaction that converts CO and water (H_2O) to H_2 and CO_2, a concentrated CO_2-rich gas mixture is produced that allows for easier removal before the H_2 is combusted [12, 15, 16]. Due to the high concentration of CO_2, pre-combustion capture typically is more efficient but the capital costs of the base gasification process are often more expensive than traditional pulverized-coal power plants [12].

1.2.4 Oxy-fuel combustion

In oxy-fuel combustion process, fuel is combusted in pure oxygen rather than air, generating a flue gas that contains mainly water vapor and CO_2, thereby, allowing efficient separation of CO_2. However, implementation of the oxy-fuel combustion technology in existing pulverized-coal fired power plants demands substantial modification of the existing plant configuration compared to the post-combustion absorption processes. This is mainly due to the fact that the combustion chemistry is altered by substituting recycled flue gas (mainly CO_2 and water) for nitrogen in the oxidizer [12]. The greatest drawback of this process is the separation of oxygen from air that imposes a very large energy penalty on the plant [17]. The estimated efficiency reduction in a coal gasification unit is 6-9% and in a natural gas unit is 5-12% [18].

1.2.5 Emerging carbon capture technologies

In addition to the capture technologies discussed above, emerging technologies such as chemical-looping combustion (CLC), advanced membrane separation, ionic liquids, metal organic frameworks, carbonation–calcination cycles, enzyme-based systems are showing greater possibility in reducing the cost of power generation and the energy penalty concerned with carbon capture. Broad overviews of these technologies and their current state of development are summarized in several articles [19-21]. Among these emerging technologies, the CLC process is suggested one of the best alternatives to reduce the economic cost of CO_2 capture [22]. Moreover, the special report on Carbon Dioxide Capture and Storage (IPCC) identified CLC as one of the cheapest technologies for CO_2 capture [7]. However, the main drawback attributed to CLC is a very low confidence level as a consequence of the lack of maturity of the technology.

1.3 Chemical-Looping Combustion

CLC is an indirect combustion system using of a metallic-oxide as oxygen transferring medium from air to the fuel avoiding the direct contact between them [23].

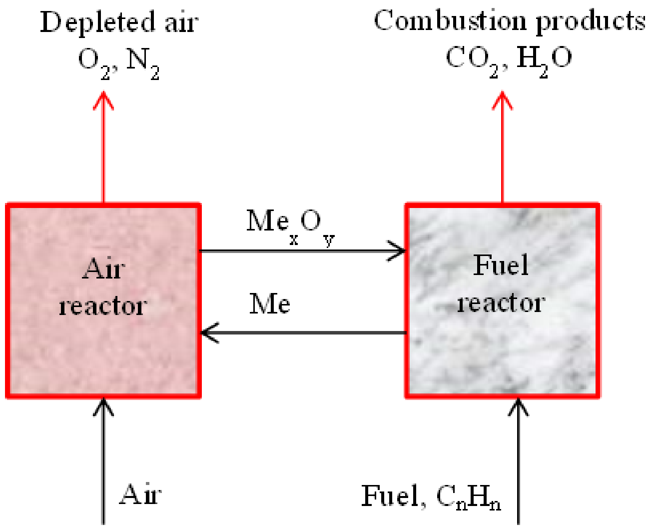

Figure 1- 4. A simplified schematic representation of the chemical-looping combustion process.

Commonly, two fluidized bed reactors are used in the CLC process, designated as air and fuel reactors, as shown in Figure 1- 4 [23]. Fuel is burned or oxidized in the fuel reactor by the metallic-oxide and it is reduced to metal. The reduced oxygen carrier is transferred into the air reactor where it is re-oxidized with air, and the material regenerated is ready to start a new cycle. The flue gas leaving the air reactor contains N_2 and un-reacted O_2 [23]. The exit gas from the fuel reactor contains only CO_2 and H_2O. After water condensation, almost pure CO_2 can be obtained with minimal energy loss and at a low cost [24]. Table 1- 1 shows a brief summary of the CLC plants that are under-going operation around the world.

Table 1- 1. Overview of existing chemical looping combustion plant status. Data from [25, 26].

Location	Unit, kW	Oxide tested	Time, h	Fuel	Year
Chalmers, Sweden	10	NiO, Fe_2O_3	1350	NG	2004
KIER, S Korea	50	NiO, CoO	28	NG	2004
CSIC, Spain	10	CuO, NiO	140	NG	2006
Chalmers, Sweden	0.3	NiO, Mn_3O_4, Fe_2O_3, ilmenite	730	NG + Syngas	2006
Chalmers, Sweden	10 (solid fuel)	ilmenite	90	Coal, Pet coke	2008
CSIC, Spain	5.0	NiO, CuO	660	NG	2009
KAIST, S Korea	1.0	NiO + Fe_2O_3	?	CH_4	2009
Vienna U.T., Austria	140	ilmenite, NiO	390	NG, CO, H_2	2009
Alstom, Connecticut, USA	15	Nio	100	NG	2009
Nanjing, China	10 (solid fuel)	NiO, Fe_2O_3	230	Coal, Biomass	2009
KIER, S Korea	50	NiO, CoO	300	NG + Syngas	2010
Nanjing, China	1.0 (solid fuel)	Fe_2O_3 (ore)	10	Coal	2010
Darmstadt, Germany	1000	ilmenite	Operational, 2011	Coal	2011
Alstom, Connecticut, USA	3000	$CaSO_4$	Operational, 2011	Coal	2011

1.4 Fluidized bed reactor

Fluidized beds are one of the most applied technologies in petroleum, chemical and energy industries, which involve highly complex multiphase flow phenomena [27]. The popularity of fluidized bed combustion is due largely to the technology's fuel flexibility. Almost any combustible material, from coal to municipal waste, can be burned, extremely high surface area contact between fluid and solid per unit bed volume, high levels of solid mixing, and frequent particle-particle and particle-wall collisions are a few of the technology’s positive characteristics. A comprehensive overview on different configuration of fluidized bed reactors and their application is given by Kunii and Levenspiel [28]. Despite the widespread application and advantages, much of the development and design of fluidized bed reactors has been empirical due to the complex flow behavior of gas–solid systems. The performance of a fluidized bed is significantly influenced by gas-solid distribution, facilitating rapid solids mixing, impacting reaction rates, product selectivity, mass transfer, heat transfer rates to immersed surfaces, and elutriation of particles from the bed [29]. Therefore, a sound understanding of the mechanisms governing the complex flow phenomena involved in a fluidized bed still remains an open technical and scientific issue.

1.5 Computational fluid dynamics

It is evident that fluidized bed reactors are part of many energy conversion and chemical processing units. For fluidized beds used in CLC application in carbon capture, process parameters such as oxygen-carrier particle attrition, agglomeration, sintering, and corresponding loss of combustion efficiency are critical for the successful implementation of this process. The efficiency of the interconnected fluidized bed CLC process depends largely on the minimization of gas leakage between the two reactors.

Clearly, the successful operation and performance of fluidized bed reactors are greatly influenced by the hydrodynamics, mass transfer, heat transfer, reaction kinetics, solid mixing, elutriation, and solid catalyst activity. Traditionally, fluidized bed reactors are designed and scaled-up based on the results from bench-scale batch reactors or continuous pilot-scale units. Although many processes have been successfully scaled-up in this manner, some notable failures have occurred [27, 30, 31] due to the flow patterns that are difficult, expensive, or impossible to study using traditional experimental techniques. Also, in some cases the laboratory-scale units exhibit different hydrodynamic behavior than do the large-scale units, and intermediate pilot-scale units are expensive to build and operate [32].

The first principle-based computational fluid dynamics (CFD) models derived from the fundamental laws of mass, momentum, energy, and species conservation have the potential to bridge the data gaps in the results of bench- or pilot-scale experiments and, thereby, to aid in the design of large-scale industrial reactors. CFD models are capable of describing chemical reactions as well as mass and heat transfer in dense or dilute gas-solids multiphase flows. They are capable of intrinsically capturing the complex hydrodynamic behavior of gas-solid in fluidized bed reactors. CFD can also provide insight useful for scale-up, design, or process optimization for reliable commercial plants reducing economic risk, and potentially allowing for rapid scale-up

[33-36]. In fact, CFD can allow for virtual experimental "measurement" that cannot be done in the physical world easily, or at all.

Hydrodynamic models have been developed and applied to describe fluidization since the early 60's [37-40]. Advances in the theory and the availability of fast, affordable computing power have facilitated solving these equations numerically.

CFD models used to describe the gas-solid fluidization systems are categorized in two groups:

- Eulerian - Lagrangian models or discrete element models (DEM)
- Eulerian - Eulerian models or two-fluid models

The Eulerian-Lagrangian models [41, 42] that consider fluids as continua and solid as discrete particles provides a direct physical interpretation of the fluid-particle, particle-particle, and particle-wall interactions, but the computational demand rises strongly with the number of tracked particles. So, the application of models based on the DEM approach is still limited to small-scale systems. The Eulerian- Eulerian models treat the particle phase as a continuum and average out motion on the scale of individual particles, which enables the model gas-solid fluidized beds of realistic size [35, 43 44]. A detailed description of this model is given in the following section.

1.5.1 Eulerian-Eulerian Two-Fluid Model

In the formulation of the two-fluid model (TFM) hydrodynamics, both the fluid and the solid phases are treated as interpenetrating continua. All the particles are considered to be identical, characterized by an effective diameter and identical material properties [32]. Thus, the conservation of mass, momentum, and energy can be preserved for each of the phase to formulate the partial differential equations that can be analytically or numerically solved for the field properties.

First Anderson and Jackson [37], and later Ishii [45] proposed the governing equations using a formal mathematical definition of local mean variables to translate the point Navier-Stokes equations for the fluid and the Newton's equation of motion for a single particle directly into continuum equations representing momentum balances for the fluid and solid phases [46].

The continuity equations for the gas and solid phase are defined as

$$\frac{\partial}{\partial t}(\varepsilon\,\rho)_g + \frac{\partial}{\partial x_i}(\varepsilon\,\rho\,U_i)_g = \sum_{n=1}^{N_g} R_{gn} \tag{1}$$

$$\frac{\partial}{\partial t}(\varepsilon\,\rho)_s + \frac{\partial}{\partial x_i}(\varepsilon\,\rho\,U_i)_s = \sum_{n=1}^{N_s} R_{sn} \tag{2}$$

The gas-phase momentum balance is expressed as

$$\left[\frac{\partial}{\partial t}(\varepsilon\,\rho\,U_i)_g + \frac{\partial}{\partial x_j}(\varepsilon\,\rho\,U_j U_i)_g\right] = -\,\varepsilon_g \frac{\partial P_g}{\partial x_i} + \frac{\partial \tau_{gij}}{\partial x_j} - \sum_{k=1}^{M} I_{kgi} + \boldsymbol{g}\,(\varepsilon\,\rho)_g + f_{gi} \tag{3}$$

The momentum equation for the mth solids phase is defined as

$$\left[\frac{\partial}{\partial t}(\varepsilon\,\rho\,U_i)_s + \frac{\partial}{\partial x_j}(\varepsilon\,\rho\,U_j U_i)_s\right] = -\,\varepsilon_s \frac{\partial P_g}{\partial x_i} + \frac{\partial \tau_{sij}}{\partial x_j} + \boldsymbol{I}_{gsi} - \sum_{k=1}^{M} \boldsymbol{I}_{ksi} + \boldsymbol{g}\,(\varepsilon\,\rho)_s \tag{4}$$

The energy balance equation for gas and solid phase are defined as

$$(\varepsilon\,\rho\,C_p)_g \left[\frac{\partial T_g}{\partial t} + U_j \frac{\partial T_g}{\partial x_j}\right]_g = -\,\frac{\partial q_{gi}}{\partial x_i} + \sum_{k=1}^{M} \gamma_{kg}(T_s - T_g) - \Delta H_g + \gamma_{Rg}(T_{Rg}^4 - T_g^4) \tag{5}$$

$$\left(\varepsilon\,\rho\,C_p\right)_s\left[\frac{\partial T_g}{\partial t}+\;U_j\frac{\partial T_g}{\partial x_j}\right]_s=-\,\frac{\partial q_{si}}{\partial x_i}-\gamma_{gs}\left(T_s-T_g\right)-\Delta H_s+\gamma_{Rs}\left(T_{Rs}^4-T_g^4\right)\qquad(6)$$

The species balance equations for gas and phase are defined as

$$\left[\frac{\partial}{\partial t}(\varepsilon\,\rho\,X_n)_g+\frac{\partial}{\partial x_i}(\varepsilon\,\rho\,U_iX_n)_g\right]=\frac{\partial}{\partial x_i}\left(D_{ng}\frac{\partial X_{ng}}{\partial x_i}\right)+R_{ng}\qquad(7)$$

$$\left[\frac{\partial}{\partial t}(\varepsilon\,\rho\,X_n)_s+\frac{\partial}{\partial x_i}(\varepsilon\,\rho\,U_iX_n)_s\right]=\frac{\partial}{\partial x_i}\left(D_{ns}\frac{\partial X_{ns}}{\partial x_i}\right)+R_{ns}\qquad(8)$$

The point variables are averaged over regions that are large with respect to the particle diameter, but small with respect to the characteristic dimension of the complete system. Since the resultant continuum approximation for the solid phase has no equation of state and lacks variables such as viscosity and normal stress [47], the average balance equations must be closed by specifying several constitutive relations, such as a fluid-phase equation of state, fluid-solids and solids-solids momentum transfer and heat transfer, and fluid and solids phase stress tensors. These closure relationships are necessary for solving practical problems of interest. This challenging task is accomplished by using a variety of approaches, ranging from empirical information to kinetic theory. Most of the differences between multiphase theories originate from such closure assumptions, some of which are the subject of much debate [32].

1.5.2 Closure relations

1.5.2.1 The kinetic theory of granular flow (KTGF)

The solid-phase stress introduced in the continuum approximation of solid momentum equation shown in equation 4 requires a constitutive relation. Lun et al. [43] first derived a constitutive relation based on kinetic theory concepts describing the flow of smooth, slightly inelastic, spherical particles to model solids stresses resulting from particle collisions and uncorrelated translations.

$$\frac{3}{2}\rho_s\left[\frac{\partial}{\partial t}(\varepsilon\,\Theta)_s+\frac{\partial}{\partial x_j}(\varepsilon\,\rho\,U_j\Theta)_s\right]=\frac{\partial}{\partial x_j}\left(\kappa_s\frac{\partial}{\partial x_j}\Theta_s\right)+\tau_{sij}\frac{\partial U_{si}}{\partial x_j}+\Pi_s-(\varepsilon\,\rho\,J)_s \tag{9}$$

Analogous to the thermodynamic temperature for gases [48], the granular temperature was introduced as a measure of the particle velocity fluctuations. Kinetic energy contained in the random particle motions is quantified in terms of granular temperature which is required to supplement the continuity and momentum balance for both phases.

1.5.2.2 Solid-phase stress tensor

The hydrostatic part of the stress tensor (solids pressure) represents the normal solid-phase forces due to particle-particle interactions. Lun et al. [43] derived the solid pressure that is widely used in CFD.

$$P_s=\varepsilon_s\rho_s\Theta_s\left(1+4\eta\sum_{n=1}^{M}\varepsilon_n\,g_0\right)=\varepsilon_s\rho_s\Theta_s+\ 4\eta\varepsilon_s\rho_s\Theta_s\ \sum_{n=1}^{M}\varepsilon_n\,\mathrm{g}_0 \tag{10}$$

The first part of the solids pressure represents the kinetic contribution and the second part represents the collisional contribution. Lun et al. [43] defined the solids bulk viscosity as the resistance of the particle suspension against compression.

$$\lambda_s=\frac{8}{3}\varepsilon_s^2\rho_s d_s g_0\eta\sqrt{\frac{\Theta_s}{\pi}} \tag{11}$$

However, the kinetic theory description for the solids shear viscosity often differs between the various two-fluid models. Table 1- 2 lists all the available solid shear viscosity models available in literature. Van Wachem et al. [46] discussed the differences between these models; however, all models show good agreement for dense gas-solid fluidized bed.

Table 1- 2. Formulations of solids shear viscosity in literature.

Lun et al. [41]	$\mu_s = \frac{5\sqrt{\pi\Theta_s}}{96}\rho_s d_s\left[\left(\frac{1}{\eta g_0}+\frac{8\varepsilon_s}{5}\right)\left(\frac{1+\frac{8}{5}\eta(3\eta-2)\varepsilon_s g_0}{2-\eta}\right)+\frac{768}{25\pi}\eta\varepsilon_s^2 g_0\right]$
Syamlal et al. [30]	$\mu_s = \frac{8}{5}\varepsilon_s^2\rho_s d_s g_0\eta\sqrt{\frac{\Theta_s}{\pi}}+\frac{\varepsilon_s\sqrt{\pi\Theta_s}}{6(3-e)}\rho_s d_s\left(1+\frac{4}{5}\eta(3e-1)\varepsilon_s g_0\right)$
Gidaspow [47]	$\mu_s = \frac{8}{5}\varepsilon_s^2\rho_s d_s g_0\eta\sqrt{\frac{\Theta_s}{\pi}}+\frac{5\sqrt{\pi\Theta_s}}{96\eta g_0}\rho_s d_s\left(1+\frac{8}{5}\eta\varepsilon_s g_0\right)^2$
Hrenya and Sinclair [48]	$\mu_s = \frac{5\sqrt{\pi\Theta_s}}{96}\rho_s d_s\left[\left(\frac{1}{\eta g_0}\frac{1}{1+\frac{\lambda_s f p}{R}}+\frac{8\varepsilon_s}{5}\right)\left(\frac{1+\frac{8}{5}\eta(3\eta-2)\varepsilon_s g_0}{2-\eta}\right)+\frac{768}{25\pi}\eta\varepsilon_s^2 g_0\right]$

1.5.2.3 Conductivity of granular energy

Similar to the solids shear viscosity, there is no general agreement in the formulation of the solids thermal conductivity.

Table 1- 3. Formulations of solids thermal conductivity in literature.

Lun et al. [43]	$\kappa_s = \frac{25\sqrt{\pi\Theta_s}}{128}\rho_s d_s\left[\left(\frac{8}{\eta g_0}+\frac{96\varepsilon_s}{5}\right)\left(\frac{1+\frac{12}{5}\eta^2(4\eta-3)\varepsilon_s g_0}{41-33\eta}\right)+\frac{512}{25\pi}\eta\varepsilon_s^2 g_0\right]$
Syamlal et al. [32]	$\kappa_s = \frac{15\sqrt{\pi\Theta_s}}{4(41-33\eta)}\varepsilon_s\rho_s d_s\left(1+\frac{12}{5}\eta^2(4\eta-3)\varepsilon_s g_0+\frac{16}{15\pi}(41-33\eta)\eta\varepsilon_s g_0\right)$
Gidaspow [49]	$\kappa_s = \frac{75\sqrt{\pi\Theta_s}}{384\eta g_0}\rho_s d_s\left(1+\frac{12}{5}\eta\varepsilon_s g_0\right)^2 + 4\varepsilon_s^2\rho_s d_s g_0\eta\sqrt{\frac{\Theta_s}{\pi}}$

It has a kinetic contribution and a collisional contribution. Table 1- 3 lists the solids thermal conductivity model used in CFD model. Solid thermal conductivity models also show good agreement for dense gas-solid fluidized bed.

1.5.2.4 Dissipation and generation of granular energy

The rate of granular energy dissipation within the solid phases due to collisions between the particles constituting the continuum is approximated using Lun et al. [43] formulation as

$$\gamma_s = 12\left(1 - e^2\right)\frac{\varepsilon_s^2 \rho_s g_0}{d_s\sqrt{\pi}}{\Theta_s}^{3/2} \tag{12}$$

The transfer of granular energy between the fluid and the solid phases represents the transfer to the fluid phase of the kinetic energy of random fluctuations in particle velocity. The expression for the rate of energy dissipation resulting from fluctuations is

$$J_s = \frac{3}{2}\frac{\mu_s \varepsilon_s \Theta_s}{d_s^2} C_{Deff} - \frac{\beta^2 d_s \left(v_g - v_s\right)^2}{4\, \varepsilon_s \rho_s \sqrt{\pi \Theta_s}} \frac{1}{2\sqrt{\pi}} d_s \beta^2 \tag{13}$$

1.5.2.5 Radial distribution function

The solid-phase stress is dependent on the radial distribution function that describes how density varies as a function of distance from a reference particle. Table 1-4 lists all the radial distribution functions. A detail discussion of these functions can be found in [46].

Table 1- 4. Formulations of radial distribution function in literature.

Carnahan and Starling [51]	$g_0 = \frac{1}{\varepsilon_g} + \frac{3\varepsilon_s}{2\varepsilon_g^2} + \frac{\varepsilon_s^2}{2\varepsilon_g^3}$
Lun and Savage [52]	$g_0 = \left(1 - \left(\frac{\varepsilon_s}{\varepsilon_{s,max}}\right)^{1/3}\right)^{-1}$
Sinclair and Jackson [53]	$g_0 = \left(1 - \left(\frac{\varepsilon_s}{\varepsilon_{s,max}}\right)^{1/3}\right)^{-1}$
Gidaspow [49]	$g_0 = \frac{3}{5}\left(1 - \left(\frac{\varepsilon_s}{\varepsilon_{s,max}}\right)^{1/3}\right)^{-1}$

1.5.2.6 Frictional stress

Frictional stress results from the flow of a viscous fluid. The frictional stress plays a critical role maximum solid packing in the gas-solid fluidization. In such a situation, the frictional stress is activated and added to the kinetic-collisional stress obtained from the KTGF [52]. Table 1- 5 lists the available frictional stress models. Farzaneh et al. [52] provided a comparative discussion for both of these models.

1.5.2.7 Interphase transfer coefficient

The interphase momentum transfer between gas and solid phases are coupled by drag force. Numerous correlations for calculating the drag coefficient of gas–solid systems have been reported in the literature. Table 1- 6 lists the generally used drag correlations in CFD model.

Table 1- 5. Formulations of frictional stress in literature.

Schaeffer [55]	$\tau_s = -P_f\boldsymbol{I} + 2\mu_f\boldsymbol{S}_s$ $\mu_f = \left\{\begin{array}{ll} \frac{\sqrt{2}P_f\sin(\emptyset)}{2\sqrt{\boldsymbol{S}_s:\boldsymbol{S}_s}} & \varepsilon_s > \varepsilon_{s,max} \\ 0 & \varepsilon_s \le \varepsilon_{s,max} \end{array}\right\}$ $P_f = \left\{\begin{array}{ll} 10^{25}\left(\varepsilon_s - \varepsilon_{s,max}\right)^{10} & \varepsilon_s > \varepsilon_{s,max} \\ 0 & \varepsilon_s \le \varepsilon_{s,max} \end{array}\right\}$
Srivastava and Sundaresan [56]	$\tau_s = -P_f\boldsymbol{I} + 2\mu_f\boldsymbol{S}_s$ $P_c = \left\{\begin{array}{ll} 10^{25}\left(\varepsilon_s - \varepsilon_{s,max}\right)^{10} & \varepsilon_s > \varepsilon_{s,max} \\ 0.5\,\frac{\left(\varepsilon_s - \varepsilon_{s,min}\right)^2}{\left(\varepsilon_{s,max} - \varepsilon_s\right)^5} & \varepsilon_{s,max} \le \varepsilon_s \le \varepsilon_{s,min} \\ 0 & \varepsilon_s \le \varepsilon_{s,max} \end{array}\right\}$ $\frac{p_f}{P_c} = \left(1 - \frac{\nabla.\boldsymbol{v}_s}{n\sqrt{2}\sin(\phi)\sqrt{\boldsymbol{S}_s:\boldsymbol{S}_s + \frac{\Theta_s}{d_s^2}}}\right)^{n-1}$ $\mu_f = \frac{\sqrt{2}P_f\sin(\emptyset)}{\sqrt{\boldsymbol{S}_s:\boldsymbol{S}_s + \frac{\Theta_s}{d_s^2}}}\left\{n - (n-1)\left(\frac{p_f}{P_c}\right)^{\frac{1}{n-1}}\right\}$ $n = \left\{\begin{array}{ll} \frac{\sqrt{3}}{2\sin(\emptyset)} & \nabla.\boldsymbol{v}_s \ge 0 \\ 1.03 & \nabla.\boldsymbol{v}_s < 0 \end{array}\right\}$

1.5.2.8 Computational tools

There are a number of open source and commercial software codes available that are capable of conducting both TFM and DEM simulations. For instance, commercially available software codes like ANSYS FLUENT, and open source codes like CFDlib [58], OpenFoam, and MFIX [59], are all capable of performing TFM simulations for chemically reacting flows. Similarly, commercially available codes like ANSYS FLUENT, ANSYS -CFX, and BARRACUDA, and open sources codes e.g. MFIX–DEM, KIVA [60], FLUENT-DPM (Discrete Particle Method) and dense phase DPM modules, and OpenFoam, are all capable of DEM simulations.

Table 1- 6. Formulations of interphase transfer coefficient in literature.

Wen and Yu [57]	$\beta = \frac{3}{4} C_D \frac{\varepsilon_g \varepsilon_s \rho_g}{d_s} \lvert \boldsymbol{v}_g - \boldsymbol{v}_s \rvert \varepsilon_g^{-2.65}$ $C_D = \begin{Bmatrix} \frac{24}{\varepsilon_g Re_p}\left\{1 + 0.15\left(\varepsilon_g Re_p\right)^{0.687}\right\} & if\ \varepsilon_g Re_p < 1{,}000 \\ 0.44 & if\ \varepsilon_g Re_p \geq 1{,}000 \end{Bmatrix}$
Syamlal et al. [32]	$\beta = \frac{3}{4} C_D \frac{\varepsilon_g \varepsilon_s \rho_g}{V_r^2 d_s} \lvert \boldsymbol{v}_g - \boldsymbol{v}_s \rvert$ $C_D = \left(0.63 + 4.8\sqrt{\frac{V_r}{Re_p}}\right)^2$ $V_r = \frac{1}{2}\left\{A - 0.06Re_p + \sqrt{\left(0.06Re_p\right)^2 + 0.12Re_p(2B - A) + A^2}\right\}$ $A = \varepsilon_g^{4.14}$ $B = \begin{Bmatrix} 0.8\varepsilon_g^{1.28} & if\ \varepsilon_s \geq 0.15 \\ \varepsilon_g^{2.65} & if\ \varepsilon_s < 0.15 \end{Bmatrix}$
Gidaspow [49]	$\beta = \begin{Bmatrix} 150\frac{\varepsilon_s^2 \mu_g}{\varepsilon_g d_s^2} + \frac{7}{4}\frac{\varepsilon_s \rho_g}{d_s} \lvert \boldsymbol{v}_g - \boldsymbol{v}_s \rvert & if\ \varepsilon_g > 0.2 \\ \frac{3}{4} C_D \frac{\varepsilon_g \varepsilon_s \rho_g}{d_s} \lvert \boldsymbol{v}_g - \boldsymbol{v}_s \rvert \varepsilon_g^{-2.65} & if\ \varepsilon_s \leq 0.2 \end{Bmatrix}$ $C_D = \begin{Bmatrix} \frac{24}{\varepsilon_g Re_p}\left\{1 + 0.15\left(\varepsilon_g Re_p\right)^{0.687}\right\} & if\ \varepsilon_g Re_p < 1{,}000 \\ 0.44 & if\ \varepsilon_g Re_p \geq 1{,}000 \end{Bmatrix}$

1.6 Objectives

The aim of this dissertation is to design and study the hydrodynamics of fluidized bed reactor used in the CLC technology for carbon capture, in order to bridge the data gaps in the results of bench- or pilot-scale experiments and, thereby, to aid in the design of large-scale industrial reactors. The hydrodynamics of the fluidized bed reactors are studied using the first principle-based on CFD, which allows for virtual experimental “measurement” that cannot be done in the physical world easily, or at all. The TFM which treats each phase (fluid and solid) as an interpenetrating continuum is used as CFD model for investigating the gas-solid hydrodynamics. The National Energy Technology Laboratory’s (NETL, USA) open-source code MFIX is used as flow solver in this study.

Chapter 1 of this dissertation introduces the concept of CCS and motivates the need for a closer study of CO_2 capture by chemical combustion technology, applying CFD. In Chapter 2, the design of a fluidized bed reactor is presented. This design is used to fabricate a prototype (100 kW_{th}) semi-batch CLC system by ZERE Energy and Biofuels, Inc. (San Jose, California) to demonstrate CO_2 capture from small-scale biogas combustion unit. In Chapter 3, a numerical technique is developed to model the fuel reactor used in CLC process, and the model is validated with lab-scale experimental measurements conducted at ZERE Energy and Biofuels, Inc. The rate of mass transfer to large and light fuel particles in a gas-solid bubbling fluidized bed of smaller and heavier particles is presented and discussed in Chapter 4. Chapter 5 presents a generalized model to select the grid size in obtaining grid-independent solution of TFM. In Chapter 6, the effect of fluidized bed temperature on the hydrodynamics and incorporation of the temperature effect through particle-particle interaction coefficient are discussed. The effect of horizontal perforated disc-baffles in breaking the bubbles in gas-solid fluidized bed is studied using CFD and presented in Chapter 7. Chapter 8 presents novel 3-D bubble detection and tracking algorithm that can be used to identify bubble, droplets, clusters, etc. from multiphase flow simulation data. Chapter 9 details the overall conclusions from the dissertation and discusses further directions in which this study can be carried.

Nomenclature

A	Constant for Syamlal et al. drag law
B	Constant for Syamlal et al. drag law
C_D	Drag coefficient
C_{Deff}	Effective drag coefficient
C_p	Specific heat of the fluid phase, J/kg·K
D_n	Diffusivity, m^2/s
d_s	Particle diameter, m
E	Coefficient of restitution
f_{gi}	Fluid flow resistance due to porous media, N/m^3
f_p	Fluid phase point property
$\mathbf{g}$	Acceleration due to gravity, m/s^2
g_0	Radial distribution function at contact
ΔH	Heat of reaction in the fluid phase, $J/m^3 \cdot s$
$\boldsymbol{I}$	Momentum transfer, N/m^3
i,j	Indices to identify vector and tensor components
J	Granular energy dissipation due to inelastic collisions, $J/m^3\,s$

M	Solid phases
N	Number of gas or solid species
n, k	Index
P	Pressure, Pa
q	Conductive heat flux, J/m^{2}s
R	Universal gas constant, Pa·m^3/kmol·K
Re	Reynolds number
R_g	Volumetric rate of generation, kg/m^{3}s
$\boldsymbol{S}$	strain rate tensor, s^{-1}
t	Time, s
T	Temperature, K
U	Velocity, m/s
V_r	Ratio of terminal velocity of a group of particles to that of an isolated particle
$\boldsymbol{v}$	Velocity vector, m/s
X	Mass fraction
$\boldsymbol{x}$	Position vector, m

Greek letters

β	Coefficient for the interphase force between the fluid and solids phases, kg/m^3·s
γ_{gm}	Fluid-solids heat transfer coefficient corrected for interphase mass

	transfer, J/m^3·K·s
γ^0_{gm}	Fluid-solids heat transfer coefficient not corrected for interphase mass transfer, J/m^3·K·s
γ_{Rg}	Fluid-phase radiative heat transfer coefficient, J/m^3·K^4·s
γ_{Rm}	Solids-phase-m radiative heat transfer coefficient, J/m^3·K^4·s
ε	Volume fraction of the fluid/solid phase
η	Function of restitution coefficient
Θ	Granular temperature of phase m; m^2/s^2
λ_{rm}	Solids conductivity function
μ	Viscosity of the fluid phase, Pa·s
ρ	Density of the fluid phase, kg/m^3
φ	Angle of internal friction
κ	Solids thermal conductivity, kg /m s
Π_s	Interphase force, N/m^{3}s

Subscripts

g	Gas phase
s	Solid phase
k	Between solid phases
i, j	Vector index
p	Particle phase

References

[1] J. Hansen, et al., "GLOBAL SURFACE TEMPERATURE CHANGE," Reviews of Geophysics, vol. 48, pp. n/a-n/a, 2010.

[2] R. K. Pachauri, et al., Climate change 2014: synthesis Report. Contribution of working groups I, II and III to the fifth assessment report of the intergovernmental panel on climate change: IPCC, 2014.

[3] D. Eversole, Andrews, A., "CLIMATE CHANGE IMPACTS IN HAWAI‘I," University of Hawai'i Sea Grant College Program2014.

[4] E. Dlugokencky, Tans, P. NOAA/ESRL. Available: http://www.esrl.noaa.gov/gmd/ccgg/trends/

[5] "Kyoto protocol to the United Nations framework convention on climate change," United Nations1998.

[6] "International Energy Outlook 2016," U.S. Energy Information Administration2016.

[7] B. Metz, et al., "Carbon dioxide capture and storage," 2005.

[8] U. DOE, "Report of the interagency task force on carbon capture and storage," ed, 2011.

[9] I. E. A. (IEA), "Energy technology perspectives: scenarios and strategies to 2050," París, France2006.

[10] A. Cuadrat-Fernández, "CHEMICAL-LOOPING COMBUSTION OF COAL USING ILMENITE AS OXYGEN-CARRIER," Ph.D., University of Zaragoza, Zaragoza, 2012.

[11] U. DOE, "Cost and Performance Baseline for Fossil Energy Plants," vol. Volume I ed, 2010.

[12] M. B. Toftegaard, et al., "Oxy-fuel combustion of solid fuels," Progress in Energy and Combustion Science, vol. 36, pp. 581-625, 2010.

[13] U. DOE. (October 27). CARBON CAPTURE R&D. Available: https://energy.gov

[14] P. Luis, "Use of monoethanolamine (MEA) for CO2 capture in a global scenario: Consequences and alternatives," Desalination, vol. 380, pp. 93-99, 2016.

[15] R. J. Allam and C. G. Spilsbury, "A study of the extraction of CO2 from the flue gas of a 500 MW pulverised coal fired boiler," Energy Conversion and Management, vol. 33, pp. 373-378, 1992.

[16] J. Gibbins, Chalmers, H., "Carbon capture and storage," Energy Policy, vol. 36, pp. 4317 - 22, 2008.

[17] M. Anheden, et al., "Denitrogenation (or oxyfuel concepts)," Oil & gas science and technology, vol. 60, pp. 485-495, 2005.

[18] A. F. Ghoniem, "Needs, resources and climate change: Clean and efficient conversion technologies," Progress in Energy and Combustion Science, vol. 37, pp. 15-51, 2011.

[19] L. I. Eide, et al., "Novel capture processes," Oil & gas science and technology, vol. 60, pp. 497-508, 2005.

[20] M. M. Hossain and H. I. de Lasa, "Chemical-looping combustion (CLC) for inherent CO2 separations—a review," Chemical Engineering Science, vol. 63, pp. 4433-4451, 2008.

[21] J. D. Figueroa, et al., "Advances in CO 2 capture technology—the US Department of Energy's Carbon Sequestration Program," International Journal of Greenhouse Gas Control, vol. 2, pp. 9-20, 2008.

[22] D. C. Thomas and S. M. Benson, Carbon Dioxide Capture for Storage in Deep Geologic Formations-Results from the CO2 Capture Project: Vol 2-Geologic Storage of Carbon Dioxide with Monitoring and Verification: Elsevier, 2015.

[23] L. F. De Diego, et al., "Impregnated CuO/Al2O3 oxygen carriers for chemical-looping combustion: avoiding fluidized bed agglomeration," Energy & Fuels, vol. 19, pp. 1850-1856, 2005.

[24] F. Luis, et al., "Synthesis gas generation by chemical-looping reforming in a batch fluidized bed reactor using Ni-based oxygen carriers," Chemical Engineering Journal, vol. 144, pp. 289-298, 2008.

[25] A. Lyngfelt, "Oxygen carriers for chemical looping combustion-4 000 h of operational experience," Oil & Gas Science and Technology–Revue d’IFP Energies nouvelles, vol. 66, pp. 161-172, 2011.

[26] J. Adanez, et al., "Progress in chemical-looping combustion and reforming technologies," Progress in Energy and Combustion Science, vol. 38, pp. 215-282, 2012.

[27] W.-c. Yang, Handbook of fluidization and fluid-particle systems: CRC press, 2003.

[28] D. Kunii and O. Levenspiel, Fluidization engineering: Elsevier, 1991.

[29] L. R. Glicksman, et al., "Bubble Properties in Large-Particle Fluidized-Beds," Chemical Engineering Science, vol. 42, pp. 479-491, 1987.

[30] A. M. Squires, et al., "Fluid beds: at last, challenging two entrenched practices," Science, vol. 230, pp. 1329-1337, 1985.

[31] M. P. Ramage, et al., "KINPTR (Mobil's kinetic reforming model): a review of Mobil's industrial process modeling philosophy," Advances in Chemical Engineering, vol. 13, pp. 193-266, 1987.

[32] M. Syamlal, Rogers, W., O'Brien, T. J., "MFIX Documentation, Theory Guide1," N. T. I. Service, Ed., ed. Springfield, 1993.

[33] A. Bakshi, et al., "Eulerian-Eulerian simulation of dense solid-gas cylindrical fluidized beds: Impact of wall boundary condition and drag model on fluidization," Powder Technology, vol. 277, pp. 47-62, Jun 2015.

[34] D. Gidaspow, Jung, J., Singh, R. K., "Hydrodynamics of fluidization using kinetic theory: an emerging paradigm," Powder Technology, vol. 148, pp. 123–141, 2004.

[35] D. Gidaspow, et al., "Hydrodynamics of circulating fluidized beds: kinetic theory approach," Illinois Inst. of Tech., Chicago, IL (United States). Dept. of Chemical Engineering1991.

[36] J. A. M. Kuipers, van Swaaij, W.P.M., "Computational fluid dynamics applied to chemical reaction engineering," Advances in Chemical Engineering, vol. 24, 1998.

[37] T. B. Anderson and R. Jackson, "Fluid mechanical description of fluidized beds. Equations of motion," Industrial & Engineering Chemistry Fundamentals, vol. 6, pp. 527-539, 1967.

[38] J. Davidson and D. Harrison, "The behaviour of a continuously bubbling fluidised bed," Chemical Engineering Science, vol. 21, pp. 731-738, 1966.

[39] M. Ishii and K. Mishima, "Two-fluid model and hydrodynamic constitutive relations," Nuclear Engineering and Design, vol. 82, pp. 107-126, 1984.

[40] P. C. Johnson and R. Jackson, "Frictional–collisional constitutive relations for granular materials, with application to plane shearing," Journal of Fluid Mechanics, vol. 176, pp. 67-93, 1987.

[41] Y. Tsuji, et al., "Discrete particle simulation of two-dimensional fluidized bed," Powder Technology, vol. 77, pp. 79-87, 1993.

[42] D. Gera, et al., "Computer simulation of bubbles in large-particle fluidized beds," Powder Technology, vol. 98, pp. 38-47, 1998.

[43] C. K. K. Lun, et al., "Kinetic theories for granular flow: inelastic particles in Couette flow and slightly inelastic particles in a general flowfield," Journal of Fluid Mechanics, vol. 140, pp. 223-256, 1984.

[44] B. Chalermsinsuwan, et al., "Kinetic theory based computation of PSRI riser: Part I—Estimate of mass transfer coefficient," Chemical Engineering Science, vol. 64, pp. 1195-1211, 3/16/ 2009.

[45] M. Ishii, "Thermo-fluid dynamic theory of two-phase flow," NASA STI/Recon Technical Report A, vol. 75, p. 29657, 1975.

[46] B. G. M. van Wachem, et al., "Comparative analysis of CFD models of dense gas-solid systems," Aiche Journal, vol. 47, pp. 1035-1051, May 2001.

[47] C. C. Pain, Mansoorzadeh, S., de Oliveira, C.R.E., "A study of bubbling and slugging fluidised beds using the two-fluid granular temperature model," International Journal of Multiphase Flow, vol. 27, pp. 527–551, 2001.

[48] S. Chapman and T. G. Cowling, The mathematical theory of non-uniform gases: an account of the kinetic theory of viscosity, thermal conduction and diffusion in gases: Cambridge university press, 1970.

[49] D. Gidaspow, Multiphase Flow and Fluidization: Continuum and Kinetic Theory Descriptions. San Diego: Academic Press, 1994.

[50] C. M. Hrenya and J. L. Sinclair, "Effects of particle-phase turbulence in gas-solid flows," Aiche Journal, vol. 43, pp. 853-869, 1997.

[51] N. F. Carnahan and K. E. Starling, "Equation of state for nonattracting rigid spheres," The Journal of Chemical Physics, vol. 51, pp. 635-636, 1969.

[52] C. Lun and S. Savage, "The effects of an impact velocity dependent coefficient of restitution on stresses developed by sheared granular materials," Acta Mechanica, vol. 63, pp. 15-44, 1986.

[53] J. L. Sinclair, Jackson, R., "Gas-Particle Flow in a Vertical Pipe with Particle-Particle Interactions," AIChE J., vol. 35, p. 1473, 1989.

[54] M. Farzaneh, et al., "The crucial role of frictional stress models for simulation of bubbling fluidized beds," Powder Technology, vol. 270, Part A, pp. 68-82, 2015.

[55] D. G. Schaeffer, "Instability in the evolution equations describing incompressible granular flow," Journal of differential equations, vol. 66, pp. 19-50, 1987.

[56] A. Srivastava and S. Sundaresan, "Analysis of a frictional–kinetic model for gas–particle flow," Powder Technology, vol. 129, pp. 72-85, 2003.

[57] C. Y. Wen and Y. H. Yu, "Mechanics of fluidization," Chemical Engineering Progress Symposium Series, vol. 62, pp. 100-111, 1966.

[58] B. A. Kashiwa and R. M. Rauenzahn, "A multimaterial formalism," American Society of Mechanical Engineers, vol. 1, pp. 19-23, 1994.

[59] M. Syamlal, "MFIX documentation: Numerical technique," National Energy Technology Laboratory, Department of Energy, Technical Note No. DOE/MC31346-5824, 1998.

[60] A. Amsden, et al., "A computer program for chemically reactive flows with sprays, Los Alamos National Laboratory Rep," LA-11560-MS1989.

CHAPTER 2

Design of a semi-batch chemical looping combustion system

Abstract

CLC is a promising combustion technology that inherently separates CO_2 from the flue gas. The process consists of two fluidized bed reactors, a fuel reactor and an air reactor, and a solid metal oxide, known as oxygen-carrier, transports oxygen from the air to the fuel. Since, there is no direct contact between fuel and air, the combustion products, primarily, contain CO_2 and H_2O, which makes CLC very efficient technology to capture CO_2. A semi-batch 100-kW CLC prototype is designed using two identical fluidized bed reactors. At any moment in time, one operates in air mode, and one operates in fuel mode in a cyclic manner. This design provides an alternative to minimize CO_2 leakage between reactors, which is a common concern for circulating fluidized bed design. Additionally, the development of a mature and reliable cost effective CLC technology requires more prototype-scale demonstration to fully understand the functionality of such system.

2.1 Introduction

The concept of CLC processes shown in Chapter 1, is based on the transfer of oxygen from air to the fuel by means of a metallic solid oxygen-carrier avoiding direct contact between fuel and air. The metal oxide is thus an oxygen and heat carrier simultaneously. This special feature makes CLC as the most promising technology for CO_2 capture. Indeed, a high surface area for fast reaction and good physical properties such as crushing strength and attrition resistance are highly desirable for any oxygen-carrier particle. Porous inert supporting material such as alumina, zirconium, and titanium dioxide are used to prepare oxygen-carrier particles from the potential metal oxide (Fe, Cu, Ni, Mn) [1-5]. The experimental results of these studies show that the rates of reaction for both the oxidation and the reduction are fast enough for practical applications.

Batch experiments and general feasibility analysis of Lyngfelt et al. [3] showed that a fluidized bed reactor concept is suitable for CLC. Recently, Kolbitsch et al. [6], Markstrom et al. [7], Strohle et al. [8], Abad et al. [9] and Lyngfel and Leckner [10] reported the design and operation of different scale-size CLC processes for gaseous and solids fuel.

In a circulating fluidized bed system, gas leakage is difficult to avoid completely. If there is a gas leakage from the fuel reactor into the air reactor, carbon dioxide will be released to the atmosphere, and the CO_2 capture efficiency decreases. If there is a leakage in the opposite direction, the CO_2 stream will be diluted with nitrogen that increases the cost of compression.

The purpose of this study is to present a conceptual design of a 100-kW$_{th}$ (thermal power) semi-batch CLC prototype working at atmospheric pressure. The design criteria are discussed, and a final design is presented.

2.2 Design of the semi-batch CLC unit

2.2.1 Design basis

For eliminating or minimizing flaring or venting of gases from dairy wastes, landfills, and waste water treatment facilities, a 100-kW$_{th}$ fuel flexible distributed combined heat and power unit is designed to demonstrate its applicability and efficiency on carbon capture. A simulated biogas (60% (mole/mole) methane, CH_4, and 40% carbon dioxide, CO_2) is to be burnt at 800 °C to get the designed thermal power.

2.2.2 Oxygen-carrier

Most crucial design input data are the type of the oxygen carrier, the metal oxide. For this prototype design, a 30% (w/w) copper oxide (CuO) on alumina (Al_2O_3) is selected as oxygen carrier. The diameter of the carrier particles was chosen to be between 300 and 500 μm, having a mean density of 1964 kg/m^3.

The required mass of the oxygen –carrier is calculated from the stoichiometric balance equation for methane combustion with oxygen-carrier:

$$CH_4 + 8CuO \rightarrow CO_2 + 2H_2O + 4Cu_2O \quad (1)$$

Amekura and Kishimoto [11] reported that, with increasing temperature, copper (I) oxide (Cu_2O) formation is likely to increase at a low pressure. Based on the design temperature in this study, the oxygen-carrier is likely to undergo partial reduction according to equation (1). The design equation to calculate the required mass of oxygen-carrier, m_{oc}, is as:

$$m_{oc} = \frac{M_m}{w_m} t \, \nu_f \, \frac{P_{th}}{\Delta H_{com}} \tag{2}$$

Where M_m is the molecular mass of copper; w_m is the mass fraction of CuO in the oxygen-carrier; t is the combustion time; ν_f is the stoichiometric coefficient for CuO; P_{th} is the thermal power; and ΔH_{com} is the heat of combustion of CH_4 at the design temperature.

2.2.3 Reactor sizing

Various reactor diameters are evaluated to determine the final dimensions of the prototype reactors. The final version of the reactor design uses an 18” schedule 40 steel pipe. This is motivated by the expected benefit of reducing the cost of fabricating the prototype. This reactor diameter is achieved by selecting a 10 min switching time between fuel- and air-mode operations of the reactors system.

2.2.4 Hydrodynamics properties

The superficial fuel velocity, $u_{0,f}$, and air velocity, $u_{0,air}$, are computed from the design equation as:

$$u_{0,f} = \frac{P_{th}}{\Delta H_{com}} \frac{RT}{y_f P A} \tag{3}$$

$$u_{0,air} = \lambda \frac{v_{ox} M_{air}}{y_{ox} \rho_{air} A} \frac{P_{th}}{\Delta H_{com}} \tag{4}$$

Where R is the ideal gas constant; T is the design temperature; y_f is the mole fraction of CH_4 in the fuel mixture; P is the reactor pressure; A is the cross-sectional area of the reactor; λ is the excess oxygen ratio in the air; v_{ox} is the stoichiometric oxygen required for CH_4 combustion; y_{ox} is the mole fraction of oxygen in the air; M_{air} is the molar mass of air; and ρ_{air} is the density of air.

The height of the solid bed under minimum fluidization condition, H_0, is calculated as

$$H_0 = \frac{1}{\varepsilon\, A\, \rho_{oc}} \frac{M_m}{w_m} t\, v_f \, \frac{P_{th}}{\Delta H_{com}} \tag{5}$$

Where ρ_{oc} is the mean density of the oxygen carrier; and ε is the bed void fraction under minimum fluidization. The characteristic of the solid oxygen-carrier particles that make them fluidize is very important in designing a fluidized bed reactor. Equations 7-9 are generally used to classify the solid particles according to Geldart classification [12].

$$Ar = \frac{d_p^3}{\mu^2} \rho_f \left(\rho_{oc} - \rho_{f/air}\right) g \tag{6}$$

$$d^*_{p,AB} = 101\left(\frac{\rho_{f/air}}{\rho_{oc}-\rho_{f/air}}\right)^{0.425} \tag{7}$$

Geldart classification of solids

$$Class = \begin{cases} Geldart\ C & if\ Ar < 1.4 \\ Geldart\ A & if\ Ar < {d^*_{p,AB}}^3 \\ Geldart\ B & if\ {d^*_{p,AB}}^3 < Ar < 9 \times 10^4 \\ Geldart\ D & if\ Ar > 9 \times 10^4 \end{cases} \tag{8}$$

where Ar is the dimensionless Archimedes number; d_p is the diameter of the oxygen-carrier particle; and d^*_{pAB} is the dimensionless particle diameter. Based on the Geldart's classification, the minimum fluidization velocity, u_{mf} is calculated as

$$u_{mf} = \frac{\mu}{\rho_{f/air}\, d_p} c_1[(1 + c_2 Ar)^{0.5} - 1] \tag{9}$$

where c_1 and c_2 are the constants suggested by Wen and Yu [13].

To predict the behavior of gas-solid fluidized bed, the contacting regime must be known. This facilitates the selection of appropriate performance expressions for that regime. In general, slugging fluidization is undesirable for efficient operation of fluidized bed reactors [14]. Slugging occurs when the slug height, H_{slug}, and velocity, u_{slug}, are higher than the minimum fluidization height, H_0 and superficial fuel velocity, $u_{0,f/air}$, respectively.

$$H_{slug} = \frac{1.9D_t}{(\rho_{oc}\, d_p)^{\,0.3}} \tag{10}$$

$$u_{slug} = u_{mf} + 0.16(1.3D_t^{0.175} - H_0)^2 \tag{11}$$

The expected bubble diameter, d_B, rise velocity, u_B, and the expanded solid bed height, H_{exp}, are calculated based the following equations [14].

$$d_B(h) = \frac{0.54}{g^{0.2}}\left(u_0(h) - u_{mf}\right)^{0.4}\left(\mathrm{h} + \frac{4}{\sqrt{N_d}}\right)^{0.8} \tag{12}$$

$$u_B(h) = \phi_B\sqrt{g\ d_B(h)} \tag{13}$$

$$\Phi_B = \begin{Bmatrix} 0.64 & if\ D_t < 0.1\ m \\ 1.6D_t^{0.4} & if\ 0.1 \le D_t < 1.0\ m \\ 1.6 & if\ D_t \ge 1.0\ m \end{Bmatrix} \tag{14}$$

$$H_{exp} = H_0\left(1 + \frac{u_0 - u_{mf}}{u_B}\right) \tag{15}$$

Where g is the acceleration of gravity; h is the instantaneous height; and D_t is the reactor diameter.

2.3 Descriptions of the reactor configurations

The hydrodynamics model described in previous section provides the necessary dimensions of the fluidized bed reactors. This exclusive design uses two identical fluidized bed reactors in parallel where, at any moment in time, one operates in air mode, and one operates in fuel mode in a cyclic manner, which eliminates the circulation solids between reactors. Each reactor is 3.36 m tall with 1.60 m of solid oxygen-carrier bed height. The mass of oxygen-carrier used to fill each reactor is 228 kg.

Figure 2- 1 shows a simplified configuration of the semi-batch chemical looping combustion system with inherent capability to capture CO_2. These reactors are nominally designed to operate in a bubbling regime, with $u_{0,air} / u_{mf} \approx 36$ when the reactor is in air

mode, and $u_{0,f} / u_{mf} \approx 9$ when the reactor is in fuel mode. The inside of the reactor is baffled to break-up bubbles, thereby ensuring a high conversion of methane in the fuel reactor.

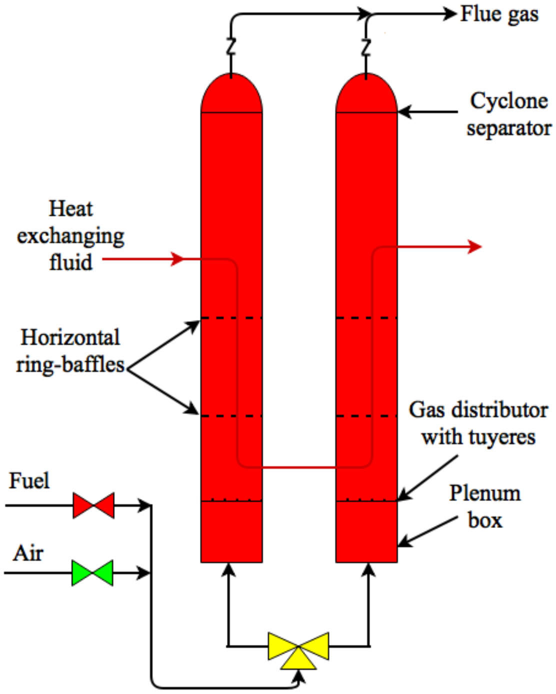

Figure 2- 1. Simplified schematic of semi-batch chemical looping combustion system with two fluidized bed reactors.

There are two horizontal ring-baffles inserted in each fluidized bed reactor, which increases the gas-solid contact and, thereby increases fuel conversion. (Breaking apart the bubbles also results in fewer particles being entrained from the bed.)

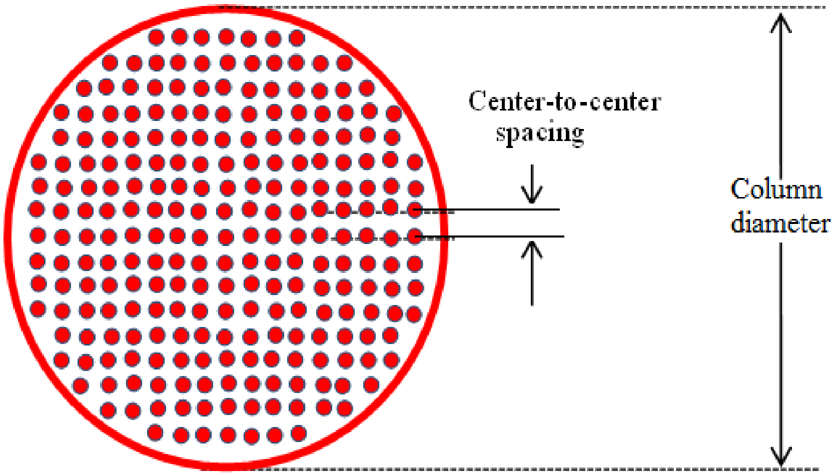

Figure 2- 2. Hole arrangement of the ring-baffle inserted in the fluidized bed reactor.

Figure 2- 2 shows the arrangement of the baffle opening used in the design of the semi-batch CLC system. It has been assumed to keep about 30% of the baffle cross sectional area open to gas flow, which is also suggested by Dutta and Suciu [15]. For this design, 31 mm is selected as the center to center distance, as shown in Figure 2- 2. The baffle is made from steel plate with numerous 20 mm holes through it, on a square pattern.

During operation, it is anticipate that fines from oxygen-carrier particles will be produced, and it would be preferable to return those fines back to the reactor. Although the reactor is configured to operate as a bubbling fluidized bed during fuel and air modes, the air velocity is high enough, especially during air mode, that many particles will be entrained. To prevent a large amount of particles from leaving the reactor, an internal cyclone is included in the design. The detailed design of the internal cyclone can be found in [16].

The gas distributor is designed with the following goals: (a) pressure drop large enough to ensure uniform distribution across the reactor cross section; (b) minimize jet velocity to reduce attrition of particles; (c) inherent design to minimize back flow of particles through distributor into chamber, when the gas flow is turned off; (d) ease of fabrication. The selected design uses "tuyeres", a common configuration in industrial fluidized-bed reactors. Because the volume of gas flow entering the reactor during air mode is nearly 7 times the volume of gas entering during fuel mode, the velocity of gas flowing through the distributor is quite different in the two cases. The pressure drop through the distributor is proportional to the square of that velocity, so that the pressure drop of air flow through the distributor is nearly 50 times that of fuel gas flowing through the same distributor. The pressure drop is a key design parameter, and an alternative approach is required. The detail is provided in Figure 2- 3 and Figure 2- 4.

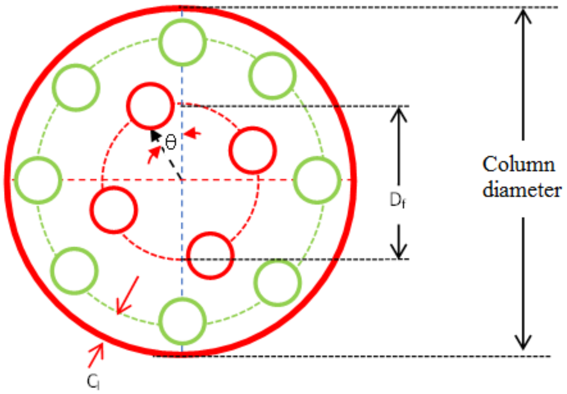

Figure 2- 3. Arrangement of the tuyeres at the gas distributor plate. In figure, C_l represents the clearance between the reactor wall and the center of the air tuyere (green); θ is the angular distance of the first fuel tuyere ((red, small circle)) from central axis; D_f is the center to center distance of fuel tuyeres in opposite locations.

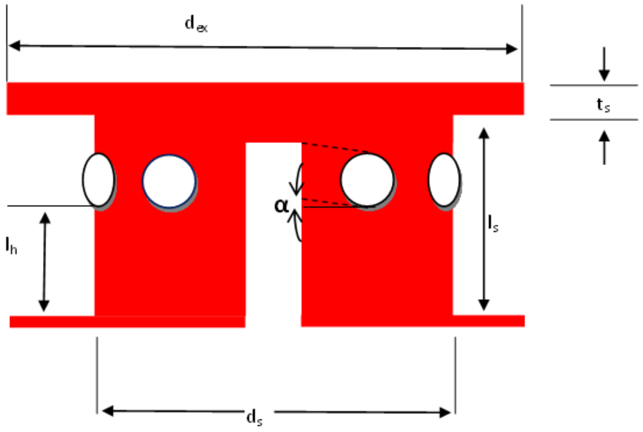

Figure 2- 4. Hole arrangement of the gas distributor in tuyere. In figure, d_{ex} and d_s represent the tuyere and tuyere-shaft diameter; t_s is the tuyere cap thickness; l_s and l_h are the shaft length and the distance of the hole from base.

The distributor has two components; 8 tuyeres are located near the pipe wall, shown in green color in Figure 2- 3. Four additional tuyeres are found closer in to the center, are shown in red color in Figure 2- 3.

Viewed from above, each tuyere has a diameter of 54 mm. Each tuyere has eight radial holes, as indicated, pointing out from the center, at 45° spacing. In this design, gas flows through either the four fuel tuyeres in fuel mode, or is distributed to all 12 tuyeres in air mode. The 8 tuyeres near the wall have only 5 of the eight holes open to gas flow. It is important to position those tuyeres with the blocked holes facing the nearby wall to prevent erosion.

When in fuel mode, fuel gas is provided through a two-tier plenum to the central four tuyeres only. When in air mode, all 12 tuyeres are utilized. This distributor design is unusual, and in both modes gas distribution would seem to be imperfect. An effort is made to balance the requirement for uniform gas distribution with practicality of fabrication and operation.

2.4 Conclusion

A 100-kW$_{th}$ semi-batch CLC prototype unit for flexible gaseous fuel is designed to operate in bubbling fluidized bed mode. The unit includes two identical fluidized bed reactors with inherent carbon capture option. At any moment in time, one operates in air mode, and one operates in fuel mode in a cyclic manner, which eliminates the circulation of solids between reactors. This configuration will minimize the gas leakage between reactors, which is a common concern in circulating fluidized bed configuration. A new design for gas distributor is presented in this study. This design study presents very useful information that can be applied in other cyclic reaction and regeneration processes.

References

[1] P. Cho, T. Mattisson, and A. Lyngfelt, "Defluidization conditions for a fluidized bed of iron oxide-, nickel oxide-, and manganese oxide-containing oxygen carriers for chemical-looping combustion," *Industrial & Engineering Chemistry Research,* vol. 45, pp. 968-977, 2006.

[2] B. Kronberger, A. Lyngfelt, G. Löffler, and H. Hofbauer, "Design and fluid dynamic analysis of a bench-scale combustion system with CO2 separation-chemical-looping combustion," *Industrial & Engineering Chemistry Research,* vol. 44, pp. 546-556, 2005.

[3] A. Lyngfelt, B. Leckner, and T. Mattisson, "A fluidized-bed combustion process with inherent CO 2 separation; application of chemical-looping combustion," *Chemical Engineering Science,* vol. 56, pp. 3101-3113, 2001.

[4] A. Lyngfelt, "Oxygen carriers for chemical looping combustion-4 000 h of operational experience," *Oil & Gas Science and Technology–Revue d'IFP Energies nouvelles,* vol. 66, pp. 161-172, 2011.

[5] J. Adanez, A. Abad, F. Garcia-Labiano, P. Gayan, and F. Luis, "Progress in chemical-looping combustion and reforming technologies," *Progress in Energy and Combustion Science,* vol. 38, pp. 215-282, 2012.

[6] P. Kolbitsch, T. Proll, J. Bolhar-Nordenkampf, and H. Hofbauer, "Design of a Chemical Looping Combustor using a Dual Circulating Fluidized Bed Reactor System," *Chemical Engineering & Technology,* vol. 32, pp. 398-403, Mar 2009.

[7] P. Markström, C. Linderholm, and A. Lyngfelt, "Chemical-looping combustion of solid fuels – Design and operation of a 100 kW unit with bituminous coal," *International Journal of Greenhouse Gas Control,* vol. 15, pp. 150-162, 2013.

[8] J. Ströhle, M. Orth, and B. Epple, "Design and operation of a 1 MWth chemical looping plant," *Applied Energy,* vol. 113, pp. 1490-1495, 2014.

[9] A. Abad, R. Pérez-Vega, L. F. de Diego, F. García-Labiano, P. Gayán, and J. Adánez, "Design and operation of a 50 kWth Chemical Looping Combustion (CLC) unit for solid fuels," *Applied Energy,* vol. 157, pp. 295-303, 2015.

[10] A. Lyngfelt and B. Leckner, "A 1000 MWth boiler for chemical-looping combustion of solid fuels – Discussion of design and costs," *Applied Energy,* vol. 157, pp. 475-487, 2015.

[11] H. Amekura and N. Kishimoto, "Fabrication of oxide nanoparticles by ion implantation and thermal oxidation," in *Toward Functional Nanomaterials*, ed: Springer, 2009, pp. 1-75.

[12] D. Geldart, "Types of gas fluidization," *Powder Technology,* vol. 7, pp. 285-292, 1973.

[13] C. Y. Wen, Yu, Y.H.,, "Mechanics of fluidization," *Chemical Engineering Progress Symposium Series,* vol. 62, pp. 100-111, 1966.

[14] D. Kunii and O. Levenspiel, *Fluidization engineering*: Elsevier, 2013.

[15] S. Dutta and G. Suciu, "An experimental study of the effectiveness of baffles and internals in breaking bubbles in fluid beds," *Journal of chemical engineering of Japan,* vol. 25, pp. 345-348, 1992.

[16] M. J. Rhodes, *Introduction to particle technology*: John Wiley & Sons, 20

CHAPTER 3

Multi-stage modeling of bubbling fluidized bed reactor used in a semi-batch chemical-looping combustion of methane using a Cu-based oxygen-carrier

Abstract

A multi-stage mathematical model for a bubbling fluidized bed has been developed to simulate the performance of the fuel-reactor used in semi-batch CLC systems. This model considers both the fluid dynamic and chemical reactions along with the mixing state of solid particles at the different heights of the fluidized bed. The main outputs of the model are the break-through time for fuel, the conversion of the oxygen carrier and the gas composition at the reactor exit, the axial profiles of gas concentrations and the fluid dynamical structure of the reactor. The model was validated using measurements from burning CH_4 in a lab-scale bubbling fluidized bed using a CuO/Al_2O_3 oxygen-carrier. The model prediction is better when the reduced state of copper oxide Cu_2O is assumed.

3.1 Introduction

Climate change is likely the largest environmental issue and engineering challenge faced by the society in modern times. A necessary strategy for reducing human contributions to climate change is to cut greenhouse gas emissions from electric power plants, which account for 40% of U.S. CO_2 emissions [1]. The conventional CO_2 separation techniques are based on post-combustion processes e.g. amine scrubbing. As opposed to the conventional CO_2 separation from exhaust gas in power plants and refineries, chemical-looping combustion (CLC) is a new combustion technology with inherent separation of CO_2. CLC utilizes two fluidized beds, an air reactor and a fuel reactor, to mix an oxygen-carrier with a combustion fuel. The "looping" term in CLC refers to the cycle by which the oxygen carrier – typically a metal oxide – undergoes reduction in the fuel reactor and is subsequently re-oxidized in the air reactor. It is an effective method for carbon dioxide capture, as CO_2 is separated from other reaction products by the nature of the process [2, 3]. Continuing research is underway to find ways to make CLC a more efficient and robust tool in the effort to curb human generated greenhouse gas emissions [4]. The current study has been carried out within framework of this project to develop a reactor model capable of predicting the experimental results from a 100 kWth pilot plant.

Modeling plays an important role in comprehension and development of chemical looping combustion. It permits to better understand the experimentally observed phenomena by testing different hypothesis. Moreover, modeling is a useful tool for transposal in other conditions and scale-up of the results to industrial scales. Different approaches have been adopted in order to mathematically describe behavior of fluidized bed reactors. The developed models can be classified globally in two categories: the pseudo-homogeneous models and the multiphase flow models. The reaction conversion in a fluidized bed varies from plug flow to well below mixed flow reactor [5]. The most common method is the two phase theory which considers that all gas in excess of minimum fluidization passes across the bed is in form of bubbles [6, 7].

The current reactor model has been developed considering both the fluid dynamics of a bubbling fluidized bed, composed of two plug flow reactors, and the rate of the oxygen-carrier reduction by gaseous fuel CH_4. Solid particles were modeled as a fixed bed reactor to account for the conversion of oxygen carriers. The mathematical model developed in this study has been validated against the lab scale experimental data conducted at the ZERE lab facility using methane as the combustion feed with CuO/Al_2O_3 particles as the oxygen carriers.

3.2 Experimental setup

Figure 3- 1 shows a simplified schematic of ZERE lab scale fluidized bed reactor. The experiments were conducted with a fluidized-bed reactor made of quartz. The reactor had a total length of 500mm and an inner diameter of 47mm. The oxygen carrying particles were placed on a porous plate placed at the bottom of the reactor. The inlet and outlet gas temperature and the bed temperature were measured using thermocouples as shown in Figure 3- 1. A three phase STACO band heater (StacoVT – 1010BCT-2) was used to heat the reactor. The temperature under the bed was used to regulate the

temperature of the heater. Temperatures in this work refer to the temperature in the bed over the porous plate.

The Cu-based oxygen carrier prepared by wet impregnation method was used in this study. The theoretical oxygen transfer capacity (R_{th}) is 20.25%, corresponding to reduction of CuO to Cu. The particles have a surface mean diameter of 357 μm, and a density of 2200 kg/m^3. A sample of 126.6 g of oxygen carrier particles was placed on the porous plate and was then initially heated in an inert atmosphere (argon) to the reaction temperature. The bed height was approximately 88 mm when the bed was not fluidized. The pre-oxidized oxygen carrier sample was then alternately exposed methane (CH_4) with argon or air with argon which was introduced from the bottom of the reactor as drawn in Figure 3- 1. The oxygen carrier used in these experiments was supplied by CLARIANT Corp.

Mass flow meters (Cole Parmer- serial 104478) were used to measure the inlet gas flow rates. The flow rate of outlet gas was not measure but a portion of the gas from the reactor was led to an electric cooler, where the water was removed, and then to a gas analyzer (Testo 350) where the concentrations of CO_2, CO, NO_x, SO_x, H_2, and CH_4 were measured.

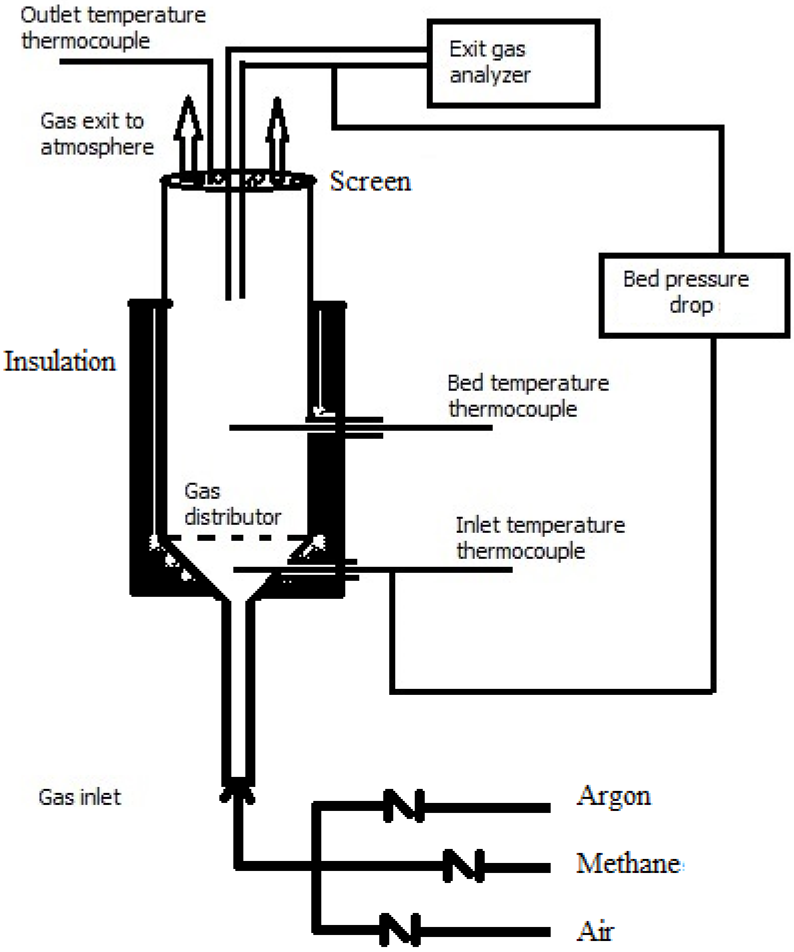

Figure 3- 1. ZERE lab scale reactor set up.

The exothermic nature of the combustion reaction means that there will be release of heat and therefore a subsequent temperature rise. To limit this temperature increase, methane was diluted with argon before fed into the reactor. Thus, large temperature increases were avoided since there was no possibility to cool the reactor in the present setup. The experiments were conducted with a methane flow of 1Ln/min along with an argon flow of 4.2 Ln/min (normalized to 1 bar and 25 °C), for the reducing periods. It was possible to establish whether the bed was fluidized or not by high-frequency measurements of the pressure drop over the bed [8].

3.3 Fuel reactor modeling

The existing models on bubbling fluidized bed reactors suggest that the hydrodynamic model has to include the effect of bubbles and associate mixing. Accounting of the proper hydrodynamic equations is crucial to develop a robust mathematical model that can be applied for scale-up and design of fluidized bed reactors. In this study, the fuel reactor used in a semi-continuous chemical looping combustion system is selected to construct the model equations. As described by Abad et al. 2010, this model also considers a steady state, isothermal bed at macroscopic level. Solid particle fragmentation or attrition and elutriation are neglected [12]. For simplicity, the model is considered to be one dimensional. The lateral exchange coefficient of gas between the bubbles and the emulsion phases is calculated based on the semi-empirical correlations [7]. The detail of the modeling of the fluidized-bed reactor is described in the following sections.

3.3.1 Fluid-dynamics of the model

In bubbling fluidized bed, fluid-dynamics is largely governed by bubble rise velocity. An understanding of the bubble rise velocity requires the knowledge about the bubble size. The bubble size changes along the length of the solid bed due to the increased gas volume fraction of gas after fuel reaction with oxygen carrier particles. To include this volume expansion, simultaneous solution of hydrodynamics and material balances are important. The changes in the gas velocity, U, and the corresponding bubble size, d_B, are incorporated through the following equations.

$$d_B(z) = \frac{0.54}{g^{0.2}}\left(U(z) - u_{mf}\right)^{0.4}\left(z + \frac{4}{\sqrt{N}}\right)^{0.8} \tag{1}$$

Here, u_{mf} is the minimum fluidization velocity which is estimated from Wen and Yu correlation [9]; N is the number of orifice for the gas distributor; and z is the height of the reactor.

The gas expansion changes the superficial gas velocity by:

$$\frac{dU}{dz} = \frac{1}{A}\frac{d}{dz}\left(\sum_j \dot{v}_J \frac{RT}{P_t}\right) \tag{2}$$

Here, ϑ is the reaction stoichiometry of methane with CuO; R and T are the ideal gas constant and temperature; P_t is the total pressure; and A is the cross-sectional area of the reactor.

Since the reactor will operate under isothermal condition, the temperature change is neglected. The solid pressure drop variation across the reactor height is expressed by:

$$\frac{dP}{dz} = -\rho_{OC}\, g\,(1 - \varepsilon_b(z))(1 - \varepsilon_{mf}) \tag{3}$$

Here, ρ_{OC} is the density of the oxygen carrier; The porosity at the minimum fluidization conditions, ε_{mf}, was obtained using the equation proposed by Grace [10].

$$\varepsilon_{mf} = 0.586\, Ar^{-0.029}\left(\frac{\rho_f}{\rho_{OC}}\right) \tag{4}$$

Where $Ar = \frac{d_p^3 \rho_f (\rho_{OC} - \rho_f) g}{\mu^2}$. Here, d_p is the mean particle diameter; ρ_f and μ are methane density and viscosity. The bubble fraction, ε_b, in the solid bed is

$$\varepsilon_b(z) = \frac{U(z) - u_{mf}}{u_B(z)} \tag{5}$$

With the consideration of the fluidized bed column diameter, the bubble rise velocity, u_B, was calculated using the equation proposed by Werther [11].

$$u_B(z) = \phi_B \sqrt{g\, d_B(z)} \tag{6}$$

Where Φ_B is taken as 0.64 based on the reactor diameter studied in this model.

3.3.2 Material balances

To predict the conversion of gas and solid in the fluidized bed reactor, the differential mole balances were performed for the reactant and products that are distributed in the bubble and the emulsion phases. The reactor was modeled as plug flow for all gas species. Two possible reaction pathways for gaseous fuel (CH_4) was considered for the CuO/Al_2O_3 oxygen-carrier :

$$CH_4 + 4CuO \dashrightarrow CO_2 + 2H_2O + 4Cu \tag{7}$$

Or $CH_4 + 8CuO \dashrightarrow CO_2 + 2H_2O + 4Cu_2O$

As described by Abad et al. 2010, a gas exchange between bubbles and emulsion is considered allowing the exchange of products and reactants between these phases by diffusive and/or bulk flow mechanism [12]. Considering all the above assumptions, the differential mole balance on a small reactor volume, dV, is derived for each gas i (CH_4, CO_2, and H_2O) for the bubble and the emulsion phases:

$$\frac{d\dot{N}_{b_i}}{dV} = \frac{d\{(U-u_{mf})C_{b_i}\}}{dz} = -K_{be}\varepsilon_b\left(C_{b_i} - C_{e_i}\right) \tag{8}$$

$$\frac{d\dot{N}_{e_i}}{dV} = \frac{d\{(1-\varepsilon_b)u_{mf}C_{e_i}\}}{dz} = K_{be}\varepsilon_b\left(C_{b_i} - C_{e_i}\right) - k'''C_{e_i}^{n}\varepsilon_{mf}(1-\varepsilon_b) \tag{9}$$

Here, $\dot{N}$ represents the molar flow rates of gas i in the differential volume element dV. The subscripts b and e represent the bubble and emulsion phases, respectively. k''' is the volumetric rate constants. C_b and C_e are the gas concentrations in the bubble and the emulsion phases. Since no reaction is assumed in the bubble phase, gas will be exchanged between the bubble and the emulsion phases through the interchange coefficient K_{be}. In the emulsion phase, methane gas will be reacting with solid oxygen carrier particles and product gases will be flowing from the emulsion to the bubble. These equations allow determining the concentration of gas i in both phases: emulsion and bubbles.

3.3.3 Kinetic model for oxygen carrier

For the heterogeneous gas-solid reaction, a shrinking unreacted-core model is used to describe the reduction of CuO/Al2O3 particles with methane under reactor conditions. In this model, chemical reaction is considered as the main resistance to the global reaction. Early studies showed that external and internal mass-transfer resistances as well as the particle size have no or minimal effect on reaction rate of CuO/Al_2O_3 particles with methane fuel [2, 12]. A platelike geometry for CuO in the porous surface of the Al_2O_3 particle with unchanging size and also with no ash layer formation was used for the kinetic model. Considering all of these assumptions, the equations that describe the conversion time, t, for plates is the following [6]

$$t = \frac{\frac{\rho_{CuO}}{MW_{CuO}}}{\vartheta k^{"} C_p^n}\left(1 - \frac{\delta}{L}\right) \tag{10}$$

Here, ρ_{CuO} and $MW_{CuO}$are the density and molecular weight of copper oxide; L and δ are the initial and unreacted thickness of CuO layer in the oxygen carrier particles. C_p is methane concentration around the particles which is equal to the emulsion phase concentration of methane; n is the reaction order, and $k^{"}$ is the surface rate constant in terms of Arrhenius equation as

$$k^{"} = k_0^{"} \, exp\left(-\frac{E_a}{RT}\right) \tag{11}$$

Here, E_a is the activation energy. The time τ required for complete conversion is given when $\delta = 0$, or $\tau = \frac{\frac{\rho_{CuO}}{MW_{CuO}}}{\vartheta k^{"} C_p^n}$. At any moment, the unreacted CuO layer thickness, η, can be found from

$$\eta = 1 - \frac{\vartheta k^{"} {C_p}_i^n}{\frac{\rho_{CuO}}{MW_{CuO}} L} t \tag{12}$$

The thickness of the layer, L, over the Al_2O_3 support was determined considering the surface area reported by the vendor and the weight fraction of active CuO in the oxygen carrier particles. Using the specific surface area and the density of the oxygen carrier particles, volumetric rate constant was estimated as $k''' = \frac{\vartheta k^{"}}{\varepsilon_{mf}}\left(1 - \varepsilon_{mf}\right) A_{SA}\, \rho_{OC}$.

3.3.4 Break-through time for fuel

Break-through is defined as when the reactant gas is first appearing at the fluidized bed reactor exit. At the start of a non-circulating fluidized bed, all the solid oxygen carriers will be available for gas-solid reactions. Soon after the reactant gas flow starts, solid particles at the entrance reduce quickly, and with the time progresses the reaction front also moves forward. This solid reduction process continues and at some point there will not be any active solid particles to react with fuel gas. When most of the solid particles will be in reduced state, part of the reactant gas will leave the reactor as unreacted. The time when a trace amount of reactant gas is noticed at the reactor exit will be referred as the break-through time. For instances, break-through time for methane is the time when a trace amount of methane is detected by the model calculations. The subsequent description provides the details about break-through time calculation.

As described in the material balance, a part of the inlet gas will be in the emulsion phase at minimum fluidization, and any gas excess to minimum fluidization has to move through the bubble phase. Since there is no reaction in the bubble phase, all the solids will be in the emulsion phase and react with methane. For the reaction, solid particles have been considered in a series of interconnected CSTRs. A multi stage model is applied where the whole bed was divided into 10 stages of the same solid mass. A simplified schematic of the used model is shown in Figure 3- 2.

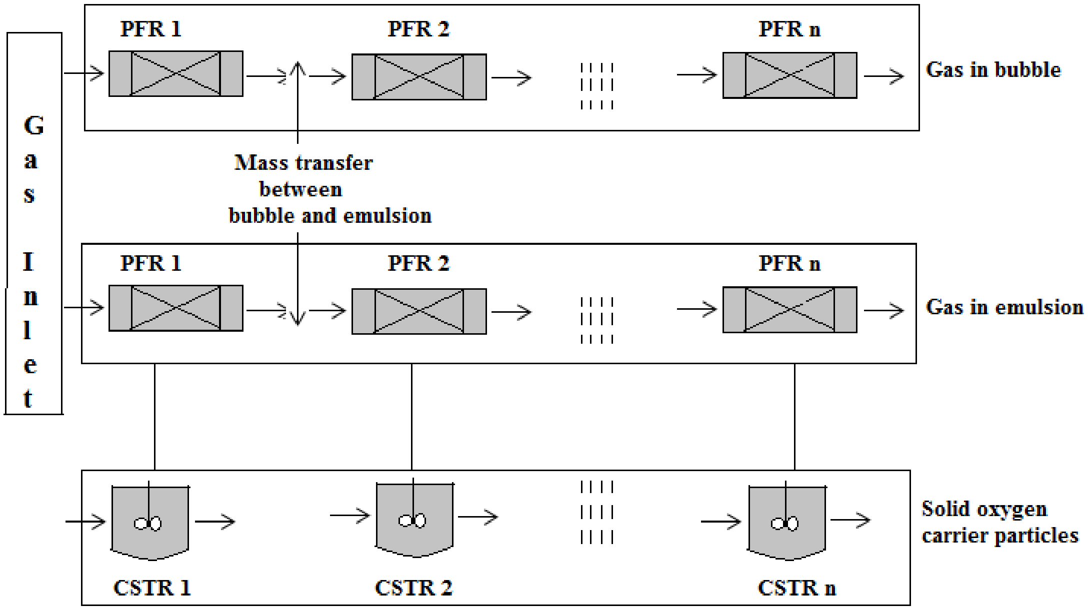

Figure 3- 2. Schematic of the overall model used in this study.

The concept of stages refers to a split of the bed length according to the amount of the solid particles in the bed. A looping algorithm is developed for this staging concept as: in the first loop methane will react with oxygen carrier particles assigned in all stages based on the average methane concentration in the respective stage and this will continue till the first stage particles are fully expired; at the start of the second loop inlet methane has no reaction in the first stage but it will possess new hydrodynamics which will be used to find the expiration time of the second stage as well as the unconverted state of the other stages. This looping will continue until all the particles in all stages are fully expired. At the end of each stage, mass and fluid-dynamic equations are solved simultaneously to update gas concentrations, C_b and C_e, the superficial gas velocity, U, the bubble rise velocity, u_B, the bubble volume fraction, ε_b, the bubble diameter, d_B, and the unconverted oxygen carrier particles throughout the length of the reactor. All the variables used in the model are updated at the starting of a new. This needs to be implemented as the most of the hydrodynamic parameters are largely depended on the bubble size. For instance, in increase in bubble size results an increase in the superficial gas velocity and thus in u_B and ε_b. To properly model the rate of mass transfer between gas and solid phases, all of these variables, thus, need to update at each stage.

3.4 Results and discussions

3.4.1 Results from laboratory experiments

Figure 3- 3 shows the inlet gas flows used for reduction of the CuO/Al_2O_3 particles with methane gas. The time between subsequent reductions is for oxidation.

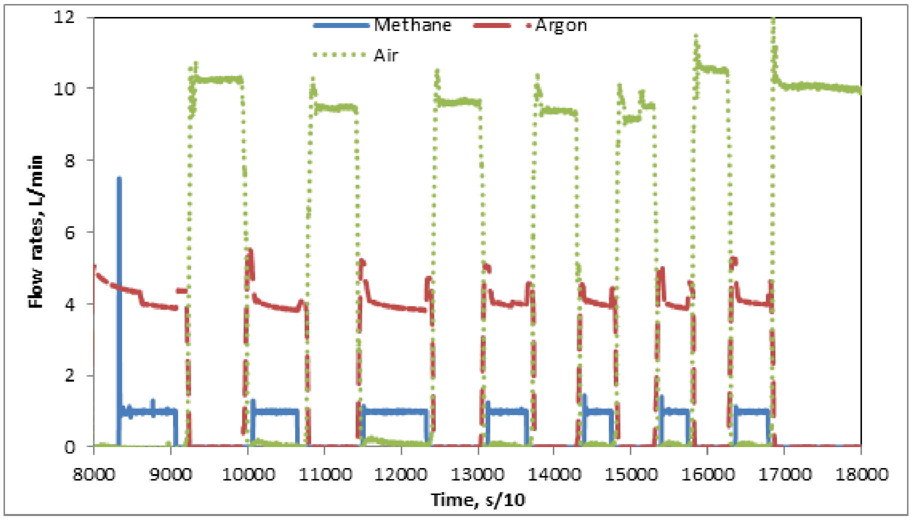

Figure 3- 3. Inlet gas flow rates during successive redox reaction of CuO/Al_2O_3 particles with methane.

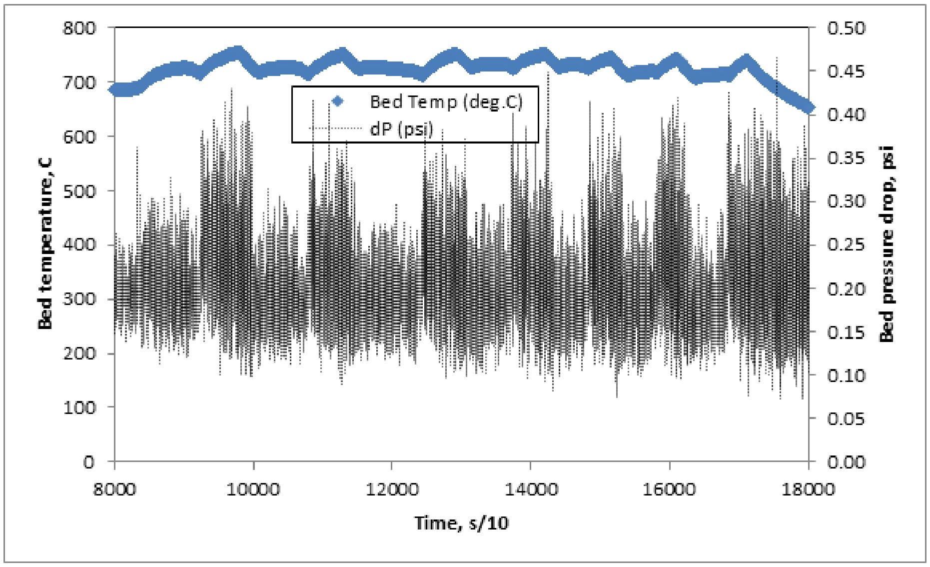

Figure 3- 4. Bed temperature and pressure drop during successive oxidation and reduction of CuO/Al_2O_3 particles.

It has been observed that the inlet gas flow time is reduced after 3rd reduction, which may refer to the degradation of the oxygen transferring capacity of CuO/Al_2O_3 particles. It may arise from the particle attrition and subsequent dust formation of oxygen carrier particles during the oxidation period where a high velocity of air has been used.

Figure 3- 4 shows the temperature and bed pressure drop variation during the redox reactions. Bed temperature remained nearly constant during reduction periods but varied during the oxidation due to the lack of quick heat removal from the system. In the oxidation state, reactions are very fast and highly exothermic, which results in temperature fluctuation.

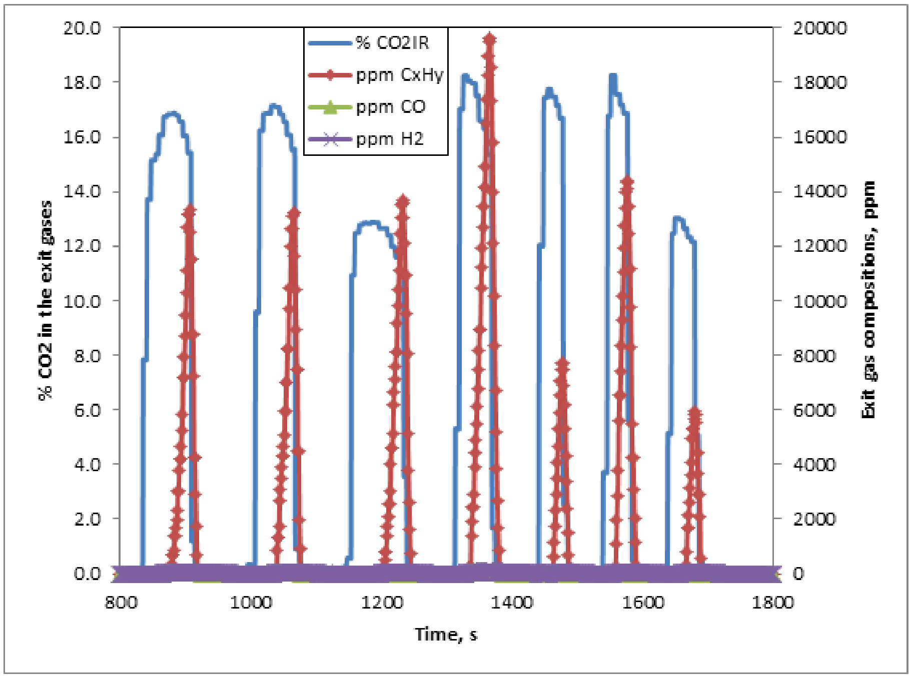

Figure 3- 5. Exit gas composition during reduction of CuO/Al_2O_3 particles with methane.

The differential pressure profile shows the bubbling characteristics of the fluidized bed. Large pressure drop is observed during the oxidation compared to the reduction ($U \approx 2.5\, u_{mf}$) periods due to the high inlet gas velocities ($U \approx 6\, u_{mf}$).

Figure 3- 5 shows the outlet gas concentrations after condensation of water as a function of time for the reducing cycles when methane was used as fuel. A sample of 126.6 g of CuO/Al_2O_3 was used at a temperature of ~720 ◦C. In Figure 3- 5, the CH_4 is turned on but the residence time in the system delays the response by 10–15s before the CO_2 rapidly increases. CO_2 reaches a maximum a few second later and remains constant before the inlet CH_4 flow turned off. On the other hand, CH_4 increases through the whole

cycle. However, methane flow has turned off after a certain volume of CH_4 is detected in the exit gas analyzer. CO and H_2 concentration remains nearly zero for all the reduction cycles. Worth noting is that all of the CH_4 reacts to form CO_2 and H_2O before any detectable CH_4 at the reactor exit. However, below 100 ppm of CO and H_2 were detected by the gas analyzer when there was CH_4 at the reactor exit. This indicates that a small fraction of the inlet CH_4 goes through partial oxidation by producing CO and H_2.

3.4.2 Comparison of model with experimental results

3.4.2.1 A different method of reactor staging

A number of authors applied the concept of dividing axially the bubbling bed in stages and considering a number of stages of the same length [13-15]. A large number of bubbles with its minimum size present at the bottom and the incoming gas, which encounters the solid particles, create turbulent motions that result in a low solid volume fraction at the bottom. As shown in Figure 3- 6, the length of the reactor is divided into 10 stages based on the equal mass percentage in each stage but of different length. This subdivision method also provides a validation for the total mass balance of the solid particles used in the experiment. It shows that there is a 25% (height was 88 mm and 110 mm at minimum fluidization and reactor conditions, respectively) bed expansion which is expected for this bubbling fluidized bed.

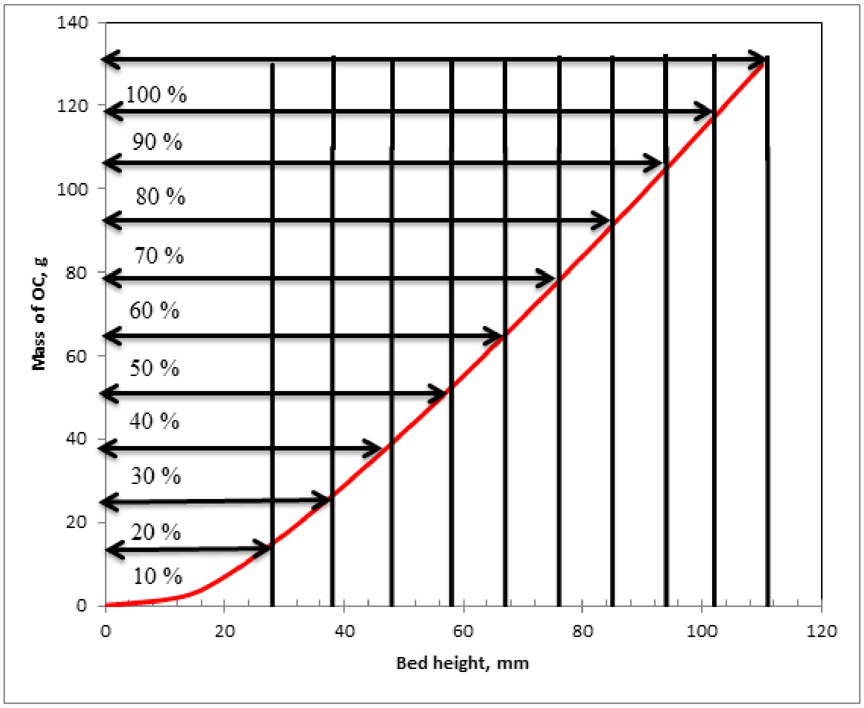

Figure 3- 6. Staging of the solid bed used in the model based on the mass of the solid oxygen carrier (OC) used in the experiment. Total mass of oxygen carrier was 126.6 g.

Figure 3- 7 shows the concentration of methane leaving from different stages of the bed. From left to right, different curves represent the unreacted methane concentration. It indicates that all the methane is consumed until the 6th stage and after that methane starts to leave the reactor as unreacted. At 10th stage, all the methane leaves the reactor as unreacted.

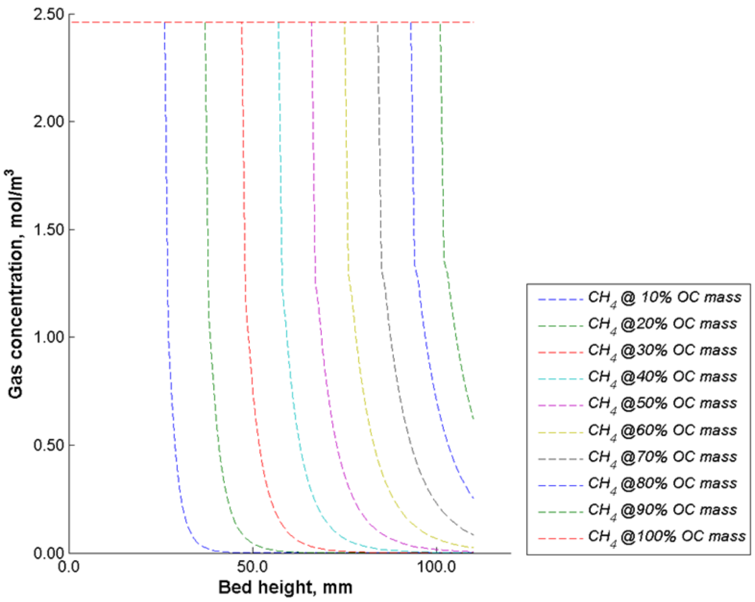

Figure 3- 7. Axial profile of CH_4 leaving from different stages considered in the model of the fluidized bed reactor.

3.4.2.2 Model validation

The lab-scale fuel-reactor described in the experimental section using a Cu-based oxygen-carrier was numerically simulated according to the model developed in this study. The physical properties used in the model are shown in Table 3-1. The operating conditions and experimental results used for this study are discussed above.

Using the physical properties of gas and solid as input parameter, the model predicts the performance indices of the reactor such as solid conversion, fuel concentration in the bubble and the emulsion phases, distribution of products and reactants (CH_4, CO_2 and H_2O) at the reactor exit. For instance, Figure 3- 8 shows the concentration of CH_4, CO_2, and H_2O in the reactor [2]. The solid concentration is shown by the unreacted amount of CuO in the oxygen carrier during the first looping step described in the model section. Experimental results showed that formation of CO and H_2 were negligible. So, the partial oxidation of methane was not considered for model validation as well. As it can be seen methane is fully consumed within the first 30 mm of bed height and all the CuO is converted to either Cu or Cu_2O.

Table 3- 1. Parameters used in the model prediction

Parameters	Values	Reference
Concentration of CH_4 at STP (kg/m^3)	0.66	[16, 17]
Viscosity of CH_4 at 720 °C (Pa s)	3.75 E-5	
Diffusivity of CH_4 through Argon (m2/s)	1.6 E-4	
Molecular weight of CuO (g/mol)	79.54	
Density of CuO (kg/m^3)	6.31 E 3	
BET surface area of oxygen carrier (m^2/g)	140	Clariant corp
Minimum fluidization velocity (cm/s)	6.0	[9]
Activation energy(kJ/mol)	60	[12]
Pre-exponential factor (mol^{1-n} m^{3n-2} s^{-1})	4.5 E-4	
Reaction order, n	0.4	
Orifice density, N (1/m^2)	350000	[9]

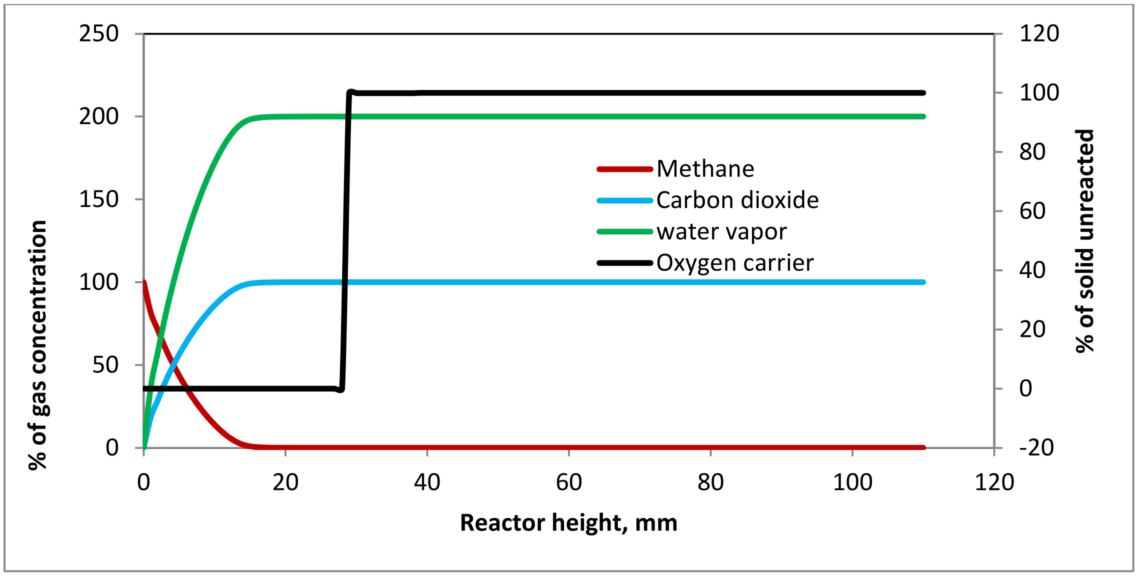

Figure 3- 8. Axial profiles of gas and solids concentration during the first looping condition.

The main goal of this model is to predict the methane break-through time for CuO/Al_2O_3 carrier particles. This will enable us to choose a best switch time for the 100 kW pilot scale reactor, which will help in overall fuel conversion and carbon capture efficiency of the pilot plant. Figure 3- 9 shows the predicted methane break-through for the first two reduction cycles of the experiment. As discussed above, cycle time decreases for reduction with methane due to the particle attrition and/or dust formation, and consequently due to the loss of those particles through elutriation during high air flow rates, the model cannot capture these. Thus, the model is validated only for the first two reduction cycles. It can be seen experimental results falls within the two reduced state of CuO/Al_2O_3 particles. In both states, the slope of the experimental curve and the model show similar trend. When most of the oxygen carrier particles are in reduced state, the reactor behaves like a plug flow and methane bleeds through the solid bed without any reaction. The model with the assumption of Cu_2O reduced state of particles shows better predictability with the experiment.

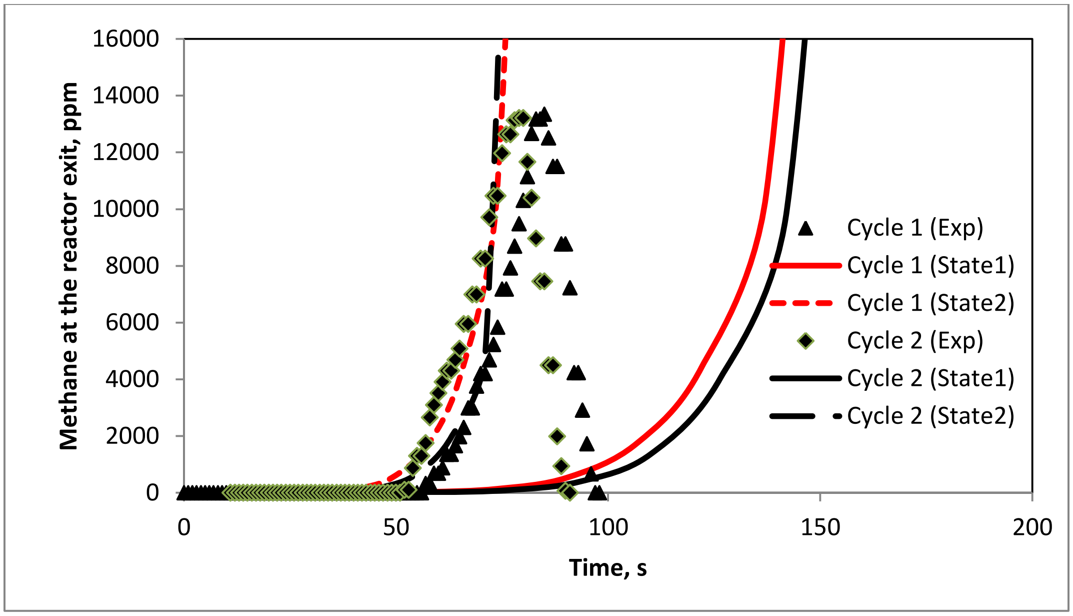

Figure 3- 9. Concentration profile for the reduction period with CH_4 as reducing gas at a temperature of ~720 ◦C. The first two reduction cycles are shown here for model prediction. State1 and state2 represent the reduced state of CuO as Cu and Cu_2O.

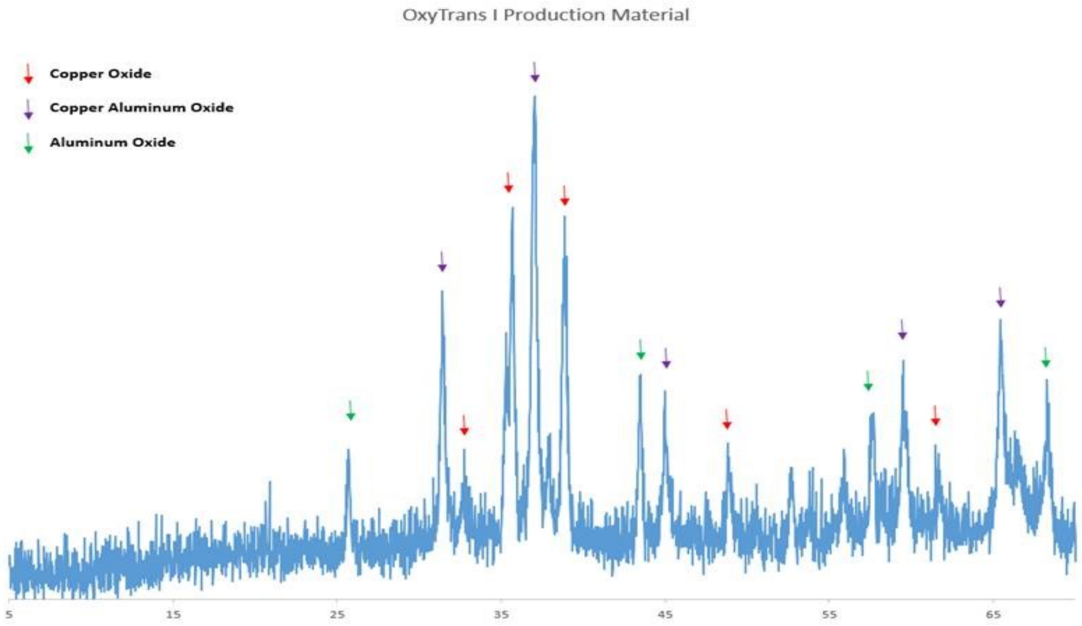

Figure 3- 10. Presence of different oxides in oxygen carrier supplied by CLARIANT (Image courtesy: Tom Pusty, Clariant).

The stoichiometric calculation of methane reaction with CuO/Al_2O_3 reveals that about 1.92 g or 0.96 g of CH4 is required for the reduced state of Cu or Cu_2O for 126.6 g particles. From Figure 3- 3, it is seen methane was fed for about 1.5 min during the first two reduction cycles at ~1.0 L/min rate, which is approximately 1.10 g of CH_4. This indicates that the exact reduced states of the oxygen carrier remains with the two reduced state of the CuO under experimental conditions. However, the emission spectroscopy of the oxygen carrier at the oxidized state shows that there is copper aluminum oxide in addition to CuO (Figure 3- 10). Further analysis of the oxygen carrier after successive oxidation and reduction phases will help better understanding of the reduction reactions and accordingly the model prediction can be improved for methane break-through time.

3.5 Conclusion

A multi-stage mathematical model has been developed to simulate behavior of a lab-scale bubbling fluidized bed reactor. In this model, the hydrodynamics of the fluids, and the reaction kinetics and pathways of solid oxygen-carrier are explicitly considered for the conversion of the gaseous fuel. Using the physical properties of gas and solid as input parameter, the model predicts the performance indices of the reactor such as solid conversion, fuel concentration in the bubble and the emulsion phases, distribution of products and reactants (CH_4, CO_2 and H_2O) at the reactor exit. The model shows better prediction with experiment when reduced state of CuO particles is assumed. By understanding the oxide and reduced states of oxygen carrier in successive cycles will improve the reaction rate calculation, and thereby the prediction of fuel break-through time from the reactor will be better predicted.

Nomenclature

A	Cross sectional area of the fluidized bed
Cb	Concentration of gas species in the bubble phase, mole/m^3
Ce	Concentration of gas species in the emulsion phase, mole/m^3
dB	Bubble diameter, m
D	Diameter of the fluidized bed, m
Dab	CH_4 diffusivity in CO_2, m^2/s
G	Acceleration of gravity, m/s^2

H	Solid bed height, m
Hmf	Bed height at minimum fluidization, m
K	Rate constant of reaction,
Kbe	Mass transfer coefficient between bubble and emulsion phases, s^{-1}
Kce	Mass transfer coefficient between cloud and emulsion phases, s^{-1}
Kbc	Mass transfer coefficient between bubble and cloud phases, s^{-1}
n	Order of reaction
Nd	Number of orifice per unit area of the bed, m^{-2}
uB	Bubble velocity, m/s
umf	Gas velocity at minimum fluidization, m/s
Ubr	Single bubble rise velocity, m/s
U0	Inlet superficial gas velocity, m/s
x	Stoichiometric coefficient
y	Stoichiometric coefficient

Greek letters

ε_{mf}	Void fraction at minimum fluidization
ρ_g	Gas density, kg/m^3
ρ_p	Particles density, kg/m^3
μ	Gas viscosity, Pa s
Φ_B	parameter for bubble diameter

Subscripts

b	Bubble phase
B	Bubble
c	Cloud phase
e	Emulsion phase
mf	Minimum fluidization
0	Initial
br	Bubble rise

References

[1] T. Stocker, D. Qin, G.-K. Plattner, M. Tignor, S. K. Allen, J. Boschung, A. Nauels, Y. Xia, V. Bex, and P. M. Midgley, *Climate change 2013: The physical science basis*: Cambridge University Press Cambridge, UK, and New York, 2014.

[2] A. Abad, J. Adanez, F. Garcia-Labiano, L. F. de Diego, and P. Gayan, "Modeling of the chemical-looping combustion of methane using a Cu-based oxygen-carrier," *Combustion and Flame,* vol. 157, pp. 602-615, Mar 2010.

[3] J. Adanez, A. Abad, F. Garcia-Labiano, P. Gayan, and F. Luis, "Progress in chemical-looping combustion and reforming technologies," *Progress in Energy and Combustion Science,* vol. 38, pp. 215-282, 2012.

[4] M. M. Hossain and H. I. de Lasa, "Chemical-looping combustion (CLC) for inherent CO2 separations—a review," *Chemical Engineering Science,* vol. 63, pp. 4433-4451, 2008.

[5] M. Yazdanpanah, A. Forret, T. Gauthier, and A. Delebarre, "Modeling of CH 4 combustion with NiO/NiAl 2 O 4 in a 10kW th CLC pilot plant," *Applied Energy,* vol. 113, pp. 1933-1944, 2014.

[6] O. Levenspiel, *Chemical reaction engineering*, 3 rd ed. NY: John Wiley & Sons, Inc., 1999.

[7] D. Kunni and O. Levenspiel, "Fluidization engineering," *Buterworth, New York,* 1991.

[8] P. Cho, T. Mattisson, and A. Lyngfelt, "Defluidization conditions for a fluidized bed of iron oxide-, nickel oxide-, and manganese oxide-containing oxygen

carriers for chemical-looping combustion," *Industrial & Engineering Chemistry Research,* vol. 45, pp. 968-977, 2006.

[9] K. Daizo and O. Levenspiel, "Fluidization engineering," 1991.

[10] J. R. Grace, "Contacting modes and behaviour classification of gas—solid and other two- phase suspensions," *The Canadian Journal of Chemical Engineering,* vol. 64, pp. 353-363, 1986.

[11] J. Werther, Ed., *Hydrodynamics and mass transfer between the bubble and emulsion phases in fluidized beds of sand and cracking catalyst* (Fluidization. Engineering Foundation. New York, 1984, p.^pp. Pages.

[12] F. Garcia-Labiano, L. De Diego, J. Adánez, A. Abad, and P. Gayán, "Reduction and oxidation kinetics of a copper-based oxygen carrier prepared by impregnation for chemical-looping combustion," *Industrial & Engineering Chemistry Research,* vol. 43, pp. 8168-8177, 2004.

[13] R. Jafari, R. Sotudeh- Gharebagh, and N. Mostoufi, "Modular simulation of fluidized bed reactors," *Chemical Engineering & Technology,* vol. 27, pp. 123-129, 2004.

[14] R. Porrazzo, G. White, and R. Ocone, "Aspen Plus simulations of fluidised beds for chemical looping combustion," *Fuel,* vol. 136, pp. 46-56, 2014.

[15] A. Hashemi Sohi, A. Eslami, A. Sheikhi, and R. Sotudeh-Gharebagh, "Sequential-based process modeling of natural gas combustion in a fluidized bed reactor," *Energy & Fuels,* vol. 26, pp. 2058-2067, 2012.

[16] J. L. Plawsky, *Transport phenomena fundamentals*: CRC Press, 2014.

[17] W. Kelly, "Perry's chemical engineers' handbook," 1973.

CHAPTER 4

Mass transfer to large and light particles in a gas-solid bubbling fluidized bed of smaller and heavier particles: Experimental and CFD study

Abstract

The rate of mass transfer in a gas-solid fluidized gasifier, consisting of large and light fuel particles in a bed of finer and heavier particles, plays a critical role in its successful design and operation. In this study, the rate of mass transfer between hygroscopic silica gel particles and humid air in a bed of finer and heavier bronze particles is investigated both experimentally and numerically in a lab-scale fluidized bed. It has been shown that the mass transfer coefficient decreases with increasing the mass of silica gel particles in the fluidize bed. A simplified form of perturbation theory is used to explain the multi-particles effect on the mass transfer rate coefficient. In order to use the semi-empirical correlation for the prediction of mass transfer rate using CFD simulations, a modification is suggested for Froessling correlation. The measured and computed rate of mass transfer show good agreement when the additive diffusional and convective resistances are incorporated in the CFD simulation by incorporating the species conservation equations. CFD analysis of mass transfer coefficient suggest that it is possible to compute the rate of mass transfer in fluidized bed reactors without using the conventional model with empirical mass transfer coefficients.

4.1 Introduction

With the increasing demand of renewable energy and reduction of CO_2 emissions from fossil fuels, biomass gasification, combustion, pyrolysis and co-firing processes have gained much attention as biomass conversion is regarded as carbon neutral [1]. Gasification of biomass in fluidized beds has been indicated as one of the most promising techniques, because of its flexibility, high efficiency, and low environmental impact [2, 3]. However, biomass gasification unit is expensive to construct and possesses complex hydrodynamic behavior.

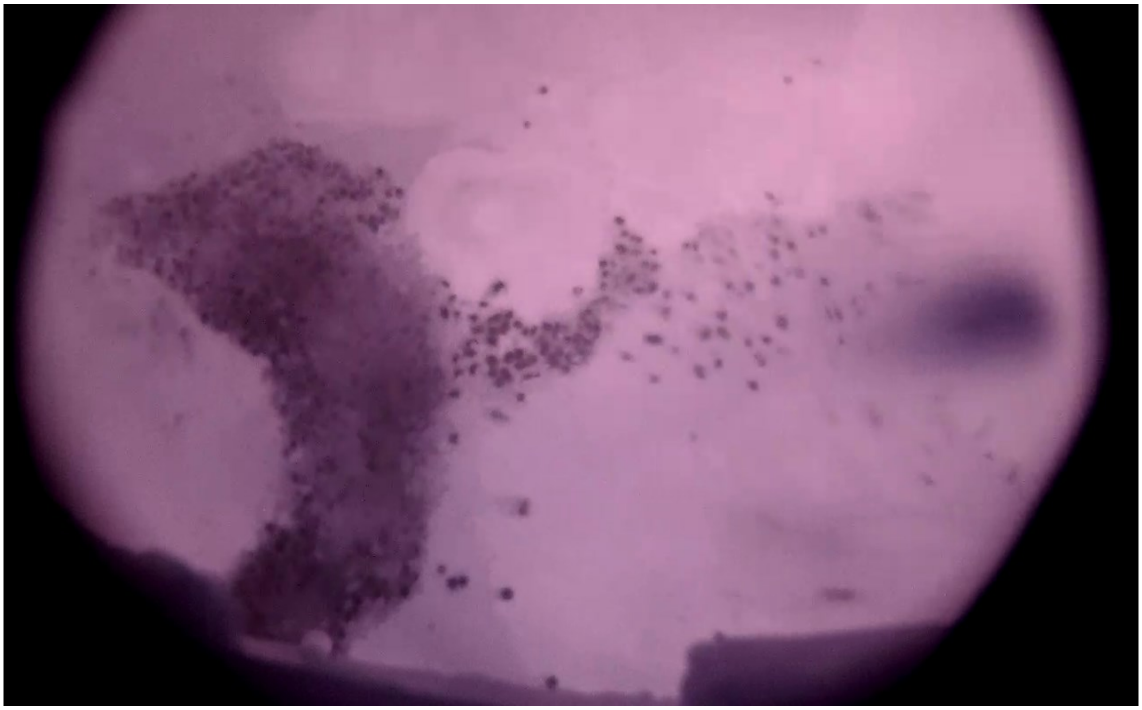

Figure 4- 1. Snapshot from a 2-4 MW steam blown biomass gasifier at Chalmers University of Technology. Photo is courtesy of Erik Sette, Chalmers University of Technology.

The image shows the bed surface of a 2-4 MW steam blown gasifier. The visible bed surface is approximately 1 m^2 and the black dots are devolatilizing wood pellet, which has the tendency to float and be grouped together on the surface of the bubbling fluidized bed. This process exhibits complex heat and mass transfer, complicating the design and scale-up of fluidized bed gasifier.

In gasification, a low mass fraction (less than 5 %) of large and light fuel particles is gasified in a bubbling fluidized bed. To ensure smooth and stable fluidization inert particles such as sand are often mixed with fuel particles. This facilitates the mixing of gas and fuel particles, providing more effective chemical reactions, mass and heat transfer [4]. Currently the design and operation of biomass gasification process rely on the knowledge of conventional fluidization and the assumption that biomass behaves similar to other conventional particles [5]. However, as shown in Figure 4- 1, the unusual properties of biomass and the possible influence on fluidization are largely underestimated. The rate of mass transfer in such gasification process plays a key role. Therefore, to be able to understand the process of gasification of biomass particles in a fluidized bed, one first needs to obtain the information on the rate of mass transfer between gas and solids in such fluidized beds.

A great deal of studies is devoted to model and measure the mass transfer coefficient in biomass gasification using thermo-gravimetric analysis [6-9]. But there are few literatures on the study of mass transfer in fluidized bed gasification process [5]. However, the study of the interface mass transfer between fluidizing gas and single solid phase has been studied using UV absorption techniques [10-12] , sampling methods [13], gas sensors [14], nuclear magnetic resonance [15], and injection of an isolated or stream of tracer bubbles [10]. The rate of mass transfer from fluidizing gas to light and large solid particles has also been the subject of many studies using many different experimental techniques, such as combustion of char/coal/carbon particles [16-20], evaporation of liquid from the surface of porous particles [21, 22], and sublimation of naphthalene particles [20, 23-26]. The rate of mass transfer is predicted based on the dimensionless mass transfer numbers (e.g. Sherwood) with semi-empirical correlations and theoretical approaches [27-29]. Note that these techniques possess some disadvantages like high costs or the use of unsafe gases, and also they often lack the required spatial and temporal resolution. Kai et al [30] measured the overall mass transfer coefficient between gas (bubble phase) and solids (emulsion phase) at ambient temperature in a fine particle fluidized bed and concluded that the rate of mass transfer were affected by the flow patterns of bubbles. This further highlights the shortcomings of experimental techniques that are not capable of intrinsically capturing the complexity of non-linear interactions between gas and solid particles.

In recent years, the first-principles based computational fluid dynamics (CFD) has emerged as a powerful and vital tool in modeling thermochemical reactors such as gasifiers. CFD allows to explore complex phenomena within a fluidized bed, including mass and/or heat transfer rates, and gas-solid, catalytic, or homogeneous reaction rates. These objectives are achieved by solving a set of conservation equations for mass, momentum and species, over spatially resolved grids, with necessary closure relations accounting for the discrepancy between fully resolved motion of particle and the continuum approximation. The most popular CFD modeling approaches being the Eulerian–Eulerian two-fluid model (TFM) [31] and the Eulerian–Lagrangian discrete particle model (DPM) [32]. The kinetic theory based TFM appears to be computationally less expensive and has been extensively validated with experimental studies [33-38].

In its early development, most of the CFD studies have focused on hydrodynamics, solid motion and heat transfer rate in gas-solid fluidized beds [3, 26, 39-43]. In contrast, limited numbers of researches have carried out the measurement of the rate of mass transfer in gas-solid fluidized beds. More specifically, most of the CFD studies on mass transfer are focused on monodispersed solid or multi-solids phase with uniform particle sizes [44-46], emphasizing the effects of meso-structure (i.e. particle cluster) on momentum and mass transfer between gas and solid phases [47, 48]. A good review of this is provided in [49]. Additionally, most of the CFD works have used instantaneous flow dynamic properties in semi-empirical and theoretical correlations to calculate the mass transfer in fluidized beds [42, 43, 50]. For example, CFD can be used to predict local gas velocity, which can be used in empirical or semi-theoretical correlations for predicting mass transfer rates [51]. However, using an empirical correlation in a CFD model fails to fully exploit the potential for CFD. Despite the importance of the rate of mass transfer phenomenon in fluidized beds of large and light fuel particles in a bed of finer and heavier particles, there has so far not been much attempt to study it numerically.

Recently, Scala [52] reviewed the available semi-empirical and theoretical correlations that are used to calculate the experimental rate of mass transfer in large and light fuel (active) particles in a bed of finer and heavier (inert) particles fluidized bed. Theoretically, he showed that the mass transfer rate per area between gas and large (reactive) particles decreases with increasing the mass fraction of reactive particles in such fluidized bed. However, no experimental data was provided to verify that phenomenon.

The above literature review clearly shows the deficiency of information regarding the rate of mass transfer in large and light fuel particles in a bed of finer and heavier particles. Further experimental and CFD studies are needed to better understand mass transfer rates in fluidized bed gasification of light fuel particles (biomass) in a bed of finer and heavier (inert) particles. The objective of the present work is to study the rate of mass transfer between fluidizing gas and large and light fuel particles in a bed of finer and heavier particles - both experimentally and computationally.

The rate of mass transfer is investigated in lab-scale fluidized bed by measuring the adsorption rate of water vapor on the surface of light and large hygroscopic silica gel particles in a bed of finer and heavier bronze particles. The physical setup is numerically simulated using the TFM by two approaches, one simplistic using semi-empirical correlations, and the second exploiting the full potential of CFD.

4.2 Froessling correlation for fluidized bed application

The exact analytical solution to the set of equations describing the boundary layer problem for mass transfer around a sphere in a gas-solid fluidized bed is not available. Empirical and semi-empirical correlations are typically used to correlate experimental results to calculate mass transfer rate. Such an extensively used correlation, proposed by

Froessling [27], has both diffusive and convective components. Chakraborty and Howard [16] modified the Froessling correlation for application to fluidized bed reactor by accounting for effects of bed voidage, ε, on the diffusive component.

$$Sh = 2\varepsilon + 0.6\, Re^{\frac{1}{2}}\, Sc^{\frac{1}{3}} \tag{1}$$

Where Sh, Re and Sc are the dimensionless Sherwood, Reynolds and Schmidt number, respectively. Equation (1) accounts for the effect of bed voidage on the diffusive component but ignores surface area effect on the convective component. In a fluidized bed, mass transfer is limited because other particles will tend to interfere with mass transfer, either by directly covering the surface area, or by blocking diffusion, or by actually capturing the gaseous species before it diffuses to the particle surface. This additional resistance to mass transport should be considered for both diffusive and convective parts of the equation, and the average interstitial velocity, (U_0/ε) should be used to calculate Reynolds number to more closely reflect the boundary layer flow. With these two modifications, the modified form of equation (1) would be

$$Sh = \varepsilon \left[2 + 0.6 \left(\frac{\rho d_p \left(\frac{U_0}{\varepsilon} \right)}{\mu} \right)^{\frac{1}{2}} Sc^{\frac{1}{3}} \right] \tag{2}$$

Where ρ and μ are the fluid density and viscosity, respectively. d_p is the particle diameter and $Re= \rho U_0 d_p / \mu$.

$$Sh = 2\varepsilon + 0.6\, \varepsilon^{\frac{1}{2}}\, Re^{\frac{1}{2}}\, Sc^{\frac{1}{3}} \tag{3}$$

Although, the local instantaneous bed void fraction and Re are unknown for experimental conditions but, for a CFD simulation, these quantities can be obtained easily. For experimental case, an average bed voidage can be used for mass transfer rate calculation.

4.3 Experiment section

4.3.1 Material

In the present study, a small number of hygroscopic silica gel particles are used as light, large (reactive) particles [53]. The median diameter (d_{50}) of silica gel particles is 3.5 mm with a size range of 2 to 5 mm. Bronze powder, with a size distribution of 45 to 125 µm, represented small, dense (inert) bed materials.

4.3.2 Apparatus and procedure

Experiments were conducted in a perspex column with inner diameter 6 cm and a height of 50 cm. A simplified schematic of experimental setup is shown in Figure 4- 2. Two sheets of fine mesh screen are used to prevent particles falling into the windbox and ensured a pressure drop across the distributor of at least 30% of the pressure drop across the bed alone at minimum fluidization. A mass flow meter with a controller is used to measure dry air flow rate. Two transmitters, (Vaisala Combined Pressure, Humidity and Temperature Transmitter, PTU300), one at the inlet and the other at the outlet of fluidized, is used to measure pressure, temperature and absolute humidity.

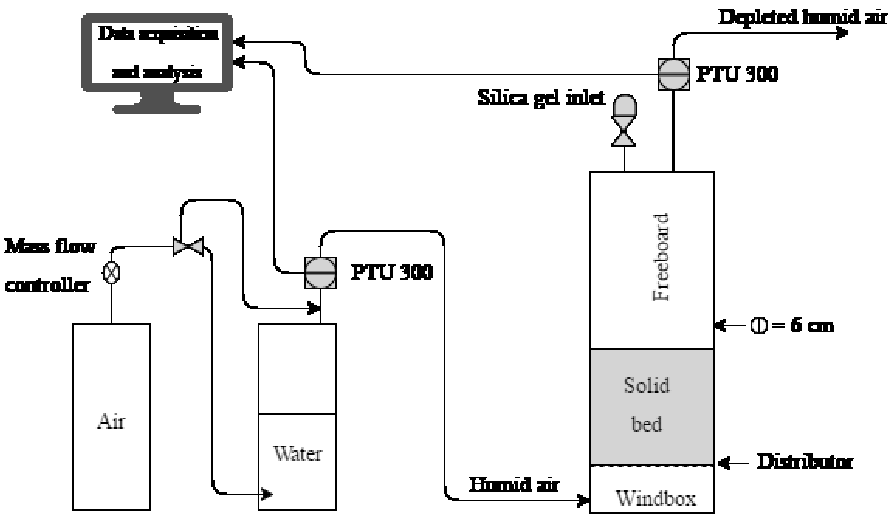

Figure 4- 2. Simplified schematic of experimental setup.

Initially, bronze particles are added in the fluidized bed and fluidized with dry air to establish a quasi-steady fluidization. Dry air flow rate is kept constant at 15 liters per min (superficial velocity = 8.84 cm/s). When fluidization has reached at quasi-steady state, dry air has flowed through water to produce humid air and to fluidize bronze particles. After bubbling through water, the air fed to the fluidized bed has humidity 7.0 g H_2O/ kg dry air, which is equivalent to 50% relative humidity at this temperature. All experiments are performed at atmospheric pressure and at room temperature.

The bed of inter solids is fluidized with humid air until there absolute humidity reading from outlet approaches that of the inlet. At this time, a mass of silica gel particles is quickly added. Three different quantities of silica gel particles, 6.3 g, 9.4 g, and 12.7 g is used in different experiments. The mass of bronze particles was kept constant at 660 g in all experiments. When the absolute humidity at the outlet has nearly reached that of the inlet, it is assumed that silica gel particles are saturated with water and there is no more mass transfer. Experiments are repeated two times for 6.3 g of silica gel to ensure consistency. The data acquisition frequency is 1Hz.

4.3.3 Experimental results

4.3.3.1 Rate of mass transfer

The rate of mass transfer measurement was calculated from the measured pressure, temperature and humidity. The rate of adsorption of water vapor by silica gel particles is computed from the measured absolute humidities before and after the fluidized bed, and from the known air flow rate.

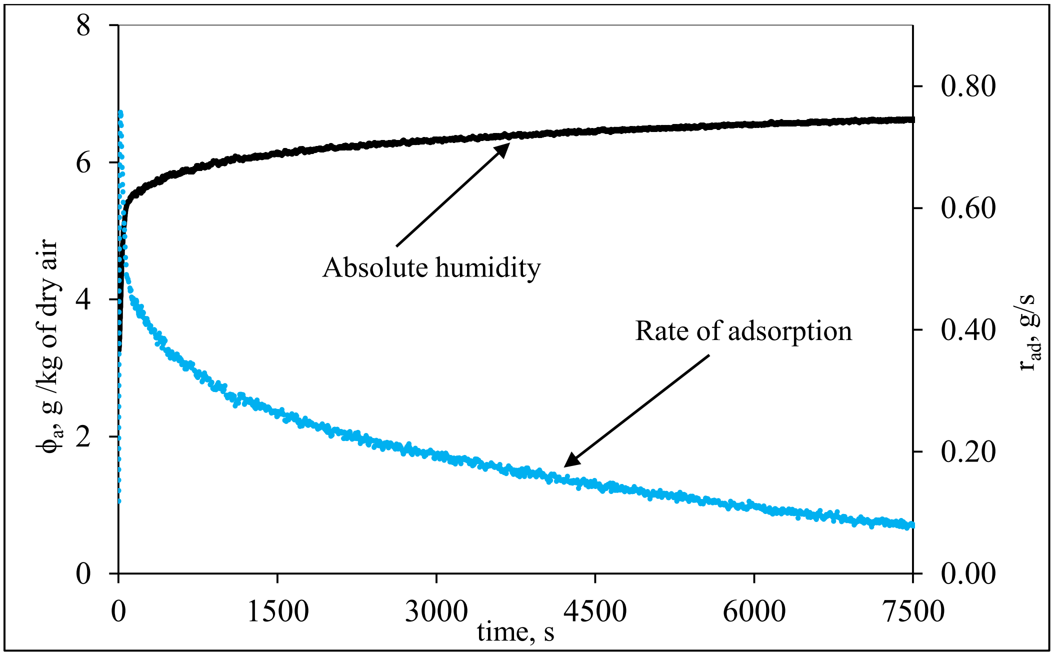

Figure 4- 3. This graph shows the measured absolute humidity in exhaust from the fluidized bed C_{out}, as a function of time, and the calculated rate of adsorption r_{ad}. Mass of silica gel was 6.3 g.

Figure 4- 3 shows representative recorded data of absolute humidity at the fluidized bed outlet and the corresponding rate of adsorption. The absolute humidity of inlet air was kept constant at 7.0 g of water vapor per kg of dry air throughout the duration of the experiment. The outlet humidity initially changed rapidly, reflecting a rapid rate of adsorption. Over time, the humidity in the outlet air approached that of the inlet air, reflecting a reduced rate of adsorption.

The driving force for mass transfer of water is the difference in water concentration (humidity) between the surrounding air and in that at the surface of the silica gel. At any moment the thermodynamic equilibrium concentration of water vapor, C_{eq} (t), at the surface of the silica gel particle is calculated from the correlation proposed by Ng et al. [54] for water-silica gel system and using ideal gas assumption for water vapor.

$$C_{eq}(t) = \frac{4.2\times10^{11}\chi(t)}{T(t)}\left(\exp\left(\frac{5160}{T(t)}\right)\right)^{-1} \qquad [g/m^3] \qquad (4)$$

Where χ(t) is the mass fraction of condensed water in silica gel particles. The instantaneous mass of water vapor at the inlet and outlet are calculated from the absolute humidity readings, and the balance of the water vapor mass between inlet and outlet is rationalized with silica gel mass to obtain χ(t). T(t) is the temperature in kelvin. Figure 4-4 shows the interphase water vapor concentration at the surface of silica gel particles. As moisture diffuses to the surface of the silica, it is adsorbed, resulting in increased moisture, χ(t). The interphase vapor concentration, calculated from equation 3, increases with time. An increase in interphase vapor concentration results in a decreased driving force for mass transfer and a reduced adsorption rate, as shown in Figure 4- 3.

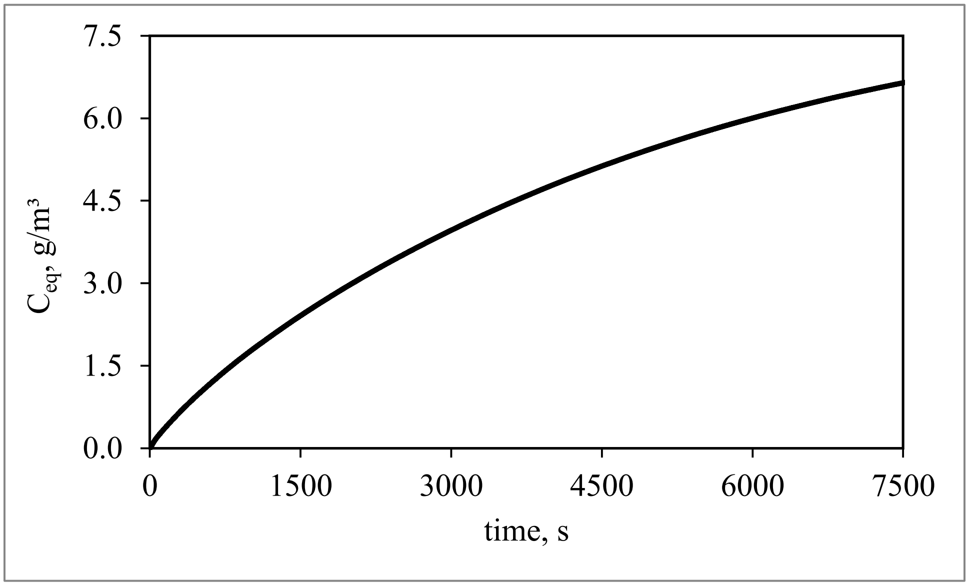

Figure 4- 4. Equilibrium water vapor concentration at the silica gel particle surface (6.3g).

As described earlier, the driving force for mass transfer is the difference between the moisture in the bulk gas and the moisture at the silica surface. In a fluidized bed, the gas flow is complex, and not well described either by plug flow or well mixed assumptions. Clearly, the driving force for mass transfer at the inlet is greater than that at the outlet. Here, we use a log mean, concentration, $\Delta C_{LMCD}(t)$, calculated based on the inlet C_{in} (t), interphase and outlet C_{out} (t),

$$\Delta C_{LMCD}(t) = \frac{(C_{in}(t)-C_{eq}(t))-(C_{out}(t)-C_{eq}(t))}{\log\left(\frac{C_{in}(t)-C_{eq}(t)}{C_{out}(t)-C_{eq}(t)}\right)} \tag{5}$$

Finally, the instantaneous mass transfer coefficient k_c (t), is calculated using the rate of water vapor adsorption by silica gel and logarithmic mean concentration differences.

$$k_c(t) = \frac{r_{ad}(\mathrm{t})}{A_S\, \Delta C_{LMCD}(t)} \tag{6}$$

Where A_s is the surface area of all silica gel particles. Figure 4- 5 shows the measured mass transfer coefficients for three amounts of silica gel particles. In each experiment, the mass transfer coefficient drops a bit during the initial few minutes. For two of the experiments, k_c held constant after the initial decrease, and in the third experiment, the rate gradually increased over time.

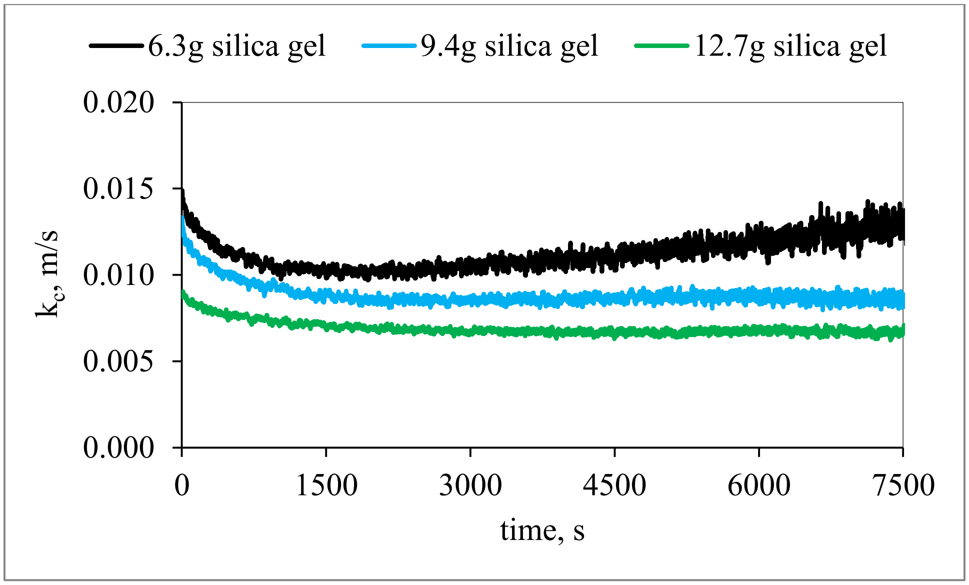

Figure 4- 5. Mass transfer coefficient for different amounts of silica gel particles.

In an ideal case, mass transfer coefficients should be constant with time. However, the experimentally measured mass transfer coefficients do change over time.

This may be due to the internal pore diffusion resistance for mass transfer inside silica gel particle, as reported by Sun and Bresant [55]. In such scenario, the water vapor diffusion resistance competes with the corresponding internal pore diffusion resistance.

A summary of the experimental results is shown in Table 4- 1. The rate of mass transfer decreases with increase of the mass of silica gel particles. The detail discussion on this is given in the following section.

Table 4- 1. Summary of mass transfer coefficient for silica gel-water vapor system.

Mass of silica gel, g	Mass transfer coefficient, k_c, m/s		
	Maximum	Minimum	Average value
6.3	0.015	0.010	0.011
9.4	0.013	0.007	0.009
12.7	0.009	0.006	0.007

4.3.3.2 Effect of mass of silica gel on mass transfer

As shown in Figure 4- 5, the rate of mass transfer is affected somewhat by the mass of silica gel particles added to the bed. While only three data points, there seems to be a clear trend that k_c decreases with increasing the mass of silica gel particles. From experimental observation, silica gel particles behave as flotsam, floating near the top of the fluidized bed due to the high density difference with inert bronze particles, giving rise to complete particles segregation. Pallarès and Johnsson [56] tracked a phosphorescent large and light tracer particle in a bed of finer and heavier particle by means of video recording and showed that tracer particle preferentially stays near the wall and close to the bed surface, and that behavior was observed in these experiments. These consequences ultimately affect the rates of adsorption of water vapor.

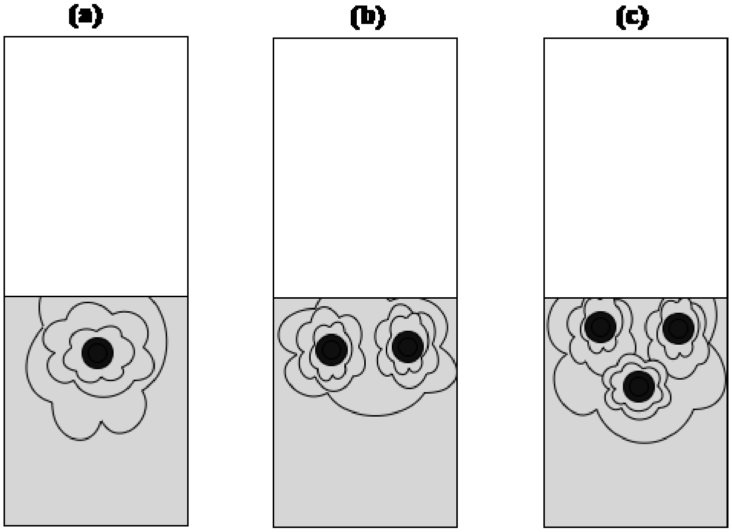

Figure 4- 6. Cartoon showing the effect of multi-particles on the concentration contour of adsorbing gas. The filled circle represents adsorbing solid (silica gel) particle surrounded with inert solid powder (gray color).

We propose here a hypothesis to explain why increasing the mass of silica particles results in reduced mass transfer coefficient. Figure 4- 6 (a) shows the contours of water vapor concentration around a silica gel particle (filled circle) in a bed of finer and heavier particles. By adding another silica gel particle, the concentration of water vapor around those particles is perturbed (Figure 4- 6 (b)) and this process continues (Figure 4- 6 (c)) with addition of more particles. Similar to concentration, Cornish [57] first pointed out that the rate of heat transfer from a sphere is decreased when other spheres are adjacent to it. It is reasonable to expect that the contours of individual silica gel particles will overlap with one another. A significant consequence is that the gas surrounding the individual particles loses moisture to other “competing” particles. Thus, the rate of mass transfer to an individual particle is reduced by the presence of nearby competing particles.

Perturbation or density function theory [58] is introduced to explain the effect of multiple particles in the system. The idea is to start with a simple system for which a mathematical solution is known, and add a weak disturbance to the system. Often times, such solution gives a power series. A simplified approach is proposed to account the effect of multiple silica gel particles on mass transfer rate as

$$k_c = k_0 \exp\{\kappa(N-1)\} \tag{7}$$

Where k_0 is the rate coefficient measured for a single particle and κ is assumed as the weak disturbance accounted from other particles. The number of silica gel particle, N, is estimated from the total mass of silica gel, assuming uniform spheres of density 2210 kg/m^3. If values for k_c are known for several values of N, the value of k_0 and κ may be calculated using any nonlinear regression method, e.g, the residual minimization Levenberg-Marquardt. In this case, we found $k_0 = 0.018$ m/s and $\kappa = -3.78 \times 10^{-3}$.

Figure 4- 7 shows the experimentally measured mass transfer coefficients as circles, along with the equation 6. The fit is reasonable. For an infinite number of particles, the value of mass transfer coefficient approaches zero, as the bed fills with silica gel and no moisture can penetrate the bed. For such a system, this correlation will not be applicable.

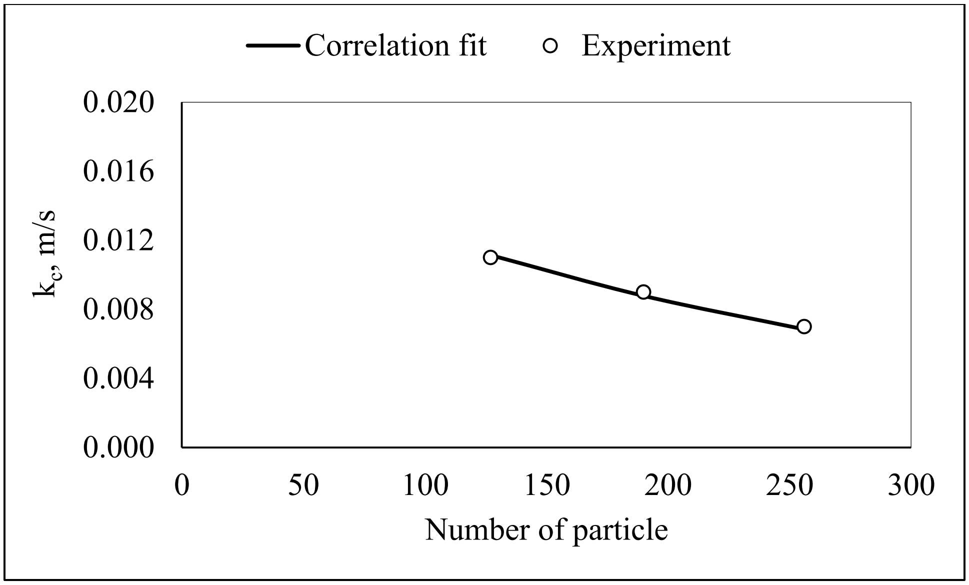

Figure 4- 7. Perturbation model and experimental measurement of mass transfer coefficient for different number/mass of silica gel particles.

4.4 CFD simulation

A common technique for simulating multiphase flows is the Eulerian-Eulerian Two-Fluid Model (TFM), which treats each phase (gas and solid) as interpenetrating continua. The TFM was used in this to simulate the lab-scale fluidized bed used to collect the data shown in Figure 4- 2. The TFM equations are coupled through constitutive relations [31]. The inter-particle interactions are modeled using the solids stress tensor, which is evaluated using the frictional theory by Schaeffer [59] in dense regions of the bed and the Kinetic Theory of Granular Flow [33] in dilute pockets of the bed. The interphase momentum transfer between gas and solid phases are coupled by drag force computed using Syamlal-O'Brien model [37]. The mass conservation of gas species are incorporated in the CFD through species conservation equations. Further details regarding the TFM, governing equations and numerical technique can be found in [60, 61].

The modified phase coupled SIMPLE scheme, which uses a solids volume fraction correction equation instead of a solids pressure correction equation, is used for pressure–velocity coupling with a second-order SuperBee spatial discretization schemes. A combination of point successive under relaxation and biconjugate gradient stabilized method (BiCGSTAB) method is employed for the linear equation solver. A maximum residual at convergence of 10^{-04} is set to improve the accuracy of the continuity and momentum equations solution. An automatic time-step adjustment with a maximum and minimum time-step of $5x10^{-04}$ s and 10^{-07} s respectively, is used to enhance the computation speed.

Table 4- 2. Summary of simulation parameters.

Particle diameter, (μm)	85
Particle density, (kg/m^3)	8800
Maximum solid packing	0.58
Uniform inlet velocity, U_0 (cm/s)	8.84
Coefficient of restitution	0.90
Angle of internal friction, (°)	30
Fluid viscosity, (kg/m/s)	1.8 x 10-5
Diffusivity of water vapor in air, (m^2/s)	2 x 10-5
Density of humid air, ρ_g (kg/m^3)	1.17
Initial bed height, (cm)	5.50

All the simulations are conducted in 2-D Cartesian coordinate. The initial conditions specify the gas flow as one dimensional at the superficial air velocity. A constant pressure is specified in all horizontal planes up through the bed of particles. The upper section of the bed, or freeboard, is assumed to be occupied by gas only. The lateral walls are modeled using no-slip velocity boundary conditions. Dirichlet boundary conditions are employed at the distributor to specify a uniform gas inlet velocity. Pressure boundary condition is fixed at the top of the freeboard. Gas phase boundary is set as no-slip and solid phase boundary is set as partial-slip. The other physical and assumed parameters used in the simulation are listed in Table 4- 2.

The computational domain is selected as 60 mm (width) × 120 mm (height), and is discretized by using a structured mesh of 4,608 (48 × 96) quadrilateral cells. To ensure that the numerical solution is not dependent on the grid size, we have tested other grids and found that the results are not sensitive when the mesh includes more than 4,200 cells. This observation is also corroborated with the recent grid study by [62].

4.4.1 Validation

Prior to using the CFD simulation to analyze the mass transfer phenomenon it is important to validate the simulation. As in previous studies [34, 37, 63], in this present study CFD simulation is validated by comparing the time averaged pressure drop between simulations and experiments. The experimental average pressure drop for 6.3 g silica gel particles is measured as 2.41 kPa with standard deviation, 0.101 kPa. The average pressure drop calculated from numerical simulation is 2.44 kPa with standard deviation 0.135 kPa. The measured and predicted average pressure drop and the amplitude of pressure fluctuation show excellent agreement. Note experimental data saving frequency is low (1 Hz) compared to simulation (100 Hz).

4.4.2 Estimation of mass transfer coefficient using empirical correlation and CFD

The average size of the finer and heaver inert particles (bronze) and the light and large particles (silica gel) are 85 μm and 3500 μm, respectively. The size and density ratios of these particles are 41 and 0.25, respectively. These two particles exhibit very different fluidization characteristics, and the bed is very much segregated [56]. The silica gel mass fraction used in the experiment is less than 2% of the total solids, which limits the application of the TFM as this model assumes all phases as continuous. At such a low volume fraction, it is not reasonable to assume a continuum of that phase, although gas and fine particles may well behave as continua. A combined Eulerian-Lagrangian discrete particle model (DPM) could solve this problem treating the inert bronze solid as continuous and the silica gel particle as discrete phase. But for detecting the particle-particle contact in DPM, the size of the smaller grid is important for the contact detection. Mio et al. [64] reported that the size of the calculation grid must be about 1.5 times the particle diameter. In this case, numerical grid should be about 5.2 mm, more than 60 times the grid size for small particles which is too coarse for the TFM [65]. Thus, we have ruled out use of a hybrid Eulerian-Lagrangian approach.

Instead, the hydrodynamics of a fluidized bed consisting of moist air and bronze particles is simulated. Silica gel particles are assumed to move much more slowly than gas or fine particles, and are relatively stationary on the bed surface. Using this approach, local gas velocities and void fractions are sampled near the bed surface, which allows use of an empirical correlation to predict mass transfer coefficient. In this case, we have used the modified form of Froessling correlation (equation (2)). Since bubble eruption in a fluidized bed is nearly random i.e. bubbles can break at any position at the bed surface, two positions – near center (x_c = 28-33 mm, y_c = 51-56 mm) and near wall (x_w = 47-52 mm, y_w = 51-56 mm) are chosen to represent silica gel particle at each position. Thus, two domains inside of the simulated bed (5 mm by 5 mm) are selected to represent the locations of stationary silica gel particles, which are not otherwise included in these simulations within each square, the velocities and void fractions are spatially averaged at any moment in time to compute the mass transfer coefficient using equation (1 & 2).

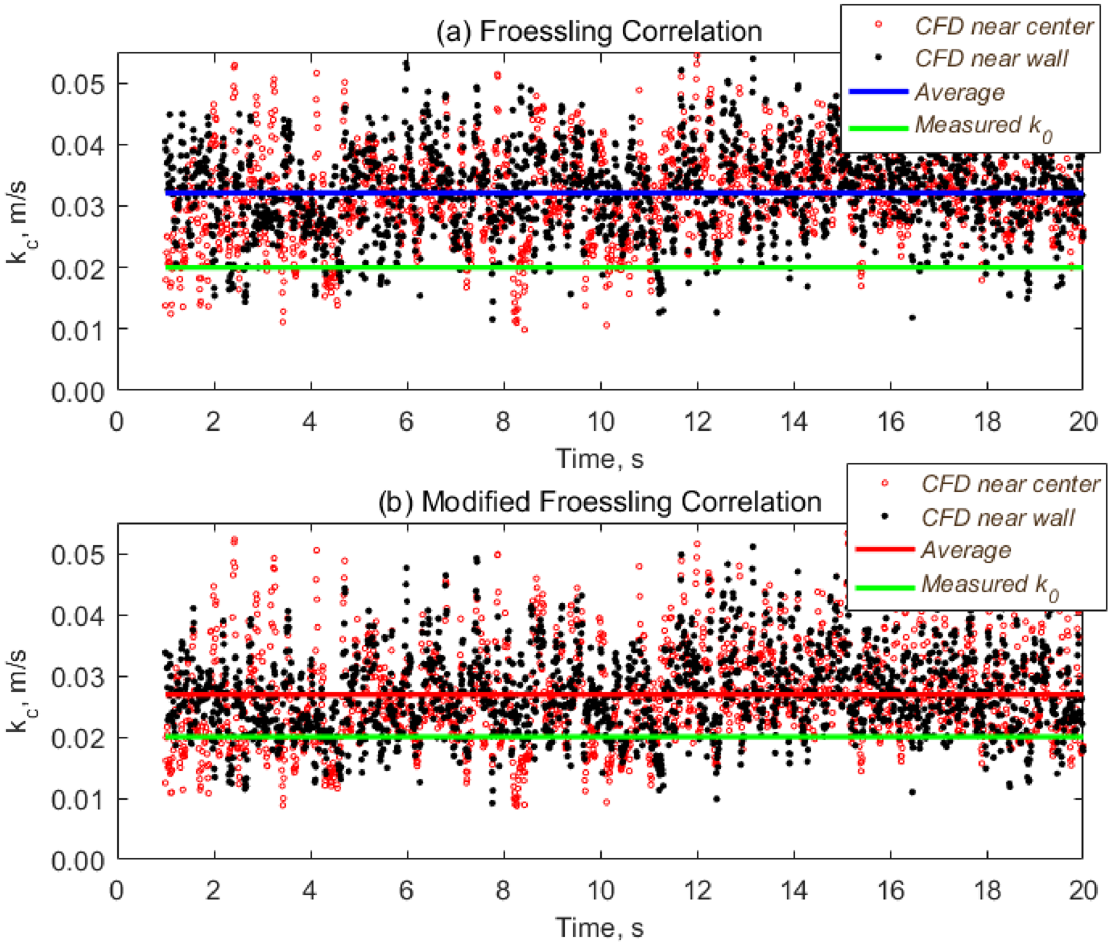

Figure 4- 8. Semi-empirical prediction of the mass transfer coefficient, k_c, for two different positions on the bed surface

Figure 4- 8 shows the mass transfer coefficient values calculated using Froessling's [27] semi-empirical correlations reported in equations (1 & 2) for the two selected locations near the bed surface. At both positions, the computed rate coefficient values fluctuated with time, reflecting the unsteady behavior of fluidized beds. In equations (1 & 3), the diffusive component (2ε) is varied with gas distribution. In fluidized bed, large bubbles rise rapidly compared to small bubbles through the bed and

increases the convective transport rate between gas and solids which, consequently, enhances the rate of mass transfer. This change of convective rate evolving from bubble size variation causes the change of mass transfer rate coefficient. In Figure 4- 8 (a), the average rate coefficients value at center (0.0317 m/s) and near the wall (0.0325 m/s) differ marginally from each other. Thus, the mean of the two average value of the rate coefficients is presented. Similar argument is true for Figure 4- 8 (b). The average rate coefficient value calculated using equation (1) (Figure 4- 8 (b)) is about 20% higher than the corresponding average value calculated using equation (3) (Figure 4- 8 (b)). As discussed before, equation (1) considers only the diffusive resistance but ignores the convective resistance due to the reduction of void volume by the surrounding solids. Consequently, it predicts a higher mass transfer rate between gas and solids.

The average mass transfer coefficient predicted by semi-empirical correlation using numerical simulation data agrees reasonably with the measured rate coefficient k_0, which is calculated using equation (7). Note this predicted rate coefficients are shown for a single silica gel particle. In order to compare with experiment, the measured rate coefficient for single particle is obtained from equation (7) using the three measured rate coefficient values shown in Table 4- 1. The consideration of convective resistance in the Froessling correlation (equation 3) improves the prediction accuracy comparing with the experimental measurement.

4.4.3 Estimation of mass transfer coefficient using CFD and Fick’s law

In the above approach, silica gel particle is not included in the numerical simulation. For the second approach, a stationary silica gel particle with a mean diameter of 3.5 mm is added near the bed surface as a boundary for flow of the two continuous phases. Adsorption of water vapor by silica gel particle is simulated by solving the gas species mass conservation equation in the CFD simulations.

$$\frac{\delta}{dt}\left(\varepsilon\rho_g X_{gi}\right) + \frac{\delta}{dx_j}\left(\varepsilon\rho_g U_{gj} X_{gi}\right) = \frac{\delta}{dx_j}\left(D_{gi}\frac{\delta X_{gi}}{dx_j}\right) + R_{gi} \qquad (8)$$

where, X_{gi}, D_{gi} and R_{gi} are the mass fraction, diffusivity, rate of generation/consumption of the of gas species i, respectively. U_{gj} is the gas velocity in j-direction. Adsorption at the surface happens by an instantaneous reaction.

In CFD simulation, only water vapor from the inlet gases is allowed to adsorb by the silica gel particle, which is also the case for experimental procedure. A 50% relative humid air, same as experiment, is used in the simulation as the inlet gas. Three different cases are studied– a single silica gel particle placed on the surface close to the wall, a single silica gel particle placed on the surface at the center, and two silica gel particles placed on the surface, one at the wall and the other in the center. In the first two cases, the location of silica gel is varied to examine the effect of local gas and solid velocities while the latter case is selected to investigate the effect of multi-particles on mass transfer. Note the volume fraction of the silica gel particle is negligible compared to the inert bronze particle used in the CFD simulation. So, it is assumed that silica particle does not influence the flow of the bulk phase. Figure 4- 9 shows representative snaps of CFD simulations for the three cases described above. The white spheres located near the surface indicate the stationary silica gel particles.

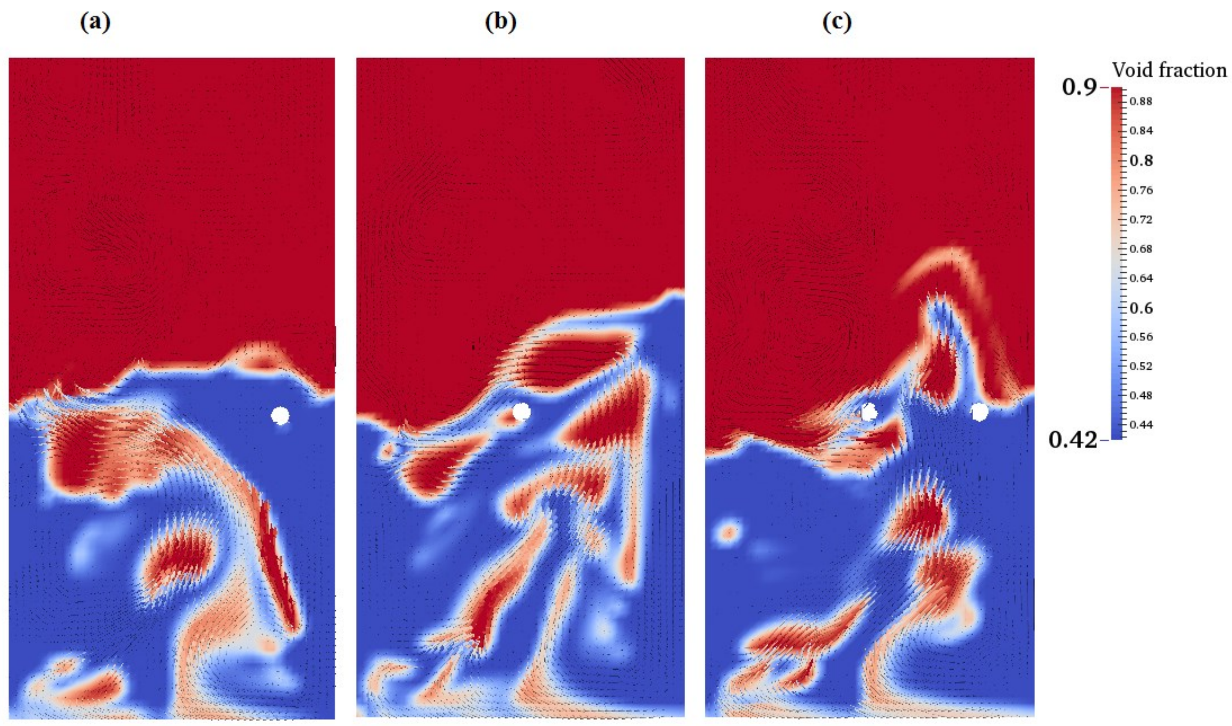

Figure 4- 9. Instantaneous void contours with gas velocity field for stationary silica gel near: (a) wall, (b) center and (c) wall and center. The white circle represents silica gel particle.

Figure 4- 9 shows time-averaged water vapor concentration in the lateral direction for two axial positions – one curve shows the lateral concentration profile at the height of the silica gel particle (H_o), and the other shows the profile above the particle (H_a). In each case, the presence of the particle is readily visible, with 0 concentration. Around the silica gel particle, water vapor shows a concentration gradient. The concentration gradient diminishes above the silica gel surface.

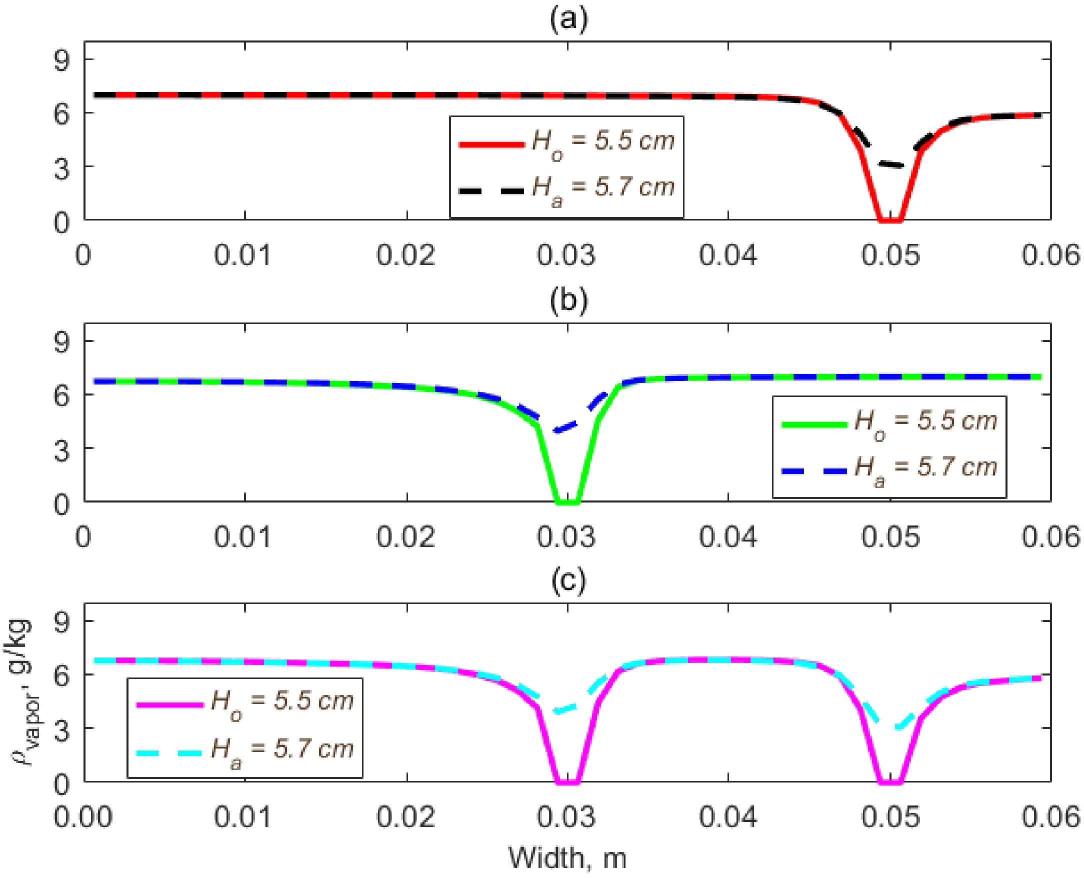

Figure 4- 10. Time-averaged water vapor concentration, ρ_{vapor}, at and above the surface of the silica gel particle when silica gel placed at: (a) wall, (b) center and (c) wall and center.

These results are analyzed in a manner analogous to the experimental data. The rate of mass transfer and corresponding rate coefficient are calculated from the rate of adsorption of water vapor of silica gel particle using equation (5). The rate of adsorption of water vapor is computed from the CFD simulation data as

$$r_{ad}(t) = \iint \rho_g \, X_{gi}(x) \, U_{gx}(x). dx \, dz \,|_{out}^{in} \tag{9}$$

Note the equilibrium water vapor concentration at the particle surface is set zero while calculating the log mean difference (equation 4) as water vapor adsorption at the silica gel surface is instantaneous. For this reason, the CFD result is expected to overestimate the rate of mass transfer.

Figure 4- 10 shows the mass transfer coefficients computed from the numerical simulations for the three cases described above. For all three cases, the mass transfer coefficient values represent a wide range of scatter distribution with time. As continuous bubbling changes the gas availability for mass transfer around the silica gel particles, the rate of mass transfer changes as well. If silica gel particle is fully submerged in fine inert solids (i.e. low gas availability), both convective and diffusive resistance is high which results a slower mass transfer rate. Similarly, if a rising bubble engulfs a silica gel particle, the rate of mass transfer increases due to high gas availability.

(a) Single silica gel particle inside bed

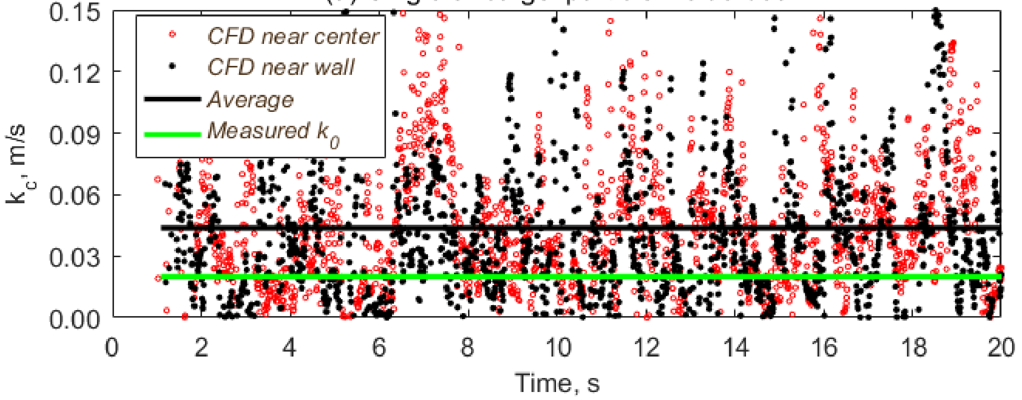

(b) Two silica gel particles inside bed

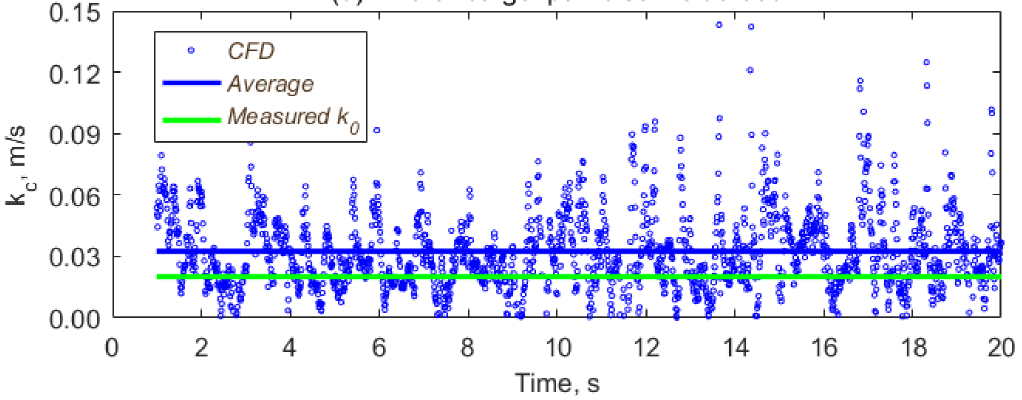

Figure 4- 11. Distribution of mass transfer coefficient for different position of silica gel particle.

In Figure 4- 11(a), the average rate coefficients value calculated for silica gel at center (0.0455 m/s) and near wall (0.0420 m/s) differ marginally from each other. Thus, the overall average rate coefficient value is presented in Figure 4- 11(a). However, these predicted average mass transfer coefficients are nearly double the measured average rate coefficient k_0. In experiment, the rate of mass transfer decreases as the amount of water vapor inside silica gel particles increases with time, as shown in Figure 4- 5. In contrary, the adsorption reaction of water vapor on the surface of silica gel particle is set instantaneous with an infinite reaction rate constant, and, consequently, a high rate of mass transfer is accounted in CFD simulation.

As discussed and shown in Figure 4- 6, the rate of mass transfer is affected by the presence of multiple light and large silica gel particles. Similar to the experiments, CFD simulation also shows a decrease in the rate of mass transfer for multiple silica gel particles. Figure 4- 11(b) highlights the effect of multiple silica gel particles on mass transfer rate coefficient. The average rate of mass transfer coefficient is decreased by 22% by the presence of nearby adsorbing particles. And the difference between CFD prediction and experimental measurement is reduced as well. The restriction of the flow spaces between the particles results in sheer velocity gradients of the gas phase, thus resulting in greater shearing stresses and an increase in resistance of the gas flow. The decrease of gas flow penetrating through the finer and heavier bronze particles to silica gel causes a high convective resistance in addition to the diffusion resistance for mass transfer.

Note that the semi-empirical correlation fails to capture this complex gas-solid interaction which highlights the shortcomings of its application in predicting the rate of mass transfer in fluidized bed. This comparative analysis suggests that, although, computationally, the solution of species conservation equation is very expensive, it should be preferably performed for complementing the CFD results with experimental measurements.

4.5 Conclusion

In this study, the rate of mass transfer between fluidizing humid air and light and large silica gel particles is measured and simulated in a lab-scale bubbling fluidized bed. The rate of adsorption of water vapor by silica gel particles decreases with time. Experimental and simulated results show that the average interphase mass transfer coefficient decreases with the increase of mass of silica gel particles in the bed. The influence of mass of silica gel particles the interphase mass transfer coefficient has been explained by accounting for the influence of nearby “competing” particles. An exponential equation describes satisfactorily the effect of multiple fuel particles on mass transfer coefficient.

A modified form of Froessling’s semi-empirical correlation to compute the mass transfer rate coefficient is suggested for its application in gas-solid fluidized bed simulation. Modification considers both the resistances from diffusion and convection of gas through solid phase. Using that modified correlation and the hydrodynamic properties of the inert solid and fluidizing gas obtained from CFD simulation, the computed mass transfer coefficient highlights the shortcomings of semi-empirical correlation for the complete description of mass transfer phenomenon in fluidized bed. Similar to experimental method, the rate of water vapor adsorption and the effect of multiple silica gel particles are investigated through CFD using an instantaneous reaction on the surface of the silica gel particle. The measured and simulated mass transfer coefficients show very good agreement. It is also shown through numerical simulations that the mass transfer coefficient decreases with the increase of number of silica gel particles. Thus, the kinetic theory based CFD simulation can successfully be used to compute the mass transfer. coefficients, by solving the species conservation equations, required for fluidized bed reactor designs, without using such parameters as inputs.

Acknowledgments

The authors would like to acknowledge the support from the California Energy Commission, Grant 07-01-37 and ZERE Energy and Biofuels, Inc.

References

[1] I. Aigner, C. Pfeifer, and H. Hofbauer, "Co-gasification of coal and wood in a dual fluidized bed gasifier," *Fuel,* vol. 90, pp. 2404-2412, 2011.

[2] A. A. Khan, W. de Jong, P. J. Jansens, and H. Spliethoff, "Biomass combustion in fluidized bed boilers: Potential problems and remedies," *Fuel Processing Technology,* vol. 90, pp. 21-50, 2009.

[3] M. Farzaneh, A.-E. Almstedt, F. Johnsson, D. Pallarès, and S. Sasic, "The crucial role of frictional stress models for simulation of bubbling fluidized beds," *Powder Technology,* vol. 270, Part A, pp. 68-82, 2015.

[4] K. Daizo and O. Levenspiel, "Fluidization engineering," 1991.

[5] D. Jia, X. Bi, C. J. Lim, S. Sokhansanj, and A. Tsutsumi, "Gas-solid mixing and mass transfer in a tapered fluidized bed of biomass with pulsed gas flow," *Powder Technology*.

[6] T. Mani, N. Mahinpey, and P. Murugan, "Reaction kinetics and mass transfer studies of biomass char gasification with CO2," *Chemical Engineering Science,* vol. 66, pp. 36-41, 2011.

[7] S. S. Vincent, N. Mahinpey, and A. Aqsha, "Mass transfer studies during CO2 gasification of torrefied and pyrolyzed chars," *Energy,* vol. 67, pp. 319-327, 2014.

[8] J. Yu, K. Zhou, and W. Ou, "Mass transfer coefficients considering effects of steam in oxy-fuel combustion of coal char," *Fuel,* vol. 111, pp. 48-56, 2013.

[9] A. Gómez-Barea and B. Leckner, "Modeling of biomass gasification in fluidized bed," *Progress in Energy and Combustion Science,* vol. 36, pp. 444-509, 2010.

[10] T. Chiba and H. Kobayashi, "Gas exchange between the bubble and emulsion phases in gas-solid fluidized beds," *Chemical Engineering Science,* vol. 25, pp. 1375-1385, 1970/09/01 1970.

[11] C. Chavarie and J. R. Grace, "Interphase mass transfer in a gas fluidized bed," *Chemical Engineering Science,* vol. 31, pp. 741-749, 1976/01/01 1976.

[12] S. P. Sit and J. R. Grace, "Interphase mass transfer in an aggregative fluidized bed," *Chemical Engineering Science,* vol. 33, pp. 1115-1122, 1978/01/01 1978.

[13] W. Wu and P. K. Agarwal, "The Effect of Bed Temperature on Mass Transfer between the Bubble and Emulsion Phases in a Fluidized Bed," *The Canadian Journal of Chemical Engineering,* vol. 81, pp. 940-948, 2003.

[14] R. Solimene, A. Marzocchella, G. Passarelli, and P. Salatino, "Assessment of gas-fluidized beds mixing and hydrodynamics by zirconia sensors," *Aiche Journal,* vol. 52, pp. 185-198, 2006.

[15] T. Pavlin, R. Wang, R. McGorty, S. M. Rosen, G. D. Cory, D. Candela, W. R. Mair, and L. R. Walsworth, "Noninvasive Measurements of Gas Exchange in a Three-Dimensional Fluidized Bed by Hyperpolarized 129Xe NMR," *Applied Magnetic Resonance,* vol. 32, pp. 93-112, 2007.

[16] R. K. Chakraborty and J. R. Howard, "Combustion of Char in Shallow Fluidized-Bed Combustors - Influence of Some Design and Operating Parameters," *Journal of the Institute of Energy,* vol. 54, pp. 48-54, 1981.

[17] I. B. Ross and J. F. Davidson, "The Combustion of Carbon Particles in a Fluidized-Bed," *Transactions of the Institution of Chemical Engineers,* vol. 60, pp. 109-114, 1982.

[18] R. D. Lanauze, K. Jung, and J. Kastl, "Mass-Transfer to Large Particles in Fluidized-Beds of Smaller Particles," *Chemical Engineering Science,* vol. 39, pp. 1623-1633, 1984.

[19] W. Prins, T. Casteleijn, W. Draijer, and W. Van Swaaij, "Mass transfer from a freely moving single sphere to the dense phase of a gas fluidized bed of inert particles," *Chemical Engineering Science,* vol. 40, pp. 481-497, 1985.

[20] G. Pal'Chenok and A. Tamarin, "Mass transfer at a moving particle in a fluidized bed of coarse material," *Journal of engineering physics,* vol. 47, pp. 916-922, 1984.

[21] E. Schlünder, "On the mechanism of mass transfer in heterogeneous systems—in particular in fixed beds, fluidized beds and on bubble trays," *Chemical Engineering Science,* vol. 32, pp. 845-851, 1977.

[22] W. Ciesielezyk, "Analogy of heat and mass transfer during constant rate period in fluidized bed drying," *Drying technology,* vol. 14, pp. 217-230, 1996.

[23] W. Resnick and R. White, "Mass transfer in systems of gas and fluidized solids," *Chemical Engineering Progress,* vol. 45, pp. 377-390, 1949.

[24] S. Oka, M. Ilic, B. Vukasinovic, and M. Komatina, "Experimental investigations of mass transfer between single active particle and bubbling fluidized bed," American Society of Mechanical Engineers, New York, NY (United States)1995.

[25] G. Donsì, G. Ferrari, and A. De Vita, "Analysis of transport phenomena in two component fluidized beds," *Fluidization IX,* pp. 421-428, 1998.

[26] S. Cobbinah, C. Laguerie, and H. Gibert, "Simultaneous heat and mass transfer between a fluidized bed of fine particles and immersed coarse porous particles," *International journal of heat and mass transfer,* vol. 30, pp. 395-400, 1987.

[27] N. Froessling, "On the evaporation of falling drops," DTIC Document1968.

[28] D. J. Gunn, "Transfer of heat or mass to particles in fixed and fluidised beds," *International journal of heat and mass transfer,* vol. 21, pp. 467-476, 1978/04/01 1978.

[29] W. Ranz and W. Marshall, "Evaporation from drops," *Chemical Engineering Progress,* vol. 48, p. 141446, 1952.

[30] T. Kai, T. Imamura, and T. Takahashi, "Hydrodynamic influences on mass transfer between bubble and emulsion phases in a fine particle fluidized bed," *Powder Technology,* vol. 83, pp. 105-110, 1995/05/01 1995.

[31] D. Gidaspow, *Multiphase Flow and Fluidization: Continuum and Kinetic Theory Descriptions*. San Diego: Academic Press, 1994.

[32] Y. Tsuji, T. Kawaguchi, and T. Tanaka, "Discrete particle simulation of two-dimensional fluidized bed," *Powder Technology,* vol. 77, pp. 79-87, 1993.

[33] J. Ding and D. Gidaspow, "A bubbling fluidization model using kinetic theory of granular flow," *Aiche Journal,* vol. 36, pp. 523-538, 1990.

[34] F. Taghipour, N. Ellis, and C. Wong, "Experimental and computational study of gas–solid fluidized bed hydrodynamics," *Chemical Engineering Science,* vol. 60, pp. 6857-6867, 2005.

[35] J. A. M. Kuipers, W. Prins, and W. P. M. Van Swaaij, "Theoretical and experimental bubble formation at a single orifice in a two-dimensional gas-fluidized bed," *Chemical Engineering Science,* vol. 46, pp. 2881-2894, 1991.

[36] M. Ishii and K. Mishima, "Two-fluid model and hydrodynamic constitutive relations," *Nuclear Engineering and Design,* vol. 82, pp. 107-126, 1984.

[37] M. Syamlal and T. J. O'Brien, "Fluid dynamic simulation of O-3 decomposition in a bubbling fluidized bed," *Aiche Journal,* vol. 49, pp. 2793-2801, Nov 2003.

[38] N. Reuge, L. Cadoret, C. Coufort-Saudejaud, S. Pannala, M. Syamlal, and B. Caussat, "Multifluid Eulerian modeling of dense gas–solids fluidized bed hydrodynamics: Influence of the dissipation parameters," *Chemical Engineering Science,* vol. 63, pp. 5540-5551, 2008.

[39] D. Gidaspow, R. Bezburuah, and J. Ding, "Hydrodynamics of circulating fluidized beds: kinetic theory approach," Illinois Inst. of Tech., Chicago, IL (United States). Dept. of Chemical Engineering1991.

[40] L. Huilin, H. Yurong, and D. Gidaspow, "Hydrodynamic modelling of binary mixture in a gas bubbling fluidized bed using the kinetic theory of granular flow," *Chemical Engineering Science,* vol. 58, pp. 1197-1205, 2003.

[41] C. Loha, H. Chattopadhyay, and P. K. Chatterjee, "Assessment of drag models in simulating bubbling fluidized bed hydrodynamics," *Chemical Engineering Science,* vol. 75, pp. 400-407, 2012.

[42] S. J. P. Romkes, E. Dautzenberg, C. M. van den Bleek, and H. P. A. Calis, "CFD modelling and experimental validation of particle-to-fluid mass and heat transfer

in a packed bed at very low channel to particle diameter ratio," *Chemical Engineering Journal,* vol. 96, pp. 3-13, Dec 15 2003.

[43] R. G. Szafran and A. Kmiec, "CFD Modeling of heat and mass transfer in a spouted bed dryer," *Industrial & Engineering Chemistry Research,* vol. 43, pp. 1113-1124, Feb 18 2004.

[44] A. Vepsäläinen, S. Shah, J. Ritvanen, and T. Hyppänen, "Interphase mass transfer coefficient in fluidized bed combustion by Eulerian CFD modeling," *Chemical Engineering Science,* vol. 106, pp. 30-38, 2014.

[45] F. Hernández-Jiménez, A. Gómez-García, D. Santana, and A. Acosta-Iborra, "Gas interchange between bubble and emulsion phases in a 2D fluidized bed as revealed by two-fluid model simulations," *Chemical Engineering Journal,* vol. 215–216, pp. 479-490, 2013.

[46] B. Chalermsinsuwan and P. Piumsomboon, "Computation of the mass transfer coefficient of FCC particles in a thin bubbling fluidized bed using two- and three-dimensional CFD simulations," *Chemical Engineering Science,* vol. 66, pp. 5602-5613, 2011.

[47] B. Hou, H. Li, and Q. Zhu, "Relationship between flow structure and mass transfer in fast fluidized bed," *Chemical Engineering Journal,* vol. 163, pp. 108-118, 2010.

[48] N. Yang, W. Wang, W. Ge, and J. Li, "CFD simulation of concurrent-up gas–solid flow in circulating fluidized beds with structure-dependent drag coefficient," *Chemical Engineering Journal,* vol. 96, pp. 71-80, 2003.

[49] C. Liu, W. Wang, N. Zhang, and J. Li, "Structure-dependent multi-fluid model for mass transfer and reactions in gas–solid fluidized beds," *Chemical Engineering Science,* vol. 122, pp. 114-129, 2015.

[50] X. Lv, H. Li, Q. Zhu, J. Li, and Z. Zou, "The experiment and simulation of mass transfer in bubbling fluidized beds," *Powder Technology,* vol. 292, pp. 323-330, 2016.

[51] D. J. Patil, J. Smit, M. V. Annaland, and J. A. M. Kuipers, "Wall-to-bed heat transfer in gas-solid bubbling fluidized beds," *Aiche Journal,* vol. 52, pp. 58-74, Jan 2006.

[52] F. Scala, "Particle-fluid mass transfer in multiparticle systems at low Reynolds numbers," *Chemical Engineering Science,* vol. 91, pp. 90-101, 2013.

[53] F. Johnsson, S. Andersson, and B. Leckner, "Expansion of a freely bubbling fluidized bed," *Powder Technology,* vol. 68, pp. 117-123, 1991.

[54] K. Ng, H. Chua, C. Chung, C. Loke, T. Kashiwagi, A. Akisawa, and B. Saha, "Experimental investigation of the silica gel–water adsorption isotherm characteristics," *Applied Thermal Engineering,* vol. 21, pp. 1631-1642, 2001.

[55] J. Sun and R. W. Besant, "Heat and mass transfer during silica gel–moisture interactions," *International journal of heat and mass transfer,* vol. 48, pp. 4953-4962, 2005.

[56] D. Pallarès and F. Johnsson, "A novel technique for particle tracking in cold 2-dimensional fluidized beds—simulating fuel dispersion," *Chemical Engineering Science,* vol. 61, pp. 2710-2720, 2006.

[57] A. Cornish, "Note on minimum possible rate of heat transfer from a sphere when other spheres are adjacent to it," *Trans. Inst. Chem. Eng.,* vol. 43, pp. T332-T333, 1965.

[58] T. Kato, *Perturbation theory for linear operators* vol. 132: Springer Science & Business Media, 2013.

[59] D. G. Schaeffer, "Instability in the evolution equations describing incompressible granular flow," *Journal of differential equations,* vol. 66, pp. 19-50, 1987.

[60] M. Syamlal, Rogers, W., O'Brien, T. J., "MFIX Documentation, Theory Guide1," N. T. I. Service, Ed., ed. Springfield, 1993.

[61] M. Syamlal, "MFIX documentation: Numerical technique," *National Energy Technology Laboratory, Department of Energy, Technical Note No. DOE/MC31346-5824,* 1998.

[62] M. H. Uddin, Coronella, C. J., "Grid effect on bed expansion of bubbling fluidized beds of Geldart B particles: a generalized rule for a grid independent solution for TFM simulations," *Particuology,* 2016.

[63] T. D. Nguyen, M. W. Seo, Y.-I. Lim, B.-H. Song, and S.-D. Kim, "CFD simulation with experiments in a dual circulating fluidized bed gasifier," *Computers & Chemical Engineering,* vol. 36, pp. 48-56, 2012.

[64] H. Mio, A. Shimosaka, Y. Shirakawa, and J. Hidaka, "Cell optimization for fast contact detection in the discrete element method algorithm," *Advanced Powder Technology,* vol. 18, pp. 441-453, Jul 2007.

[65] J. Wang, M. Van der Hoef, and J. Kuipers, "Why the two-fluid model fails to predict the bed expansion characteristics of Geldart A particles in gas-fluidized

beds: a tentative answer," *Chemical Engineering Science,* vol. 64, pp. 622-625, 2009.

CHAPTER 5

Grid effect on bed expansion of bubbling fluidized beds of Geldart B particles: a generalized rule for a grid independent solution for TFM simulations

Abstract

Numerical simulation of gas-solid fluidized beds based on the kinetic theory of granular flow shows a strong dependence on domain discretization. Bubble formation, bubble size and shape are largely depended on discretization and the lack of proper scale resolution leads to inaccurate prediction of fluidization hydrodynamics. In this study, grid independent solution of the two fluid model (TFM) has been studied by comparing the bed expansion obtained from numerical simulation with experimental results and empirical predictions. It is observed that the grid independent solution of the TFM model possesses reliance on Geldart B bubbling fluidized beds. For Geldart B bubbling fluidized beds, grid independence is achieved with grid resolution equal to 18 times the particle diameter. The result is compared with previously published works. This will serve as guideline for choosing the appropriate grid size and to minimize time and expense associated with large simulations.

5.1 **Introduction**

Bubbling fluidized beds are widely used in the process industries, such as chemical, petroleum, pharmaceutical, agricultural, biochemical, food, electronic, and power-generation. Despite their widespread application, much of the development and design of fluidized bed reactors has been empirical due to the complex flow behavior of gas–solid systems. Therefore, a comprehensive study of the bed expansion characteristics of bubbling fluidized bed is crucial for several reasons: In reactive fluidized-bed systems, the information on mass of solids per unit bed volume (the bed density) is important because this influences the chemical conversion[1]. Hydrodynamics has profound effects on mass transfer rates and hence reaction rates. Bed expansion gives the bed voidage, which is necessary to predict the heat transfer coefficient, and the bed height, which may determine the heat transfer surface. It has been suggested that the bed expansion can be used for velocity load turn-down, i.e. to adjust the heat transfer automatically to different loads on a boiler [2].

To advance the knowledge of the bed expansion characteristics and also to obtain empirical correlations for design purposes, a great deal of experimental and theoretical studies have been dedicated in the past few decades using Geldart A and Geldart B particles [1-8]. Bed expansion is profoundly affected by bubbling phenomena, which in turn is determined by gas flow rate, physical properties (e.g., particle diameter and density, gas density and viscosity) and by bed design (column diameter, distributor design). Until now, a single universal correlation has remained elusive.

In addition to those experimentally derived empirical or semi- empirical approaches, first-principles-based computational fluid dynamics (CFD) has become an emerging and effective tool to explore the complex hydrodynamics behavior in gas-solid fluidized bed. Complex hydrodynamics and transport phenomena can be explored intimately by CFD in ways unavailable by an experimental approach. CFD can provide insight useful for scale-up, design, or optimization [9-11]. Different approaches have been taken to apply CFD methods to fluidized beds, including direct numerical simulation (DNS) [12], discrete particle method (DPM) [13] and two-fluid method (TFM) [14]. Among these methods the TFM appears to be the model which has best potential to be used for large-scale fluidized beds, due to relatively smaller computational cost. The general idea in formulating the TFM model is to treat each phase (fluid and solid) as an interpenetrating continuum, and therefore to construct integral balances of continuity, momentum and energy for both phases, with appropriate boundary conditions and transfer conditions for phase interfaces. The phase said to represent solids has proprieties found by application of the kinetic theory of granular materials [15]. The TFM applies averaging techniques and assumptions to obtain momentum balance for the solids phases since the resultant continuum approximation for the solid phase has no equation of state and lacks variables such as viscosity and normal stress [16]. The TFM equations are coupled with constitutive relations derived from data or analysis of nearly homogeneous systems [15]. The interphase momentum transfer between gas and solid phases are coupled by drag force. Numerous correlations for calculating the drag coefficient of gas–solid systems have been reported in the literature, including those of Syamlal and O' Brien (1989) [17], Gidaspow (1994) [15], and Wen and Yu (1966) [18].

It is well accepted that gas-solid flows exhibit heterogeneous structures over a wide range of length and time scales. However, TFM equations are usually closed with constitutive laws that are based on the assumption of homogeneity at the level of computational cells. In order to capture the prevailing phenomena in gas-fluidized beds, the grid size used in numerical simulations should be sufficiently small[19-27]. When these structures are not properly resolved, drag force can be significantly overestimated as reported for riser flows and circulating beds [21, 28]. Literature studies on the grid sizes required for grid-independent solutions suggest very fine grids, of the order of 2–4 particle diameters for Geldart A systems for bubbling beds [20, 29] and 10 particle diameters for circulating and riser flow simulations [26]. However, there is no such guidance for simulating bubbling fluidized bed of Geldart B particles. Using CFD study, Cloete et al. 2015 showed that grid-independent solution of TFM applied in fluidized bed simulation for 200 µm particles can be obtained with a grid size of 7.8 particle diameters. The same study claimed to obtain a grid-independent TFM solution at 98.4 particle diameters for 1000 µm particle [30]. However, these claims were not validated against experimental evidence.

An extensive literature review (Table 5- 1), shows that different research groups have reported grid-independent solutions for TFM for simulations of bubbling fluidized bed of Geldart B particles by comparing different experimental parameters such as bed expansion, axial and lateral solid concentration, solid velocity profile, pressure fluctuation for different type and size of particles and for different bed geometries [8, 31-39].

Table 5- 1. Experimental investigations used for CFD grid independency validation

Investigator	Fluidized bed			Bed particles			Bed type	U_0/u_{mf}	Remarks
	*D_c, m	H_c, m	h, m	Type	ρ, kg/m^3	d_p, μm			(Conclusion based on)
(Taghipour, et al., 2005)	0.28 x 0.025	1.0	0.40	Glass beads	2500	250 ~ 300	Pseudo 2-D	1.00 ~ 12.30	Average experimental bed expansion and pressure drop
(H. Wang, et al., 2006)	0.14 x 0.14	2.8	0.20	Sands	2600	300	Pseudo 2-D	3.33 ~ 16.67	Experimental solid concentration profile
(Xie, et al., 2008)	0.14 x 0.14	1.0	0.20 - 0.50	Silica	2000	400	Pseudo 2-D	1.25 ~ 4.04	Axial and radial average solid volume fraction
(Busciglio, et al., 2009)	0.18 x 0.015	0.8	0.20 - 0.36	Glass beads	2500	212 ~ 250	Pseudo 2-D	3.00 ~ 7.00	Average experimental bed expansion
(Vejahati, et al., 2009)	0.28 x 0.025	1.2	0.40	Glass beads	2500	250 ~ 300	Pseudo 2-D	2.00 ~ 12.30	Average experimental bed expansion and pressure drop
(Nguyen, et al., 2012)	0.285 x 0.11	2.13.0	0.62	Silica	2466	250	Pseudo 2-D	1.00 ~ 4.00	Average experimental bed expansion and pressure drop
(Makkawi, et al., 2006)	0.138	1.5	0.20	Glass ballotini	2500	350	3-D	2.00 ~ 12.30	Experimental radial solid concentration profile using Electrical capacitance tomography
(Reuge, et al., 2008)	0.05	1.0	0.20	Alumina	3900	221	3-D	1.80 ~ 3.20	Average experimental bed expansion
(Li, 2015)	0.138	1.5	0.20	Glass ballotini	2500	350	3-D	2.00 ~ 12.30	Experimental radial solid concentration profile using Electrical capacitance tomography.
(Asegehegn, Schreiber, & Krautz, 2012)	0.32 x 0.02	1.2	0.50	Glass beads	2500	246 ~ 347	Pseudo 2-D	2.50 ~ 4.00	Average experimental bed expansion and pressure drop

* Column width/diameter, D_c; Column height, H_c; Solid bed height, h; Particle density, ρ; particle diameter, d_p; Superficial gas velocity, U_0; minimum fluidization velocity, u_{mf}

The grid sizes reported by researchers listed in Table 5- 1 as grid-independent TFM simulations for Geldart B bubbling fluidized bed are presented in Figure 5- 1. Each of these data points is validated against experimental results.

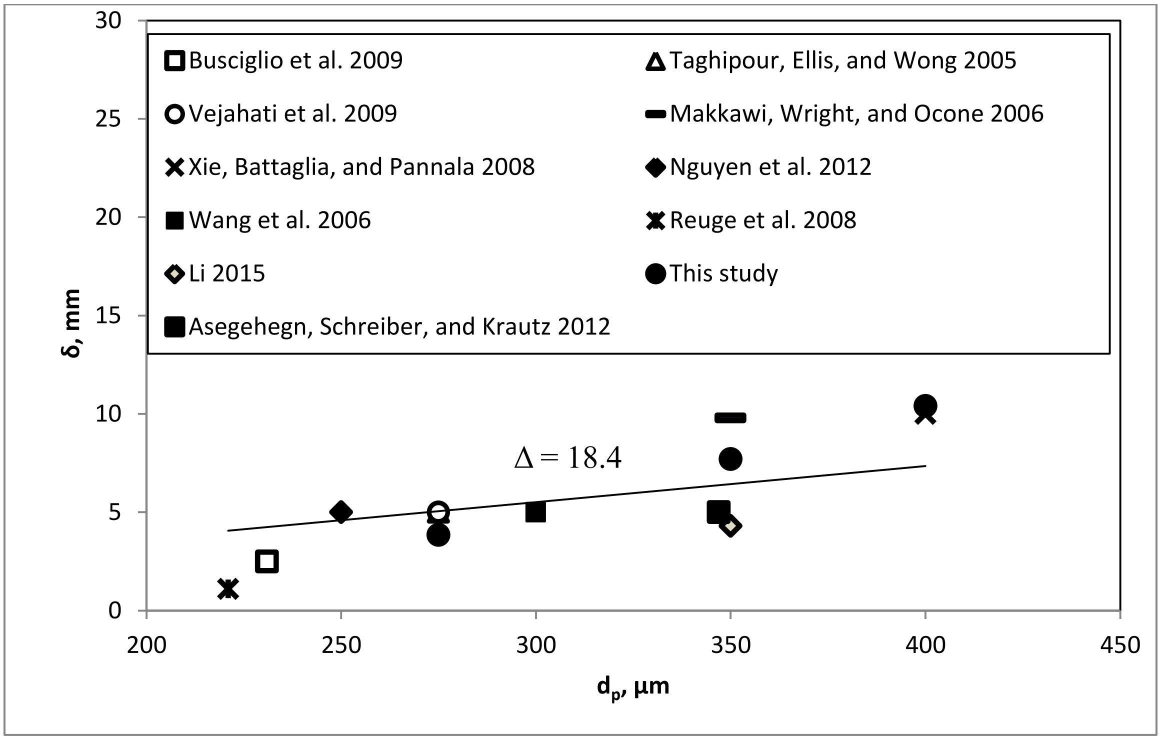

Figure 5- 1. Grid size reported for the grid independent solution of TFM applied Geldart B bubbling fluidized beds. Data refers to literature listed in Table 5- 1. δ represents grid size.

These results show small scatter behavior. For instance, for particle size of 350 μm, Li 2015 [40] used the experimental data of Makkawi et al. 2006 [38] in their newly developed 2.5-D symmetric simulation and reported a lower grid size than Makkawi. Clearly, more investigation is needed to better understand the effect of particle size on grid independent behavior of Geldart B particle bubbling fluidized bed.

Recognizing the importance of bed expansion characteristics for bubbling fluidized beds and the effect of particle size on the grid-independent solution of TFM, a set of simulations were performed with different particle sizes and different grid sizes. Simulation results were analyzed and compared with published experimental result as well as with semi-empirical correlations. Effects of particle size on grid independent solution of TFM were compared with the data shown in Figure 5- 1.

5.2 **Experimental facility**

Simulation predictions were compared with experimental measurements by Geldart [3]. Experiments were carried out in a 30.8 cm diameter perspex column. The gas distributor consisted of perforated metal having holes 3.2 mm diameter on triangular pitch with 5.0 mm centers making a total of 3100 holes. Two sheets of filter paper above and below the perforated plate prevented particles falling into the wind box and ensured a pressure drop across the distributor of at least 50% of the pressure drop across the bed alone at minimum fluidization. The bed material was sand with a mean particle size of 275 μm, and was fluidized with air at room temperature. A standard meter-rule marked in millimeters, still 35-mm photographs, and 16-mm high speed cine pictures were used to measure the bed height visually.

5.3 **Simulation**

5.3.1 **Numerical model**

The physical setup described above was simulated as a 2-D fluidized bed using the TFM. As discussed above, the TFM is well developed, and has been extensively applied to simulate fluidized beds of various configurations. The complete set of equations is available[41, 42]. An empirical drag model that bridges the results of Wen and Yu [18] for dilute systems and the Ergun approach for dense systems is that of Syamlal-O'Brien was used [43] , and was used in this work.

5.3.2 **Flow solver and solver settings**

The National Energy Technology Laboratory's (NETL's) open-source code MFIX was used as flow solver [41]. The modified phase coupled SIMPLE scheme, which uses a solids volume fraction correction equation instead of a solids pressure correction equation, was used for pressure–velocity coupling. The second-order SuperBee scheme was used for the spatial discretization of all remaining equations. A combination of point successive under relaxation and biconjugate gradient stabilized method (BiCGSTAB) method were used for the linear equation solver. A maximum residual at convergence of 10^{-03} was used to ensure the accuracy of the continuity and momentum equations solution. First order implicit temporal discretization was used to ensure stable and accurate solutions. It has been shown that 2nd order time discretization is necessary for accurate solution of fast-moving riser flows with the TFM [44], but this is not the case for dense bubbling beds where the vast majority of the bed moves relatively slowly. An automatic time-step adjustment with a maximum and minimum time-step of $5\text{x}10^{-04}$ s and 10^{-07} s respectively was used to enhance the computation speed.

5.3.3 **Geometry and meshing**

The dimensions of the fluidized bed are given in Table 5- 2. All the simulations were conducted in 2-D cylindrical coordinate with uniform structured grid. It has been found recently that 3D simulations show better grid independence behavior than 2-D simulations [33], implying that conclusions from 2-D simulations should be safely extendable to 3D simulations. Different grid sizes were used in this study to find a grid independent TFM solution. In these CFD simulations, the grid size in the radial direction (dr) is taken equal to the grid size in the axial direction. The uniform grid size, δ was scaled with the particle diameter, d_p to define a dimensionless grid size (Δ) as:

$$\Delta \equiv \frac{\delta}{d_p} \tag{1}$$

In all of the following discussions, mesh size is discussed in terms of this dimensionless variable.

5.3.4 **Initial and boundary conditions**

Initially, the settled bed was set to 0.30 m deep for simulations with maximum solids volume fraction 0.60. For all simulations, nonzero fluid flow was initiated in the vertical direction. The gas pressure was initialized at the value found from static pressure, depending on height. The upper section of the simulated geometry, or freeboard, was considered to be occupied by gas only at time zero. The walls were modeled using partial-slip velocity boundaries, with no-slip for the gas and free-slip for the solid phase. Dirichlet boundary conditions were employed at the distributor to specify a uniform gas inlet velocity. Pressure boundary conditions were employed at the top of the freeboard, where gas exits the geometry. Neumann boundary condition was used for the gas flow, i.e. all flow quantities were given zero normal gradient. The axis of the fluidized bed was simulated as a symmetric boundary.

5.3.5 **Simulation summary**

A summary of the physical properties and simulation parameters are given in Table 5- 2.

Table 5- 2. Physical properties of simulation parameters

Properties	Experiment [3]		Simulation	
Mean particle diameter, μm	275	275	350	400
Particle density, kg/m^3	2600	2600	2600	2600
Gas density, kg/m^3	1.20	1.20	1.20	1.20
Gas viscosity, 10^6 kg/m/s	18.0	18.0	18.0	18.0
Minimum fluidization velocity, m/s	5.60	5.60	7.9•	10.7•
Inlet gas velocity, m/s	10.5	10.5	19.0	36.0
Maximum solid packing	0.60*	0.60	0.60	0.60
Restitution coefficient		0.90	0.90	0.90
Angle of internal friction		30°	30°	30°
Bed diameter, cm	30.8	30.8	30.8	30.8
Static bed height, cm	30.0	30.0	30.0	30.0

*Based on measured minimum voidage; • Wen and Yu correlation [18]

5.3.6 Data post-processing

The bed expansion is used in this study to compare the results between experiment and simulation. The instantaneous area-averaged axial solid volume fraction, $\overline{\varepsilon_s}(h,t)$, is calculated as a function of the bed height:

$$\overline{\varepsilon_s}(h,t) = 1 - \frac{\int_0^R \int_0^{2\pi} \varepsilon_g(r,h,t)\, r\, dr\, d\theta}{\int_0^R \int_0^{2\pi} r\, dr\, d\theta} \quad (2)$$

Where, r and h are any radius and height in the bed from distributor respectively. R is the bed radius. The cumulative, instantaneous bed mass at any height χ(h, t) can be expressed as:

$$\chi(h,t) = A \cdot \rho_s \int_0^h \overline{\varepsilon_s}(h,t) dh \quad (3)$$

Where A is the cross-sectional area of the bed (π R^2) and ρ_s is the particle density. The height of the bed that contains a certain mass of the bed particles at any moment of time is normalized with the static bed height, H(0) that contains the same mass to obtain the expanded height, as proposed by Syamlal and O'Brien [42]. The bed height as a function of time H(t) is then the height at which χ(H(t),t) = 0.9 χ(H(0) ,0).

5.4 Results and discussions

5.4.1 Effect of grid size on bubble formation

CFD models can be validated by comparing the time averaged bed height and pressure drop between simulations and experiments [8, 36]. While time-average predictions such as the gas pressure and the void fraction in the fluidized bed are useful for describing the fluidization, these parameters leave out the transient motion of the solid and gas phases and hence, do not provide the complete description of the hydrodynamics. For instance, the formation of gas bubbles is one of the most important characteristic phenomena of Geldart B fluidized beds. Many important properties of fluidized beds can be related directly to the presence of bubbles and are dominated by their behavior. Prediction of reaction rates, erosion, and heat transfer, for example, can be done by finding representative bubbles by numerical simulation. Relatively small bubbles form at the gas distributor. As bubbles rise through the bed, they tend to coalesce stochastically and grow. Initial bubble size (at the distributor) depends on many factors, especially distributor design and superficial velocity. Here we consider only the effect of grid size, assuming a porous plate gas distributor, with uniform velocity [45].

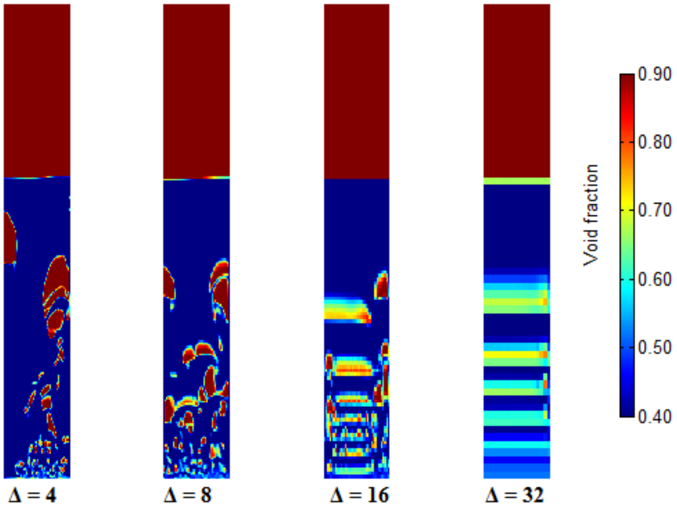

Figure 5- 2. Effect of grid resolution on bubble formation pilot-scale size bubbling fluidized bed simulation. This is a snapshot at 1.0 s of simulation time of one symmetric part of the fluidized bed.   The left wall of each image is the axis of symmetry.

Figure 5- 2 shows a contour plot of gas volume fraction at 1.0 s simulation time where, inside the dense bed, the red contours are void of particles; when these regions appear below the bed surface, they are recognized as bubbles. Figure 5- 2 shows four different contours; each was developed from simulations using increasingly coarse grid resolution (left to right).

Looking at the bottom of each image in Figure 5- 2, it is seen that the initial bubble formation depends significantly on the scale resolution of the numerical simulations. As the grid resolution decreases, the shape of bubbles formed at the distributor become misshaped. As shown in Figure 5- 2, when Δ is 4, numerical simulation creates many small and distinct bubbles near the distributor, with bigger bubbles above the distributor. By reducing the grid resolution, the shape of these bubbles becomes flat (e.g. Δ = 16) and distorts completely (e.g. Δ = 32).

When Δ is in between 4 and 16, numerical simulation is able to generate bubble shapes and sizes that are distinct, and also comparable with literature. This is expected behavior of bubbling fluidized beds of Geldart B particles where small bubbles form at the distributor, move upward, and coalesce to form large bubbles and erupt at the bed surface [1, 46].

However, this phenomenon is apparently lacking when Δ is 32. This implies that if the grid sizes are not sufficiently small enough, the averaged two fluid model (TFM) equations that are used to solve the flow fields of a fluidized bed are unable to represent the proper hydrodynamic behavior. This lack of scale resolution is therefore important factor to consider while reporting results gathered from numerical simulation [20].

Spatiotemporal structures must be resolved sufficiently to use the homogeneity of flow field at the level of individual grid cells.

5.4.2 Effect of grid size on bed expansion

Figure 5- 3 shows the instantaneous bed expansion ratio defined as $L = \frac{H(t)}{H(0)}$, for different dimensionless grid size, Δ. Here H(t) and H(0) are the instantaneous and the initial bed heights. For all cases shown, the bed expands initially until it levels off at a quasi-steady-state height. We define a time, $\tau = \varepsilon_0 \frac{H(0)}{U_0}$ where ε_0 is the initial gas volume fraction in the dense bed (0.4), and U_0 is the inlet gas velocity. For any value of Δ and for time < τ, a single large bubble rises through the bed, until it erupts at the surface, after which the bed drops back down to a nearly steady height. After that small initial collapse in height, the bed surface fluctuates in a semi ordered manner.

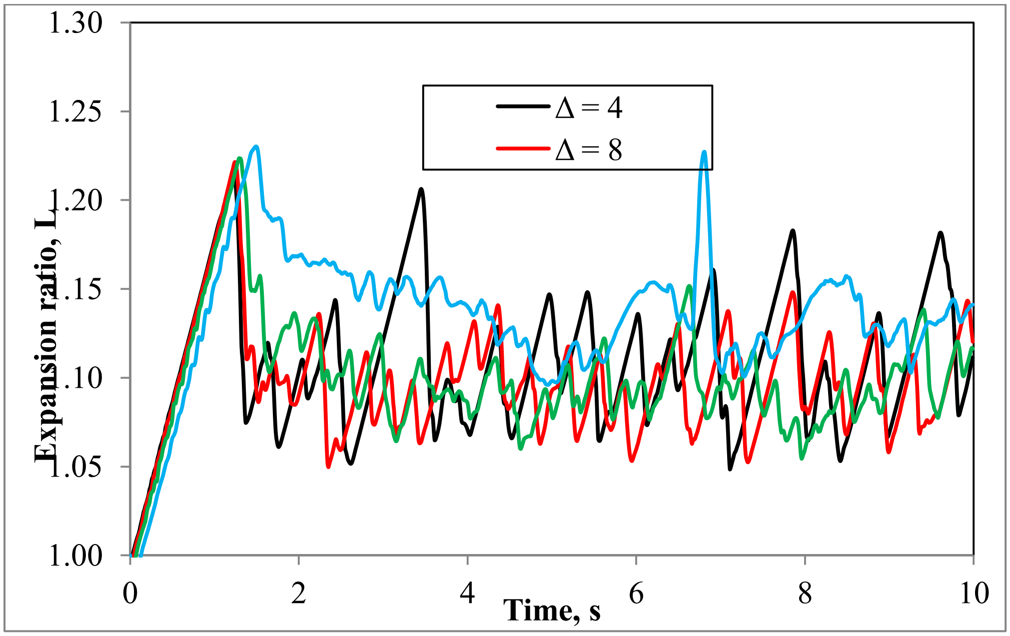

Figure 5- 3. Instantaneous bed expansion for different grid resolutions (275 μm particles).

In Figure 5- 3, the bed surface oscillates steadily for all the grid resolutions after the initial bed collapse. The initial time to reach quasi-steady state seems to show grid dependence. As the grid size increases, the initial time for quasi steady condition increases slightly. So, simulation data gathered before the value of τ are not considered for further analysis as the beds have not yet reached a quasi-steady. As shown in Figure 5- 2, finer grid ($\Delta < 10$) simulations produce many small bubbles at the bottom, which coalesce and grow as they move upward. Before bursting at the bed surface, large bubbles cause the bed to expand to its maximum. At $\Delta = 16$, bed surface oscillates in between the oscillation amplitudes of $\Delta = 4$ and 8. However, when Δ is 32, an irregular fluctuation is seen and oscillation period is much longer than other small grids. Due to the lack of proper spatiotemporal resolution, bubble formation, growth and subsequent eruption at the surface shows unrealistic behavior.

5.4.3 Effect of particle sizes on bed expansion

Figure 5- 4 shows the bed expansion for different grid resolutions for a mean particle sizes of 275 μm, 350 μm, and 400 μm. As described above, when simulation reaches a quasi-steady state, the solids distribution in the bed is time-averaged to obtain the expanded bed height. Simulation data were saved at a frequency of 100 Hz, and 701 time-frame data (3.0 -10.0 s) is time-averaged to obtain average bed expansion for all simulations. For 275 μm, CFD results were compared with Geldart's experimental data [3] as well as with his predictive correlation [1]. However, to validate the other simulation results, bed expansions were compared with semi-empirical correlations for

bubbling fluidized beds of Geldart B particles by Geldart [1] and Darton [47] (Table 5-2).

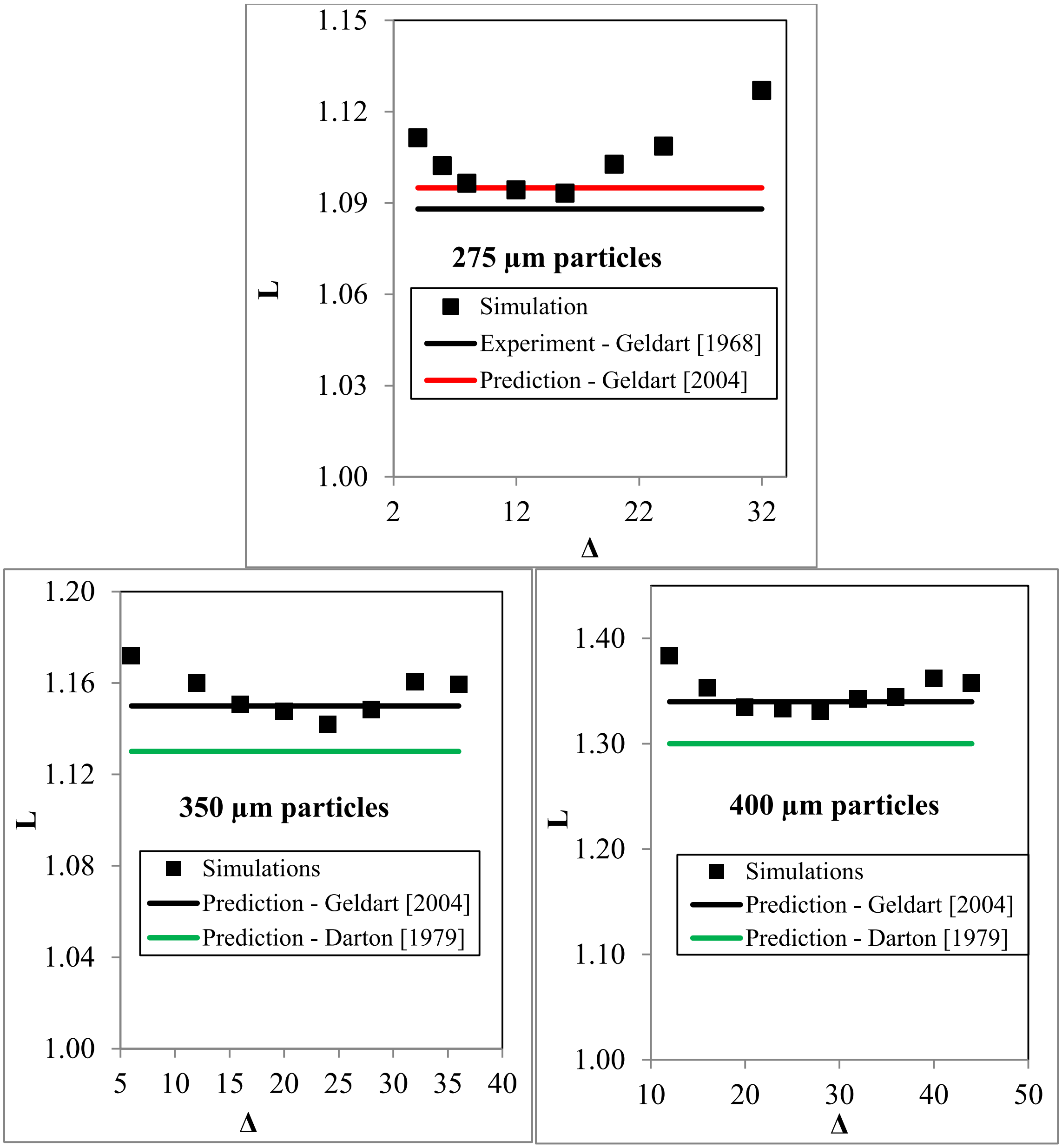

Figure 5- 4. Average bed expansion for different grid resolution for different mean particles size.

Table 5- 3. Bed expansion correlations used in this work.

Author	Correlation
Geldart [1]	$\frac{H}{H_{mf}} = \frac{\phi\sqrt{g d_b}}{\phi\sqrt{g d_b} - 1.64\, Ar^{0.2635} \times \left(U_0 - u_{mf}\right)}$ $d_b = \frac{0.54}{g^{0.2}} \left(U_0 - u_{mf}\right)^{0.4} \left(H + 4\sqrt{A_0}\right)^{0.8}$ $\phi = \begin{Bmatrix} 0.64 & if\ d_t \le 0.1\, m \\ 1.6\, d_t^{0.4} & if\ 0.1 < d_t < 1.0\, m \\ 1.6 & if\ d_t \ge 1.0\, m \end{Bmatrix}$
Darton [47]	$\frac{H}{H_{mf}} = 1 + 2 \frac{\left(U_0 - u_{mf}\right)^{\frac{4}{5}}}{\left(g H_{mf}\right)^{\frac{2}{5}}} \times \left(\left(\frac{4\sqrt{A_0}}{H_{mf}} + \frac{H}{H_{mf}} \right)^{\frac{3}{5}} - \left(\frac{4\sqrt{A_0}}{H_{mf}} \right)^{\frac{3}{5}} \right)$

It is remarkable to note that for each particle size, a similar pattern is observed, with a minimum bed height predicted at some value of Δ. Bed expansion is high for fine grid simulations, and then expansion decreases with increasing the grid size and it reaches a minimum point where expanded bed height good agreement with Geldart's experiment [3] as well as empirical predictions (Table 5- 3). This behavior of bed expansion can be correlated with the drag force between gas and solid particles. As reported by Agrawal et al [21] and Zhang and VanderHeyden [28], drag force is likely to be significantly overestimated if spatiotemporal-scale structures are not resolved properly, which results in over-predicting bed expansion [48].

Figure 5- 5 shows the drag coefficient throughout the domain of the fluidized bed at one instant. One image is shown for each of four different grid resolutions. As shown in Figure 5- 5, at the finest grid there are numerous interactions between gas and solid particles almost all calculation cells due to the large number of bubbles formation. When the TFM applies volume averaging techniques, required to approximate the particles as a

continuum, on such small grid cells (Δ = 4), the over prediction of drag force and, thereby, drag coefficient is possible.

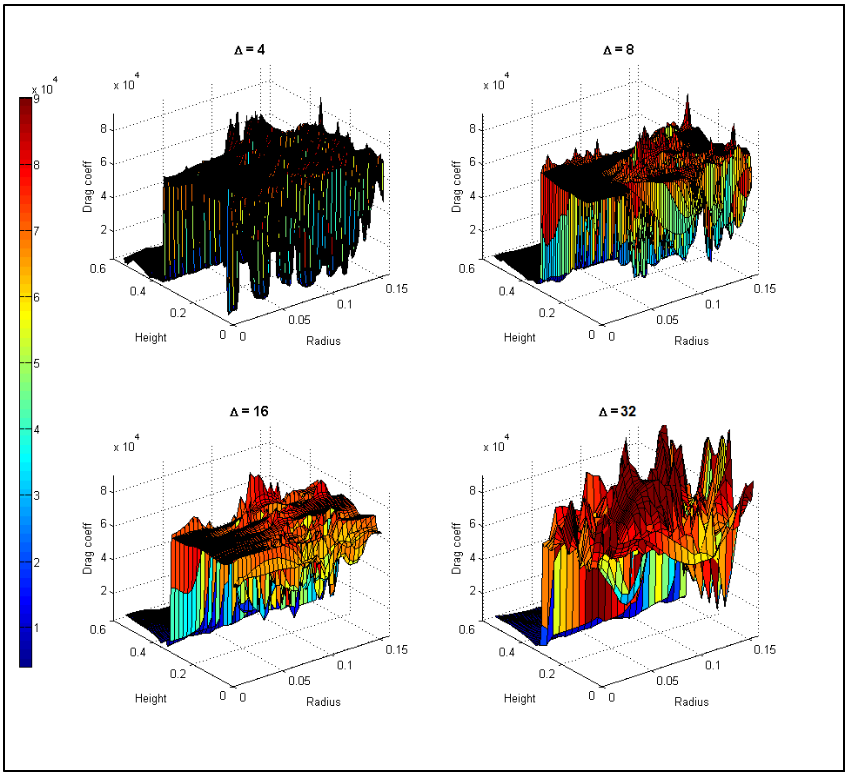

Figure 5- 5. Effect of discretization resolution on drag coefficient. Results shown for 275 µm particles, at t = 5.0 s.

Recently, Bakshi et al [49] extended Celmins' [50] empirical formula for the lower bound on the averaging volume used in the TFM for case of homogeneous distribution of particles, i.e. no obvious particle clusters, periodic or random, inside the averaging volume. They showed that a grid resolution of at least 8 particle diameters is required while simulating solid–gas flow using Cartesian grids. Their study also suggested that simulations using a grid resolution not conforming to this constraint violate the continuum assumption of the TFM and may yield unphysical predictions, artifacts of the numerical solution. This conclusion agrees with the average bed expansion calculated from excessively resolved fine grid simulations shown in Figure 5-4 for all particle sizes.

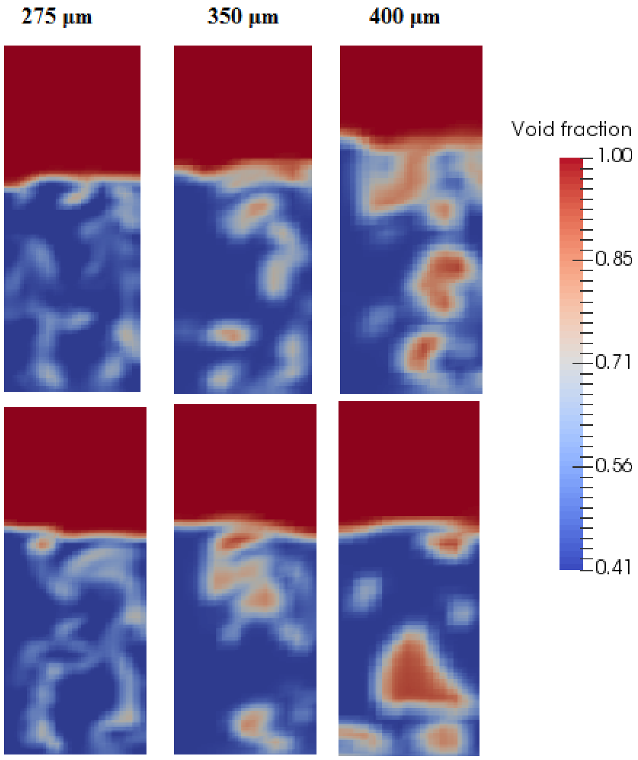

Figure 5- 6. Instantaneous gas phase volume fractions for different particle sizes at Δ = 32. Two images for each particle size are shown. Fluidization conditions are U_0= 6 U_{mf}.

The coarsest grid simulations, on the other hand, are unable to solve the spatiotemporal structures. In such case, gas distribution shows very uneven characteristics resulting in severe channeling or spouting behavior (as shown in Figure 5-2 and Figure 5- 6 at Δ = 32). The bed exhibits Geldart D type fluidization. Bubbles rise more slowly than the rest of the gas percolating through the emulsion causing lower slip velocity. Solid particles in such cases try to move upward as an aggregate. A decrease in the slip velocity leads to a higher drag coefficient, thus over-predicting higher drag force which results a higher bed expansion.

It appears from above discussion that grid-independent solution of TFM is bounded by lower limit of an average computational cell-volume and by inaccurate calculation of drag coefficient at coarse grid simulations. Considering both restrictions, results shown in Figure 5- 4, suggests that all of these simulations show a grid-independent solution for TFM in the neighborhood of 18 particle diameters for a mean particle size of 275, 350 and 400 μm comparing with the empirical prediction of bed expansions. These results are also presented in Figure 5- 1. This study shows that particle size has small effect on dimensionless grid size for the grid-independent solution of TFM for simulation of Geldart B particle fluidized beds.

The wake-dominated micro-hydrodynamics near the interface of a bubble and the dense phase may cause this grid dependency on particle size. Initially it is assumed that gas and solid particles are uniformly distributed in fluidized bed. As the gas flows through the bed, solid particles' movement deviates significantly from the gas streamlines, resulting in particle collisions and formation of particle aggregates. Cloete et al. [30] defined a particle relaxation time and concluded that smaller particles rapidly accelerate into transient eddies. Therefore, slip velocity between small particles and gas quickly reaches a steady value. If the grid is not sufficiently fine to resolve rapid streamline curvature, the particle will never depart from the gas phase and unrealistic flow artifact can be seen. Small particles, therefore, require higher grid resolution to perform very fine scale motions in the TFM simulation. However, large particles show relatively higher eddies and have higher relaxation time. They can escape from the streamlines and join a particle aggregate. Therefore, a smaller discretization resolution (i.e., large grid size) is sufficient to resolve the spatiotemporal structures for simulations of large particles.

5.4.4 Generalized grid size for grid independent solution of TFM

As presented in Figure 5- 1, the grid size required for grid-independent solution of TFM for Geldart B particle bubbling fluidized bed shows small reliance on particle size. In this present study, effect of particle size is shown through bed expansion behavior of Geldart B particle fluidized bed. This analysis agrees well within the experimental results reported by others. Although results from other researchers and from the present study on grid-independent TFM solution show some scattering, a closer inspection of Figure 5- 1 depicts that there is a linear dependence of grid size on particle diameter for a grid-independent solution. In order to come up with a general grid size that covers the whole range of particle sizes of Geldart B and also encompasses both 2-D and 3-D simulations, we have only used the published literature data points to fit a linear scale (Figure 5- 1) and found that 18 particle diameters ($\Delta \approx 18$) would be sufficient to obtain grid independent solution of TFM apply to bubbling fluidized bed simulation.

According to the Courant number analysis of explicit/implicit numerical techniques, the time step of a transient solution must reduce proportionally to the discretization grid size[51]. The Courant number (C) is a measure of how much information traverses (U_0) a computational grid cell (Δx) in a given time-step (Δt), where

$C = \frac{U_0 \Delta t}{\Delta x}$. Study shows that computational time is inversely proportional to the square and the cube of the grid size for 2-D and 3-D domain, respectively [52]. For transient solution, computational cost in terms of time increases by one order (i.e.$\text{computation time } \alpha \frac{1}{\Delta \mathrm{x}^3}$ $\textit{and}$ $\frac{1}{\Delta \mathrm{x}^4}$) for 2-D and 3-D cases, respectively. If this claim is hold, simulation of large Geldart B particle fluidized bed will be cheaper. For instance, if one tries to simulate a 2-D fluidized bed with 200 μm and 400 μm particles, the simulation will be 2^3 = 8 times faster for the 400 μm particles than for the 200 μm particles. For 3-D, this proportion will be 2^4 = 16. Consequently, this will allows conducting large scale simulation of industrial-scale bubbling fluidized bed of large Geldart B particles within the scope of interest.

5.5 **Conclusions**

Prediction of bed expansion behavior of bubbling fluidized bed of Geldart B particles carried out with the TFM is strongly dependent on grid resolution. Bubble formation, bubble sizes and shapes depend substantially on proper grid resolution. If the discretization resolutions are not sufficient, the volume-averaged TFM equations are unable to capture the proper hydrodynamic behavior. It is shown that excessively resolved grid simulations may produce unphysical behavior of fluidized bed due to the violation of lower bound of volume average used for TFM and, hence, erroneous the bed expansion of bubbling fluidized bed of Geldart B particles. Drag force may contribute to the over-prediction of bed expansion for both finest and coarsest grid simulation. Particle size has a minor effect on the requirements for achieving grid independent solutions of TFM applied to Geldart B particles bubbling fluidized bed. According to this study and findings from a literature survey, it is shown that the required grid size increases approximately in direct proportion to particle size. We propose a grid size of 18 particle diameters would be sufficient to obtain a grid-independent solution of TFM simulation of a bubbling fluidized bed of Geldart B particles.

Acknowledgments

The authors would like to acknowledge the financial support from the California Energy Commission (Grant: 07-01-37) and Clean EnGen L.L.C.

List of symbols

A	Cross-sectional area, m^2
Ar	Archimedes number
A_0	Distributor hole cross-sectional area, m^2
d_b	bubble diameter, m
d_p	Particle diameter, m
d_t	Bed diameter, m
g	Acceleration of gravity, m^2/s
H	Height, m
H_{mf}	Bed height at minimum fluidization, m
L	Expansion ratio
t	Time, s
u_{mf}	Gas velocity at minimum fluidization, m/s

U_0	Inlet superficial gas velocity, m/s

Greek Letters

ε_0	Void fraction
δ	Grid size, μm
Δ	Dimensionless grid size
τ	Characteristics time, s
ϕ	Bubble fraction

References

[1] D. Geldart, "Expansion of Gas Fluidized Beds," *Ind. Eng. Chem. Res.,* vol. 43, pp. 5802-5809, 2004.

[2] F. Johnsson*, et al.*, "Expansion of a freely bubbling fluidized bed," *Powder Technology,* vol. 68, pp. 117-123, 1991.

[3] D. Geldart, "The expansion of bubbling fluidised beds," *Powder Technology,* vol. 1, pp. 355-368, 1968.

[4] D. J. Gunn and N. Hilal, "The expansion of gas-fluidised beds in bubbling fluidisation," *Chemical Engineering Science,* vol. 52, pp. 2811-2822, 1997.

[5] J. Werther, Wein, J., "Expansion behavior of gas fluidized bed in the turbulent regime," *A.I.Ch.E. Symposium Series,* vol. 90, pp. 31-44, 1994.

[6] J. G. Yates, "Experimental observations of voidage in gas-fluidized beds," in *Non-invasive Monitoring of Multiphase Flows. Elsevier, Amsterdam, pp.141–160*, J. Chaouki, Larachi, F., Dudukovic, M. P., Ed., ed Amsterdam: Elsevier, 1997, pp. 141–160.

[7] A. Hepbasli, "Estimation of bed expansions in a freely-bubbling three-dimensional gas-fluidized bed," *International Journal of Energy Research,* vol. 22, pp. 1365–1380, 1998.

[8] F. Taghipour*, et al.*, "Experimental and computational study of gas–solid fluidized bed hydrodynamics," *Chemical Engineering Science,* vol. 60, pp. 6857-6867, 2005.

[9] D. Gidaspow, Jung, J., Singh, R. K., "Hydrodynamics of fluidization using kinetic theory: an emerging paradigm," *Powder Technology,* vol. 148, pp. 123–141, 2004.

[10] D. Gidaspow*, et al.*, "Hydrodynamics of circulating fluidized beds: kinetic theory approach," Illinois Inst. of Tech., Chicago, IL (United States). Dept. of Chemical Engineering1991.

[11] J. A. M. Kuipers, van Swaaij, W.P.M., "Computational fluid dynamics applied to chemical reaction engineering," *Advances in Chemical Engineering,* vol. 24, 1998.

[12] R. D. Moser*, et al.*, "Direct numerical simulation of turbulent channel flow up to Re= 590," *Phys. Fluids,* vol. 11, pp. 943-945, 1999.

[13] Y. Tsuji*, et al.*, "Discrete particle simulation of two-dimensional fluidized bed," *Powder Technology,* vol. 77, pp. 79-87, 1993.

[14] C. Lun*, et al.*, "Kinetic theories for granular flow: inelastic particles in Couette flow and slightly inelastic particles in a general flowfield," *Journal of Fluid Mechanics,* vol. 140, pp. 223-256, 1984.

[15] D. Gidaspow, *Multiphase Flow and Fluidization: Continuum and Kinetic Theory Descriptions*. San Diego: Academic Press, 1994.

[16] C. C. Pain, Mansoorzadeh, S., de Oliveira, C.R.E., "A study of bubbling and slugging fluidised beds using the two-fluid granular temperature model," *International Journal of Multiphase Flow,* vol. 27, pp. 527–551, 2001.

[17] M. Syamlal, O’Brien, T.J., "Computer simulation of bubbles in a fluidized bed," *A.I.Ch.E. Symposium Series,* vol. 85, pp. 22-31, 1989.

[18] C. Y. Wen, Yu, Y.H.,, "Mechanics of fluidization," *Chemical Engineering Progress Symposium Series,* vol. 62, pp. 100-111, 1966.

[19] J. Wang, "Length scale dependence of effective inter-phase slip velocity and heterogeneity in gas–solid suspensions," *Chemical Engineering Science,* vol. 63, pp. 2294-2298, 2008.

[20] J. Wang*, et al.*, "Why the two-fluid model fails to predict the bed expansion characteristics of Geldart A particles in gas-fluidized beds: a tentative answer," *Chemical Engineering Science,* vol. 64, pp. 622-625, 2009.

[21] K. Agrawal*, et al.*, "The role of meso-scale structures in rapid gas–solid flows," *Journal of Fluid Mechanics,* vol. 445, pp. 151-185, 2001.

[22] A. T. Andrews IV*, et al.*, "Coarse-grid simulation of gas-particle flows in vertical risers," *Industrial & Engineering Chemistry Research,* vol. 44, pp. 6022-6037, 2005.

[23] S. Benyahia, "On the effect of subgrid drag closures," *Industrial & Engineering Chemistry Research,* vol. 49, pp. 5122-5131, 2009.

[24] S. Benyahia*, et al.*, "Study of the ability of multiphase continuum models to predict core-annulus flow," *Aiche Journal,* vol. 53, pp. 2549-2568, 2007.

[25] J. De Wilde, "Reformulating and quantifying the generalized added mass in filtered gas-solid flow models," *Physics of Fluids (1994-present),* vol. 17, p. 113304, 2005.

[26] C. Guenther*, et al.*, "A numerical investigation of an industrial scale gas–solids CFB," *Circulating Fluidized Bed Technology VII,* pp. 483-488, 2002.

[27] Y. Igci*, et al.*, "Filtered two-fluid models for fluidized gas-particle suspensions," *Aiche Journal,* vol. 54, pp. 1431-1448, 2008.

[28] D. Z. Zhang and W. B. VanderHeyden, "The effects of mesoscale structures on the macroscopic momentum equations for two-phase flows," *International Journal of Multiphase Flow,* vol. 28, pp. 805-822, 2002.

[29] J. Wang*, et al.*, "CFD study of the minimum bubbling velocity of Geldart A particles in gas-fluidized beds," *Chemical Engineering Science,* vol. 65, pp. 3772-3785, 2010.

[30] S. Cloete*, et al.*, "Grid independence behaviour of fluidized bed reactor simulations using the Two Fluid Model: Effect of particle size," *Powder Technology,* vol. 269, pp. 153-165, 2015.

[31] J. Ding and D. Gidaspow, "A bubbling fluidization model using kinetic theory of granular flow," *Aiche Journal,* vol. 36, pp. 523-538, 1990.

[32] A. Busciglio*, et al.*, "Analysis of the bubbling behaviour of 2D gas solid fluidized beds: Part II. Comparison between experiments and numerical simulations via digital image analysis technique," *Chemical Engineering Journal,* vol. 148, pp. 145-163, 2009.

[33] T. Li*, et al.*, "CFD simulations of circulating fluidized bed risers, part I: Grid study," *Powder Technology,* vol. 254, pp. 170-180, 2014.

[34] F. Vejahati*, et al.*, "CFD simulation of gas–solid bubbling fluidized bed: a new method for adjusting drag law," *The Canadian Journal of Chemical Engineering,* vol. 87, pp. 19-30, 2009.

[35] N. Xie*, et al.*, "Effects of using two-versus three-dimensional computational modeling of fluidized beds: Part I, hydrodynamics," *Powder Technology,* vol. 182, pp. 1-13, 2008.

[36] T. D. Nguyen*, et al.*, "CFD simulation with experiments in a dual circulating fluidized bed gasifier," *Computers & Chemical Engineering,* vol. 36, pp. 48-56, 2012.

[37] H. Wang*, et al.*, "Study of bubbling and slugging fluidized beds by simulation and ECT," *Aiche Journal,* vol. 52, pp. 3078-3087, 2006.

[38] Y. T. Makkawi*, et al.*, "The effect of friction and inter-particle cohesive forces on the hydrodynamics of gas–solid flow: a comparative analysis of theoretical predictions and experiments," *Powder Technology,* vol. 163, pp. 69-79, 2006.

[39] N. Reuge*, et al.*, "Multifluid Eulerian modeling of dense gas–solids fluidized bed hydrodynamics: Influence of the dissipation parameters," *Chemical Engineering Science,* vol. 63, pp. 5540-5551, 2008.

[40] T. Li, "Validation of a 2.5 D CFD model for cylindrical gas–solids fluidized beds," *Powder Technology,* vol. 286, pp. 817-827, 2015.

[41] M. Syamlal, Rogers, W., O'Brien, T. J., "MFIX Documentation, Theory Guide1," N. T. I. Service, Ed., ed. Springfield, 1993.

[42] M. Syamlal and T. J. O'Brien, "Fluid dynamic simulation of O-3 decomposition in a bubbling fluidized bed," *Aiche Journal,* vol. 49, pp. 2793-2801, Nov 2003.

[43] J. Wang*, et al.*, "Coarse grid simulation of bed expansion characteristics of industrial-scale gas–solid bubbling fluidized beds," *Chemical Engineering Science,* vol. 65, pp. 2125-2131, 2010.

[44] S. Cloete*, et al.*, "On the effect of cluster resolution in riser flows on momentum and reaction kinetic interaction," *Powder Technology,* vol. 210, pp. 6-17, 2011.

[45] J. A. M. Kuipers*, et al.*, "Theoretical and experimental bubble formation at a single orifice in a two-dimensional gas-fluidized bed," *Chemical Engineering Science,* vol. 46, pp. 2881-2894, 1991.

[46] K. Daizo and O. Levenspiel, "Fluidization engineering," 1991.

[47] R. Darton, "A bubble growth theory of fluidized bed reactors," *Trans IChemE,* vol. 57, p. 134, 1979.

[48] L. Mazzei and P. Lettieri, "A drag force closure for uniformly dispersed fluidized suspensions," *Chemical Engineering Science,* vol. 62, pp. 6129-6142, 2007.

[49] A. Bakshi*, et al.*, "Towards accurate three-dimensional simulation of dense multi-phase flows using cylindrical coordinates," *Powder Technology,* vol. 264, pp. 242-255, 2014.

[50] A. Cleminņš, "Representation of two-phase flows by volume averaging," *International Journal of Multiphase Flow,* vol. 14, pp. 81-90, 1988/01/01 1988.

[51] R. Courant*, et al.*, "Über die partiellen Differenzengleichungen der mathematischen Physik," *Mathematische Annalen,* vol. 100, pp. 32-74, 1928.

[52] C. J. Hearn, *The dynamics of coastal models*: Cambridge University Press, 2008.

CHAPTER 6

3-D face-masking detection and tracking algorithm for bubble dynamics: method and validation for gas-solid fluidized beds

Abstract

The transient behavior of rising bubbles plays a critical role on the performance of fluidized bed reactors, but predicting bubble dynamics is difficult. CFD has been shown to be capable of reproducing bubbling phenomena, but data interpretation and visualization is challenging. In this study, a 3-D detection and tracking algorithm, called face-masking, is developed and validated by numerical simulations of lab-scale and pilot-scale gas-solid fluidized beds. This algorithm identifies discrete bubbles using the instantaneous whole-field void fraction data. Individual bubbles are characterized in detail, including size, shape and location. The algorithm tracks bubbles across successive time frames and computes axial and lateral bubble velocities. Bubble dynamics predicted by the face-masking algorithm are validated against four different published experimental measurements. The face-masking algorithm provides a new tool for post-processing large-scale three-dimensional fluidized-bed simulations data. This algorithm can also be applicable in other areas of multiphase flows where characterization of bubbles, droplets, clusters, is necessary.

6.1 Introduction

Fluidized beds are one of the most applied technologies in petroleum, chemical and energy industries [1]. They are challenging to design and scale up, primarily, due to the complex transient characteristics created by the formation of bubbles inside the bed. The performance of a fluidized bed is, therefore, significantly influenced by the formation of gas bubbles and their distribution, facilitating rapid solids mixing, impacting reaction rates, product selectivity, mass transfer, heat transfer rates to immersed surfaces, and elutriation of particles from the bed [2].

According to the classical two-phase theory by Toomey and Johnstone [3] and the Davidson theory for bubble movement [4], any fluid flow exceeding the minimum fluidization velocity passes through the fluidized bed as bubbles. Many studies including experimental and computational showed that rising bubbles in gas-solid fluidized bed has a significant impact on solids motion [5-12]. However, there is still no precise pattern that links solids movement and bubble dynamics due to the lack of experiments simultaneously measuring the solids and bubble motion, for a range of particle properties and operating conditions.

A sound understanding of bubble dynamics is, therefore, of primary importance for investigating behavior of fluidized beds. The formation and development of bubbles in gas-solid fluidized bed has been extensively studied employing different intrusive and non-intrusive techniques, like optical signals [13, 14], pressure fluctuations [15-17] or electrical pulses [18, 19], high speed cameras and digital image analysis [20-22], X-Ray [23-26], electrical capacitance [23] and MRI [27]. From this range of measurement techniques, it is evident that the key difficulty in analyzing fluidization quality and bubble dynamics is concerned with the measurement of bubbles and their physical properties in the bed such as position, dimensions, axial and lateral velocities in a gas-solid fluidized bed.

Advances in the theory and numerical techniques and the availability of fast affordable computing power has allowed researchers using the first-principles based computational fluid dynamics (CFD) towards a predictive tool to explore complex hydrodynamic behavior of gas-solid fluidized bed. CFD is capable of intrinsically capturing the complexity of bubble formation and the resulting non-linear interactions because of its fundamental basis in the conservation of mass, momentum, species and energy. Many authors recognize the advantage of CFD that it can provide insight useful for scale-up, design, or process optimization for reliable commercial plants reducing economic risk, and potentially allowing for rapid scale-up [28-31]. In fact, CFD can allow for virtual experimental "measurement" that is cannot be done in the physical world easily, or at all. However, the majority of bubble dynamics are restricted to pure two-dimensional (2-D) or slices of three-dimensional (3-D) cylindrical beds [12, 25, 28, 32] or pseudo-2-D rectangular beds of small thickness [33-35]. Although 2-D bubble statistics provides valuable information on fluidization, many authors recognize the limitation of 2-D analysis [17, 34, 36, 37]. Nevertheless, all practical gas–solid flows are three-dimensional, and studies of bubble statistics are limited in literature because of the difficulties associated with flow visualization and measurements –both experimentally and computationally [25].

Recently, Bakshi et al. [38] developed a 3-D bubble statistics algorithm that used void fraction data from a 3-D simulation to calculate bubble properties. In that algorithm, initially, a threshold was set to discard a large portion of void fraction data from computational cells, and then remaining data cells were interpolated using a fine grid (a cube with side of 2 mm, irrespective of CFD grid size) for resolving bubble boundaries. Verma et al. and Sobrino et al. used a reconstructive method that processed 2-D contours in consecutive horizontal sections at different axial locations and then stacking them to obtain bubble properties [25, 37]. A sequence of target-grid and pending-grid method, known as flood-fill method, is developed by Lu et al. [32] to determine bubble properties from 2-D CFD data.

The above observations suggest that whichever the method employed, these approaches, except Bakshi et al. [38], may be inefficient when applied to large volumes of simulation data from pilot/commercial-scale three-dimensional beds. It is true that the computational cost for bubble statics using Bakshi et al. [38] method will be less expensive but the accuracy of bubble statistics may be affected applying that algorithm as it discards a large amount of void field data. In the present work, a new 3-D algorithm, called as “face-masking”, is developed that will enable processing large volume of 3-D numerical simulations data for determining bubble properties. This algorithm uses the instantaneous whole-field of void fraction data of a 3-D fluidized bed. The algorithms identifies discrete bubbles, characterize the size and shape of those bubbles, and tracks the bubbles as they rise through a bed, including splitting and coalescence. This algorithm is validated by computing bubble properties using data from 2-D and 3-D fluidized bed simulations and comparing them with experimental measurements for a wide range of particle sizes and for different bed geometries (lab- and pilot-scale). In addition, bubble properties computed by this algorithm are also compared with commonly used semi-empirical correlations from literature. This is a complete algorithm and can be easily extended to other areas of multiphase flow for characterizing bubbles, droplets, clusters, etc. and validating 3-D numerical simulations.

6.2 Experimental studies

Bubble dynamics characterized by face-masking algorithm from simulation data are compared with four different experimental measurements by Velarde et al.[39], Rüdisüli et al. [15], Verma et al. [25], and Geldart [40]. Velarde et al. [39] used glass beads as bed material in a pseudo-2-D quartz column with bed width, depth and height of 0.25, 0.015 and 0.7 m respectively. Bubble sizes are measured from images captured by a Dantec Flowsense 16 M camera coupled with an optical endoscopic laser. Rüdisüli et al. [15] carried out experiments using γ- Al_2O_3 as bed materials in a glass column with internal diameter 14.5 cm. Bubble sizes were measured using reflective-type optical probes at a sampling frequency of 400 Hz. A bubble linking algorithm that used the measured response from two probes placed 1 cm apart was used to determine bubble rise velocity. Verma et al. [25] conducted their experiments in a polycarbonate cylindrical column with inner diameter of 0.1 m using glass as bed material. An ultrafast electron beam X-ray scanner acquiring data at 1000 Hz with a high spatial resolution of about 1 mm was placed at three cross-sections of the bed. Images from experiments were reconstructed using an algorithm to determine bubble properties. In Geldart's experiment

[40], sand particle was used as bed material in a perspex column with inner diameter 30.8 cm. A standard meter-rule marked in millimeters, still 35-mm photographs, and 16-mm high speed cine pictures were used to analyze bubble sizes.

Table 6- 1. Experimental conditions

Physical properties	Velarde et al. [39]	Rüdisüli et al. [15]	Verma et al.[25]	Geldart [40]
Bed width/diameter, m	0.25	0.145	0.10	0.308
Static bed height, m	0.375	0.50	0.20	0.20
Measuring height, m	0.2 - 0.35	0.23, 0.45	0.05 - 0.20	0.05 - 0.20
U/U_{mf}	3.0	2.3–6.8	1.25–3.0	1.0 -3.0
Type of geometry	Pseudo- 2-D	3-D	3-D	3-D

Table 6- 2. Properties of particles used in experimental studies

Type	Diameter (d_p), μm	Density (ρ), kg/m^3	U_{mf}, m/s	Researchers
Glass beads	500	2500	0.21	Velarde et al. [39]
Alumina	289	1350	0.041	Rüdisüli et al. [15]
Glass	1000	2526	0.67	Verma et al.[25]
Silica sand	275	2600	0.056	Geldart [40]

All of these experiments described above were operated in the regime of bubbling fluidization using Geldart B and D particles. A summary of all the experimental conditions and particle properties is presented in Table 6- 1and Table 6- 2, respectively

6.3 Simulation setup

6.3.1 Two-fluid model (TFM)

In this study, the Two Fluid Model (TFM) is used which treats each phase (fluid and solid) as an interpenetrating continuum, and therefore to construct integral balances of continuity, momentum and energy for both phases, with appropriate boundary and leap conditions for phase interfaces. TFM applies averaging techniques and assumptions to obtain momentum balance for the solids phases since the resultant continuum approximation for the solid phase has no equation of state and lacks variables such as viscosity and normal stress [41]. The evaluation of the solid phase stress tensor is based on the flow regimes - the viscous regime where the stress tensor is evaluated using the Kinetic Theory of Granular Flow (KTGF) and the plastic flow regime where the theory of Schaeffer [42] is employed to account for the frictional effects [43]. The TFM equations are coupled with constitutive relations derived from data or analysis of nearly homogeneous systems. The interphase momentum transfer between gas and solid phases are coupled by drag force. Numerous correlations for calculating the drag coefficient of gas–solid systems have been reported in the literature, including those of Syamlal and O' Brien (1989) [44], Gidaspow (1994) [43], and Wen and Yu (1966) [45]. Syamlal-O'Brien drag model that bridges the results of Wen and Yu [45] for dilute systems and the Ergun approach for dense systems is used in this work. The detailed description of the conservation of mass, momentum, and energy equation and drag model of the TFM is described in somewhere else [46].

6.3.2 Initial and boundary conditions

The standard initial conditions were used to describe both 2-D and 3-D simulations. The bed was assumed to be under minimum fluidization with superficial gas velocity equal to u_{mf} initially. Lateral gas velocities were set to zero for initial conditions. A constant pressure was defined in all horizontal planes up through the bed of particles depending upon static pressure. The upper section of the simulated geometry, or freeboard, was considered to be occupied by gas only at time zero. For both 2-D and 3-D simulations, the lateral walls were modeled using partial-slip boundaries, with no-slip for gas and free-slip for solid phase. The particle-wall interactions are modeled using the Johnson-Jackson model [47], which evaluates the solids slip velocity at the walls by considering momentum and granular energy balance. Dirichlet boundary conditions were employed at the distributor to specify a uniform gas inlet velocity, U_0. Pressure boundary conditions were employed at the top of the freeboard.

6.3.3 Flow solver and solver settings

The National Energy Technology Laboratory's (NETL, USA) open-source code MFIX was used as flow solver [46]. The modified phase-coupled SIMPLE scheme, which uses a solids volume fraction correction equation instead of a solids pressure correction equation, was used for pressure–velocity coupling. The second-order SuperBee scheme was used for the spatial discretization of all equations. A combination of point successive under relaxation and biconjugate gradient stabilized method (BiCGSTAB) method were used for the linear equation solver. A maximum residual at convergence of 10^{-03} was used to improve the accuracy of the continuity and momentum equations solution. First order implicit temporal discretization was used to ensure stable and accurate solutions. An automatic time-step adjustment was used to enhance the computation speed, with a maximum and a minimum time-step of $2x10^{-04}$ s and 10^{-07} s respectively. A summary of other simulation parameters is given in Table 6- 3.

Table 6- 3. Summary simulation parameters

Parameters		Validated for TFM simulation
Restitution coefficient	0.99*, 0.90	[28, 48]
Coefficient of particle wall collision	1.0	[28]
Specularity coefficient	0.6	[28, 49]
Angle of internal friction, °	30, 33.3†	[50]
Angle of internal friction at wall, °	0.0	[50]
Temperature, K	293	

* used for [39] based on [51]; † measured by [13]

6.3.4 Geometry and discretization

The dimensions of the fluidized beds are shown in Table 6- 3. 2-D Cartesian (for [39]) and 3-D Cylindrical (for [13, 25, 40]) coordinates are used in the simulations with unstructured mesh sizes. A careful investigation of mesh-refinement is essential for meaningful validation and prior to interpretation of CFD results. For this study mesh sizes are chosen for the grid-independent solution of TFM based on the experimentally validated mesh-refinement studies, and is shown in Table 6- 4.

Table 6- 4. Mesh resolutions used for simulations.

Type	Width or diameter, m	Height, m	d_p, μm	Number of mesh for grid -independent TFM, ($N_r \times N_z \times N_\theta$)	References
Lab-scale [39]	0.250	1.00	500	50 × 200	[51-53]
Lab-scale [13]	0.145	0.85	289	23 × 170 × 12	[28]
Lab-scale [25]	0.100	0.40	1000	16 × 120 × 16	[25, 28]
Pilot-scale [40]	0.308	0.55	275	35 × 125 × 14	[28]

6.4 Method of analysis

6.4.1 Bubble identification

The spatially resolved field variables data, associated with the flow model applied in simulation, is input to the algorithm as a matrix. Void fraction (gas volume fraction), εg is the predominant field variable used by the algorithm to identify and characterize bubble properties. First, εg data is read in MATLAB, and, then, smoothed and interpolated for accurately resolving bubble boundaries, as described below. There is some unique value of void threshold $\varepsilon_g = c_b$, where c_b is a threshold constant, that can be used to identify the circumference (for 2-D) or shell (for 3-D) of each bubble. In this study, cb is set at 0.7 (based on [13, 25, 39]). Thus any cell with εg > cb is designated as part of a bubble. The algorithm reads the void fraction data matrix ***M*** as

$$\boldsymbol{M} = \left|\left(k, x_k, y_k, z_k, \varepsilon_{g,k}\right) \in \mathbb{R}\right|$$

where ***M*** is a matrix of size $m \times 4$ with m grid cells and each cell k associated with coordinates (x_k, y_k, z_k) and void fraction $\varepsilon_{g,k}$. The following sequences are used to identify bubbles from matrix ***M*.**

Steps:

a) First, the face-masking algorithm considers the input matrix ***M*** as a regularly spaced Cartesian grid, with each element connected to its nearest neighbors. Note that simulations (3-D) are in Cylindrical coordinates. However, this algorithm converts Cylindrical coordinates (r, θ, z) into Cartesian coordinates (x, y, z) without loss of generality of ***M***, and is applicable for any grid (non-orthogonal/unstructured).

b) Second, the algorithm examines matrix ***M***: by investigating the neighboring cells in a clockwise direction from top to bottom and left to right, comparing the values of each block of four neighboring elements (i.e., a cell) in the matrix to the value c_b. The resulting surface scan can have 16 (2-D) or 32 (3-D) possible values of void fraction. If the point in space does not match with defined c_b, the algorithm performs an interpolation to locate the point at which the c_b crosses the edges of the cell. The next step is handled differently for 2-D and 3-D simulations:

    I. For 2-D, the algorithm returns a matrix ***B*** of size $2 \times (p + n)$ with p number of grid points and n number of bubbles that comprises the vertices of the bubble boundaries.

    $$\boldsymbol{B} = \left|\left(k_n, x_{k_n}, y_{k_n}, \varepsilon_{g,k_n}\right) \in \mathbb{R} \mid \boldsymbol{\varepsilon_g} \geq \boldsymbol{c_b}\right|$$

When a set of vertices forms a circumference, these vertices are connected but they are disconnected from other circumference vertices for the same constant, c_b. The algorithm, next, connects two points to produce a segment of a circumference and marches forward to complete a circumference line and assigns a unique identity to eachboundary. This step is repeated until all bubble boundaries are separated and identified from $\boldsymbol{B}$. This step along with (a) and (b) is schematically represented in Figure 6- 1.

II. For 3-D, the algorithm returns a set of matrix, $\boldsymbol{Q}$, comprising the vertices and the triangular-face vertices of volume spaces confined by c_b. To generate an isosurface of a volume space, the algorithm connects first-three points to form a triangular face of a volume space, and then march forward to form and join other triangular faces to complete a volume space.

$$\boldsymbol{Q} = \{\boldsymbol{q_1}, \boldsymbol{q_2} \in \mathbb{R} \mid \varepsilon_g \geq c_b\}$$

Here, $\mathbf{q_1}$ is a matrix of size $s\times 3$ with s number of unique vertices, and $\mathbf{q_2}$ is a matrix of size $w\times 3$ with w number of faces for n number of bubbles. A logical filter is developed to separate faces of a volume space, i.e. "bubble" from $\mathbf{q_2}$ and vertices from $\mathbf{q_1}$.

Algorithm: Bubble identification in 3-D

```
//Primary loop for searching connectivity among faces
$n_{vc}$ = number of vertices
$jj = 1$
for $k \epsilon q_{2,k}$
        if $n_{vc}(q_{2,k} \cup q_{2,k+1}) \neq n_{vc}\left(\sum_k^{k+1} q_{2,k}\right)$ then
        //faces are connected
        $T_{jj} = (q_{2,k}, q_{2,k+1})$ // Matrix T for connected faces
        else $jj = jj + 1$

// Resolve connectivity and bubble numbering
$n = 1$ // number of bubble
for $l \epsilon T$
    if $n_{vc}(T_l \cup T_{l+1}) \neq n_{vc}\left(\sum_l^{l+1} T_l\right)$ then
        $T_l = T_l \cup T_{l+1}$
    else $bubble(n) = T_l$; $l = l + 1$
```

This method is schematically shown in Figure 6- 2. For instance, in Figure 6- 2 (a), when faces 1 and 2 of a volume space are connected, the masked/combined face 1 (Figure 6- 2 (b)) must have less number of unique vertices than the total number of vertices of faces 1 and 2 (Figure 6- 2(a)). In the next step, the algorithm search for connectivity between the masked face 1 (Figure 6- 2 (b)) and the next face 3. This searching continues until a discontinuity is found. At this stage, the algorithm identifies a list of connected and disconnected faces with unique number of vertices' index from which individual volume space is separated and identified. Similar to 2-D method, a unique identity is assigned for each volume space.

c) Concurrent to detection, the algorithm determines bubble properties, i.e. diameter, centroids, aspect ratio, velocity, etc. from the coordinates encapsulating a bubble circumference (2-D) or volume space (3-D).

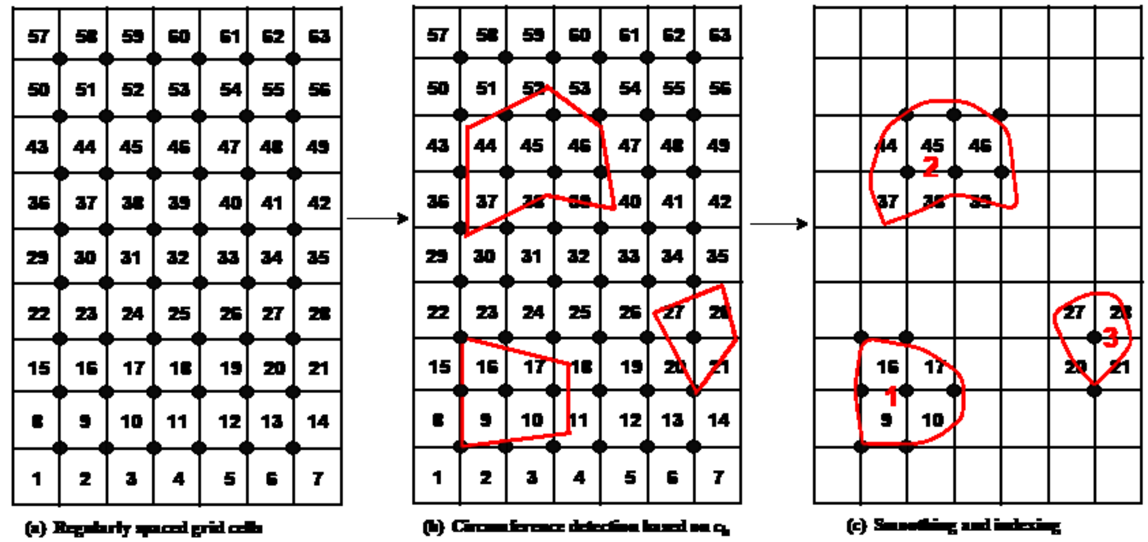
(a) Regularly spaced grid cells (b) Circumference detection based on c_k (c) Smoothing and indexing

Figure 6- 1. Steps involved in bubble identification from 2-D simulation data.

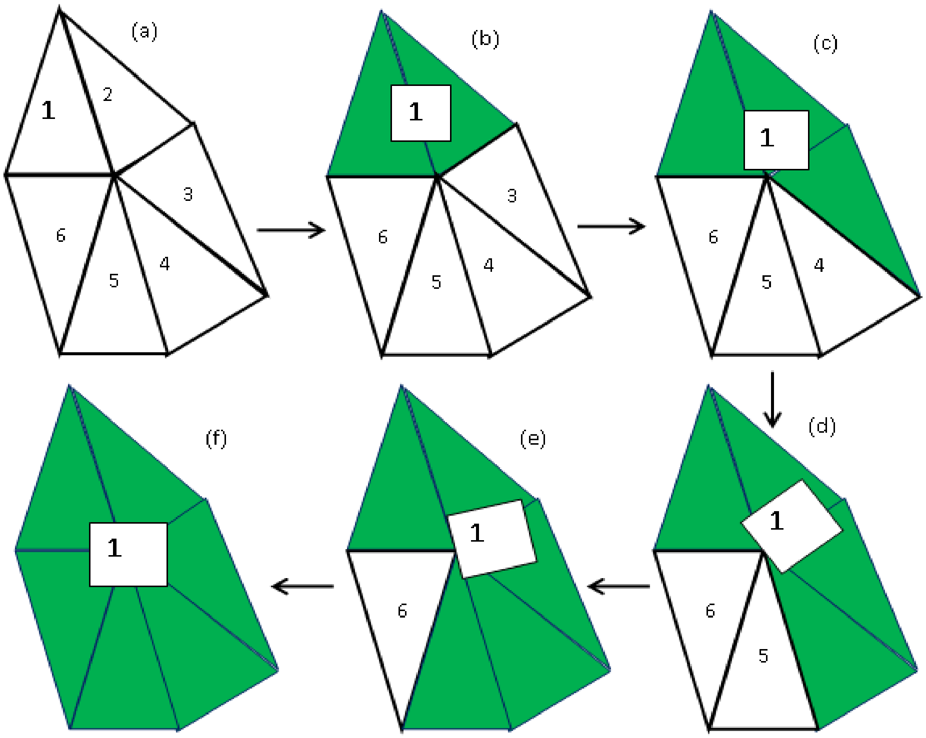

Figure 6- 2. Logical sequences of face-masking algorithm for 3-D simulation data.

A representative illustration of the face-masking algorithm is shown in Figure 6- 3 for the determination of bubble properties from 2-D and 3-D simulation data. Figure 6- 3 (a) shows the void field matrix ***M***, which is interpolated and smoothed for determining bubble boundaries (Figure 6- 3 (b)). Based on the void threshold, $c_b = 0.7$, bubbles are identified and numbered accordingly (Figure 6- 3 (c)).

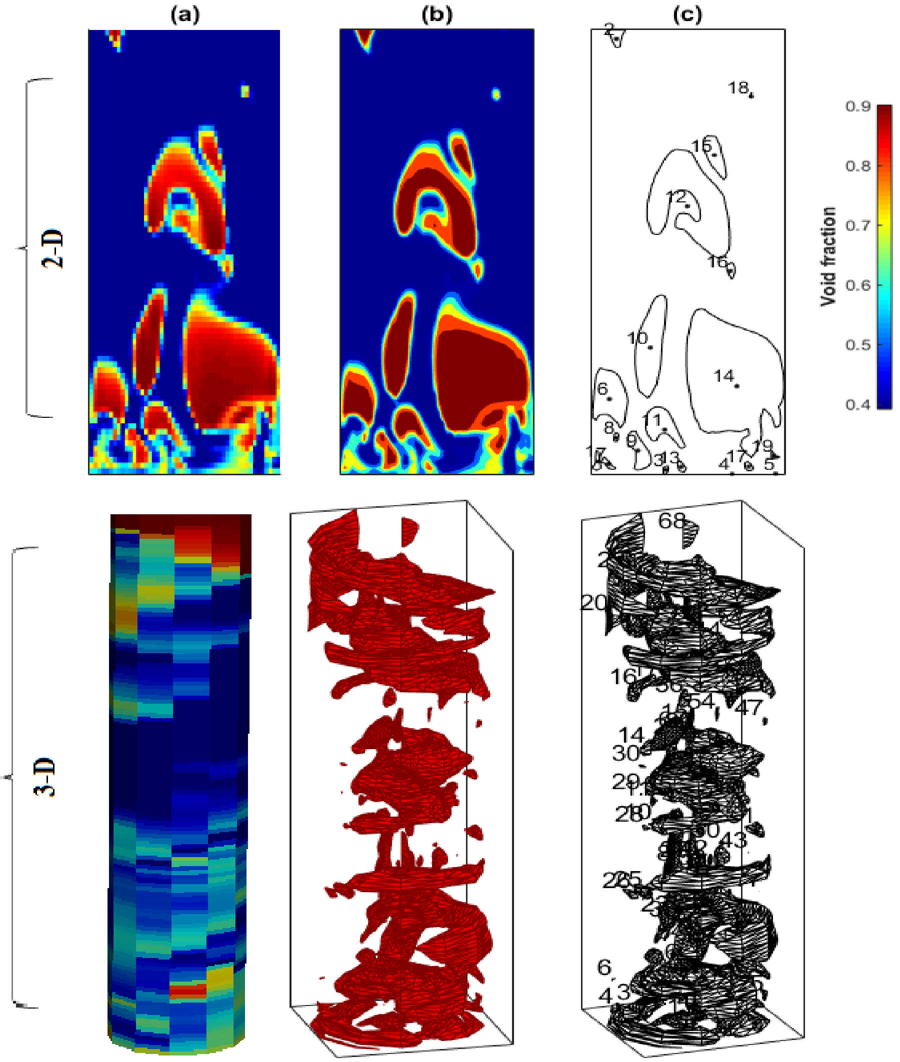

Figure 6- 3. Snapshot from 2-D (Lab-scale [39]) and 3-D (Lab-scale [15]) simulations (left) smoothed (center) and identified (right) based on void threshold for determining bubble properties.

6.4.2 Bubble diameter

The bubble diameter is difficult to define due to the irregular shape of the bubbles in a fluidized bed. However, authors in literature use a volume/area equivalent bubble diameter [1]. Thus, the equivalent diameter, $D_{b,n}$ of *n-th* bubble can be calculated assuming that the bubbles are spheres.

$$D_{b,n} = \sqrt[3]{\frac{6\,V_{b,k}}{\pi}} \tag{1}$$

For 2-D cases, the area based bubble diameter may be defined similarly as $\sqrt{4A_{b,n}/\pi}$. Here, $A_{b,n}$ and $V_{b,n}$ represent the area and volume of *n-th* bubble for 2-D and 3-D cases, respectively. The area of a bubble can be expressed by the magnitude of the cross-product of two edge vectors and can be calculated from the vertices in matrix $\boldsymbol{B}$.

$$A_{b,n} = \frac{1}{2}\sum(x_k\, y_{k+1} - x_{k+1}\, y_k)\ \in \boldsymbol{B} \tag{2}$$

The volume of individual bubbles can be calculated using tetrahedra [54] , defined as a convex polyhedron consisting of four triangular faces that can be specified by its polyhedron vertices. The volume of a bubble can be expressed based on the vertices in matrix $\boldsymbol{q_1}$ and $\boldsymbol{q_2}$.

$$V_{b,n} = \sum\left(\frac{1}{3!}\begin{vmatrix} x_{k,1} & y_{k,1} & z_{k,1} & 1 \\ x_{k,2} & y_{k,2} & z_{k,2} & 1 \\ x_{k,3} & y_{k,3} & z_{k,3} & 1 \\ x_{k,4} & y_{k,4} & z_{k,4} & 1 \end{vmatrix}\right) \in \boldsymbol{q_1}, \boldsymbol{q_2} \tag{3}$$

6.4.3 Bubble centroids and aspect ratio

The centroid of a bubble can be expressed in terms of the average coordinates of the bubble boundaries (2-D) or volume space (3-D) and can be evaluated for the *n-th* bubble as follows

$$x_{c,n} = \frac{1}{N_{b,n}} \sum x_k \in \boldsymbol{B} \; or \; \boldsymbol{q_1}$$

where $N_{b,n}$ is the total number of vertices encompassed by *n-th* bubble (and similarly $y_{c,n}$ and z_{cn}). Note that bubble centroid can be inside or outside of bubble boundary depending on the bubble shape.

Bubble aspect ratio *AR* for *n-th* bubble is defined here as the ratio of axial and lateral maximum bubble dimension.

$$l_{z,n} = \Delta z \, (\max(z_k) - \min(z_k)) \in \boldsymbol{B} \; or \; \boldsymbol{q_1}$$

$$l_{x,n} = \Delta x \, (\max(x_k) - \min(x_k)) \in \boldsymbol{B} \; or \; \boldsymbol{q_1} \qquad AR_{x,n} = \frac{l_{z,n}}{l_{x,n}}$$

$$l_{y,n} = \Delta y \, (\max(y_k) - \min(y_k)) \in \boldsymbol{B} \; or \; \boldsymbol{q_1} \qquad AR_{y,n} = \frac{l_{z,n}}{l_{y,n}}$$

Here $l_{z,n}$ is the maximum axial (vertical) dimension and $l_{x,n}$ and $l_{y,n}$ are lateral maximuma of bubble dimensions, in Cartesian coordinates. Δx and Δy, and Δz are the corresponding mesh sizes.

6.4.4 Bubble rise velocity

The motion of bubbles is analyzed by tracking the centroid of bubbles. The trajectories that individual bubble centroid follows are thought of as "recording" the path of a fluid element in the flow over a certain period, similar to a streakline. The direction of the path can be determined by the tangent of the centroidal path at each moment in time. The bubble velocity (axial and lateral) is computed from 1st order numerical differentiation in time of the centroids' location. However, tracking of bubble centroid is not trivial as bubble in one time-frame may disappear, may change its position, may combine with another (coalesce), or it may split (into two or more bubbles) in the next time frame. After identification of bubbles in a time frame, *f*, the best estimated positions of the bubble in the next time frame can be estimated using Eulerian tracking of bubbles. To prevent erroneous association of bubbles and bubble velocity due to coalescence and splitting, three commonly imposed restrictions [12, 13, 21, 32, 38] are used in this study to select bubbles for determination of bubble velocity – (i) equal number of bubbles in frame f and f+1 after time step Δt; (ii) positive axial velocity with maximum velocity bounded by the maximum expected value (based on maximum bubble size correlation by Mori and Wen [55]); (iii) the lateral displacement must be smaller in magnitude than 50% of the vertical rise. Note these filters ensure accurate and reliable tracking and has been validated previously using experimental study of Geldart B-[15, 25] and D-[25] particles and verified using 3-D simulation visualizations for the present study. By use of these filters, the number of bubbles positively associated with a specific bubble in the previous frame is a small fraction of the total number of bubbles. Bubble velocities are determined from 17 s of real time simulation that is recorded at 100 Hz (total 1700 frames) in order to find reliable and statistically independent properties.

6.5 Results and discussions

The simulations are completed for 20 s of real flow time for all cases and the first 3 s data are discarded to minimize the transient start-up effects. Consequently, the bubble properties reported in this study consist of the last 1700 time-frames, and are validated against experimental results reported in literature. First, bubble properties computed by the face-masking algorithm for 2-D numerical simulation is compared with the lab-scale experimental result reported by Velarde et al. [39] for a pseudo-2-D rectangular bubbling fluidized bed. Second, bubble properties measured from two lab-scales experiments (3-D Cylindrical) are compared with simulation results determined by the algorithm.

Table 6- 5. List of semi-empirical correlations used in this study for equivalent mean bubble diameter and bubble rise velocity.

Authors	Correlation	Application
Shen et al. [20]	$d_b = \frac{0.89}{g^{0.33}} ((U_0 - u_{mf})\left(H + \frac{4A_0}{\delta}\right)^{0.67}$	Pseudo-2-D bed
Darton [56]	$d_b = \frac{0.54}{g^{0.2}} \left(U_0 - u_{mf}\right)^{0.4} \left(H + 4\sqrt{A_0}\right)^{0.8}$	Geldart B
Mori and Wen [55]	$d_b = d_{bm} - (d_{bm} - d_{b0}) \exp\left(-\frac{0.3z}{d_t}\right)$ $d_{bm} = 0.65\left(0.785 d_t^2 (U_0 - u_{mf})\right)^{0.4}$ $d_{b0} = \frac{1.3}{g^{0.2}}\left(\frac{U_0 - u_{mf}}{N_{or}}\right)^{0.4}$	Geldart B and D
Werther [57]	$V_b = \psi(U_0 - u_{mf}) + 0.711\alpha\sqrt{\mathrm{gd_b}}$ $\psi = \begin{Bmatrix} 0.65\ for\ Geldart\ B \\ 0.26\ for\ Geldart\ D \end{Bmatrix}$ $\alpha = \begin{Bmatrix} 2d_t^2\ for\ Geldart\ B \\ 0.87\ for\ Geldart\ D \end{Bmatrix}$	Geldart B and D

Lab-scale experiment conducted by Rüdisüli et al. [15] is characterized as Geldart-B bubbling fluidization whereas Verma et al. [25] experiment is characterized as Geldart-D bubbling fluidization. Finally, bubble properties computed for a pilot-scale bubbling fluidized bed from numerical simulation is compared with Geldart's [40] experimental (3-D Cylindrical) results. In addition, numerical simulation results determined by the algorithm are compared with predicted results from widely used semi-empirical correlations (shown in Table 6- 5). Furthermore, the computation time used by the algorithm is recorded and discussed.

6.5.1 Validation based on pseudo-2-D study (lab-scale) by Velarde et al. [39]

For measuring average bubble diameter, Velarde et al. used an ePIV (Endoscopic-laser Particle Image Velocimetry) recording images from experiments which are post-processed to distinguish the bubble and emulsion phases based on pixel intensity. They concluded that 1500 ~ 2000 time-frames were sufficient to obtain reliable time-averaged data. Likewise, 1700 time-frame data from simulation is used to compare with experimental results. The face-masking algorithm detects the discrete bubbles from time-frame series and identifies their locations in the bed.

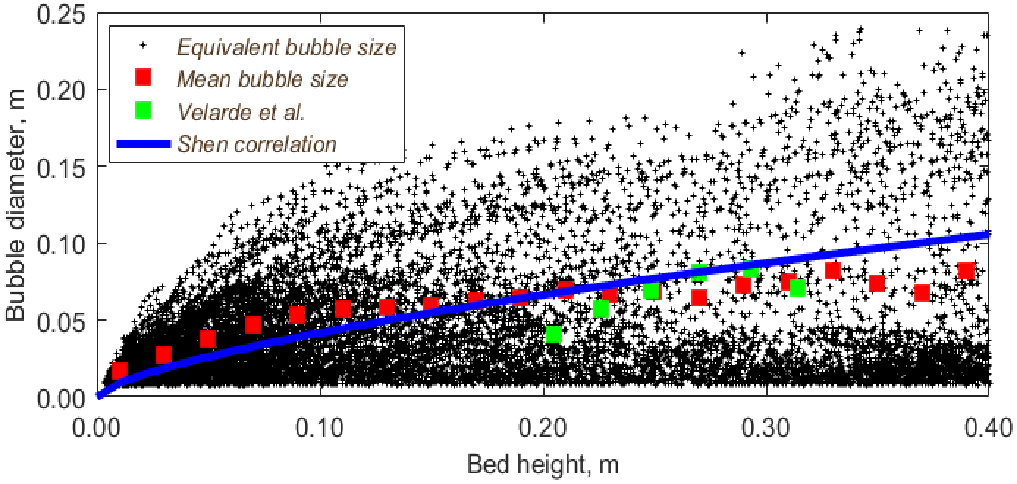

Figure 6- 4. Distribution of equivalent bubble diameter and comparison of mean bubble diameters obtained from 2-D simulations with experiment [39] and semi-empirical correlation. Small black dots indicate bubbles found from face masking analysis of simulation results.

Figure 6- 4 shows the equivalent bubble size distribution computed by the algorithm using the whole-field void fraction data for 2-D numerical simulations stated in Table 6- 4. The bubble diameters show a wide range of size distributions at any position within the fluidized bed. Note that there are small bubbles at every bed height above distributor. This scatter is characteristic of bubble size and is also confirmed with the experimental observations by other researchers [24, 58, 59]. In many instances, small bubbles appear and disappear randomly at any bed height. Sometimes these small bubbles do not coalesce but travel axially without interaction.

Area-averaged bubble diameters are computed from the CFD results, shown in the Figure 6-, and compared with experimental measurements [39]. In addition, the average bubble diameter calculated by the empirical correlation of Shen et al. [20] is plotted. The mean bubble diameter calculated by the algorithm from simulation data agrees quite reasonably with experimental and empirical predictions.

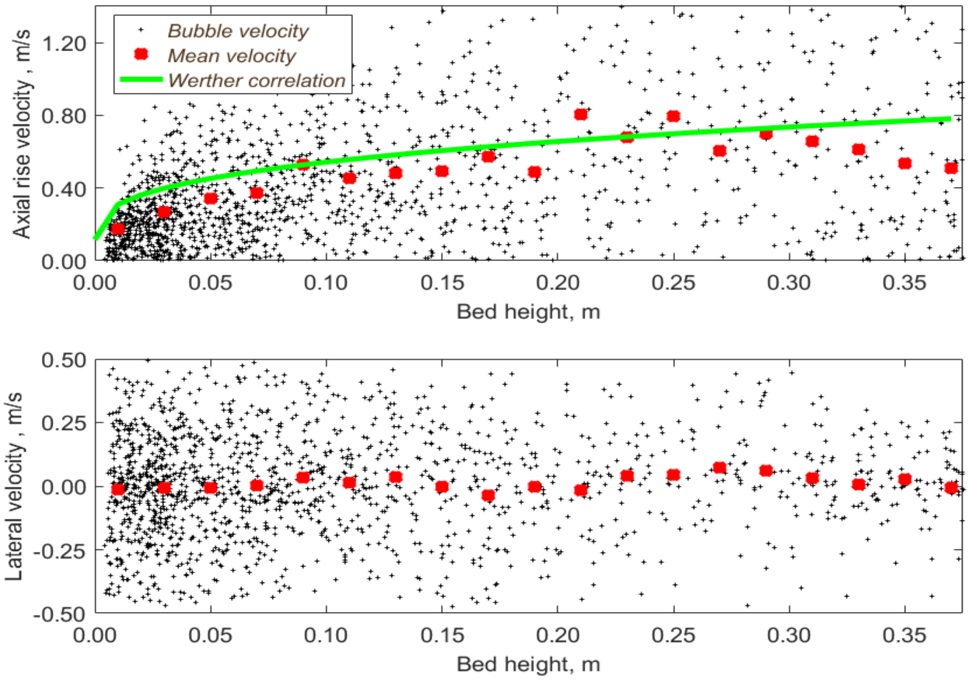

Figure 6- 5. Distribution of bubble rise velocity (top) and lateral velocity (bottom).

Figure 6- 5 shows the distribution of bubble velocities – axial and lateral. As outlined in the methodology, bubbles that are connected to each other in successive frames are considered for the determination of bubble velocities. Likewise, the bubble size distribution, both axial and lateral bubble velocities represent a wide range of distribution throughout the fluidized bed. This scatter behavior of bubble velocities, which is consistent with literature [21, 24, 32], is due to the wide variation of the bubble sizes. Note that the number of bubbles that are positively connected with previous time frame is much smaller than the overall number of bubbles shown in Figure 6- 4.

The mean axial bubble rise velocity computed by the algorithm from simulation data is compared with the average rise velocity calculated using the empirical correlation by Werther [57]. The bubble diameter used in Werther correlation is calculated using Shen et al. [20] correlation. As seen in Figure 6- 5, the mean axial rise velocity agrees well with the average rise velocity predicted by the semi-empirical correlation. However, there is no empirical correlation that correlates the lateral bubble velocity in fluidized bed. Busciglio et al. [21] reported a scatter behavior of lateral bubble velocity for glass ballotini particles of size 250 μm in a pseudo-2-D experiment, which is also seen in this present study. More prominent lateral bubble movements are accounted next to the distributor height, which may be due to coalescence of small bubbles. Besides, small bubbles are greatly affected by the motion of big bubbles, which may accelerate them in lateral direction.

6.5.2 Validation based on studies (3-D lab-scale) by: (i) Rüdisüli et al. [15] and (ii) Verma et al. [25]

The distributions of equivalent bubble diameters calculated by the face-masking algorithm from simulations are shown in Figure 6- 6 as function of distance from distributor. This distribution highlights the complex behavior of bubbles. In general, bubble size increases with bed height. However, in Figure 6- 6 (a & b), large bubbles can be found next to the distributor height. This is due to the coalescing of small bubbles next to entrance height. This highlights bubbles above a certain height from the distributor should not be accounted for analysis. Note such entrance effect was not observed for the bubble size distribution shown in Figure 6- 4 for 2-D simulation. It is true that there is no tangential motion of bubbles in 2-D which may hinder bubbles to coalesce next to the distributor height. Overall, this indicates a limitation of 2-D bubble dynamics when applied to a 3-D fluidized bed modeling.

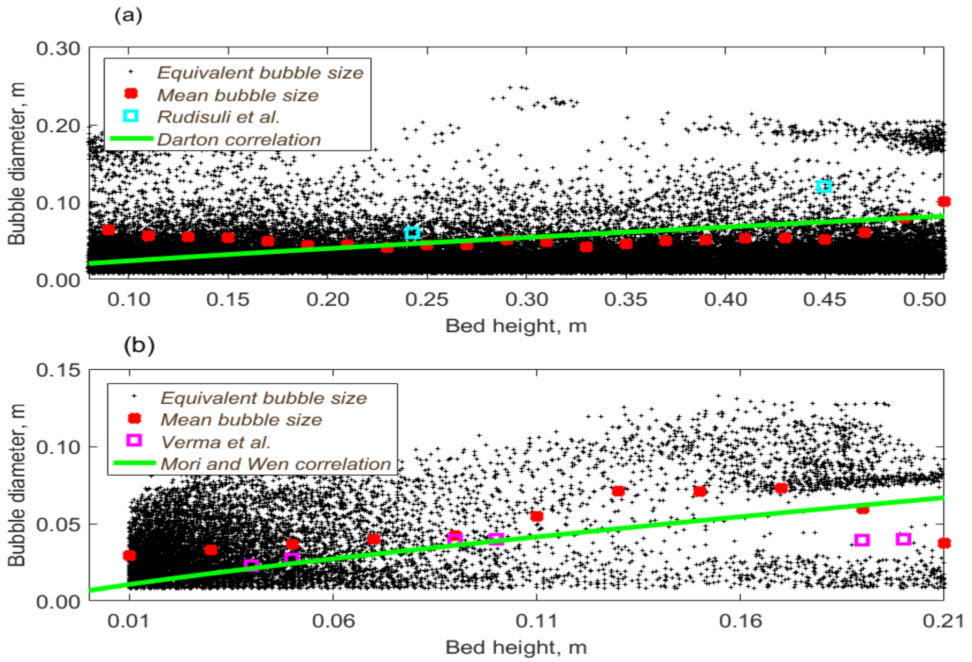

Figure 6- 6. Distribution of equivalent bubble diameters and comparison of mean bubble diameters obtained from 3-D simulations with experiments [15, 25] and semi-empirical correlation; (a) $d_p = 289$ µm, (b) $d_p = 1000$ µm.

Moreover, in Figure 6- 6 (a), about 80% of the bubbles detected using the 3-D algorithm are small (<0.03 m) and these small bubbles are seen throughout the fluidized bed. This observation is consistent with Rüdisüli et al. [15]. For large particle fluidized bed simulation (Figure 6- 6 (b)), most of the small bubbles are detected in the lower region of the fluidized bed. Note this simulation is performed with large particle (Geldart-D) and bubbles in large Geldart-D particles bed coalesce rapidly and grow to large size [60].

The volume-averaged bubble diameters computed from simulations are compared with experimental [15, 25] measurements (Figure 6- 6). It is observed that numerical predictions coincide reasonably well with experimental measurements. In addition, two semi-empirical correlations – Darton [56] for Geldart-B particles and Mori and Wen [55] Geldart-D particles are used to calculate the mean bubble size to compare with the mean bubble size determined from simulations. Practically, semi-empirical and numerical predictions agree quite well for both cases.

Figure 6- 7 shows the axial bubble rise velocity distributions obtained from numerical simulations. The scatter behavior of axial bubble rise velocity is also consistent with experimental observations [15, 25]. In Figure 6- 7 (a), both numerical estimation and experimental measurement of the average axial bubble rise velocity shows small variation throughout the solid bed height. However, for large particle bed, the average axial bubble rise velocity increases with bed height, as shown Figure 6- 7 (b). Werther [57] semi-empirical correlation is used to calculate the average axial bubble rise velocity and compared with numerical results. There is good agreement among numerical, experimental and semi-empirical prediction of the average axial bubble rise velocity. Note that the algorithm has selected only bubbles that are positively identified in two consecutive time frames, resulting in a relatively small fraction of the overall number of bubbles for velocity computation.

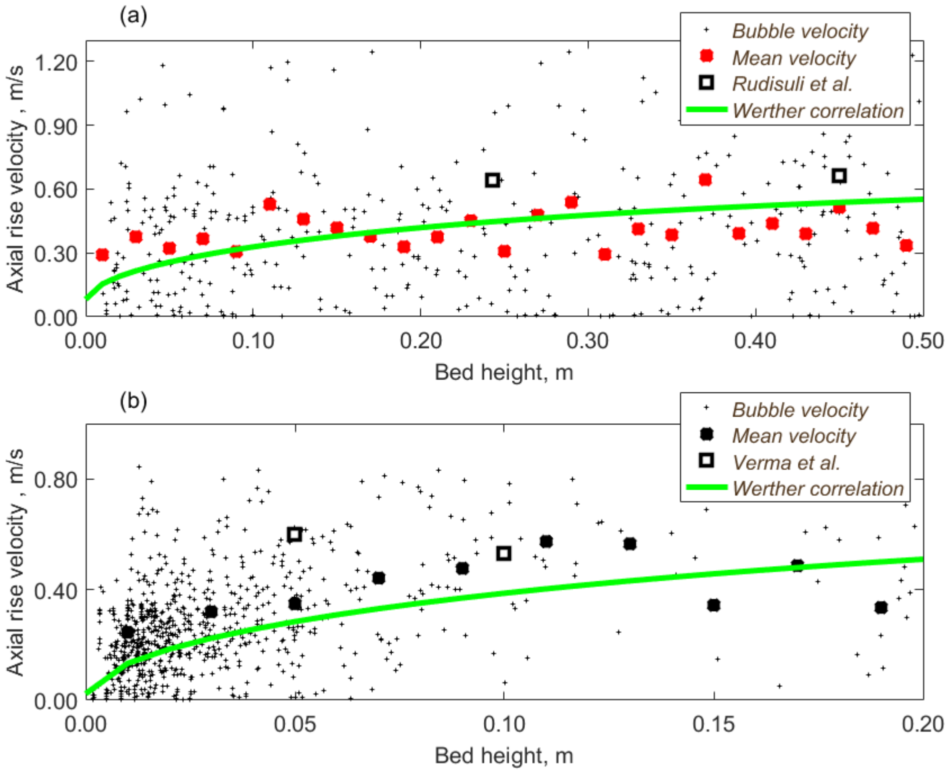

Figure 6- 7. Axial bubble rise velocity distribution and comparison of mean axial rise velocity obtained from 3-D simulations with experiments [15, 25] and semi-empirical correlation; (a) d_p = 289 µm, (b) d_p = 1000 µm.

6.5.3 Validation based on Geldart's [40] experiment (pilot-scale)

Figure 6- 8 shows the equivalent bubble size and axial bubble rise velocity distribution computed from numerical simulation applying the face-masking algorithm. Both the average bubble diameter and axial rise velocity results from numerical simulation show good agreement with experimental measurement [40] and semi-empirical correlation predictions.

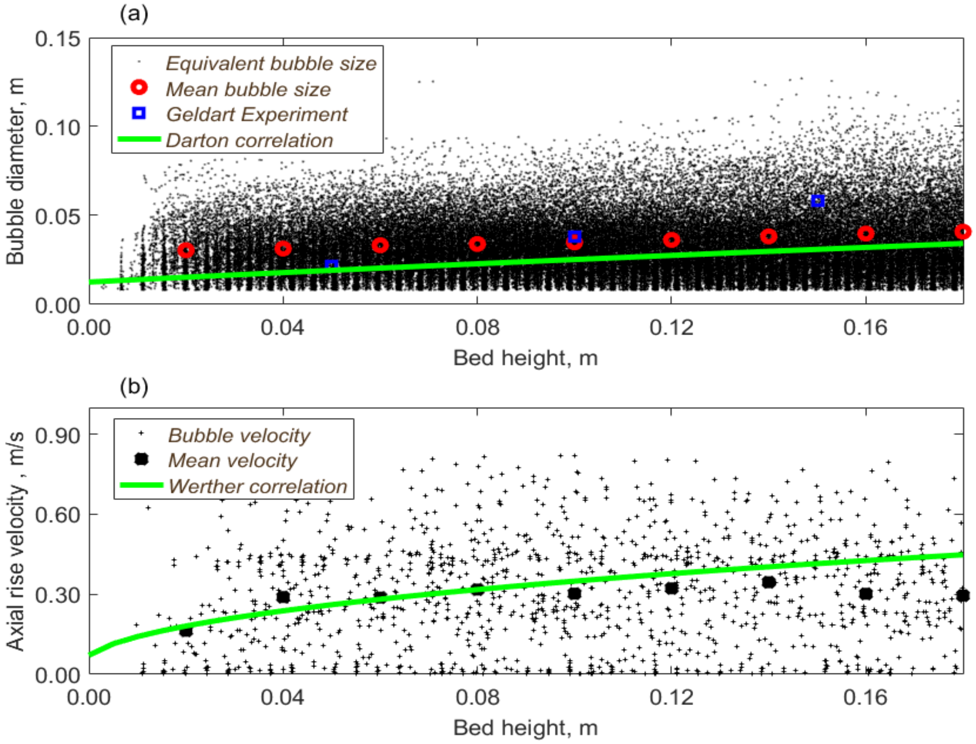

Figure 6- 8. Equivalent bubble diameter (a) and axial bubble rise velocity (b) distribution obtained from 3-D simulations and comparison with experiment [40] and semi-empirical correlation.

Bubble aspect ratio (defined in methodology section) for 3-D simulations is shown in Figure 6- 9 (a). Elongated bubbles are indicated by higher aspect ratio whereas flattened bubbles are indicated by a lower aspect ratio. The AR varied quite substantially, with 95% of computed values falling between 0.11 and 2.16. Accounting for both AR_x and AR_y, the mean is 0.7, indicating that, on average, bubbles are approximately hemispherical. The wide distribution of values of bubble aspect ratios indicates the diversity of bubble shapes detected in the bed. Thus, the face masking algorithm is successfully identifying all shapes of bubble.

Figure 6- 9 (b) represents the average bubble lateral velocity as function of bed height. A relatively slower motion is accounted along lateral distance. On average, lateral bubble motion is close to 0 m/s, but can be either positive or negative, as expected. At the base of the reactor, it is apparent that bubbles are flowing toward the axis.

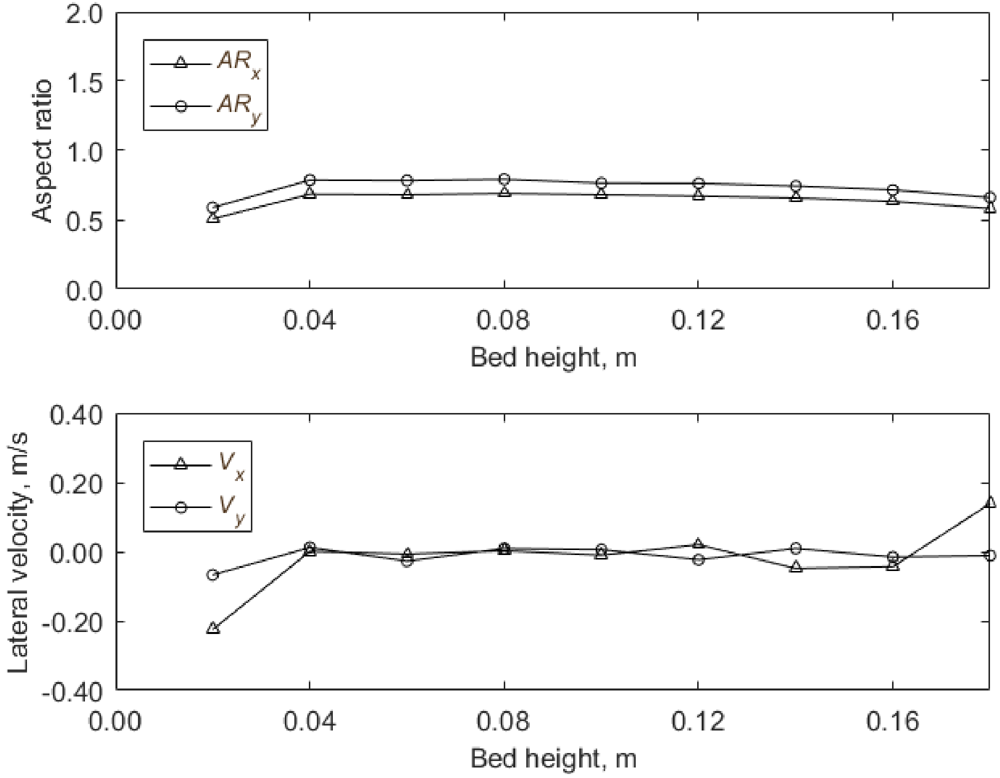

Figure 6- 9. Average aspect ratios of bubble diameters (a) and lateral bubble velocities (b) obtained from 3-D simulations (pilot-scale fluidized bed. The CDF was done in cylindrical coordinates, but the representation here is in Cartesian coordinates.

6.5.4 Observed bubbling phenomena

Over the past 50 years, numerous studies of bubbling phenomena have shown that bubbles tend to follow certain trends. Here we compare trends observed with the bubbles found by the face-mask algorithm with expected behavior.

Comparing the bubble size distribution from 2-D study (Figure 6- 4) with 3-D studies shown in Figure 6- 6 (a) and Figure 6- 8 (a), it is apparent that the number density of bubbles observed in 3-D simulations is significantly higher than that observed in 2-D case. Bakshi et al. [38] also reported a similar characteristic between 2-D and 3-D bubble dynamics. This is, of course, due to the fact that the 3-D simulations allow for a depth of view not possible in 2-D simulations. Similarly, 3-D simulations capture 3-D flow phenomena; many bubbles do exhibit a swirling motion as they rise (Figure 6- 9), something that cannot be observed or even predicted in 2-D simulations.

The experimental studies used to compare with numerical (3-D) simulations shows differences in bed diameters, depths, particle sizes and fluidization velocities (Table 6- 1 and Table 6- 2). For instance, Rüdisüli et al. [15] used a column diameter which is smaller than half of column diameter used Geldart's experiment [40]. A similar size Geldart-B particle is used in both simulations but the mean bubble diameters (Figure 6- 6 (a)) are significantly smaller in pilot-scale simulation for Geldart experiment than the corresponding mean values (Figure 6- 8 (a)) in lab-scale simulation of Rüdisüli et al. experiment [15]. In addition to fluidization velocity effect, wall effects are expected to play a stronger role in the smaller bed. Large size bed has little or no wall effects and consequently, reduced slugging effects [61]. Also, the axial bubble rise velocity follows the similar characteristics – the average bubble rise velocity for pilot-scale simulation is slightly lower than the corresponding lab-scale simulation results (Figure 6- 7). This is because bubble velocity is proportional to the square root of bubble diameter [57].

Besides, bed depth plays critical role in fluidization dynamics. Static bed height for pilot-scale simulation is less than half of the corresponding static bed height used for the simulation of Rüdisüli et al. experiment [15]. The bubble size distribution shown in Figure 6- 6 (a) and Figure 6- 8 (a) depicts the bed height effect on bubble diameter. It is well-known that, in a shallow bed, bubbles do not have sufficient fully develop on their way to the bed surface. Similarly, in a deep bed, a bubble expands more in the lateral direction and has an increased tendency to coalesce with surrounding bubbles. Moreover, a higher pressure head due to the weight of the particle bed in the deeper bed may force the bubbles to have a flatter shape that may increase slugging tendency of fluidization [1].

Furthermore, fluidization dynamics depends largely on particle size. Geldart-B particles are used in numerical simulation results shown in Figure 6- 6 (a), Figure 6- 7 (a) and Figure 6- 8 whereas results shown in Figure 6- 6 (b) and Figure 6- 7 (b) are for Geldart-D particles. A large number of small size bubbles are observed in entire solid beds of Geldart-B particles but majority of the small bubbles is seen at the lower part of the bed and larger bubbles are encountered at the upper part of bed for Geldart-D particles. This characteristic is expected for large Geldart-D particles fluidized beds [60].

Overall, such random distribution of bubble sizes and velocities throughout the fluidized bed reaffirms the general behavior of fluidization dynamics that evolve from the physical properties of particles as well as geometry. In general, bubbles rise through the bed, interact with each other and coalesce so that the average bubble size increases and also rises faster with distance above the distributor. All of these well-known phenomena are also observed in numerical simulations conducted in this present study. This further corroborates the validity of the numerical simulations conducted using the TFM and the algorithm developed for 3-D simulation data analysis.

6.5.5 Efficiency of the algorithm

The face-masking algorithm developed in this study is capable of reading and processing large quantities of the whole-field void data automatically. Table 6- 6 shows the breakdown of average computational cost of bubble dynamics for 1700 time-frames using Intel Core i7 2.6 GHz processor. Note all computation tasks for bubble dynamics are completed in serial (non-parallel) mode in MATLAB. The computation cost for 2-D simulation is insignificant compared to any 3-D bubble dynamic analysis. For shallow bed height, the computation time for 3-D bubble dynamics is less than 30 s per time-frame, which indicates the superior applicability of the 3-D algorithm. However, the computation cost for bubble dynamics analysis increases by one order of magnitude for deep bed (3-D) compared any shallow bed (Table 6- 6). In deep bed, there is large number of bubbles (Figure 6- 6 (a)) that adds the increased time for detection.

Table 6- 6. Computation time for bubble property determination

Type	Static bed height, m	Number of cells in matrix ***M***	Time for bubble identification per frame, s	Time for bubble properties computation per frame, s	Total time per frame, s
Lab-scale 2-D [39]	0.38	10000	0.3	0.06	0.36
Lab-scale 3-D [25]	0.20	30720	15	0.10	15.1
Pilot-scale 3-D [40]	0.20	61250	24	0.20	24.2
Lab-scale 3-D [15]	0.50	46920	290	0.40	290.4

Although a longer computational time is accounted for bubble dynamics analysis for deep bed, the total time required for bubble dynamics is still insignificant compared to the total simulation cost for the 3-D cases. Note that the computation cost can be further reduced upto one order of magnitude using parallel-looped vectorized equations in MATLAB. While the algorithm could be further optimized, the insignifican comutation cost of 3-D simulation data is promising to apply the face-masking algorithm for large-scale indutrial fluidized bed simulations.

6.6 Conclusions

In this study, an algorithm defined as face-masking that processes the whole-field void fraction data from 3-D CFD simulations for computing 3-D bubble dynamics is developed. The face-masking algorithm identifies discrete bubbles based on the predefined void threshold, associates bubbles across successive frames and finally, evaluates bubble properties such as centroids, equivalent diameter, aspect ratio and velocity.

The face-masking algorithm is validated using measurements from lab-scale (pseudo-2-D and 3-D) and pilot-scale fluidized beds. Bubble diameters computed from numerical simulations shows increasing trend with the bed height, and the trend agrees well with experimental measurements [15, 25, 39, 40] as well as with semi-empirical correlations shown in Table 6- 5. Large number of small bubbles is observed throughout the dense bed of Geldart -B bubbling fluidized beds whereas significant amount of small bubbles is seen near the distributor for large Geldart -D fluidized bed. It is seen that 2-D bubble dynamics possesses significant limitations which should be carefully considered interpreting in case of 3-D design and scale-up. Also, bubbles show a non-uniform shape in 3-D bed. Bubble movement in lateral directions is slower compared to axial displacement. By recording the computation time for bubble dynamics for different cases, it is shown that the face-masking algorithm is efficient and cost effective for large-scale applications.

The extensive application of the face-masking algorithm described in this study for a range of bed geometries and particle properties provides a convenient, reliable basis for its application in large-scale fluidized bed modeling study. As an automatic method, this face-masking algorithm overcomes the excessive manual work of data post-processing and is able to process large amount of data. Even though this study is focused on evaluating bubble dynamics in gas-solid fluidized beds, the algorithm itself can be easily applied and extended for detecting bubbles, drops and clusters in other areas of 2-D and 3-D multiphase flows.

Acknowledgments

The authors would like to acknowledge the support from the California Energy Commission Grant 07-01-37 and ZERE Energy and Biofuels, Inc.

References

[1] W.-c. Yang, *Handbook of fluidization and fluid-particle systems*: CRC press, 2003.

[2] L. R. Glicksman, W. K. Lord, and M. Sakagami, "Bubble Properties in Large-Particle Fluidized-Beds," *Chemical Engineering Science,* vol. 42, pp. 479-491, 1987.

[3] R. Toomey and H. Johnstone, "Gaseous fluidization of solid particles," *Chemical Engineering Progress,* vol. 48, pp. 220-226, 1952.

[4] J. Walters and J. Davidson, "The initial motion of a gas bubble formed in an inviscid liquid Part 1. The two-dimensional bubble," *Journal of Fluid Mechanics,* vol. 12, pp. 408-416, 1962.

[5] P. N. Rowe, Partiridge, B.A., Cheney, A.G., Henwood, A.G., "The mechanism of solids mixing in fluidised beds," *Trans. Inst. Chem. Eng.,* vol. 43, pp. 271-286, 1965.

[6] P. N. Rowe and A. W. Nienow, "Particle mixing and segregation in gas fluidised beds. A review," *Powder Technology,* vol. 15, pp. 141-147, 1976/11/01 1976.

[7] J. Werther, "Convective solids transport in large diameter gas fluidized beds," *Powder Technology,* vol. 15, pp. 155-167, 1976.

[8] T. Litka and L. Glicksman, "The influence of particle mechanical properties on bubble characteristics and solid mixing in fluidized beds," *Powder Technology,* vol. 42, pp. 231-239, 1985.

[9] N. Kobayashi, R. Yamazaki, and S. Mori, "A study on the behavior of bubbles and solids in bubbling fluidized beds," *Powder Technology,* vol. 113, pp. 327-344, Dec 6 2000.

[10] O. Oke, P. Lettieri, P. Salatino, R. Solimene, and L. Mazzei, "Numerical simulations of lateral solid mixing in gas-fluidized beds," *Chemical Engineering Science,* vol. 120, pp. 117-129, 2014.

[11] H. Norouzi, N. Mostoufi, Z. Mansourpour, R. Sotudeh-Gharebagh, and J. Chaouki, "Characterization of solids mixing patterns in bubbling fluidized beds," *Chemical Engineering Research and Design,* vol. 89, pp. 817-826, 2011.

[12] C. Altantzis, R. Bates, and A. Ghoniem, "3D Eulerian modeling of thin rectangular gas–solid fluidized beds: estimation of the specularity coefficient and its effects on bubbling dynamics and circulation times," *Powder Technology,* vol. 270, pp. 256-270, 2015.

[13] M. Rüdisüli, T. J. Schildhauer, S. M. Biollaz, and J. R. van Ommen, "Bubble characterization in a fluidized bed by means of optical probes," *International Journal of Multiphase Flow,* vol. 41, pp. 56-67, 2012.

[14] C. Sobrino, A. Acosta-Iborra, D. Santana, and M. De Vega, "Bubble characteristics in a bubbling fluidized bed with a rotating distributor," *International Journal of Multiphase Flow,* vol. 35, pp. 970-976, 2009.

[15] M. Rüdisüli, T. J. Schildhauer, S. M. Biollaz, A. Wokaun, and J. R. van Ommen, "Comparison of bubble growth obtained from pressure fluctuation measurements to optical probing and literature correlations," *Chemical Engineering Science,* vol. 74, pp. 266-275, 2012.

[16] M. Liu, Y. Zhang, H. Bi, J. R. Grace, and Y. Zhu, "Non-intrusive determination of bubble size in a gas–solid fluidized bed: an evaluation," *Chemical Engineering Science,* vol. 65, pp. 3485-3493, 2010.

[17] A. Acosta-Iborra, C. Sobrino, F. Hernández-Jiménez, and M. De Vega, "Experimental and computational study on the bubble behavior in a 3-D fluidized bed," *Chemical Engineering Science,* vol. 66, pp. 3499-3512, 2011.

[18] J. Werther, "Influence of the bed diameter on the hydrodynamics of gas fluidized beds," in *AIChE Symp. Ser*, 1974, pp. 53-62.

[19] C. Van Lare, H. Piepers, J. Schoonderbeek, and D. Thoenes, "Investigation on bubble characteristics in a gas fluidized bed," *Chemical Engineering Science,* vol. 52, pp. 829-841, 1997.

[20] L. Shen, F. Johnsson, and B. Leckner, "Digital image analysis of hydrodynamics two-dimensional bubbling fluidized beds," *Chemical Engineering Science,* vol. 59, pp. 2607-2617, 2004.

[21] A. Busciglio, G. Vella, G. Micale, and L. Rizzuti, "Analysis of the bubbling behaviour of 2D gas solid fluidized beds: Part II. Comparison between experiments and numerical simulations via digital image analysis technique," *Chemical Engineering Journal,* vol. 148, pp. 145-163, 2009.

[22] S. Movahedirad, A. Molaei Dehkordi, M. Banaei, N. Deen, M. van Sint Annaland, and J. Kuipers, "Bubble size distribution in two-dimensional gas–solid fluidized beds," *Industrial & Engineering Chemistry Research,* vol. 51, pp. 6571-6579, 2012.

[23] C. Rautenbach, R. F. Mudde, X. Yang, M. C. Melaaen, and B. Halvorsen, "A comparative study between electrical capacitance tomography and time-resolved X-ray tomography," *Flow Measurement and Instrumentation,* vol. 30, pp. 34-44, 2013.

[24] I. Hulme and A. Kantzas, "Determination of bubble diameter and axial velocity for a polyethylene fluidized bed using X-ray fluoroscopy," *Powder Technology,* vol. 147, pp. 20-33, 2004.

[25] V. Verma, J. T. Padding, N. G. Deen, J. Kuipers, F. Barthel, M. Bieberle, M. Wagner, and U. Hampel, "Bubble dynamics in a 3- D gas–solid fluidized bed using ultrafast electron beam X- ray tomography and two- fluid model," *Aiche Journal,* vol. 60, pp. 1632-1644, 2014.

[26] G. Brouwer, E. Wagner, J. Van Ommen, and R. Mudde, "Effects of pressure and fines content on bubble diameter in a fluidized bed studied using fast X-ray tomography," *Chemical Engineering Journal,* vol. 207, pp. 711-717, 2012.

[27] C. M. Boyce, D. J. Holland, S. A. Scott, and J. S. Dennis, "Adapting data processing to compare model and experiment accurately: a discrete element model and magnetic resonance measurements of a 3d cylindrical fluidized bed," *Industrial & Engineering Chemistry Research,* vol. 52, pp. 18085-18094, 2013.

[28] A. Bakshi, C. Altantzis, R. B. Bates, and A. F. Ghoniem, "Eulerian-Eulerian simulation of dense solid-gas cylindrical fluidized beds: Impact of wall boundary condition and drag model on fluidization," *Powder Technology,* vol. 277, pp. 47-62, Jun 2015.

[29] D. Gidaspow, Jung, J., Singh, R. K., "Hydrodynamics of fluidization using kinetic theory: an emerging paradigm," *Powder Technology,* vol. 148, pp. 123–141, 2004.

[30] D. Gidaspow, R. Bezburuah, and J. Ding, "Hydrodynamics of circulating fluidized beds: kinetic theory approach," Illinois Inst. of Tech., Chicago, IL (United States). Dept. of Chemical Engineering1991.

[31] J. A. M. Kuipers, van Swaaij, W.P.M., "Computational fluid dynamics applied to chemical reaction engineering," *Advances in Chemical Engineering,* vol. 24, 1998.

[32] Y. Lu, J. Huang, and P. Zheng, "A CFD–DEM study of bubble dynamics in fluidized bed using flood fill method," *Chemical Engineering Journal,* vol. 274, pp. 123-131, 2015.

[33] T. W. Asegehegn, M. Schreiber, and H. J. Krautz, "Influence of two-and three-dimensional simulations on bubble behavior in gas–solid fluidized beds with and without immersed horizontal tubes," *Powder Technology,* vol. 219, pp. 9-19, 2012.

[34] L. Cammarata, P. Lettieri, G. D. M. Micale, and D. Colman, "2D and 3D CFD Simulations of Bubbling Fluidized Beds Using Eulerian-Eulerian Models," *International Journal of Chemical Reactor Engineering,* vol. 1, 2003.

[35] N. Xie, F. Battaglia, and S. Pannala, "Effects of using two-versus three-dimensional computational modeling of fluidized beds: Part I, hydrodynamics," *Powder Technology,* vol. 182, pp. 1-13, 2008.

[36] A. Bakshi, C. Altantzis, and A. F. Ghoniem, "Towards accurate three-dimensional simulation of dense multi-phase flows using cylindrical coordinates," *Powder Technology,* vol. 264, pp. 242-255, 2014.

[37] C. Sobrino, A. Acosta-Iborra, M. A. Izquierdo-Barrientos, and M. de Vega, "Three-dimensional two-fluid modeling of a cylindrical fluidized bed and validation of the Maximum Entropy method to determine bubble properties," *Chemical Engineering Journal,* vol. 262, pp. 628-639, 2015.

[38] A. Bakshi, C. Altantzis, R. B. Bates, and A. F. Ghoniem, "Multiphase-flow Statistics using 3D Detection and Tracking Algorithm (MS3DATA): Methodology and application to large-scale fluidized beds," *Chemical Engineering Journal,* vol. 293, pp. 355-364, Jun 1 2016.

[39] I. C. Velarde, F. Gallucci, and M. van Sint Annaland, "Development of an endoscopic-laser PIV/DIA technique for high-temperature gas–solid fluidized beds," *Chemical Engineering Science,* vol. 143, pp. 351-363, 2016.

[40] D. Geldart, "The expansion of bubbling fluidised beds," *Powder Technology,* vol. 1, pp. 355-368, 1968.

[41] C. C. Pain, Mansoorzadeh, S., de Oliveira, C.R.E., "A study of bubbling and slugging fluidised beds using the two-fluid granular temperature model," *International Journal of Multiphase Flow,* vol. 27, pp. 527–551, 2001.

[42] D. G. Schaeffer, "Instability in the evolution equations describing incompressible granular flow," *Journal of differential equations,* vol. 66, pp. 19-50, 1987.

[43] D. Gidaspow, *Multiphase Flow and Fluidization: Continuum and Kinetic Theory Descriptions*. San Diego: Academic Press, 1994.

[44] M. Syamlal, O'Brien, T.J., "Computer simulation of bubbles in a fluidized bed," *A.I.Ch.E. Symposium Series,* vol. 85, pp. 22-31, 1989.

[45] C. Y. Wen and Y. H. Yu, "Mechanics of fluidization," *Chemical Engineering Progress Symposium Series,* vol. 62, pp. 100-111, 1966.

[46] M. Syamlal, Rogers, W., O'Brien, T. J., "MFIX Documentation, Theory Guide1," N. T. I. Service, Ed., ed. Springfield, 1993.

[47] P. C. Johnson and R. Jackson, "Frictional–collisional constitutive relations for granular materials, with application to plane shearing," *Journal of Fluid Mechanics,* vol. 176, pp. 67-93, 1987.

[48] C. Loha, H. Chattopadhyay, and P. K. Chatterjee, "Assessment of drag models in simulating bubbling fluidized bed hydrodynamics," *Chemical Engineering Science,* vol. 75, pp. 400-407, 2012.

[49] S. Benyahia, M. Syamlal, and T. J. O'Brien, "Study of the ability of multiphase continuum models to predict core- annulus flow," *Aiche Journal,* vol. 53, pp. 2549-2568, 2007.

[50] M. Syamlal and T. J. O'Brien, "Fluid dynamic simulation of O-3 decomposition in a bubbling fluidized bed," *Aiche Journal,* vol. 49, pp. 2793-2801, Nov 2003.

[51] C. Loha, H. Chattopadhyay, and P. K. Chatterjee, "Effect of coefficient of restitution in Euler–Euler CFD simulation of fluidized-bed hydrodynamics," *Particuology,* vol. 15, pp. 170-177, 2014.

[52] J. Ding and D. Gidaspow, "A bubbling fluidization model using kinetic theory of granular flow," *Aiche Journal,* vol. 36, pp. 523-538, 1990.

[53] J. Kuipers, K. Van Duin, F. Van Beckum, and W. Van Swaaij, "Computer simulation of the hydrodynamics of a two-dimensional gas-fluidized bed," *Computers & Chemical Engineering,* vol. 17, pp. 839-858, 1993.

[54] D. Hughes-Hallett, A. Iovita, and O. K. Bretscher, *Calculus: single and multivariable* vol. 3: Wiley New York, NY, 1998.

[55] S. Mori and C. Y. Wen, "Estimation of Bubble Diameter in Gaseous Fluidized-Beds," *Aiche Journal,* vol. 21, pp. 109-115, 1975.

[56] R. C. Darton, La Nauze, R.D., Davidson, J. F., Harrison, D., "Bubble growth due to coalescence in fluidized beds," *Trans IChemE,* vol. 55, p. 274, 1977.

[57] J. Werther, Ed., *Hydrodynamics and mass transfer between the bubble and emulsion phases in fluidized beds of sand and cracking catalyst* (Fluidization. Engineering Foundation. New York, 1984, p.^pp. Pages.

[58] K. Godard and J. Richardson, "Bubble velocities and bed expansions in freely bubbling fluidised beds," *Chemical Engineering Science,* vol. 24, pp. 663-670, 1969.

[59] D. Kunii and O. Levenspiel, "CHAPTER 5 - Bubbles in Dense Beds," in *Fluidization Engineering (Second Edition)*, D. K. Levenspiel, Ed., ed Boston: Butterworth-Heinemann, 1991, pp. 115-135.

[60] D. Kunii and O. Levenspiel, *Fluidization engineering*: Elsevier, 2013.

[61] S. Karimipour and T. Pugsley, "A critical evaluation of literature correlations for predicting bubble size and velocity in gas–solid fluidized beds," *Powder Technology,* vol. 205, pp. 1-14, 2011.

CHAPTER 7

CFD Hydrodynamic model of the semi continuous reactors

Abstract

CFD simulations of fluidized bed of air and fuel reactors with 300 µm of Geldart B particle have been carried out with the standard TFM approach, with and without internal horizontal baffles in beds. Fluidized bed without internal baffles shows large bubbles and results in poor mixing, whereas fluidized bed with internal baffles have relatively small bubbles with good mixing of gas and solid. Due to the smaller bubble size, baffled fluidized bed expands more than that of unbaffled bed. Pressure fluctuation in the air reactors is higher than fuel reactors as air reactors operate at much higher velocity than fuel reactors. There is no elutriation of particles at the reactor exit after the simulation reach a quasi-steady state.

7.1 Introduction

Fluidized beds are widely used in the process industries including chemical-looping combustion (CLC) process where the oxygen carrier serves as the bed medium. A consensus has been established to use a bubbling fluidized bed for the fuel reactor and a circulating fluidized bed for the air reactor [1, 2]. Despite their widespread application in the process industries the design of fluidized bed reactors are still very challenging. Complex gas–solid hydrodynamics inherent to these reactors is closely coupled to heat transfer and reaction kinetics. Because of this intimate coupling leading to a highly non-linear system, the use of empirical models for scale up is challenging.

First-principles based computational fluid dynamics (CFD) has become an emerging and effective tool to explore the complex hydrodynamics behavior in gas-solid fluidized bed. CFD offers the advantage that it can provide more insight into the physical origin underlying the various phenomena transpiring in fluidized beds, and can be used for scale-up, design, or optimization [3-5]. Different approaches have been taken in early attempts to apply CFD methods including direct numerical simulation (DNS), discrete particle method (DPM) and two-fluid method (TFM) to explore the phenomena prevailing in gas-fluidized beds [6]. DNS and DPM are limited to a relatively small scale application due to their high computational costs. Amongst these methods the TFM based on adaptations of the kinetic theory of gases is computationally less expensive. The general idea in formulating the TFM model is to treat each phase as an interpenetrating continuum, and therefore to construct integral balances of continuity, momentum and energy for both phases, with appropriate boundary conditions and leap conditions for phase interfaces. TFM applies averaging techniques and assumptions to obtain momentum balance for the solids phase(s) since the resultant continuum approximation for the solid phase has no equation of state and lacks variables such as viscosity and normal stress [7]. The TFM equations are coupled with constitutive relations derived from data or analysis of nearly homogeneous systems [8]. The interphase drag force between gas and solid phases is modeled by various empirical correlations reported in the literature, including those of Syamlal and O' Brien (1989) [9], Gidaspow (1994) [8], and Wen and Yu (1966) [10].

Traditionally, gas-solids friction coefficients have been expressed using semi-empirical correlations such as the well-known Wen-Yu and Ergun correlations [10], but recently, similar expressions were fitted to simulation data obtained using physical models based on first principles. These recently derived drag models were obtained by finely resolving the fluid flow around the particles, and the friction or drag can be obtained by integrating the fluid viscous stress acting on the particles according to Newton's law of viscosity. Such models are known as filtered drag correlations [11-14].

In this study we used the TFM to simulate the prototype fluidized bed of air and fuel reactor of ZERE with the filtered-drag model proposed by [14].

7.2 ZERE prototype reactors configuration

Two fluidized bed reactors will operate in parallel. At any moment in time, one operates in air mode, and one operates in fuel mode, and after 10 minutes in operation the reactors switch their operation mode. So, the operational cycle time in each mode (define cycle time) is 10 minutes. In either case, the reactor temperature is nominally 800 °C.

Each reactor will be filled with 228 kg of particles with diameter 300 μm, made with 30% copper loaded on porous alumina support. Both reactors have identical configuration, and are fabricated from 18-inch (ID = 0.42 m) Schedule 40 steel pipe.

These reactors are nominally designed to operate in a bubbling regime, with $\frac{U_0}{u_{mf}} \approx 36$ when the reactor is in air mode, and $\frac{U_0}{u_{mf}} \approx 9$ when the reactor is in fuel mode. Here U_0 and u_{mf} are the inlet and the minimum fluidization gas velocities respectively. The inside of the reactor will be baffled to break-up bubbles, thereby ensuring a high conversion of methane in the fuel during fuel mode, and reducing particle entrainment during oxidation mode. Two baffles are inserted in each bed to break apart bubbles, which will increase the gas-solid contact by promoting mass transfer, and, thereby increase fuel conversion. The baffle is made from a $^3/_8$-inch steel plate with numerous 2.0-cm holes through it, on a square pattern and center-to-center spacing is 3.1 cm. The baffle is designed to keep about 30% of the baffle cross sectional area open to gas flow.

At the distributor plate, there are 12 tuyeres for flow of fuel gas during fuel mode and air during air mode. In this novel design, gas flows through the four tuyeres nearest the center of the distributor during fuel mode, and is distributed to all 12 tuyeres in air mode.

7.3 Simulated reactors configuration

The majority of numerical simulations of pilot or large scale fluidized beds are carried out with a two-dimensional flow assumption in which a cut-plane along the axis of the cylindrical column is used. Combinations of the aforementioned simplifications can be found in many simulations, for example 2D cold flow simulations of riser flow in FCC process [15]. In our 2-D model, the volumetric flow rate of inlet gas is taken to be a constant value equal to the average of inlet and outlet volumetric flow rate. For example, the volumetric flow rate of inlet fuel gas for the 100 kW fuel reactors is $0.016\frac{m^3}{s}$ but after oxidation of the fuel, the volume flow rate increases to $0.036\frac{m^3}{s}$. In simulation we have used the average volumetric flow rate of $0.026\frac{m^3}{s}$ as a constant flow rate throughout the reactor during fuel mode. Similarly, the average volumetric flow rate for air reactor of $0.097\frac{m^3}{s}$ is used.

The baffles were modeled as impermeable surfaces where gas and solids can flow through 2-cm openings from the holes. About 33% of the baffle cross sectional area is opened to gas flow. There are seven 2-cm openings on each baffle.

ZERE gas distributors are specially designed for the fluidized bed. However, in the fuel mode of prototype design, fuel gas flows only through the center 4 tuyeres. Gas flowing through the tuyeres will be at a high velocity, prior to decelerating in the bed. To accommodate for that in the simulation, a single central jet is introduced in the fuel reactor by maintaining inlet velocity with the aforementioned jet velocity emitting from the tuyeres. For instance, gas flows through either of the four fuel tuyeres having 32 jets of $5.0\ mm$ size. All of these jets are altogether considered as a single central jet for the fuel reactor simulation. The (single) jet opening in the simulation is calculated as $32 \times 5\ mm = 160\ mm$ for fuel mode.

7.4 Simulation setup

7.4.1 Geometry and discretization

The dimensions of the simulated beds are shown in Table 7- 1. Two dimensional (2D) Cartesian coordinates were used with uniform structured grid cells. There was a 63×487 ($axial \times vertical$) mesh resolution, corresponding to a computational mesh with $\partial x = \partial y = 6.7\ mm$ in the 2-D geometry. From our past experience and literature studies, we believe that this grid resolution will give grid independent results.

7.4.2 Numerical model

The interpenetrating two-fluid model (TFM) [8, 16-19] based on the Eulerian-Eulerian flow field was applied to simulate the gas-solid hydrodynamics of fluidized bed. This approach has been confirmed to give adequate representations of the hydrodynamics of fluidized bed units [4, 20, 21]. In order to consider the effect of unresolved sub-grid scale heterogeneous structures on the inter-phase drag force, we used the filtered drag correlation proposed by Milioli et al. which is obtained from very fine grid simulation [14].

7.4.3 Flow solver and solver settings

The National Energy Technology Laboratory's (NETL's) computational fluid dynamics (CFD) open-source code MFIX [22] was used as flow solver. The modified phase coupled SIMPLE scheme, which uses a solids volume fraction correction equation instead of a solids pressure correction equation, was used for pressure–velocity coupling.

The second-order higher accuracy SuperBee schemes was used for the spatial discretization of all remaining equations. A combination of point successive under relaxation and biconjugate gradient stabilized method (BiCGSTAB) method were used for the linear equation solver. A maximum residual at convergence of 10^{-03} was used to improve the accuracy of the continuity and momentum equations solution. First order implicit temporal discretization was used to ensure stable and accurate solutions. It has been shown that 2^{nd} order time discretization is necessary for accurate solution of fast-moving riser flows with the TFM [23], but this is not the case for dense bubbling beds where the vast majority of the bed moves very slowly. An automatic time-step adjustment with a maximum and minimum time-step of 4×10^{-03} s and 10^{-07} s respectively was specified.

7.4.4 Initial and boundary conditions

The standard initial conditions were used to describe the 2D simulations. Initially, bed height was $1.6\ m$ with 50% void fraction. Initial bed pressure drop was $15\ kPa$, which is the hydrostatic bed pressure. It was assumed that initially bed was under the minimum fluidization condition with the minimum fluidization velocities of $2.4 \frac{cm}{s}$ for air and $2.8 \frac{cm}{s}$ for fuel reactors, respectively.

Boundary conditions (BC) were specified over flow planes/2D surfaces that are normal to one of the coordinate directions and coincide with a face of the scalar control-volume. A constant gas flow rate was specified at the distributor of the fluidized bed as inlet boundary and a constant pressure at the top of the domain was used as outflow boundary. The wall boundaries were specified as partial slip with no-slip for gas and free-slip for solid phase. As indicated above, baffles were specified as internal surfaces, and specified as impermeable for gas and solids. Internal surfaces acted as free-slip walls in stress computations.

7.4.5 Simulation summary

A summary of the physical properties and simulation parameters are given in Table 7- 1.

Table 7- 1. Physical properties of simulation parameters

	Designed Prototype	Simulated reactors	
		Air reactor	Fuel reactor
Particle diameter, µm	300~500	300	300
Particle density, kg/m^3	1964	1964	1964
Gas density, kg/m^3	0.31~0.34	0.34	0.31
Gas viscosity, kg/m/s	(37 ~44) x 10^{-6}	44 x 10^{-6}	37 x 10^{-6}
Gas velocity, cm/s	11~87	67.5	18
Minimum fluidization velocity, cm/s	2.40 ~ 2.80	2.40	2.80
Maximum packing limit		0.58	0.58
Particle–particle restitution		0.90	0.90
Angle of internal friction		30°	30°

Bed diameter, m	0.42	0.42	0.42
Static bed height, m	1.60	1.60	1.60
1st baffle position, m	0.70	0.70	0.70
2nd baffle position, m	1.40	1.40	1.40
Reactor height, m	3.26	3.26	3.26
Temperature, K	1073	1073	1073

7.5 Results and discussions

7.5.1 Bubble size and frequency

The hydrodynamics of a fluidized bed have a primary influence on bed characteristics such as solid and gas mixing, heat transfer to immersed surfaces and elutriation of particles from the bed. For beds operating in the bubbling regime, the bed hydrodynamics are largely governed by the number, size and motion of bubbles passing through the bed and erupting on the surface. Contours of the void fraction observed in the 2D fluidized bed at one instant are shown in Figure 7- 1, Figure 7- 2 and Figure 7- 3. The shapes of the bubbles are far from the spherical or ellipsoidal forms observed in small particle beds. However, similar bubble shapes were observed in the two-dimensional bed [24].

The influence of complex flow structures on reactor performance is complicated. Internal baffles may be introduced to modify the gas-solid flow structures, in an effort to form a more uniform and active gas-solid flow to enhance heat and mass transfer so as to improve the overall performance of fluidized bed reactors, especially to facilitate scale-up. Figure 7- 1 and Figure 7- 2 illustrate the effect of internal baffles on bed hydrodynamics, especially on bubbles, clusters, and non-uniform flow structures.

When a bed does not contain internals of any sort, the movement of bubbles in the bed is unrestricted. As bubbles rise, they gradually increase in size and tend to move horizontally toward the center of the bed. Much of the gas flow is ‘short-circuited’ through the bubbles, which greatly limits interaction between particles and gaseous reactants, and thus impact the conversion and selectivity of a chemical reaction, especially for the Group B particles at high superficial gas velocities (Figure 7- 1). It shows that the maximum bubble diameter appears to be as wide as the bed diameter, a phenomenon called “slugging”. Such large bubbles would violently shake the unit as tons of oxygen carrier splashed when they come out of the bed surface. In addition, mass transfer from such an enormous bubble would be so poor that it would significantly reduce the rate of reaction [25].

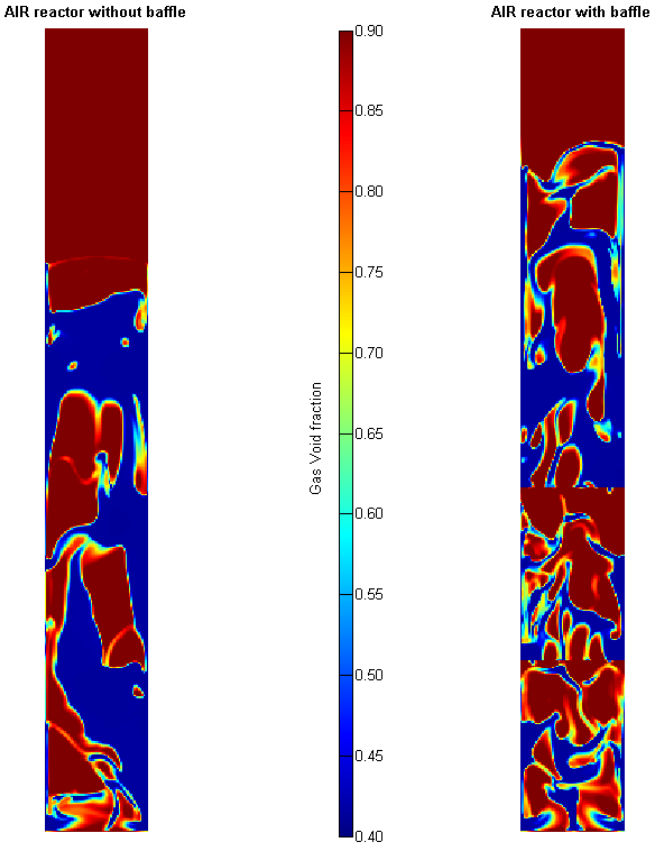

Figure 7- 1. Effect of baffles on bubble break-up in the **air reactor.** Contour of gas volume fraction at t= 6.0 s with uniform inlet gas velocity = **0.675 m/s**.

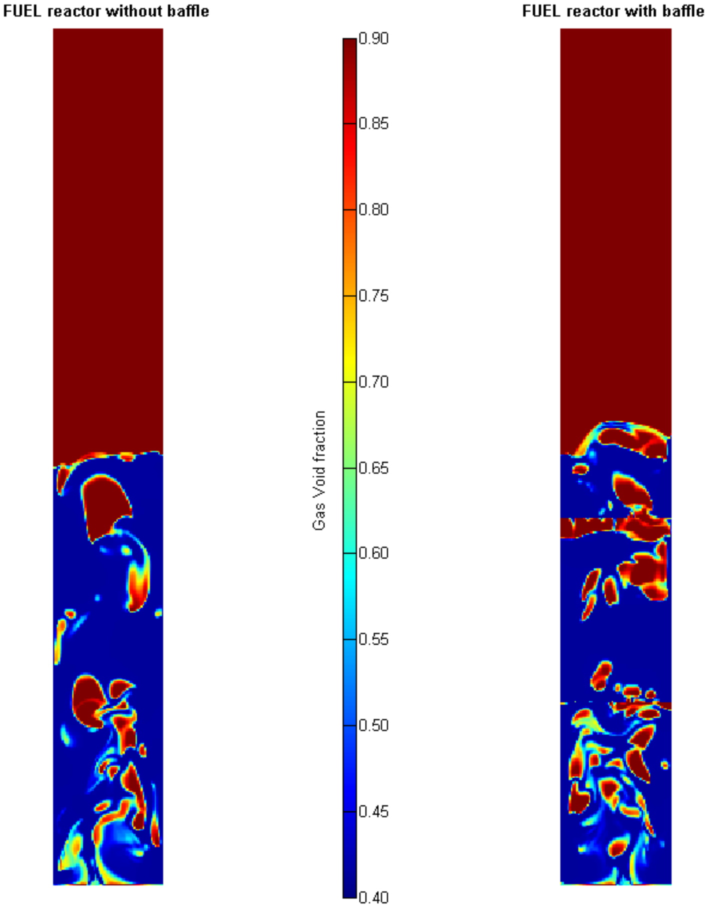

Figure 7- 2. Effect of baffles on bubble break-up in the **fuel reactor.** Contour of gas volume fraction at t= 6.0 s with uniform inlet gas velocity = **0.18 m/s**.

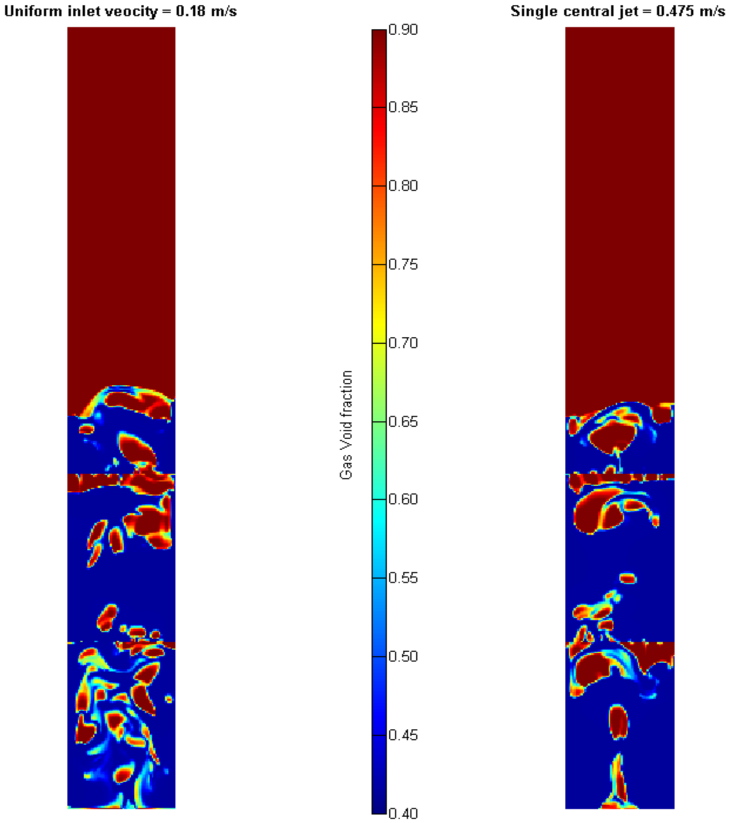

Figure 7- 3. Effect of inlet gas velocity condition in the **fuel reactor.** Contour of gas volume fraction at t= 6.0 s. In both cases, 33% open area in the baffle hole.

The performance of a fluidized bed reactor can be improved by decreasing the bubbles' size and renewing the bubbles surface for interchanging the gas between bubbles and the interstitial gas in the emulsion phase. Table 7- 2 shows quantitatively the effect of baffle insertion in the fluidized bed on bubble break-up (sample calculation has shown in the appendix). In all cases shown, baffles are effectively breaking large bubbles and reducing the size except in the case of jet flow effect. The number of bubbles becomes almost twice in case of baffled bed. However, when a high velocity central jet flow of gas is considered for fuel reactor instead of a uniform inlet gas velocity, bubble size is even larger than unbaffled bed (Figure 7- 3). It is to be noted here that the average bubble size in air reactor also appears to be doubled as compared to the fuel reactor. This is due to the high inlet gas velocity at air reactor.

Table 7- 2. Summary of bubbles

	Air reactor		Fuel reactor		
	W/O baffle	W/ baffle	W/O baffle	W/ baffle	Jet W/ baffle
Number of bubbles	23.0	41.0	16.0	34.0	23.0
Total area of bubbles, cm^2	2820.42	3352.16	509.96	797.46	691.53
Average diameter of bubbles, cm	8.59	7.90	4.41	4.25	5.07
Number of bubbles having area > 0.5 cm^2	19	40	13	32	21
Total area of bubbles (area > 0.5 cm^2), cm^2	2820.16	3352.09	509.70	797.16	690.79
Average diameter of bubbles (area > 0.5 cm^2), cm	10.35	8.09	5.37	4.50	5.49

The net effect of incorporating baffles is to reduce average bubble size by an average of about 22% in the case of the air reactor. Furthermore, there is a 16% reduction of bubble size in case of fuel reactor with uniform fuel gas velocity. For the fuel reactor, comparing the scenario of uniform gas distribution to the scenario of gas distribution in a single jet, both baffled, we find that the effect of a single jet is to cause an increase in bubble size. This is unsurprising, since bubble size in the bed depends significantly on the size of bubbles formed at the distributor, which in turn is determined by the gas velocity at the distributor.

7.5.2 Bed expansion

An understanding of the bed expansion characteristics of bubbling fluidized bed is crucial for several reasons: Most importantly, bed expansion is used to design a reactor to be built. In reactive fluidized-bed reactor systems, the information on mass of solids per unit bed volume (the bed density of fluidized bed) is important because this influences the chemical conversion calculation [26]. When the heat transfer is to be calculated, the bed expansion gives the bed voidage, which is necessary to predict the heat transfer coefficient, and the bed height, which defines the heat transfer surface

As the demarcation of bed surface is nearly impossible to identify in a vigorously bubbling fluidized bed, either in the case of a simulation or in an actual bubbling fluidized bed. Thus, reporting the bed height at any moment in time is not straightforward. The gas volume fraction distribution must be post-processed in some manner to determine the bed height. We have adopted a method suggested in the literature, in which the bed height is said to be the height below which 90% of the bed weight is found [27].

The instantaneous area-averaged axial solid volume fraction, $\boldsymbol{\bar{\varepsilon}_s(h, t)}$, is calculated as a function of the bed height

$$\overline{\varepsilon_s}(h,t) = 1 - \frac{\int_0^W \int_0^h \varepsilon_g(x,y,t)dy\,dx}{\int_0^W \int_0^H dy\,dx} \tag{1}$$

where, W and H are the reactor dimension in x and y direction respectively. h is the vertical coordinate above the gas distributor. The instantaneous bed mass can be expressed as:

$$\chi(h,t) = A \cdot \rho_s \int_0^h \overline{\varepsilon_s}(h,t)dh \tag{2}$$

where A is the cross-sectional area of the bed and ρ_s is the particle density.

Figure 7- 4, Figure 7- 5 and Figure 7- 6 show the bed height as a function of time for air and fuel mode with and without baffles. In all cases, initially bed expands with time until it levels off at a quasi-steady bed height. After the initial expansion and collapse, the bed surface fluctuation is more orderly over time. It has been noticed that baffled fluidized bed expands more than unbaffled bed. The baffles cause larger bubbles to break apart and produce smaller bubbles which rise through the bed more slowly. Thus small bubbles reside in the bed a longer time, and cause the bed to expand relative to the effect of larger bubbles.

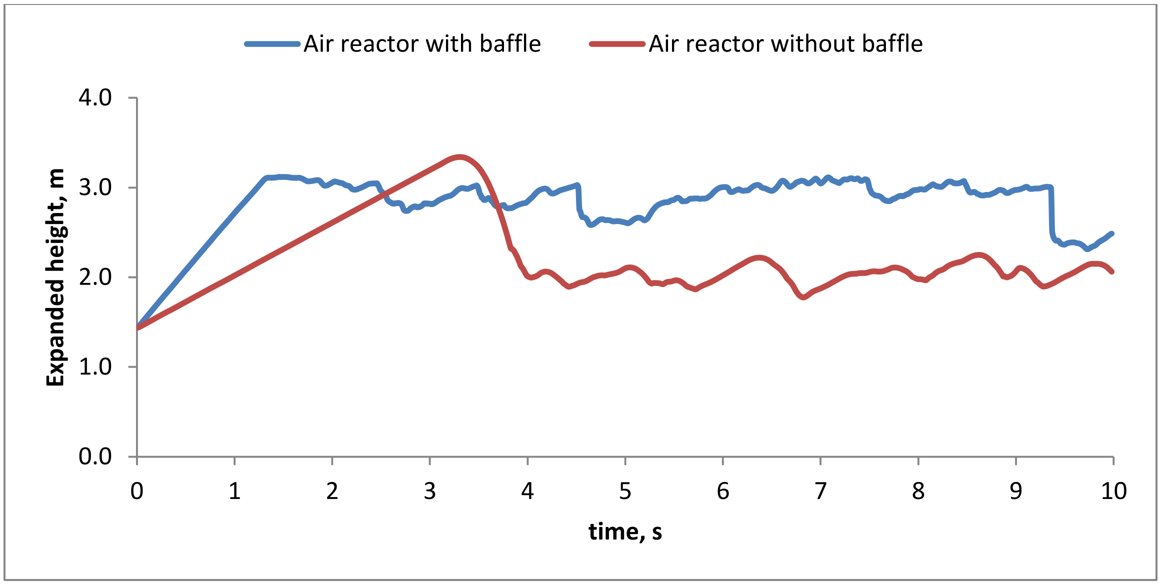

Figure 7- 4. Baffle effect on bed expansion in the **air reactor.** (Uniform inlet gas velocity = **0.675 m/s**).

Comparing Figure 7- 4 and Figure 7- 5, air reactor expansion is much higher than fuel reactor. This large expansion results from the higher superficial gas velocity at the gas distributor. The ratio of the inlet to the minimum fluidization gas velocity ($\frac{U_0}{u_{mf}} \approx$ 28) for air reactor falls in the vigorously bubbling regime but in the fuel reactor case ($\frac{U_0}{u_{mf}} \approx 7$) it falls in the gently bubbling regime [28]. Another fact to note from Figure 7- 4 is that the initial time to reach a quasi-steady state for an unbaffled bed is twice as long as the baffled bed.

It has been expected that the introduction of a central jet instead of uniform gas distribution at the fuel reactor will cause the bed to expand but Figure 7- 6 shows that both models for the gas distribution produce similar results for bed height. This implies that the uniform gas distribution assumption for fuel is safe enough to apply in the simulation for the purpose of finding bed height.

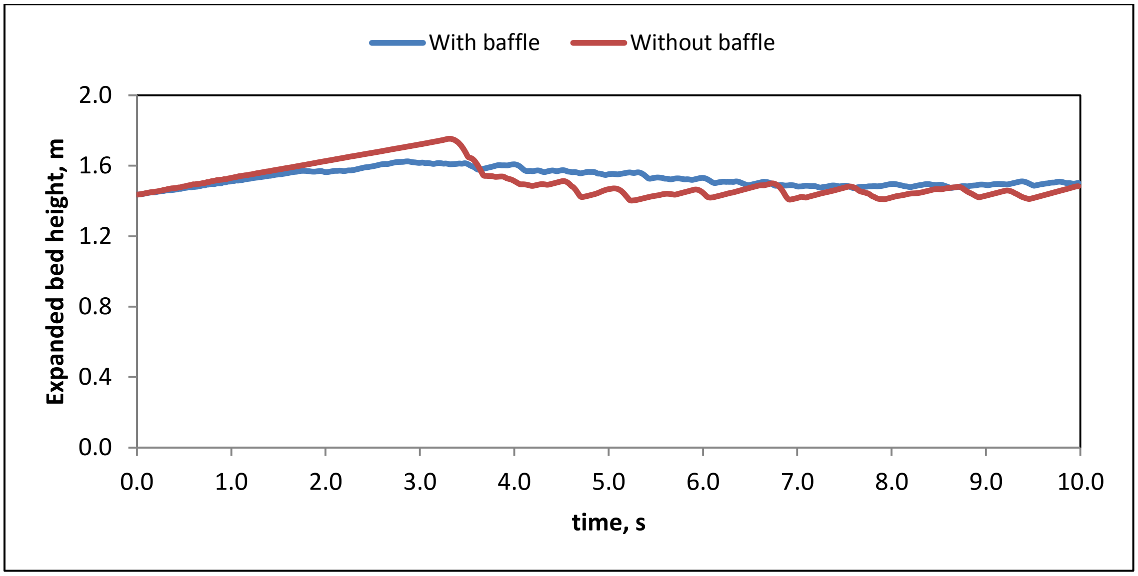

Figure 7- 5. Baffle effect on bed expansion in the fuel reactor. (Uniform inlet gas velocity = 0.18 m/s).

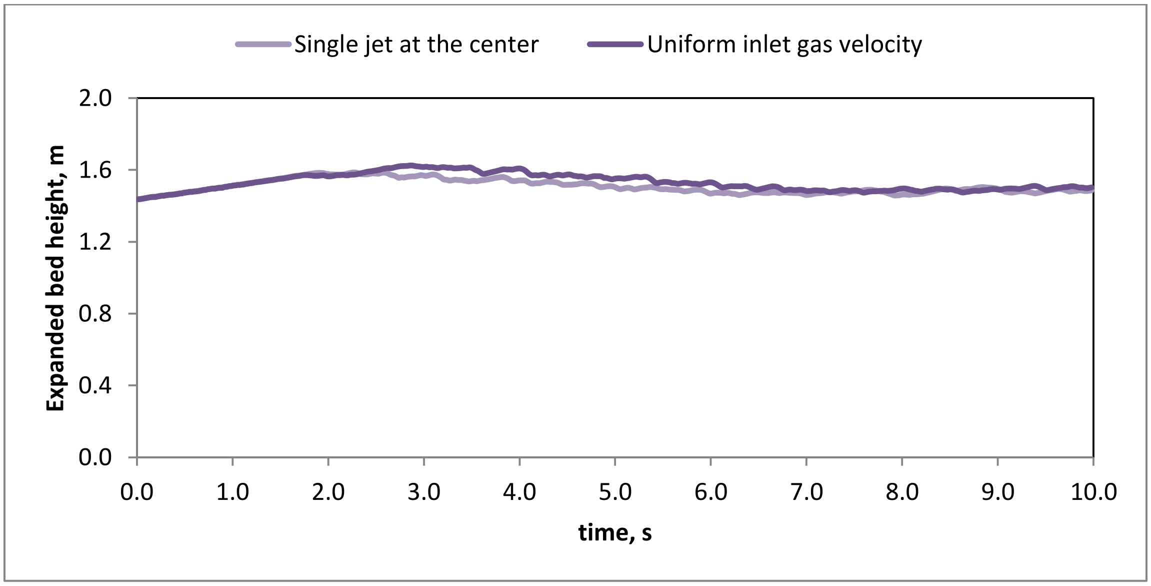

Figure 7- 6. Baffle effect on bed expansion in the fuel reactor. (Uniform inlet gas velocity = 0.18 m/s and jet velocity = 0.475 m/s).

7.5.3 Average bed expansion

After a quasi-steady state is achieved, the solids distribution in the bed is time-averaged to get the simulated bed height. The height determined this way is normalized by comparison to the value corresponding to 90% of the initial bed height (0.90*1.60 m). Table 7- 3 shows the average bed expansion for air and fuel reactors with and without baffles. The data is averaged from 3.0 -10.0 s of simulation time since beds reach, in all cases, quasi-steady state approximately after 3.0s. As discussed in the previous section, a baffled bed creates more bubbles and those bubbles are small in sizes which causes the beds to expand more than the un-baffled bed condition.

In the case of operation in air mode with baffles, bed expansion is significant; the bed height is predicted to be 2.45 m, and it is expected that additional solids are present above this nominal bed height. The real value of the baffles comes from the reduced bubble size, which will cause better interaction between air and the particles, promoting faster particle oxidation. Also, because the bubbles erupting on the bed surface are relatively small, it is expected that the rate of particle entrainment from the bed to the cyclones is somewhat reduced (discussed below). Finally, the reduced pressure fluctuations (discussed below) mean that the system is likely to require less maintenance, since large pressure fluctuations can be very hard on both upstream and downstream gas processing equipment.

Table 7- 3. Summary of average bed expansion

	Air reactor		Fuel reactor		
	W/O baffle	W/ baffle	W/O baffle	W/ baffle	Jet
Expanded height, m	2.10	2.45	1.47	1.53	1.50
% of expansion	46.16	70.45	2.28	5.97	3.94
Expansion ratio, H/H_0	1.46	1.70	1.02	1.06	1.04

7.5.4 Bed pressure drop

Pressure fluctuation data obtained from fluidized beds are a rich source of information on the hydrodynamic states of these systems [29] [30]). The resulting time series data can be analyzed by a number of different methods, including standard deviation, probability density functions, autocorrelation analysis, and power spectral density (PSD) analysis [31]. One of the most common pressure fluctuation analyses is standard deviation. It has often been used to identify different regimes in fluidized beds, where a maximum value with respect to inlet gas velocity is associated with the transition from a bubbling to turbulent fluidization regime. Standard deviation has also been used to determine minimum fluidization velocity [32] and to detect the onset of defluidization in operating fluidized beds [33].

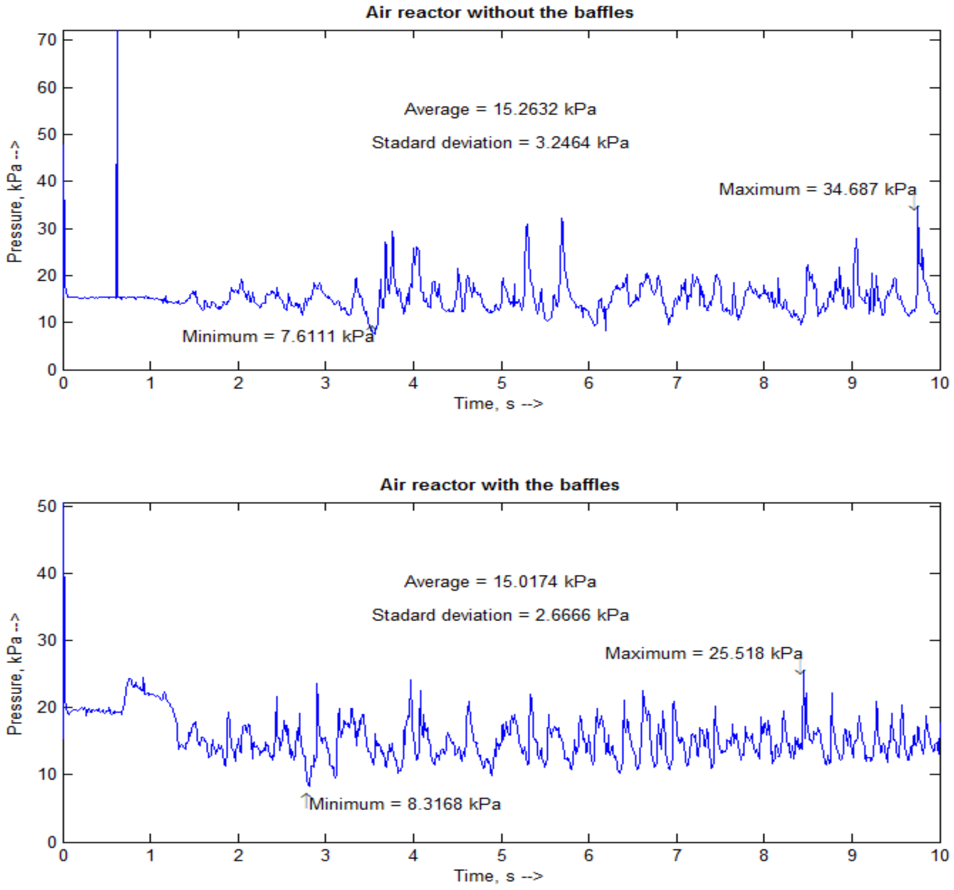

Figure 7- 7. Baffle effect on bed pressure drop fluctuation in the **air reactor**. (Uniform inlet gas velocity = **0.675 m/s**).

Figure 7- 7, Figure 7- 8 and Figure 7- 9 show the pressure fluctuation for air and fuel reactors with and without baffles. The initial hydrostatic bed pressure drop is 15 kPa ($\Delta P = (1 - \varepsilon_0)\ H_0\ \rho_s\ g$). The average pressure drop shown here in all cases closely represents the bed hydrostatic pressure. All the pressure drop data considered here for analysis is 1.0 ~10.0 s of simulation period; the simulation at times before 1.0 s is excluded, since no bubbles have erupted yet on the bed surface, creating a relatively smooth pressure trace. As previously mentioned, standard deviation has often been used

to identify different fluidization regimes in fluidized beds. Comparing the standard deviation of air and fuel reactors pressure drops, it is understandable that air reactors shows vigorously bubbling characteristics and fuel reactors are moderately bubbling.

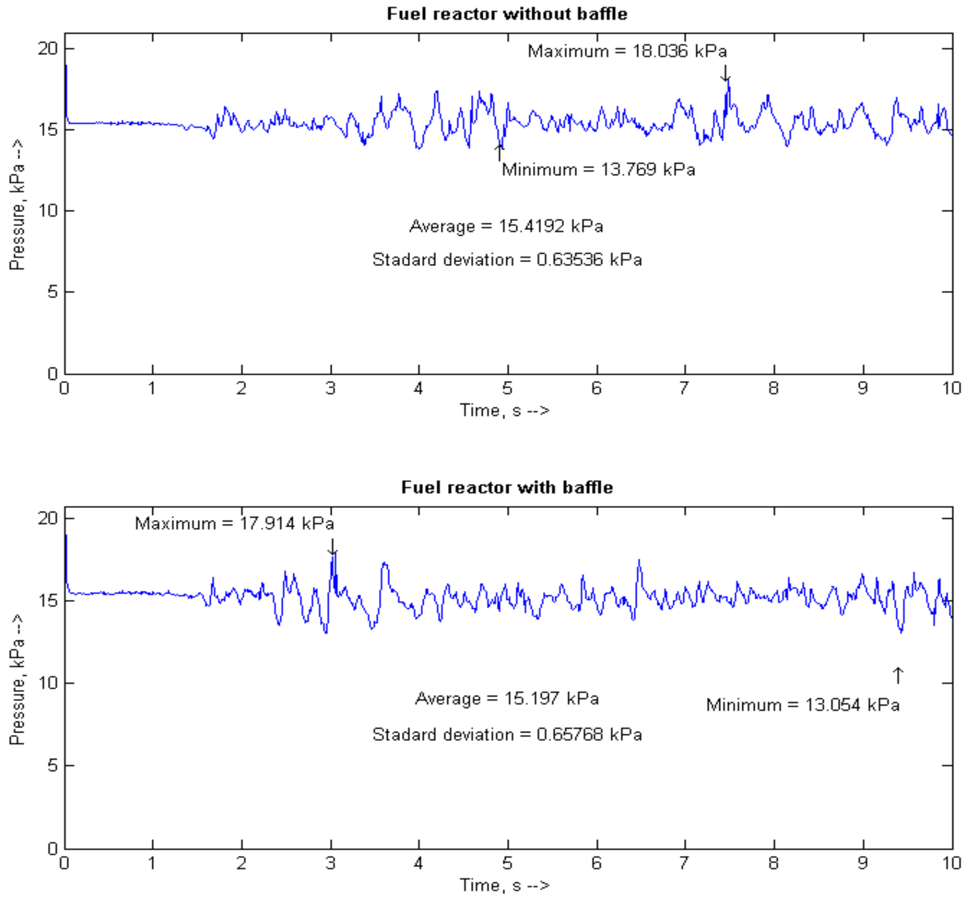

Figure 7- 8. Baffle effect on bed pressure drop fluctuation in the **fuel reactor**. (Uniform inlet gas velocity = **0.18 m/s).**

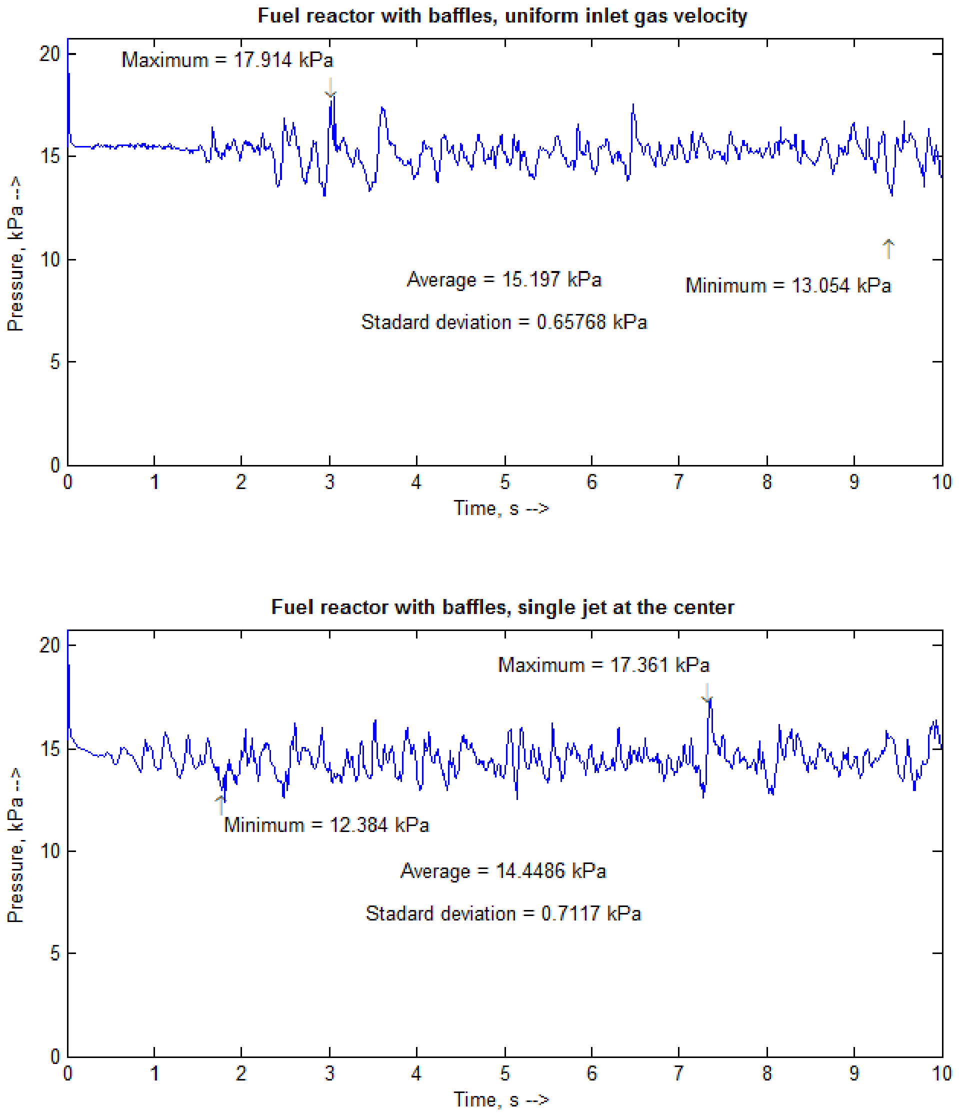

Figure 7- 9. Baffle effect on bed pressure drop fluctuation in the fuel reactor. (Uniform inlet gas velocity = 0.18 m/s and jet velocity = 0.475 m/s).

The difference in standard deviation between baffled and unbaffled reactors highlights the effect of baffles, especially in air mode. Bubbles grow without restriction in an open bed, causing higher pressure drop fluctuation (Figure 7- 7). However, such deviation is not present in case of fuel reactor (Figure 7- 8).

As the fuel reactor with central jet flow of gas operates at a velocity higher than uniform gas velocity condition, the standard deviation also depicts that effect with slightly higher values than uniform one. As shown in Table 7- 2, bubble size is a little bigger in jet flow than uniform flow.

7.5.5 Particle entrainment

In the bubbling zone of a fluidized bed, bubbles grow by coalescence and rise to the surface of the bed where they break. As bubbles break at the surface of the bed, particles are thrown up in the freeboard zone and are entrained by the upward flowing gas stream. In this zone some particles are carried far above the bed surface and are elutriated while others fall back to the bed. The freeboard zone usually affords an opportunity for the disengagement of particles and for the lean phase reactions. During the operation of a fluidized bed, a large amount of fine particles could be elutriated continuously.

In order to examine the elutriation from the air reactor, solid flux is calculated at the gas outlet located at the top of the domain. Solid volume fraction, $\boldsymbol{\varepsilon_s(x,t)}$, at the exit of the reactor height, H is defined as

$$\varepsilon_s(x,t) = 1 - \varepsilon_g(x,t) \tag{3}$$

Solid particle velocity has two components, but the x-component of the velocity has no effect on particle entrainment from the reactor. Y-component of solid particle velocity, $\boldsymbol{V_s(x,H,t)}$ at the exit of the reactor height, H can easily be obtained from simulation. Average solid flux at the reactor exit is defined as

$$\phi_s(t) = \rho_s \frac{\int_0^W \varepsilon_s(x,H,t)\, V_s(x,H,t)dx}{\int_0^W dx} \tag{4}$$

Figure 7- 10 shows the solid flux time profile for air reactor with and without baffles. During the initial unsteady period, solid elutriation is much higher in unbaffled air reactor than baffled one, even though the bed surface is lower. This is due to the unrestricted growth of bubbles in unbaffled reactor. However, excluding the unsteady period, bed shows no elutriation in either of the cases. No elutriation is predicted for operation during fuel mode, with or without baffles.

7.6 Conclusions

CFD simulations of bubbling fluidized bed of air and fuel reactors with and without internal horizontal baffles have been presented in this study. It shows that internal baffles are effectively breaking large bubbles. This will enhance the interchange of gas between the bubbles and the emulsion phase. Chemical reactions and mass transfer can be improved when bubbles are small and evenly distributed throughout the bed volume. However, experimental data is required for further validation of the simulation results.

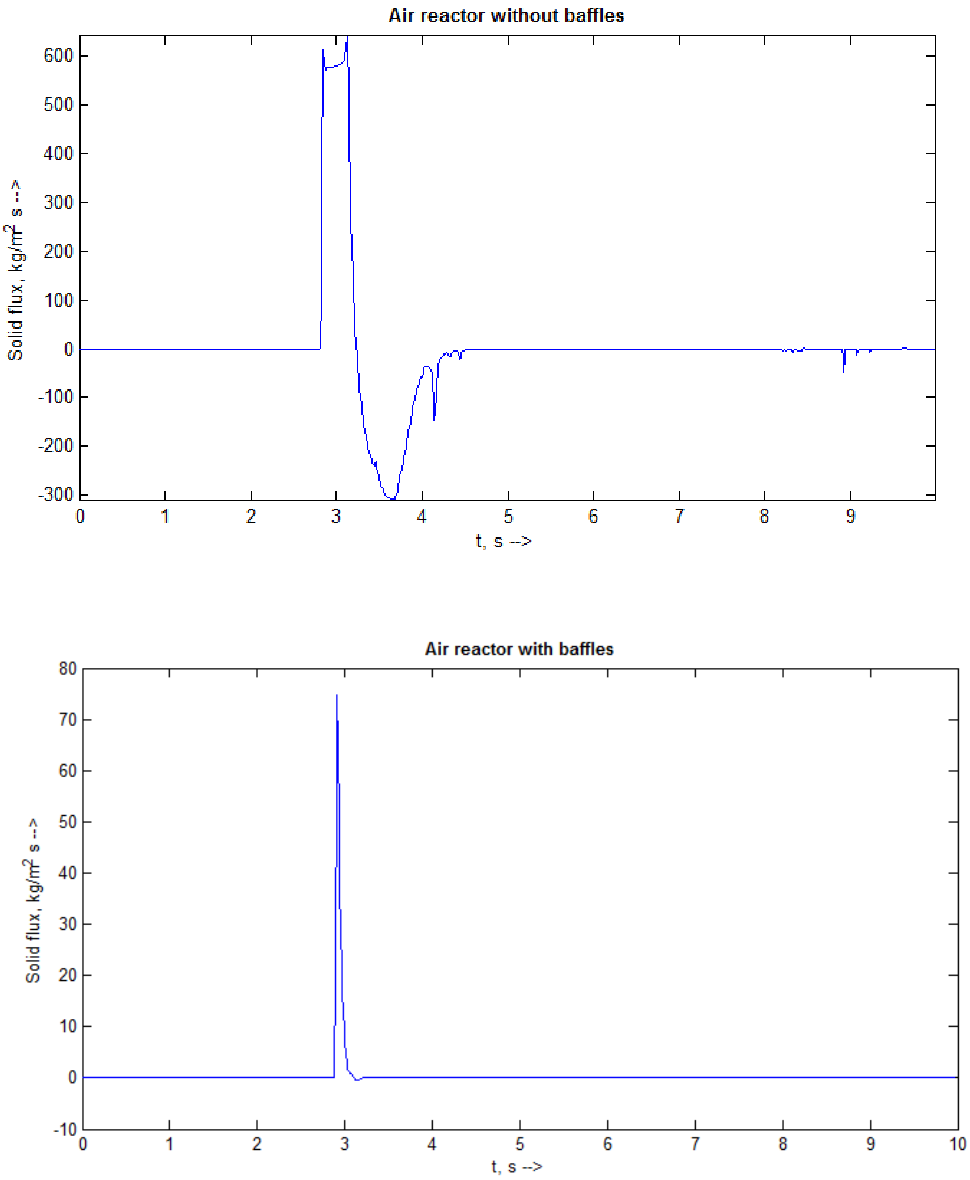

Figure 7- 10. Baffle effect on solid flux in the **air reactor**. (Uniform inlet gas velocity = **0.675 m/s**).

References

[1] P. Kolbitsch*, et al.*, "Design of a Chemical Looping Combustor using a Dual Circulating Fluidized Bed Reactor System," *Chemical Engineering & Technology,* vol. 32, pp. 398-403, Mar 2009.

[2] P. Kolbitsch*, et al.*, "Modeling of a 120 kW chemical looping combustion reactor system using a Ni-based oxygen carrier," *Chemical Engineering Science,* vol. 64, pp. 99-108, Jan 1 2009.

[3] D. Gidaspow, Jung, J., Singh, R. K., "Hydrodynamics of fluidization using kinetic theory: an emerging paradigm," *Powder Technology,* vol. 148, pp. 123–141, 2004.

[4] D. Gidaspow*, et al.*, "Hydrodynamics of circulating fluidized beds: kinetic theory approach," Illinois Inst. of Tech., Chicago, IL (United States). Dept. of Chemical Engineering1991.

[5] J. A. M. Kuipers, van Swaaij, W.P.M., "Computational fluid dynamics applied to chemical reaction engineering," *Advances in Chemical Engineering,* vol. 24, 1998.

[6] M. A. van der Hoef, van Sint Annaland, M., Deen, N. G., Kuipers, J. A. M., "Numerical simulation of dense gas–solid fluidized beds: a multi scale modeling strategy," *Annual review of fluid mechanics,* vol. 40, pp. 47–70, 2008.

[7] C. C. Pain, Mansoorzadeh, S., de Oliveira, C.R.E., "A study of bubbling and slugging fluidised beds using the two-fluid granular temperature model," *International Journal of Multiphase Flow,* vol. 27, pp. 527–551, 2001.

[8] D. Gidaspow, *Multiphase Flow and Fluidization: Continuum and Kinetic Theory Descriptions*. San Diego: Academic Press, 1994.

[9] M. Syamlal, O'Brien, T.J., "Computer simulation of bubbles in a fluidized bed," *A.I.Ch.E. Symposium Series,* vol. 85, pp. 22-31, 1989.

[10] C. Y. Wen, Yu, Y.H.,, "Mechanics of fluidization," *Chemical Engineering Progress Symposium Series,* vol. 62, pp. 100-111, 1966.

[11] A. T. Andrews IV*, et al.*, "Coarse-grid simulation of gas-particle flows in vertical risers," *Industrial & Engineering Chemistry Research,* vol. 44, pp. 6022-6037, 2005.

[12] S. Benyahia, "On the effect of subgrid drag closures," *Industrial & Engineering Chemistry Research,* vol. 49, pp. 5122-5131, 2009.

[13] Y. Igci*, et al.*, "Filtered two- fluid models for fluidized gas- particle suspensions," *Aiche Journal,* vol. 54, pp. 1431-1448, 2008.

[14] C. C. Milioli*, et al.*, "Filtered two- fluid models of fluidized gas- particle flows: New constitutive relations," *Aiche Journal,* vol. 59, pp. 3265-3275, 2013.

[15] T. Li*, et al.*, "CFD simulations of circulating fluidized bed risers, part I: Grid study," *Powder Technology,* vol. 254, pp. 170-180, 2014.

[16] M. Ishii and T. Hibiki, *Thermo-fluid dynamics of two-phase flow*: Springer Science & Business Media, 2010.

[17] M. Ishii and K. Mishima, "Two-fluid model and hydrodynamic constitutive relations," *Nuclear Engineering and Design,* vol. 82, pp. 107-126, 1984.

[18] J. Boure*, et al.*, "Review of two-phase flow instability," *Nuclear Engineering and Design,* vol. 25, pp. 165-192, 1973.

[19] D. A. Drew, "Mathematical modeling of two-phase flow," *Annual review of fluid mechanics,* vol. 15, pp. 261-291, 1983.

[20] C. K. K. Lun*, et al.*, "Kinetic theories for granular flow: inelastic particles in Couette flow and slightly inelastic particles in a general flowfield," *Journal of Fluid Mechanics,* vol. 140, pp. 223-256, 1984.

[21] B. Chalermsinsuwan*, et al.*, "Kinetic theory based computation of PSRI riser: Part I—Estimate of mass transfer coefficient," *Chemical Engineering Science,* vol. 64, pp. 1195-1211, 3/16/ 2009.

[22] M. Syamlal, Rogers, W., O'Brien, T. J., "MFIX Documentation, Theory Guide1," N. T. I. Service, Ed., ed. Springfield, 1993.

[23] S. Cloete*, et al.*, "On the effect of cluster resolution in riser flows on momentum and reaction kinetic interaction," *Powder Technology,* vol. 210, pp. 6-17, 2011.

[24] L. R. Glicksman*, et al.*, "Bubble Properties in Large-Particle Fluidized-Beds," *Chemical Engineering Science,* vol. 42, pp. 479-491, 1987.

[25] Y. Jin*, et al.*, "Effect of Internal Tubes and Baffles," *Handbook of Fluidisation and Fluid-Particle Systems,* pp. 171-200, 2003.

[26] D. Geldart, "Expansion of Gas Fluidized Beds," *Ind. Eng. Chem. Res.,* vol. 43, pp. 5802-5809, 2004.

[27] M. Syamlal and T. J. O'Brien, "Fluid dynamic simulation of O-3 decomposition in a bubbling fluidized bed," *Aiche Journal,* vol. 49, pp. 2793-2801, Nov 2003.

[28] K. Daizo and O. Levenspiel, "Fluidization engineering," 1991.

[29] R. C. Brown and E. Brue, "Resolving dynamical features of fluidized beds from pressure fluctuations," *Powder Technology,* vol. 119, pp. 68-80, 2001.

[30] E. Brue and R. C. Brown, "Use of pressure fluctuations to validate hydrodynamic similitude in fluidized media: bubbling beds," *Powder Technology,* vol. 119, pp. 117-127, 2001.

[31] J. Yates and S. Simons, "Experimental methods in fluidization research," *International Journal of Multiphase Flow,* vol. 20, pp. 297-330, 1994.

[32] C. Sobrino*, et al.*, "Standard deviation of absolute and differential pressure fluctuations in fluidized beds of group B particles," *Chemical Engineering Research and Design,* vol. 86, pp. 1236-1242, 2008.

[33] J. R. van Ommen*, et al.*, "Rapid detection of defluidization using the standard deviation of pressure fluctuations," *Chemical Engineering and Processing: Process Intensification,* vol. 43, pp. 1329-1335, 2004.

CHAPTER 8

Incorporating the effect of fluidized-bed temperature in CFD simulation through particle-particle interaction coefficient

Abstract

The hydrodynamics of gas–solid fluidized-bed reactor at high temperature is investigated through the particle-particle restitution coefficient in numerical simulations. CFD results show that decreasing the coefficient of restitution results in larger bubbles, increased pressure fluctuation, and decreased granular temperature. A shift of fluidization regime – bubbling to near slugging and splitting of bubbles due to ‘channel-like’ solid flow thorough – is observed at high temperature. The effect of particle-particle interactions on hydrodynamics can be interpreted through the two-phase theory of fluidization. When particles experience elastic collisions, i.e. no loss of energy, there is no change in total particle momentum. However, inelastic collisions result in a loss of kinetic energy and reduced particle velocity. As the fluid passes by particles with reduced velocity, the bed experiences increased relative fluid velocity. In two-phase theory, any fluid flow exceeding the minimum fluidization velocity passes through the bed as bubbles. Thus, decreased coefficient of restitution can result in increased bubble size, higher pressure fluctuation and lower granular temperature.

8.1 Introduction

Experimental studies on the hydrodynamics of dense gas-solid fluidized beds at elevated temperatures are very limited. This lack of studies is due to difficulties associated with measuring techniques under these conditions. However, numerous industrial applications of fluidized beds are at high temperatures, e.g., combustion and gasification, and it is desired to better understand the effects of temperature on hydrodynamics [1].

In dense gas-solid fluidized bed, particle-particle interactions play a vital role at high temperature, which in turn has a substantial impact on the hydrodynamics of fluidized bed [2]. Cui et al. [3] showed that the local solids hold up, as well as emulsion fraction and the solids concentration decrease as temperature increases (up to 420 °C). The changes of fluid physical properties, such as density and viscosity are not sufficient to describe the hydrodynamic behavior of fluidized beds at high temperature [4]. The first-principles based computational fluid dynamics (CFD) is an effective tool to explore the complex hydrodynamics behavior in gas-solid fluidized bed at elevated temperature.

In this study, the effect of temperature on fluidized bed hydrodynamics is studied through numerical simulation by changing the particle-particle interaction coefficient, known as restitution coefficient, in addition to fluid physical properties. A previously developed and validated bubble detection and tracking algorithm for CFD data is used to calculate the hydrodynamic properties. The results are compared and validated against experimental high temperature measurements by Velarde et al. [3].

8.2 Velarde et al. experiment

Velarde et al. [4] used glass beads as bed material in a pseudo-2-D quartz column with bed width, depth and height of 0.25, 0.015 and 0.7 m respectively. The bed was installed in the internal chamber of an industrial electrical furnace capable to operate up to 1000 °C. Inconel alloy metal was used for the distributor chamber and freeboard. The porous plate is made of ceramic material with a mean pore size of 40 μm. An Inconel heater is connected to the gas inlet to assure the fed gas enters the fluidized bed at the same temperature as the furnace. Table 8- 1 summarizes the experimental setup used by Velarde et al. [4].

Table 8- 1. Experimental conditions

Physical properties	Velarde et al. [4]
Bed width/diameter, m	0.25
Static bed height, m	0.375
Measuring height, m	0.2 - 0.35
u_0/u_{mf}	3.0
u_{mf}, m/s	0.21
Particles	Glass beads
Particle size, μm	400-600
Particle density, kg/m^3	2500
Type of geometry	Pseudo- 2-D

Bubble sizes are measured from images captured by a Dantec Flowsense 16 M camera coupled with an optical endoscopic laser. Illumination is provided by the Nd:Yag double pulse laser Evergreen 70 mJ coupled with custom made high temperature endoscope. The laser is trigged together with the camera shutter to allow 1 ms delay between two consecutive images with a frequency of 2 Hz. Measurements at temperatures up to 450 °C were presented to demonstrate the capability of the technique.

8.3 Simulation setup

8.3.1 Two-fluid model

The Eulerian-Eulerian Two Fluid Model (TFM) which treats fluid and solid as distinct but interpenetrating continuous phase is applied in this study. The integral balance equations of continuity, momentum and energy for both phases are solved numerically with appropriate boundary and leap conditions for phase interfaces. An averaging techniques and assumptions to obtain momentum balance for the solids phases are followed since the resultant continuum approximation for the solid phase has no equation of state and lacks variables such as viscosity and normal stress [5]. The evaluation of the solid phase stress tensor is based on the flow regimes - the viscous regime where the stress tensor is evaluated using the Kinetic Theory of Granular Flow (KTGF) and the plastic flow regime where the theory of Schaeffer [6] is employed to account for the frictional effects [7]. The TFM equations are coupled with constitutive relations derived from data or analysis of nearly homogeneous systems. The interphase momentum transfer between gas and solid phases are coupled by drag force. Numerous correlations for calculating the drag coefficient of gas–solid systems have been reported in the literature, including those of Syamlal and O' Brien (1989) [8], Gidaspow (1994) [7], and Wen and Yu (1966) [9]. Syamlal-O'Brien drag model that bridges the results of Wen and Yu [9] for dilute systems and the Ergun approach for dense systems is used in this work. The detailed description of the conservation of mass, momentum, and energy equation and drag model of the TFM is described in elsewhere [10].

8.3.2 Initial and boundary conditions

The bed was assumed to be under minimum fluidization with superficial gas velocity equal to u_{mf} initially. Lateral gas velocities were set to zero for initial conditions. A constant pressure was defined in all horizontal planes up through the bed of particles depending upon static pressure. The upper section of the simulated geometry, or freeboard, was considered to be occupied by gas only at time zero. The lateral walls were modeled using partial-slip boundaries, with no-slip for gas and free-slip for solid phase. The particle-wall interactions are modeled using the Johnson-Jackson model [11], which evaluates the solids slip velocity at the walls by considering momentum and granular energy balance. Dirichlet boundary conditions were employed at the distributor to specify a uniform gas inlet velocity, u_0. Pressure boundary conditions were employed at the top of the freeboard.

8.3.3 Flow solver and solver settings

The National Energy Technology Laboratory's (NETL, USA) open-source code MFIX was used as flow solver [10]. The modified phase-coupled SIMPLE scheme, which uses a solids volume fraction correction equation instead of a solids pressure correction equation, was used for pressure–velocity coupling. The second-order SuperBee scheme was used for the spatial discretization of all equations. A combination of point successive under relaxation and biconjugate gradient stabilized method (BiCGSTAB) method were used for the linear equation solver. A maximum residual at convergence of 10^{-3} was used to determine convergence of the continuity and momentum equations solution. First order implicit temporal discretization was used to ensure stable and accurate solutions. An automatic time-step adjustment was used to enhance the computation speed, with a maximum and a minimum time-step of $5\text{x}10^{-4}$ s and 10^{-6} s respectively. A summary of other simulation parameters is given in Table 8- 2.

Table 8- 2. Summary simulation parameters

Parameters		Validated for TFM simulation
Coefficient of particle wall collision	1.0	[12]
Specularity coefficient	0.6	[12, 13]
Angle of internal friction, °	30	[14]
Angle of internal friction at wall, °	0.0	[14]

8.3.4 Geometry and discretization

The dimension of the fluidized bed shown in Table 8- 1 is used in the simulations with unstructured mesh sizes. A careful investigation of mesh-refinement is essential for meaningful validation and prior to interpretation of CFD results. For this study mesh sizes are chosen for the grid-independent solution of TFM based on the experimentally validated mesh-refinement studies, and is shown in Table 8- 3.

Table 8- 3. Mesh resolutions used for simulations.

Type	Width or diameter, m	Height, m	d_p, μm	Number of mesh for grid -independent TFM, ($N_x \times N_y \times N_z$)	References
Lab-scale [4]	0.250	1.00	500	50 × 200 × 1	[15-17]

8.3.5 Method of analysis: bubble statistics

The 3-D face-masking technique developed in a previous chapter of this dissertation using commercial software MATLAB is applied in this study to obtain the bubble statistics. The steps are:

- Whole field-void data collection - obtaining void fraction data from simulations that are interpolated and smoothed to resolve bubble boundaries
- Bubble recognition – identifying bubbles by applying a void-threshold criteria and masking neighboring cells
- Numbering bubbles – assigning unique bubble number to each masked circumference by resolving conflicts arising in irregular-shape bubbles
- Bubble properties – describing bubbles (e.g. location, size, span, shape) by masking cells forming individual bubbles

To derive meaningful statistics and prevent erroneous linking of bubbles due to coalescence and splitting, data is collected at 100 Hz for 20 s (2000 frames in total).

8.4 Results and discussions

The simulations are completed for 20 s of real flow time for all cases and the first 3 s data are discarded to minimize the transient start-up effects. Consequently, the statistically averaged data presented in this study consists of the last 1700 time-frames.

8.4.1 Validation

Before arguing about the incorporation of the fluidized-bed temperature effect through particle-particle restitution coefficient in CFD simulation, it is necessary to validate the numerical results with experimental measurement. Velarde et al. [4] measured the equivalent bubble diameter by both LED-PIV/DIA and ePIV/DIA at room temperature and compared with the calculated bubble diameter using the semi-empirical correlation of Shen et al. [18]. They concluded that 1500 ~ 2000 time-frames were sufficient to obtain reliable time-averaged data.

Similar to experimental method, the equivalent bubble computed from numerical simulation data at room temperature is compared with experimental measurement and with the prediction given by Shen correlation [18]. Figure 8- 1 shows the area-equivalent average bubble diameter as a function of height for simulation using different particle-particle restitution coefficients. In this study, void-threshold is set at 0.7 (based on [4, 19, 20]) to differentiate between bubble and emulsion phases. As expected, small bubbles, for all cases, are formed close to the distributor coalescing to form larger bubbles higher up in the bed.

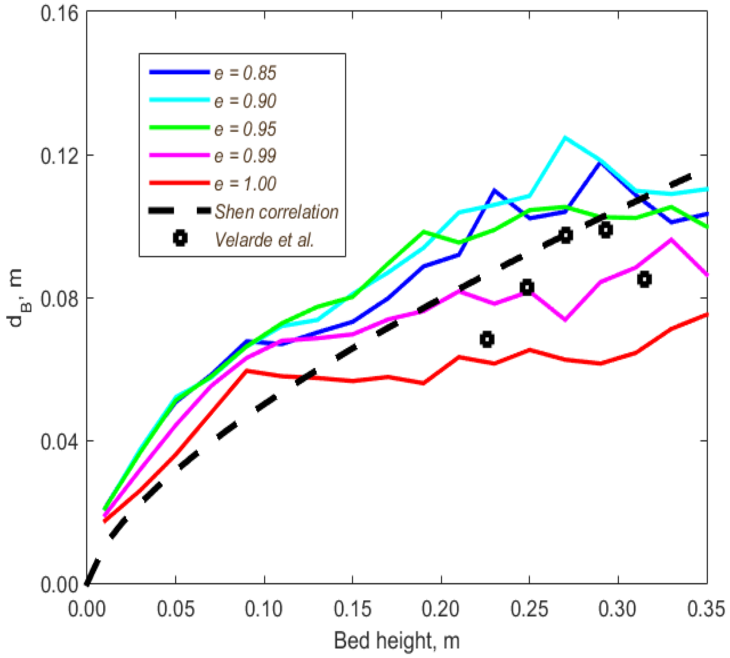

Figure 8- 1. Comparison of average equivalent bubble diameter, d_B, with empirical correlation [18] and experimental measurement for different restitution coefficient (e) at 20 °C temperature.

The coefficient of restitution has an effect on bed hydrodynamics which is most pronounced when near the point of elasticity. Decreasing the particle-particle restitution coefficient in CFD simulation results an increasing bubble size at room temperature. Figure 8- 2 shows snapshots of the simulations for different values of the coefficient of restitution. During an elastic collision (i.e., e = 1.0), there is no net loss of kinetic energy which results in a loose-packed solid distribution. As collisions become less ideal i.e. inelastic, the kinetic energy is then conserved through the fluid phase. Particles become closely packed in the densest regions of the bed, resulting in sharper porosity contours and larger bubbles. Goldschmidt et al. [21] also reported similar behavior of fluidization due to increase of energy dissipation through numerical simulation and comparison with experimental snapshots.

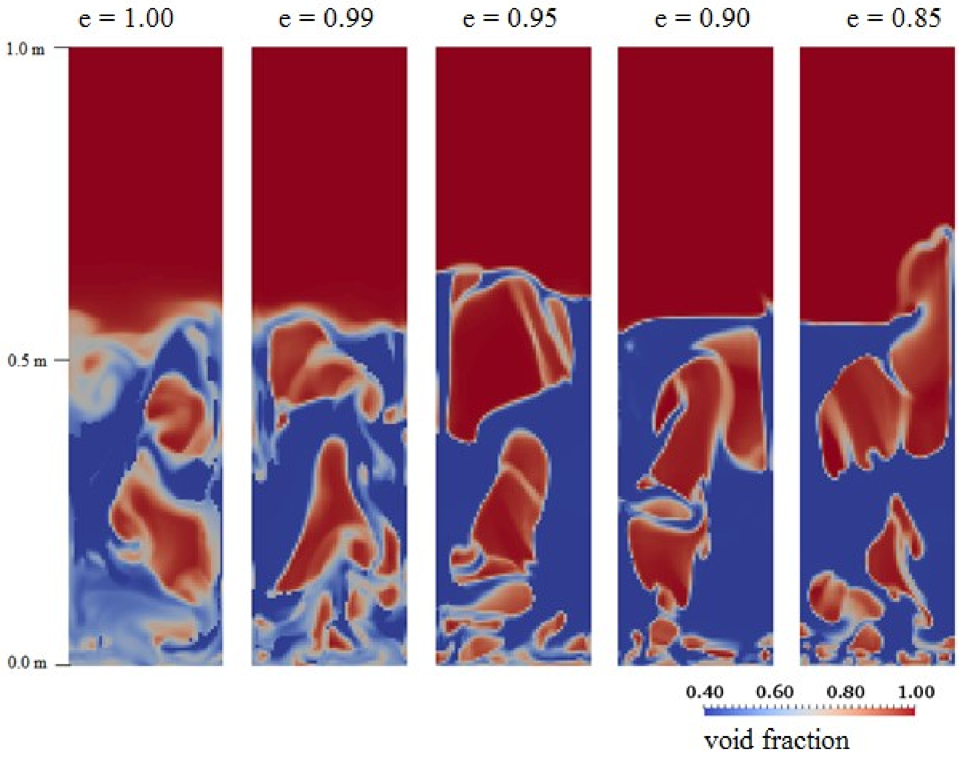

Figure 8- 2. Snapshots from CFD simulation, showing the change of hydrodynamic behavior with particle-particle restitution coefficient at room temperature.

The effect of particle-particle interactions on bubble size can be explained through the two-phase theory of fluidization. When particles experience elastic collisions, i.e. no loss of energy, there is no change in total particle momentum. However, inelastic collisions result in a loss of kinetic energy and reduced particle velocity. As the fluid passes by particles with reduced velocity, the bed experiences increased relative fluid velocity. In two-phase theory, any fluid flow exceeding the minimum fluidization velocity passes through the bed as bubbles. Thus, decreased coefficient of restitution can result in increased bubble size

Shown in Figure 8- 1, predictions of time-averaged bubble diameter calculated for 0.95< e ≤ 0.99 reveal excellent agreement with experimental measurements. It is true that the coefficient of restitution depends strongly on the hardness, particle shape, and impact velocity of particles. The glass-bead particles' used in Velarde et al. [4] experiment is a relatively hard material, and the impact velocity of particles is small in the case of bubbling fluidized bed [22]. The lower impact velocity and harder material together in turn led to the higher coefficient of restitution, which agreed well with the experimental hydrodynamic behavior. Loha et al. [17] reported similar conclusion about the coefficient of restitution for glass spheres using numerical simulation and comparing with the experimental measurement at room temperature.

8.4.2 Temperature effect on hydrodynamics

Figure 8- 3 illustrates snapshots from the simulations at different coefficient of restitutions as well as different temperatures. The fluidization behavior shows dependency on coefficient of restitutions as well as fluidization temperature. Comparing Figure 8- 2 and Figure 8- 3, the bubble shape and size changes at higher temperatures with decreasing the coefficient of restitution (i.e. allowing more energy dissipation). At elevated temperatures with high energy loss (e.g. restitution coefficient, e <0.90), the bubbles become large enough that many of them look like a slug rather than a bubble. Particles try to penetrate through the slug creating a 'channel-like' flow pattern.

This change in fluidization behavior occurs due to inter-particle forces, which change the gas-solid distribution in the bed. Geldart and Kapoor [23] also reported the onset of slugging more easily at 300 °C temperature for spherical steel shot particles.

Recently, Velarde et al. [4] video-recorded the behavior of fluidization at high temperature using an endoscopic laser technique. The snapshots from their experimental measurements are presented in Figure 8- 4 at three temperatures. At each temperature, three representative snaps are shown. This experimental observation corroborates the change of fluidization pattern at elevated temperature.

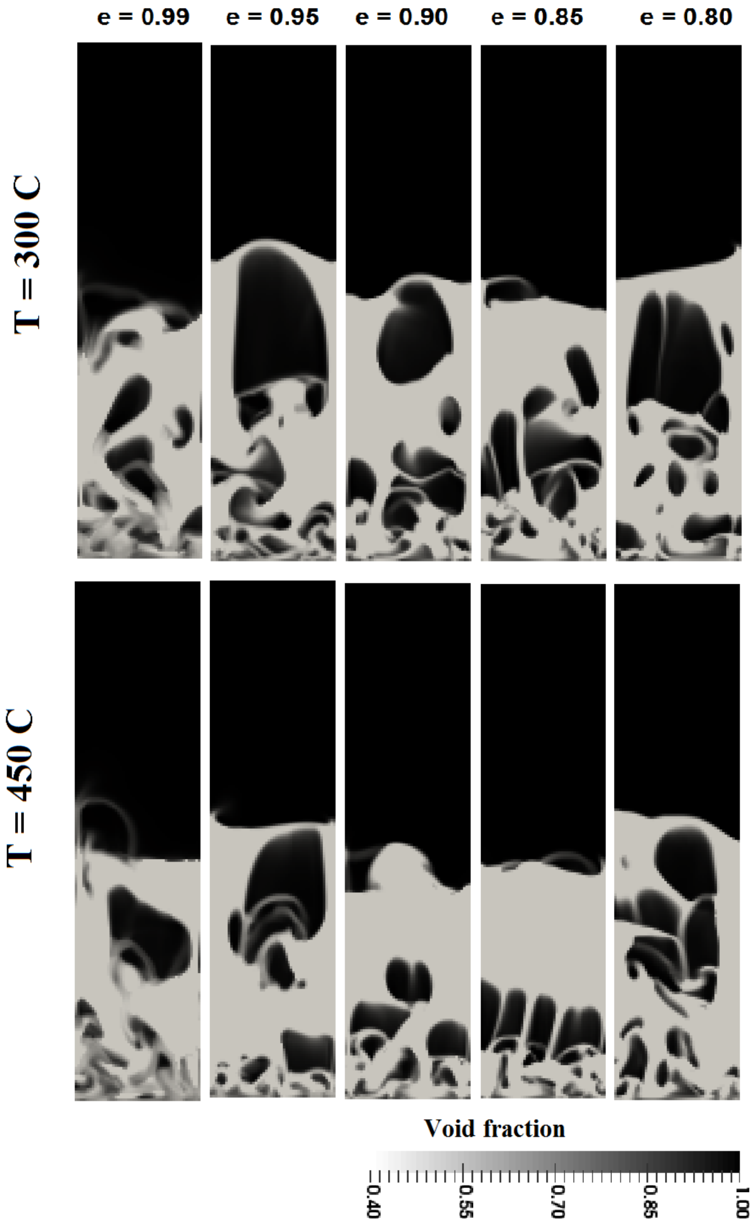

Figure 8- 3. Snapshots from CFD simulations showing the change of hydrodynamics e.g. bubble size and shape with particle-particle restitution coefficient at elevated temperatures.

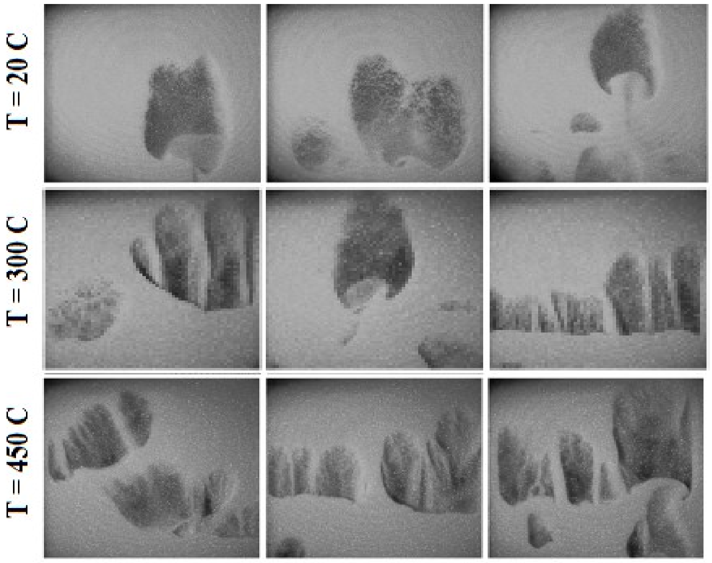

Figure 8- 4. Snapshots from experimental measurements showing the change of hydrodynamics e.g. bubble size and shape with temperatures. This figure is adapted from Velarde et al. [4], with permission from publisher 'Elsevier'.

Figure 8- 5 shows the bubble diameter calculated by the 3-D face-masking algorithm using the simulation data at different temperatures. As expected, the bubble size increases with the coefficient of restitutions when e ≥ 90, at all temperatures. However, when e is 0.8<e<0.9, the bubble size seems to be approximately constant. This fluctuation can be realized by visual inspection of Figure 8- 3. It appears that there is a single big bubble or slug in be bed when e<0.90. However, by defining bubble boundary with a specified void threshold, the slug bubble is not identifiable as a whole rather it splits in several small bubbles. It is apparent that the particle 'channels' are cutting the

slug vertically into parts, confounding the comparison of bubble size and shape for the restitution coefficient values smaller than 0.90.

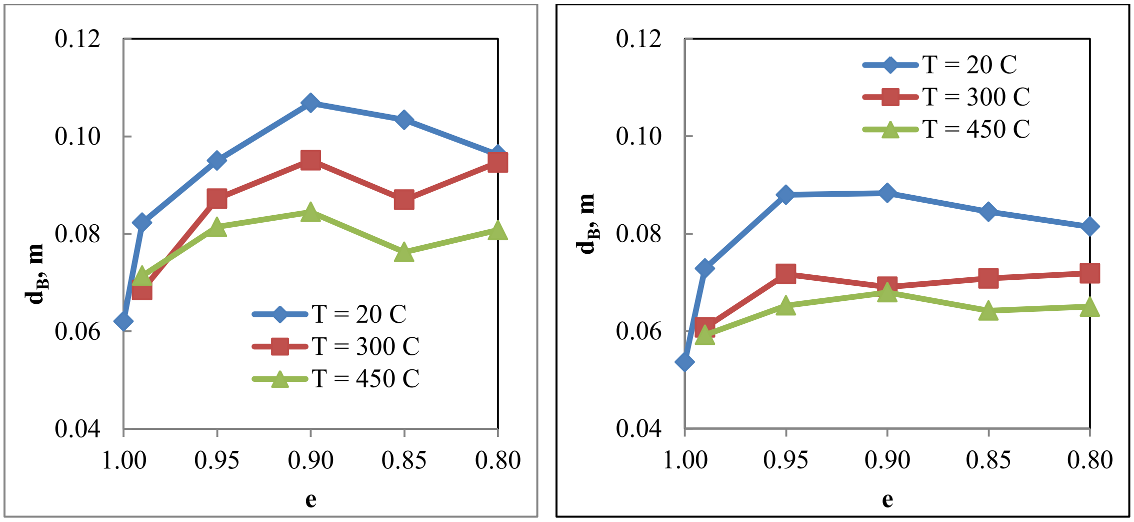

Figure 8- 5. Change in average equivalent bubble diameter, d_B, with restitution coefficients and temperatures at two axial heights: (a) H = 0.30 m and (b) H = 0.20 m. Initial bed height is 0.37 m. Note e = 1.0 is investigated for T = 20 °C. In all other cases, e is between 0.99 and 0.80.

Figure 8- 5 also highlights that the average bubble size decreases with increasing temperatures. When compared under equivalent conditions, at 300 and 450 °C bubbles are 80 - 90% of the sizes observed at room temperature. Similar reduction of bubble size was also reported by Geldart and Kapoor [23].

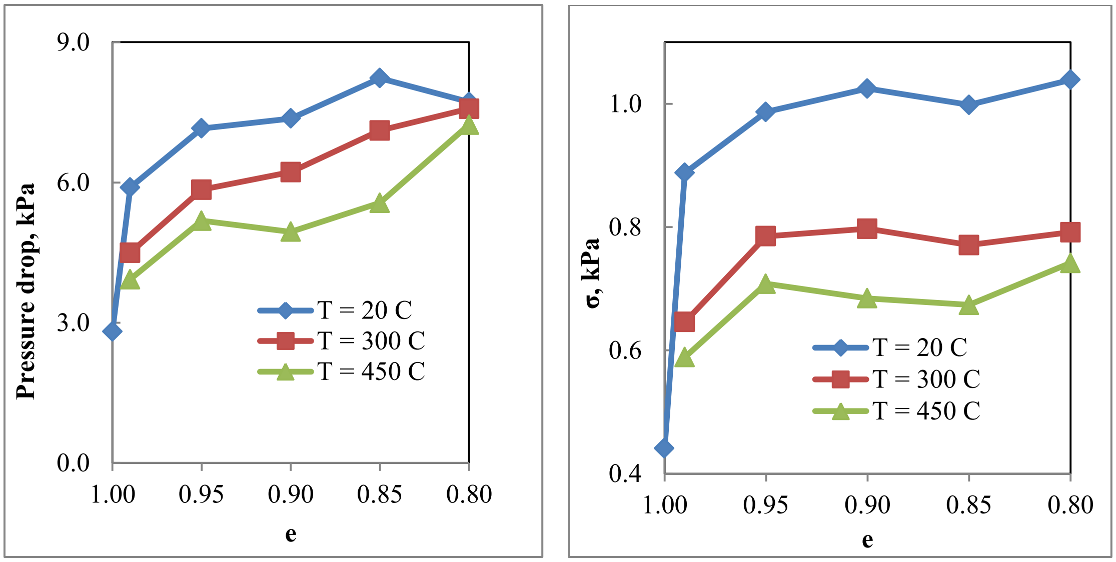

Figure 8- 6. Pressure fluctuation with restitution coefficients at different temperatures: (a) pressure drop and (b) root mean-square (RMS) of pressure fluctuations.

Figure 8- 6 represents the pressure drop and the RMS of the pressure fluctuations behavior of the CFD simulation for different values of the coefficient of restitutions at different temperatures. Similar to bubble sizes, pressure fluctuation increases with decreasing the coefficient of restitution, and it decreases with temperatures. This may be attributed due to the smaller bubble sizes at elevated temperature compared to the size of bubble at room temperature. The smallest pressure drop is accounted near the point of elasticity (0.99 <e≤1). Since, in practice no collision is ideal, the simulation at ideal condition (e=1.0) is discarded at elevated temperatures.

8.4.3 Effect on granular temperature

The granular temperature is proportional to the "granular energy" of the continuum, where granular energy is defined as the specific kinetic energy of the random fluctuating component of the particle velocity [10]. Figure 8- 7 shows the time-averaged particle phase state variables, granular temperature, for a specific value of the coefficient of restitution, e=0.95. For the two axial positions shown in Figure 8- 7 (a) & (b), the amplitude of the granular energy fluctuation decreases with increasing the fluidized-bed temperatures.

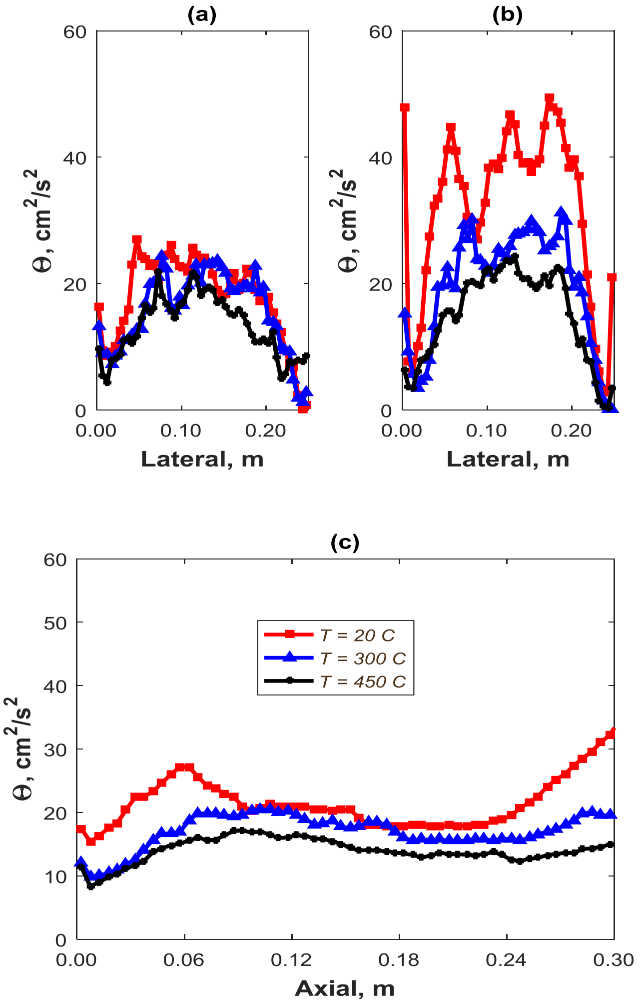

Figure 8- 7. Change in time-averaged granular temperature with fluidized-bed temperatures at e=0.95: (a) axial height at H = 0.30 m; (b) at H = 0.20 m and (c) cross-sectional average.

To gain more insight into the influence of the coefficient of restitution on bed dynamics, granular temperature is also investigated for different values of the coefficients of restitution at 450 °C fluidized-bed temperature. Figure 8- 8 shows the time-averaged granular temperature behavior with the change of particle-particle interaction coefficient. As particle-particle interactions become less ideal with decreasing the coefficient of restitution, more fluctuating kinetic energy is generated by particle pressure and viscous shear. This energy is almost completely dissipated by inelastic deformation of particles upon collision. Goldschmidt et al. [21] and Loha et al. [17] also reported this characteristic of granular temperature with the coefficient of restitution using numerical simulation at room temperature.

It is noticeable that granular temperature shows substantial fluctuation for $e \geq 0.90$, as shown in Figure 8- 8 (a & b). The fluctuation decreases and becomes less pronounced for $e < 0.90$. It is also observed that the granular temperature increases with an increase in bed height in Figure 8- 8 (c).

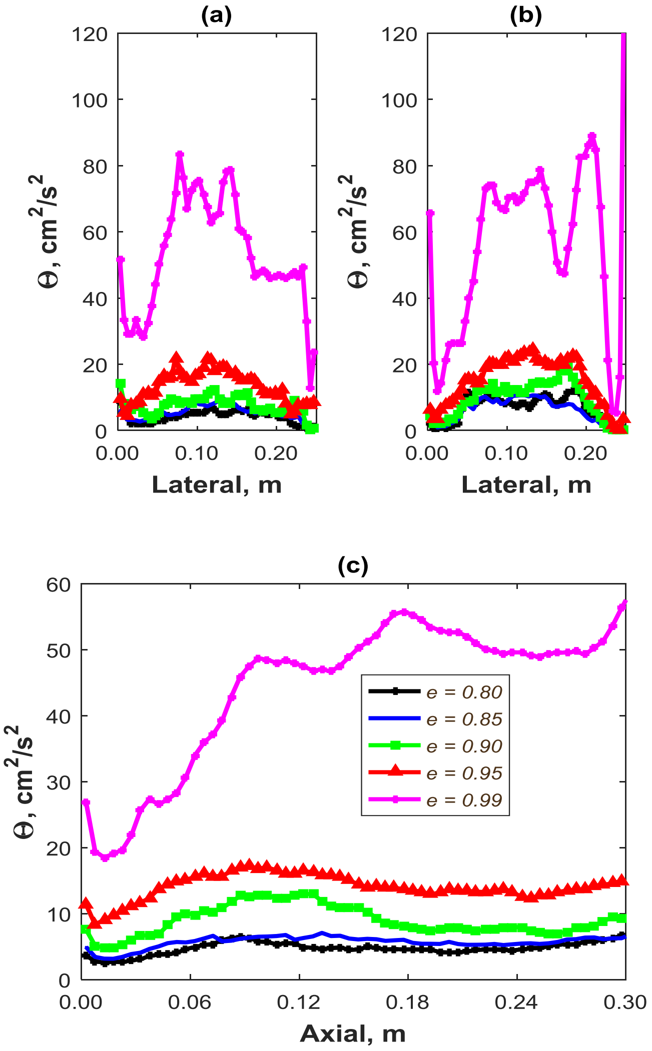

Figure 8- 8. Change in time-averaged granular temperature with restitution coefficients at fluidized-bed temperature of 450 °C: (a) axial height at H = 0.30 m; (b) at H = 0.20 m and (c) cross-sectional average. All data is time averaged from 3 to 20 s.

8.5 Conclusions

1. The hydrodynamics of dense gas-solid fluidized bed is influenced by the amount of energy dissipated through particle-particle interaction i.e. restitution

coefficient. The effect of elastic collision should be considered carefully in order to obtain realistic hydrodynamic behavior from numerical simulations.

2. The effect of particle-particle interaction coefficient can be used to describe the fluidized-bed temperature effect on hydrodynamics behavior. Experimental observation claimed that, with increasing temperature, fluidized bed experiences larger bubbles and change in fluidization behavior e.g. bubbling to slugging. Through CFD simulation, it is also shown in this study that similar hydrodynamic behavior is expected for fluidized bed operating at elevated temperature.

3. The average equivalent bubble diameter decreases with increasing fluidized-bed temperature.

4. The pressure drop and RMS of pressure fluctuations show dependency on restitution coefficient.

5. The granular temperature decreases with increasing fluidized-bed temperature and restitution coefficient.

References

[1] D. Kunii and O. Levenspiel, *Fluidization engineering*: Elsevier, 1991.

[2] S. Sanaei*, et al.*, "Hydrodynamic characteristics of gas–solid fluidization at high temperature," *The Canadian Journal of Chemical Engineering,* vol. 88, pp. 1-11, 2010.

[3] H. Cui*, et al.*, "High temperature fluidized bed reactor: measurements, hydrodynamics and simulation," *Chemical Engineering Science,* vol. 58, pp. 1071-1077, 2003.

[4] I. C. Velarde*, et al.*, "Development of an endoscopic-laser PIV/DIA technique for high-temperature gas–solid fluidized beds," *Chemical Engineering Science,* vol. 143, pp. 351-363, 2016.

[5] C. C. Pain, Mansoorzadeh, S., de Oliveira, C.R.E., "A study of bubbling and slugging fluidised beds using the two-fluid granular temperature model," *International Journal of Multiphase Flow,* vol. 27, pp. 527–551, 2001.

[6] D. G. Schaeffer, "Instability in the evolution equations describing incompressible granular flow," *Journal of differential equations,* vol. 66, pp. 19-50, 1987.

[7] D. Gidaspow, *Multiphase Flow and Fluidization: Continuum and Kinetic Theory Descriptions*. San Diego: Academic Press, 1994.

[8] M. Syamlal, O'Brien, T.J., "Computer simulation of bubbles in a fluidized bed," *A.I.Ch.E. Symposium Series,* vol. 85, pp. 22-31, 1989.

[9] C. Y. Wen, Yu, Y.H.,, "Mechanics of fluidization," *Chemical Engineering Progress Symposium Series,* vol. 62, pp. 100-111, 1966.

[10] M. Syamlal, Rogers, W., O'Brien, T. J., "MFIX Documentation, Theory Guide1," N. T. I. Service, Ed., ed. Springfield, 1993.

[11] P. C. Johnson and R. Jackson, "Frictional–collisional constitutive relations for granular materials, with application to plane shearing," *Journal of Fluid Mechanics,* vol. 176, pp. 67-93, 1987.

[12] A. Bakshi*, et al.*, "Eulerian-Eulerian simulation of dense solid-gas cylindrical fluidized beds: Impact of wall boundary condition and drag model on fluidization," *Powder Technology,* vol. 277, pp. 47-62, Jun 2015.

[13] S. Benyahia*, et al.*, "Study of the ability of multiphase continuum models to predict core- annulus flow," *Aiche Journal,* vol. 53, pp. 2549-2568, 2007.

[14] M. Syamlal and T. J. O'Brien, "Fluid dynamic simulation of O-3 decomposition in a bubbling fluidized bed," *Aiche Journal,* vol. 49, pp. 2793-2801, Nov 2003.

[15] J. Ding and D. Gidaspow, "A bubbling fluidization model using kinetic theory of granular flow," *Aiche Journal,* vol. 36, pp. 523-538, 1990.

[16] J. Kuipers*, et al.*, "Computer simulation of the hydrodynamics of a two-dimensional gas-fluidized bed," *Computers & Chemical Engineering,* vol. 17, pp. 839-858, 1993.

[17] C. Loha*, et al.*, "Effect of coefficient of restitution in Euler–Euler CFD simulation of fluidized-bed hydrodynamics," *Particuology,* vol. 15, pp. 170-177, 2014.

[18] L. Shen*, et al.*, "Digital image analysis of hydrodynamics two-dimensional bubbling fluidized beds," *Chemical Engineering Science,* vol. 59, pp. 2607-2617, 2004.

[19] V. Verma*, et al.*, "Bubble dynamics in a 3- D gas–solid fluidized bed using ultrafast electron beam X- ray tomography and two- fluid model," *Aiche Journal,* vol. 60, pp. 1632-1644, 2014.

[20] M. Rüdisüli*, et al.*, "Bubble characterization in a fluidized bed by means of optical probes," *International Journal of Multiphase Flow,* vol. 41, pp. 56-67, 2012.

[21] M. Goldschmidt*, et al.*, "Hydrodynamic modelling of dense gas-fluidised beds using the kinetic theory of granular flow: effect of coefficient of restitution on bed dynamics," *Chemical Engineering Science,* vol. 56, pp. 571-578, 2001.

[22] J. Jung*, et al.*, "Measurement of two kinds of granular temperatures, stresses, and dispersion in bubbling beds," *Industrial & Engineering Chemistry Research,* vol. 44, pp. 1329-1341, 2005.

[23] D. Geldart, Kapoor, D. S., "Bubble sizes in a fluidized bed at elevated temperatures," *Chemical Engineering Science,* vol. 31, pp. 842-843, 1976.

CHAPTER 9

Summary, Conclusions and Future Work

Global climate change is eminent due to greenhouse gas CO_2 and the need for CO_2 capture technologies is critical. Chemical looping combustion technology represents one of the most promising processes for capturing CO_2 and is the closest to commercialization due to the retrofitting advantages onto the existing power plants. Computational fluid dynamics (CFD) is a powerful-tool to provide insight useful for scale-up, design, or process optimization for reliable commercial plants reducing economic risk, and potentially allowing for rapid scale-up.

9.1 Summary of research and contributions

A 100-kW_{th} semi-batch chemical looping combustion (CLC) prototype unit for flexible gaseous fuel is designed to operate in bubbling fluidized bed condition. The unit includes two identical fluidized bed reactors - at any moment in time, one operates in air mode, and one operates in fuel mode in a cyclic manner, which eliminates the circulation solids between reactors. This configuration will minimize the gas leakage between reactors, which is a common concern in circulating fluidized bed configuration. A new design for gas distributor is presented in this study. This design study presents very useful information that can be applied in other cyclic reaction and regeneration processes.

A multi-stage numerical model has been developed to investigate the behavior of fuel reactor used in CLC. The model considers all the processes affecting to the reaction of fuel gas with the oxygen-carrier, such as reactor fluid dynamics, reactivity of the oxygen-carrier and the reaction pathway. The model predicts reasonably well when compared with experimental measurement. By understanding the oxide and reduced states of oxygen carrier in successive cycles in CLC will improve the reaction rate calculation, and thereby the prediction of fuel break-through time from the reactor will be better predicted.

The rate of mass transfer between fluidizing humid air and light and large silica gel particles is measured and computed in a lab-scale bubbling fluidized bed. It has been shown that the average interphase mass transfer coefficient decreases with the increase of mass of silica gel particles in the bed. The influence of mass of silica gel particles the interphase mass transfer coefficient has been explained using a simplified form of perturbation theory.

A modified form of Froessling's semi-empirical correlation to compute the mass transfer rate coefficient is suggested for its application in gas-solid fluidized bed simulation. It is also shown through numerical simulations that the mass transfer coefficient decreases with the increase of number of silica gel particles. Thus, the kinetic theory based CFD simulation can successfully be used to compute the mass transfer coefficients, by solving the species conservation equations, required for fluidized bed reactor designs, without using such parameters as inputs.

The Eulerian-Eulerian two-fluid model (TFM) depends strongly on grid resolution. If the discretization resolutions are not sufficient, the volume-averaged TFM equations are unable to capture the proper hydrodynamic behavior. It is shown that excessively resolved grid simulations may produce unphysical behavior of fluidized bed due to the violation of lower bound of volume average used for TFM. According to this study and findings from a literature survey, it is shown that the required grid size increases approximately in direct proportion to particle size. We propose a grid size of 18 particle diameters would be sufficient to obtain a grid-independent solution of TFM simulation of a bubbling fluidized bed of Geldart B particles.

An algorithm defined as face-masking that processes the whole-field void fraction data from 3-D CFD simulations for computing 3-D bubble dynamics is developed. The face-masking algorithm identifies discrete bubbles based on the predefined void threshold, associates bubbles across successive frames and finally, evaluates bubble properties such as centroids, equivalent diameter, aspect ratio and velocity. By recording the computation time for bubble dynamics for different cases, it is shown that the face-masking algorithm is efficient and cost effective for large-scale applications. As an automatic method, this face-masking algorithm overcomes the excessive manual work of data post-processing and is able to process large amount of data. Even though this study is focused on evaluating bubble dynamics in gas-solid fluidized beds, the algorithm itself can be easily applied and extended for detecting bubbles, drops and clusters in other areas of 2-D and 3-D multiphase flows.

The air and fuel reactor used in CLC process is thoroughly studied by CFD simulations - with and without internal horizontal baffles. It shows that internal baffles are effectively breaking large bubbles which assume to enhance the interchange of gas between the bubbles and the emulsion phase. Chemical reactions and mass transfer can be improved when bubbles are small and evenly distributed throughout the bed volume. However, experimental data is required for further validation of the simulation results.

The fluidized-bed temperature effect is incorporated in the CFD simulation by adjusting the particle-particle interaction coefficient. It is shown that the hydrodynamics of fluidized bed is influenced by the amount of energy dissipated through particle-particle interaction i.e. restitution coefficient. Through CFD simulation, it is also shown in this study that fluidization regime changes at elevated temperature, which agrees with experimental observations. The average equivalent bubble diameter decreases with increasing fluidized-bed temperature. The granular temperature decreases with increasing fluidized-bed temperature and restitution coefficient.

9.2 Future work

A number of research directions can be followed to continue this work further:

- As discussed in introduction, there are several frictional stress models available in literature which differ from one another by order of magnitudes. There is no systematic study on application of these stress models on bubbling fluidized bed simulation. In addition, when the solids volume fraction approaches that of maximum packing, the frictional stress plays a major role. Therefore, a comprehensive study on these stress models along with the consideration of the maximum solid packing limit can a future research topic. This will strengthen the predictability of CFD results in design and scale-up of CLC processes.

- This dissertation has attempted to explore and understand the parameters that influence the hydrodynamics of fluidized bed at elevated temperature. Using the quantitative experimental measurement, the fluidized-bed temperature effect can be further extended to fully understand the overall fluidization at high temperature. Reactions need to be included in the CFD model to compare predictions with experimental measurements.
- Accurate prediction of interaction force is the primary concern in the TFM CFD models. With the advent of modern computational power, lab-scale CFD simulation using the Lagrangian discrete-element model (DEM) needs to perform to fully understand the interaction force in TFM. Thus, an improvement of drag model used in the TFM model can be incorporated.

APPENDIX

ELSEVIER LICENSE
TERMS AND CONDITIONS

Oct 20, 2016

This Agreement between Md H Uddin ("You") and Elsevier ("Elsevier") consists of your license details and the terms and conditions provided by Elsevier and Copyright Clearance Center.

License Number	3973181301003
License date	Oct 20, 2016
Licensed Content Publisher	Elsevier
Licensed Content Publication	Chemical Engineering Science
Licensed Content Title	Development of an endoscopic-laser PIV/DIA technique for high-temperature gas–solid fluidized beds
Licensed Content Author	I. Campos Velarde,F. Gallucci,M. van Sint Annaland
Licensed Content Date	2 April 2016
Licensed Content Volume Number	143
Licensed Content Issue Number	n/a
Licensed Content Pages	13
Start Page	351
End Page	363
Type of Use	reuse in a thesis/dissertation
Portion	figures/tables/illustrations
Number of figures/tables/illustrations	2
Format	electronic
Are you the author of this Elsevier article?	No
Will you be translating?	No
Order reference number	
Original figure numbers	Fig. 11 and 13
Title of your thesis/dissertation	CFD simulation of chemical looping combustion system
Expected completion date	Dec 2016
Estimated size (number of pages)	200
Elsevier VAT number	GB 494 6272 12
Requestor Location	Md H Uddin 669 Sadleir way Apt 8 RENO, NV 89512 United States Attn: Md H Uddin
Total	0.00 USD
Terms and Conditions	